Polymer Mediated Assembly of Magnetic Nanoparticles, and the Effect of Nanoparticle Morphology on the Magnetic Properties of Next Generation Theranostic Agents

Sarah Martyn, B.Sc.

Thesis submitted for the Award of Doctor of Philosophy

School of Chemical Sciences

Dublin City University

Supervisors: Dr. Dermot Brougham (University College Dublin)

Dr. Blánaid White (Dublin City University)

June 2018

I hereby certify that this material, which I now submit for assessment on the programme of study leading to the award of Doctor of Philosophy is entirely my own work, and that I have exercised reasonable care to ensure that the work is original, and does not to the best of my knowledge breach any law of copyright, and has not been taken from the work of others save and to the extent that such work has been cited and acknowledged within the text of my work.

Signed: ____

ID Number: ____

Date: ____

This Thesis is dedicated to my parents with thanks and love.

Acknowledgements

Firstly, I would like to thank my supervisor, Dr. Dermot Brougham, for all of the support, advice, guidance and patience he has given me over the past few years. I have had some wonderful opportunities as part of his group and I am very grateful to have been given the opportunity to develop my skills as a chemist and to further my interest in science and research in such a supportive and approachable environment.

I would like to sincerely thank my lab colleagues and friends over the course of this Project; Dr. Jenny Merlin, Dr. Fadwa El Haddassi, Dr. Bing Wu, Dr. José Hierrezuelo, Ms. Cara Moloney, Ms Patricia Monks, Mr. Kevin Behan, Mr. Eoghan McMahon, and all the others who have made this experience both memorable and enjoyable. In particular, I'd like to thank Ms. Orla Carron, your support, encouragement and late-night writing dates have gotten me to this point, 2018 is definitely our year!

My work has greatly benefited from the different Collaborators that I have had the opportunity to work. I would like to thank Dr. Andreu Cabot and his Group in Barcelona, with particular thanks to Mr. Gihan Joshua; Prof. Siegfried Stapf; Professor Thorfinnur Gunnlaugsson and Dr. Esther Surrender; and, Dr. Andrew Kellett and Dr. Creina Slator.

I owe a particular thanks to the wonderful technical support staff in both DCU and UCD. This work would not have been possible without you and I am so grateful for all of your support and guidance over the last few years. To Mr. Vincent Hooper for your knowledge and expertise in ICP-AES, to Ms Mary Ross for all of your support and expertise in so many techniques, and to Ms. Aisling McCarthy and Mrs. Tiina O'Neill for all of your assistance and support with electron microscopy. I am eternally grateful to have had such a wonderful support team behind me through this work, Thank you.

To my friends in both Universities, there are too many of you to name individually, but you know who you are, thank you for the cups of coffee, the occasional biscuit (or 10), the motivation to get back into the lab when experiments have been going badly and the

support when I’ve needed to take a break and just complain about uncooperative samples. You have kept me (somewhat) sane, and have been the most amazing support system. I love you all and don’t know how I would have done this without you.

I can’t thank people without mentioning Spence, you have always been there with love and support (and chocolate). No matter how big or small the problem, you have been there for me and I don’t think I’ll ever be able to repay you. Thank you so much for everything.

Finally, I would like to acknowledge the love and support of my family. You have always believed in me and encouraged me to push further and achieve whatever I set my sights on. To my parents, who have fostered a love of science and curiosity in me since I was a child, thank you for all the times that you convinced me to go for an opportunity, took your free time to drive me to whichever university course I was doing that particular Saturday afternoon, and for encouraging me to do what I loved and be the best I could be. We don’t say it often enough, but I love you so much, and will forever be in your debt. This Thesis is dedicated to you, thank you.

Contents

Chapter 2: Experimental Techniques

Chapter 3: Polymer Mediated Assembly of Spherical Iron Oxide Nanoparticles

Chapter 4: Investigation into the Potential Theranostic Capabilities of Magnetic Nanoparticle Assemblies

Chapter 5: Formation and Properties of Monodisperse Cubic Iron Oxide Nanoparticles and Steps Towards Size Control

Chapter 6: Towards the Application of Polymer Mediated Assembly to Cubic Nanoparticles

List of Abbreviations

APTES	**(**3-Aminopropyl) triethoxysilane
B_{ACQ}	Acquisition field
BA	Benzyl Alcohol
BSE	Backscattered electrons
CMC	Critical Micelle Concentration
CPMG	Carr-Purcell Meiboom Gill
d-Hyd	Hydrodynamic Diameter as Determined by Dynamic Light Scattering
di-H_2O	Deionised water
d-TEM	Diameter of Nanoparticle as Determined by Transmission Electron Microscopy
DLS	Dynamic Light Scattering
EDLY	Echo Delay
FE-SEM	Field emission scanning electron microscopy
FFC-NMR	Fast Field Cycling Nuclear Magnetic Resonance
FID	Free Induction Decay
ICP-AES	Inductively Coupled Plasma – Atomic Emission Spectroscopy
IONP	Iron Oxide Nanoparticle
k_B	Boltzmann’s Constant
MFH	Magnetic Fluid Hyperthermia
MRI	Magnetic Resonance Imaging
MHz	Megahertz (1 x 10^6 Hertz)
NMR	Nuclear Magnetic Resonance
NMRD	Nuclear Magnetic Relaxation Dispersion
NP	Nanoparticle
NPC	Nanoparticle Cluster
NP/S	Non-Polarized Sequence
nm	Nanometre (1 x 10^{-9} meters)
OA	Oleic Acid

PEO	Poly (ethylene oxide)
PMA	Polymer Mediated Assembly
PPO	Poly (propylene oxide)
PDI	Polydispersity Index
PP/S	Pre-Polarized Sequence
R_1	Longitudal (spin-lattice) relaxation rate
R_2	Transverse (spin-spin) relaxation rate
r_1	Relaxivity (s^{-1} $mmol^{-1}$)
RCF	Relative Centrifugal Force
RF	Radio frequency
SAR	Specific Absorption Rate
SE	Secondary electron
SEM	Scanning Electron Microscopy
SLP	Specific Loss Power
STEM	Scanning Transmission Electron Microscopy
SPION	Superparamagnetic iron oxide nanoparticle
T_1	Spin Lattice Relaxation Time
T_2	Spin-Spin Relaxation Time
TEM	Transmission Electron Microscopy
THF	Tetrahydrofuran
σ	Standard Deviation
τ	Delay Tau
ω_L	Larmor Frequency

Thesis Abstract – Sarah Martyn, Polymer Mediated Assembly of Magnetic Nanoparticles, and the Effect of Nanoparticle Morphology on the Magnetic Properties of Next Generation Theranostic Agents

Superparamagnetic iron oxide nanoparticles are of great interest in the field of biomedicine at present due to their highly tuneable magnetic properties, which can be modulated by the application of an external magnetic field. Controlled assembly of these nanoparticles to form functional clusters allows for the improved and nuclear magnetic response, while retaining advantageous superparamagnetic character. In the first half of this thesis a novel approach for the controlled assembly of nanoparticles by a polymer mediated approach to form superparamagnetic clusters is introduced. Process optimization and the effects of assembly on the magnetic and magnetic resonance response are investigated. In the second half, nanoparticle morphology is addressed; in particular the production of cubic nanoparticles and the assembly of these into functional clusters with higher inherent magnetocrystalline anisotropy is described.

Thesis outline

Chapter 1 provides an introduction to many of the underlying principles of importance to this thesis. The underlying theories of magnetism and magnetic resonance properties are discussed, as are the practical applications of these techniques, magnetic resonance imaging (MRI), and nuclear magnetic relaxation dispersion (NMRD) analysis. The classification of magnetic materials based on their magnetic properties is discussed with a specific emphasis on superparamagnetic iron oxide nanoparticles. A review of the literature surrounding the preparation of these materials and their emergent use in clinical applications is also provided.

In Chapter 2 a closer focus is placed on the experimental techniques that are commonly used in subsequent chapters, including NMRD analysis, dynamic light scattering (DLS), electron microscopy, and atomic absorption techniques. In each case the relevant theory is presented alongside experimental conditions used and any practical considerations that should be taken when using such a technique.

Chapter 3 introduces a polymer mediated approach to nanoparticle assembly. A review of the literature surrounding magnetic nanoparticle assembly is presented, followed by the development and optimization of a new approach, Polymer Mediated Assembly (PMA). Subsequently, experiments are discussed investigating any potential systematic behaviour. By careful control over the NP and polymer conditions, assembly can be carefully controlled and is highly reproducible.

The materials developed in Chapter 3 are assessed for their theranostic potential in Chapter 4. Magnetic resonance properties are assessed using NMRD techniques and comparisons are drawn with similar materials previously analysed, allowing conclusions to be drawn about the internal architecture of nanoparticle clusters, NPCs. Addition experiments including magnetic tracking and toxicity studies are also presented.

In Chapter 5 iron oxide nanoparticles with cubic morphology are discussed. 3 synthesis strategies are assessed in the attempted development of a highly reproducible synthesis method for the preparation of monodisperse cubic NPs with well-defined edges and vertices, by thermal decomposition of iron precursors. Transmission Electron Microscopy (TEM) analysis is of vital importance to this chapter as the morphology of NPs cannot be determined by dynamic light scattering experiments.

Finally, in Chapter 6, a potential application of the PMA method developed in Chapter 3, to the NPs prepared in Chapter 5 is presented. Specifically, electron microscopy and magnetic resonance analysis techniques are used to investigate the success of the application. It is found that while complex processes are involved, and the assembly process is highly sensitive, promising NPCs have successfully been produced, and that PMA may be a suitable method for the assembly of a much wider range of NP types.

Chapter 1: Introduction and Literature Survey

1.1. Magnetization and Magnetic Materials

Magnetic nanoparticles (NPs) are particles of magnetic material typically <100nm in diameter that have been developed by one of a number of methods for use in biological or engineering applications. Magnetic NPs have attracted a lot of attention in recent years due to the significant advances that they may bring in the diagnosis, prevention and treatment of diseases. Biological sensing, pathogen separation, hyperthermia treatments and MRI imaging are only a few of the many avenues currently being explored in the area of NP research[1–3] NPs are of particular interest due to their tuneable size[2], simple preparation[4], high biocompatibility, relatively simple surface modification and their efficiency as T_2 contrast agents in MRI imaging[5].

Of the NP types being produced for commercial or research purposes, iron oxide is one of the most promising. In its bulk form iron oxide behaves as a permanent ferromagnet, however at sizes smaller than ~50 nm this behaviour changes as the material enters the single domain range. Single domain iron oxide NPs display superparamagnetic properties which is advantageous for bio-applications as it helps to ensure that the NPs are well dispersed and do not agglomerate in vivo. Aggregation could cause blockages in the lymphatic or vascular systems. A further advantage is the increased shelf life of any potential commercial suspensions of magnetic NPs. Superparamagnetism is also useful for hyperthermia treatment as the magnetic moments of the NPs may be stimulated to move by an external field[6] resulting in a local heating effect. NPs of different shapes are also of interest as the morphology of the NP affect its volume-to-surface area ratio and the dynamics of the moments, and as a result the emergent magnetic properties. Various shapes have successfully been prepared and analysed using electron microscopy as shown in Figure 1.1

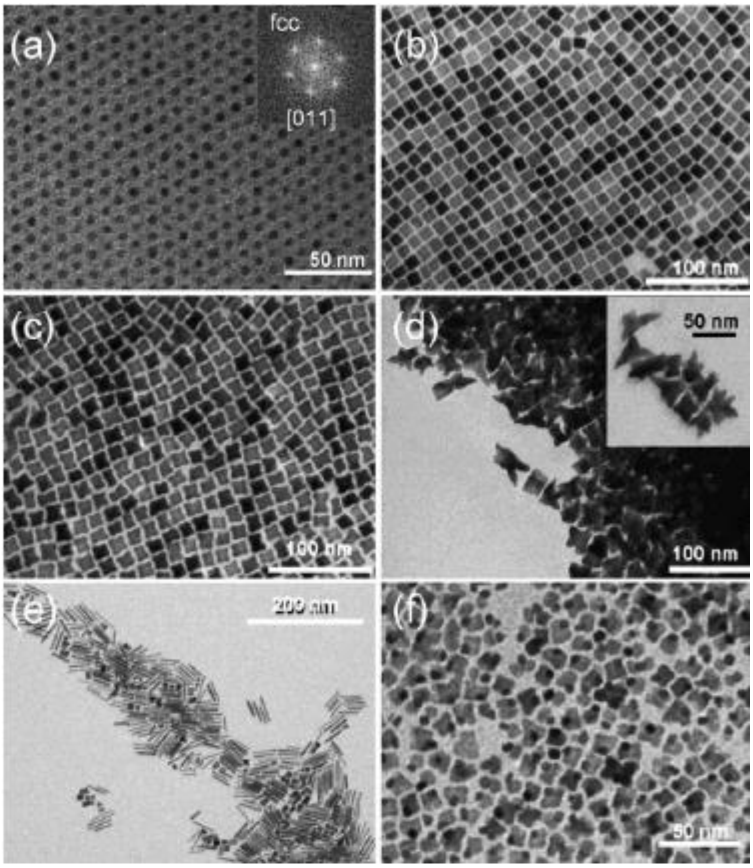

Figure 1. 1: TEM images of magnetic FePt nanoparticles of various shapes highlighting the wide variety of materials that can be produced and the controllability achievable with these materials[7]

Magnetisation is a physical force caused by the presence of unpaired electrons, resulting in attractive and repulsive forces between ‘magnetic’ objects. There are many types of magnetisation including ferromagnetism, antiferromagnetism, diamagnetism, paramagnetism and superparamagnetism. Permanent magnetisation occurs when there is an interaction between the magnetic spin states of neighbouring atoms (this is most commonly associated with ferromagnetism). Diamagnetic and paramagnetic materials develop relatively weak magnetic properties in the presence of a magnetic field (negative magnetic susceptibility and positive magnetic susceptibility), but lose these properties rapidly when the external field is removed due to thermal effects[8]. These types of behaviour are illustrated in Figure 1. 2.

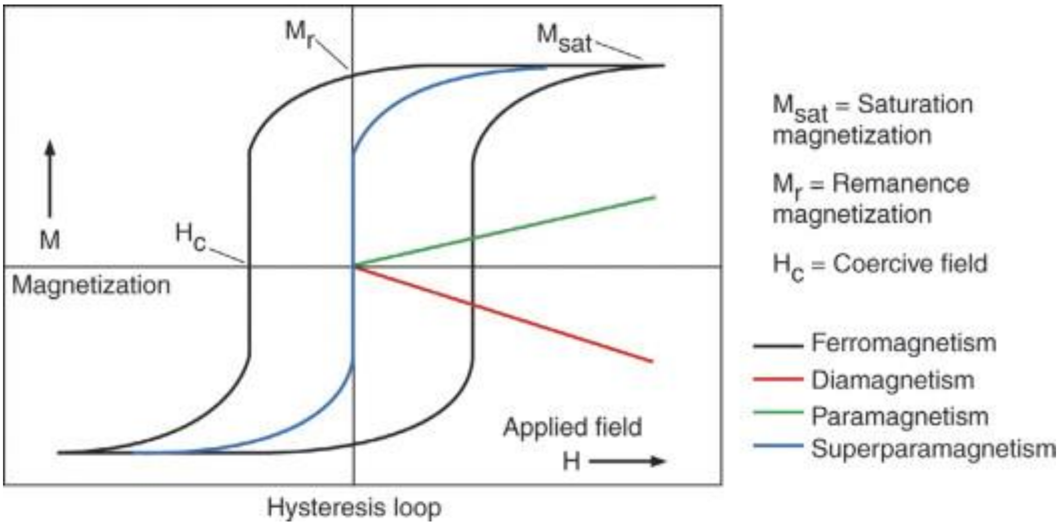

Figure 1. 2: Diagram indicating the response of different magnetic materials to the presence of an external magnetic field[9]. Paramagnetic and diamagnetic materials exhibit weak magnetic susceptibility (positive and negative respectively) in the presence of an external magnetic field, they exhibit no net magnetization when this field is removed. Ferromagnetic materials, conversely, exhibit strong magnetic susceptibility and also demonstrate magnetic coercivity, that is, to become fully de-magnetized, a magnetic field of opposite direction must be applied. Superparamagnetic materials, the subject of this thesis, behave in a similar manner to ferromagnetic materials in the presence of an external magnetic field, with no magnetic coercivity. [9]

Ferromagnetic and anti-ferromagnetic materials however, usually retain magnetisation when an external magnetic field is removed, and demonstrate magnetic coercivity. This coercivity is usually due to inter-atomic quantum mechanical exchange, which causes coupling between neighbouring atomic moments (parallel interactions in ferromagnetic materials and anti-parallel interactions in anti-ferromagnetic materials. This exchange interaction is isotropic – meaning there is no inherent directionality to the process. However, within crystal lattice structures not all directions are equivalent leading to preferred axes within the structure. In the simplest instance this is known as uniaxial anisotropy where there is one distinct preferred directionality and the magnetic moment flips about a 180° axis along this preferred axis[8].

The volume within which atomic spin states align collinearly (parallel or anti-parallel) is known as a magnetic domain. In small particles of a ferromagnetic material (< 50 nm) single domain structures are observed – the magnetization is uniform throughout the particle. In larger particles of ferromagnetic material, multi domain behaviour is observed. Each domain consists of a set of spin states aligned collinearly however, naturally these domains are ordered in such a way as to minimize magnetostatic energy. When placed into a high magnetic field, saturation magnetization is reached, forcing all domains (and thus all atomic spin states) to align with the field. This can allow the development of a permanent dipole moment within the sample – the sample retains its magnetisation even after the magnetic field has been removed[8] due to strong interdomain coupling.

Superparamagnetism occurs in magnetic nanoparticles[10] materials when the particle size is small enough to ensure that only single domain behaviour is observed, i.e. the domains are thermodynamically independent. In the presence of an external magnetic field a net magnetisation is observed aligned with the magnetic field. On the removal of the magnetic field the net magnetisation is lost as the orientation of the moments of each particle becomes randomized. It should be noted that all ferromagnetic materials display paramagnetic properties above a certain temperature (the Curie temperature), superparamagnetism can be observed below this temperature[8].

Superparamagnetic NPs are therefore extremely useful in biological applications as the net magnetisation of a suspension of NPs is zero resulting in reduced self-aggregation. Another major attraction of superparamagnetic NPs is their potential as theranostic agents. Modern medicine, in particular, cancer therapy, is wrought with horrific side effects to the patient. Multiple medicines may also interact causing unpredictable side effects. Therefore, any new agent introduced to a comprehensive treatment plan must undergo extensive trials to ensure patient safety. Combination therapies including hyperthermia are not subject to the same level of unpredictable multi-drug interactions that drastically affect conventional combination chemotherapy. Theranostic agents reduce the need for multi-drug treatments due to their ability to behave as both a diagnostic agent (MRI, Diffuse Optical Spectroscopy, etc) and as therapeutic agents (Hyperthermia, Targeted Drug Delivery, etc), thus minimising the number of agents that a patient will be exposed to, further reducing the risk of unpredictable agent interactions, and increasing treatment efficiency. The range of applications of NPs, from superconductors to self-cleaning windows, is beyond the scope of this report; however, the biological applications of superparamagnetic iron oxide nanoparticles of interest to this body of work, nuclear magnetic resonance imaging (MRI), magnetic fluid hyperthermia, and targeted drug delivery, are discussed below.

1.1.1. Nuclear Magnetic Resonance Imaging (MRI)

1.1.1.1. Nanoparticles as Contrast Agents in Magnetic Resonance Imaging

Magnetic resonance imaging (MRI), is a biological diagnostic tool based on the fundamental principles of NMR. The nucleus of interest is ^{1}H due to its abundance in the human body and its high gyromagnetic ratio. In the MRI scanner the macroscopic ^{1}H magnetization within an object placed into the external magnetic field B_0 is detected and digitally processed to form an image[11]. MRI is a highly effective diagnostic tool; it is not restricted to a particular type of diagnosis, as most tissue types contain the ^{1}H nuclei. There is also no form of radioactivity associated with this technique allowing it to be used on small children and pregnant women without any additional risks. It is a non-invasive (excluding the use of contrast agents) and highly sensitive technique.

Superparamagnetic iron oxide nanoparticles have been reported to be effective contrast agents in MRI. When accumulated in tissues magnetic NPs provide MR contrast enhancement by shortening both the spin-lattice and spin-spin relaxation times of surrounding ^{1}H nuclei. T_1 shortening processes require a close interaction between the NP and the ^{1}H which may be inhibited by a surfactant layer coating the nanoparticles. T_1 agents are generally chelates or free ions of paramagnetic materials such as gadolinium or manganese. Iron oxide NPs on the other hand are more suited to T_2 shortening effects caused by the formation of microscopic magnetic field gradients as a result of the large susceptibility difference between the NPs and the surrounding medium[12]. Dephasing of the MR signal is induced by the movement of the ^{1}H nuclei through these micro-gradients. The effect of these T_2- shortening effects can be seen clearly in the following images (Figure 1. 3), and the mechanism of these effects will be explained in more detail in the following sections.

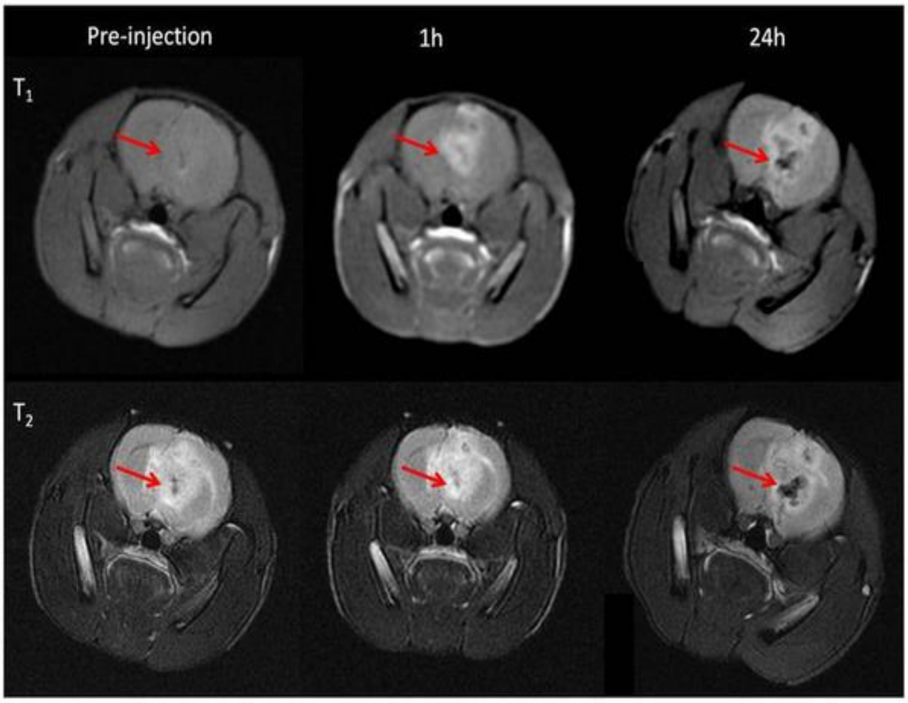

Figure 1. 3: Magnetic Resonance Image illustrating the effectiveness of a contrast agent in both T_1 weighted and T_2 weighted images. Reproduced from Huang et.al[13].

The major advantage of iron oxide nanoparticles over Gd and Mn as potential contrast agents is their low toxicity[14], high biocompatibility, higher relaxivities[15] and their potential as multimeric theranostic agents[6].

1.1.1.2. Nuclear Spin

The nuclear spin of any given nucleus arises due to combination of the spins of the individual protons and neutrons in that nucleus. The emergent nuclear spin can be considered a vector which is aligned parallel to the ‘axis of rotation’ of the particle and has a magnitude $\boldsymbol{I}$ as defined by Equation 1. 1[16]. Note: vector quantities shall be highlighted in **bold** while scalar quantities shall be in standard text format

$$|\boldsymbol{I}| = \hbar\sqrt{I(I+1)}$$

Equation 1. 1

Where h is Planck’s constant and I is the spin quantum number. All nuclei with an angular spin momentum also have an associated magnetic moment, μ, the magnitude of which is proportional to its spin and is given by Equation 1. 2

$$\mu = \gamma I$$

Equation 1. 2

Where γ is a proportionality constant, the gyromagnetic ratio, which is unique for a given isotope. The γ value for ^{1}H is 2.6752 10^{-8}rad T^{-1} s^{-1}.[17]

1.1.1.3. Behaviour of Nuclear Spins in an External Magnetic Field

The most commonly used nuclei in NMR experiments are those with spin = $\frac{1}{2}$, e.g. ^{1}H, ^{19}F, ^{13}C and ^{31}P. When placed into an external magnetic field, B_0, nuclei with a spin angular momentum will orient themselves parallel with B_0. By convention B_0 is defined as the z-axis of the Cartesian coordinate system. If a sample is placed within B_0 the moments of individual ^{1}H nuclei will begin to rotate about the magnetic field. The moments will be tilted slightly away from the axis of the magnetic field and rotate about B_0 in the direction given by the “right hand screw rule”. The motion of each ^{1}H nucleus can be described by a unique set of x, y and z coordinates where x, y $\neq$ 0 and vary with time and z is constant. The frequency of rotation about the B_0 field is proportional to the magnetic field strength and is given by the Larmor equation, Equation 1. 3

$$\omega = \gamma . B_0$$

Equation 1. 3

Where ω is the Larmor Frequency and γ is the gyromagnetic ratio.

There is a constant z-component to the precessional axis of the sample, and as a result a non-zero coupling between the ^{1}H and B_0 occurs, known as the Zeeman interaction. This coupling causes a difference in energy (ΔE) between moments aligned parallel to the B_0 field and those aligned anti-parallel to the B_0 field, where $\Delta E \propto B_0$[11].

The orientation parallel to B_0 is of lower energy, indicating that there will be more moments parallel to B_0 than anti-parallel to B_0 at a given time. The population ratio is given by the Boltzmann distribution, Equation 1.4.

$$\frac{N_{upper}}{N_{lower}} = e^{\frac{-\Delta E}{kT}}$$

Equation 1. 4

Where k is Boltzmann's constant (1.381×10^{-23} J K^{-1}) and T is the temperature in Kelvin, N_{upper} and N_{lower} are the number of magnetic moments aligned against B_0 (in the upper energy level), and aligned with the field (lower energy level) respectively, and ΔE is the difference in energy between these energy levels.

At room temperature there is typically an excess of 1×10^6 ^{1}H nuclei in the lower energy level. This unequal distribution results in a weak, but detectable net magnetic moment aligned parallel with B_0 with a magnitude of M_0[11]. The macroscopic M_0 is calculated as the vector sum of all the individual microscopic magnetic moments μ. This is the lowest energy configuration of a sample within an external magnetic field and is the state that the system will revert to following any perturbation[11], and a graphical representation of the distribution of magnetic moments at equilibrium is shown in Figure 1. 4.

If vector addition is performed on all ^{1}H nuclei in a given sample there will be no net magnetization in the xy-plane ($B_{XY} = 0$) as all of the nuclei are randomly distributed about the magnetic field (z) and rotate at the same Larmor frequency[11]. However, there is a magnetization due to the z component of the rotating magnetic moment. The signal produced by a single ^{1}H is very difficult to detect, and even within the limits of technically achievable magnetic fields (≈ 3T for medical NMR systems) the bulk NMR signal is considered weak by comparison to other spectroscopic techniques. However, the number of atoms in a standard NMR sample is very large ($\approx 10^{23}/\ cm^3$) meaning that a detectable signal can be obtained[16].

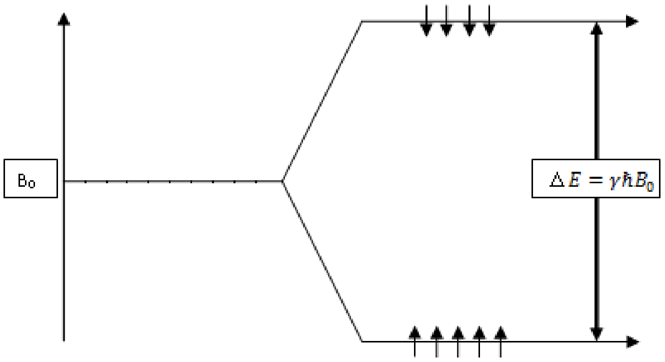

Figure 1. 4: Representation of the distribution of magnetic moments in the presence of an external magnetic field at thermal equilibrium, for a nucleus with spin = $\frac{1}{2}$

1.1.1.4. The Single Pulse NMR Experiment

In pulsed NMR a radio frequency (RF) coil is used to generate an RF pulse of frequency $\upsilon_{L.}$ This can be considered as a second field, $B_{1,}$ perpendicular to B_0. The equilibrium magnetization M_0, which is static in the xy plane, will then begin to rotate towards the xy-plane, the angle through which the net magnetization will rotate is determined by the time for which the pulse is applied. Immediately following the RF pulse M_0 will have a component in the xy-plane. If B_1 is removed, this component will continue to rotate about B_0 at the Larmor frequency. The rotating magnetization M_{XY} will induce a measurable current in the B_1 coil, (it is not sensitive to M_{Z})[16]. Traditionally the RF transmission and signal receiving are performed by the same coil (not simultaneously). After B_1 has been turned off, M_0 will begin to relax towards its equilibrium position and thus the signal observed as M_{XY} will decay to zero. This occurs by two distinct relaxation processes, spin-lattice relaxation (T_1) and spin-spin relaxation (T_2).

1.1.1.5. Spin-Lattice Relaxation

Spin-lattice relaxation, also known as T_1- relaxation is the mechanism responsible for the Z component of the magnetization returning to its equilibrium position[16], T_1 is the time taken for M_z to return to 63% of its original value[11]. This process is exponential with time, so, after $3*T_1$ 95% of the original magnetization has been restored[11]. Several processes can drive T_1 relaxation including magnetic dipole-dipole interactions, chemical shift anisotropy interactions, scalar coupling interactions and spin rotation interactions[16]. In short, any mechanism which causes fluctuations (at υ_L) in the magnetic field can potentially drive T_1 relaxation.

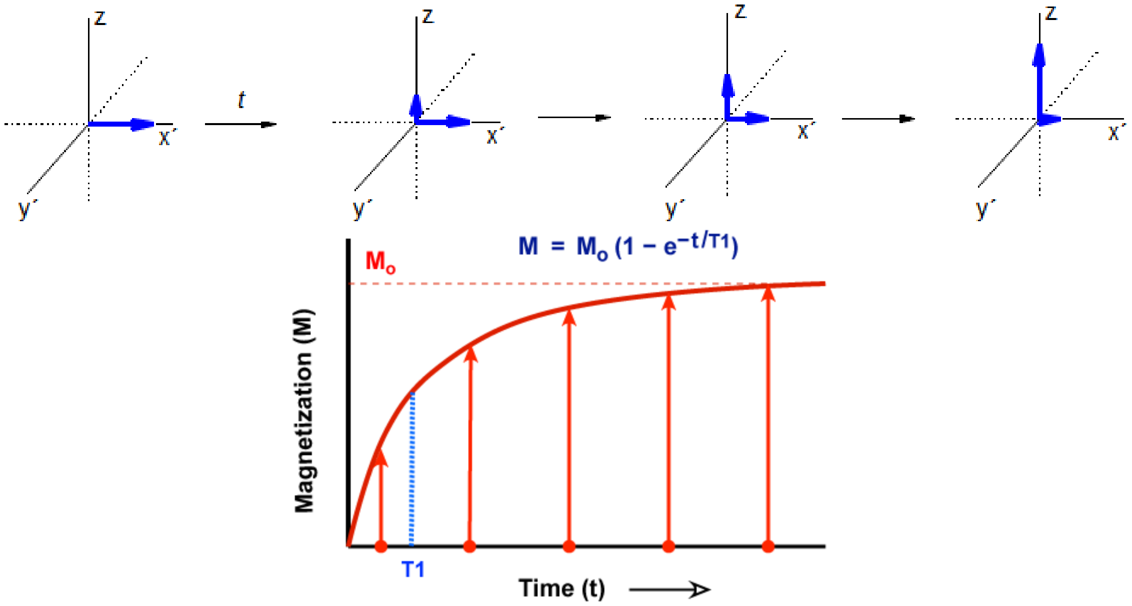

Figure 1. 5: Mechanism of T_1 Relaxation, shown in the rotating frame (top), and the corresponding magnetization recovery curve (bottom). Reproduced from Hans J. Reich, University of Wisconsin[18]

It is important to note that at equilibrium the individual magnetic moments are randomly orientated within the xy-plane, and there is a higher number of moments aligned parallel to B_0 (α state) than aligned anti-parallel to B_0 (β state). On excitation by the B_1 pulse, these moments are aligned by the RF field along one axis (in the x, y plane), i.e. the moments continue to precess about B_0, however they are no longer randomly distributed. Additionally, the number of moments aligned with the field and against the field is equal $(\frac{N\alpha}{N\beta} = 1)$. These two phenomena result in an observable magnetization in the x, y plane, but no net magnetization in the z plane. On the removal of B_1 the magnetic moments return to equilibrium $(\frac{N\alpha}{N\beta} > 1)$, as shown in Figure 1. 5. This process is known as spin-lattice relaxation, and it is a bulk phenomenon observed in the experiment for the entire sample ^{1}H magnetisation. It is also important to note that the relaxation time of a sample is dependent on its molecular environment, meaning a ^{1}H nucleus bound in a lipid molecule and a ^{1}H nucleus in an aqueous environment, will have very different relaxation times. This property largely gives rise to the tissue contrast in MRI[16].

1.1.1.6. Spin-Spin Relaxation

Spin-spin relaxation, sometimes referred to as spin dephasing, is a separate relaxation process. Immediately following an RF pulse the individual spins rotate coherently around the B_0 field at the Larmor frequency. Over time random fluctuations in the magnetic field can induce "flip-flop" transitions in the moments, where neighbouring spins change energy states (aligned parallel or anti-parallel to the field). A transition such as this can also lead to a loss of phase coherence[16]. As phase coherence is lost, M_{XY} will again decrease to zero in an exponential process, as shown in Figure 1. 6. T_2 is the time taken for the transverse component of M (M_{XY}) to decay to 37% of its original value following an RF pulse[11]. The T_2 relaxation process can occur on a much faster timescale than T_1 and it is much less dependent on the magnetic field strength than T_1. The timescale for T_2 relaxation cannot exceed that of T_1 relaxation, however, additional processes such as the spin "flip-flop" process from α to β states contribute to T_2 without affecting T_1. It has also been shown that in biological tissues T_1 increases proportionally with B_0 whereas T_2 is relatively independent on the external magnetic field[16], due to the random nature of "flip-flop" events.

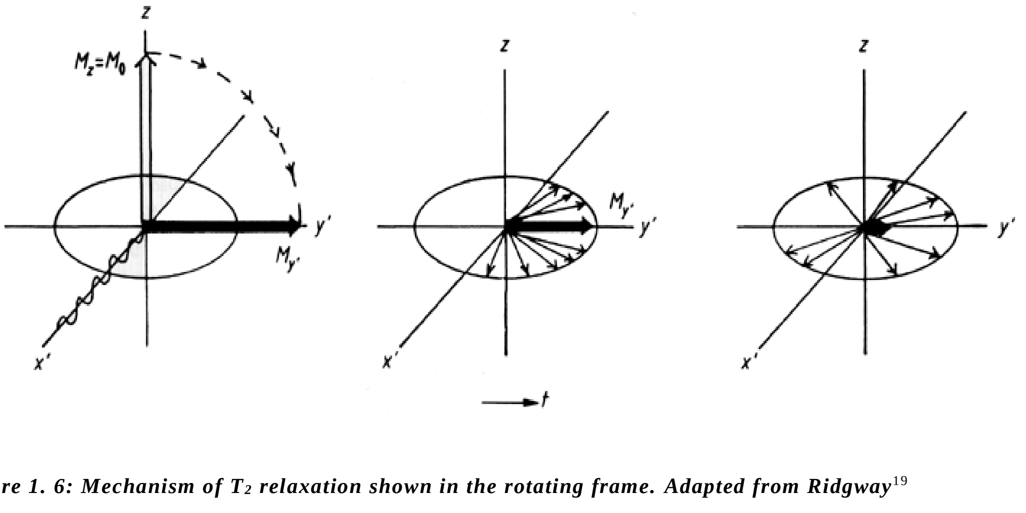

Figure 1. 6: Mechanism of T_2 relaxation shown in the rotating frame. Adapted from Ridgway[19]

The bulk M_{xy} will also dephase if there are inhomogeneities in the external magnetic field (B_0). A magnetic moment will rotate at the Larmor frequency of the field and as can be seen in Equation 1. 3 this frequency is field dependent. Hence spins in a particular volume element will spin at a different frequency to spins in an adjacent volume element if bulk field inhomogeneities are present. This can cause rapid dephasing of the M_{XY} signal, referred to as T_2* relaxation. The T_2* process does not reflect any intrinsic properties of the sample and so should be kept to a minimum. T_2* effects can be refocused to enable the measurement of T_2 using a spin-echo pulse sequence. The details of which will be outlined in Chapter 2.

1.2. NMRD Analysis

Relaxation processes arise due to fluctuations caused by dipolar (^{1}H-^{1}H, or ^{1}H- e^-) interactions. These dynamic processes happen along the same timescale as the Larmor frequency (ω). NMRD analysis can provide information relating to the motional dynamics of the molecules being probed, in the form of a spectral density function, J(ω). For a random process a plot of J(ω) against frequency, shows, that up to a frequency of $\omega \sim \tau_c^{-1}$ the available power is approximately constant, above this frequency the power available rapidly decreases, Figure 1. 7. The measurement of T_1, as a function of ν_L, enables determination of the frequency dependence of this power requirement. The mean time between the reorientational steps for a molecule, the correlation time (τ_c), is the inverse of the reorientational rate of the random motion. So, the rate can be directly determined from the half-width of the spectral density function (which is Lorentzian for a random process). The correlation time will be shorter for smaller molecules or higher temperature (faster tumbling) while the spectral density extends to higher frequencies.

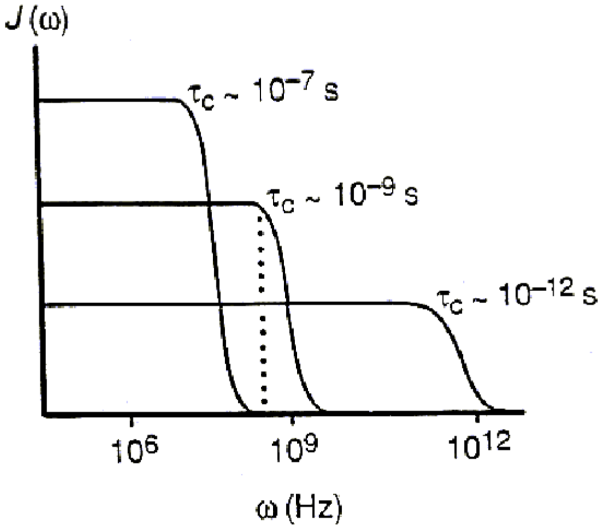

Figure 1. 7: Graphical representation of the relationship between J(ω) and ω on τ_c. Adapted from Dr. Angel C. de Dios, Georgetown University [20]

For a system where relaxation is driven by a single motion, the spin-lattice relaxation rate is determined by Equation 1. 5

$$\frac{1}{T_1} = \frac{9}{8}\left(\frac{\mu_0}{4\pi}\right)^2 \gamma^4 \left(\frac{h}{2\pi}\right)^2 \frac{1}{r^6}\left[\frac{4}{15}J(\omega) + \frac{16}{15}J(2\omega)\right]$$

Equation 1. 5

Where J(ω) and J(2ω) are the spectral density functions evaluated at the Larmor frequency and twice the Larmor frequency. ω and 2ω are the only allowed frequencies as they relate directly to the induced single- and double-spin flip transitions between the energy levels of the spin system. The NMRD profile maps out the spectral density of the motional system under study. In the case of relaxation due to a single random dynamic process, the profile is the superposition of two Lorentzian functions. For more complex dynamics the spectral densities may be non-Lorentzian (non-random), or super-positions of multiple (more than one process) Lorentzian forms. Data is acquired using a technique known as field-cycling NMR which shall be explained in more detail in section 2.1.1.

In the case of MNP suspension the solvent relaxation is driven by interaction with the dispersed NPs. This interaction is determined as a function of T_1 called relaxivity (r_1)

where r_1 is the concentration corrected relaxation rate for a given sample. NMRD profiles are a data plot of relaxivity against the Larmor frequency. In the work presented in this thesis, the r_1 values are determined over a frequency range of 100 kHz – 40 MHz. The NMRD profiles are useful for investigating the relaxation behaviour of colloidally stable magnetic suspensions. The generally accepted theory for solvent relaxation due to the presence of dispersed superparamagnetic nanoparticles (SPM theory) was developed by the Muller Group[21]. SPM theory extends the classical theory of spin relaxation to include the presence of a high Curie component, even at moderate fields, and the presence of strong magneto-crystalline anisotropy.

In this model different relaxation processes give rise to the different responses across the range of frequencies analysed. High-frequency relaxation is driven by diffusion of the solvent, with the position of the r_1 inflection point being determined by the inverse correlation time (τ_D^{-1}) for solvent diffusion past the static moment of the NP (locked to the field), and hence indirectly related to the primary particle size. This is indicated with a red dot in Figure 1. 8. The position of the peak maximum moves towards lower frequencies as the size of the primary particles increases (shorter τ_D^{-1}), and towards higher frequencies as the particle size decreases.

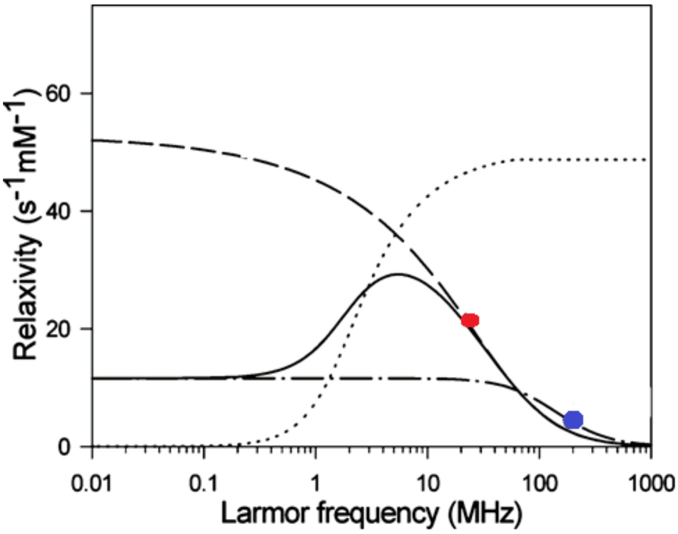

Figure 1. 8: Visual representation of the formation of a standard NMRD profile for superparamagnetic NPs from Lorentzian fits[22] where the solid line represents the NMRD profile generated, the dotted line represents the Langevin curve, the dashed line represents Brownian relaxation and the dotted and dashed line represents Néel relaxation.

Low field relaxation is governed primarily by the rate of fluctuation of the magnetization of a particle with uniaxial anisotropy, Néel relaxation. The inverse correlation time for this process is indicated with a blue dot in Figure 1. 8. This process is turned off at high field as the moments are locked. The frequency the response is a superposition of the two mechanisms, weight by the Langevin function (dotted line in Figure 1. 8).

In effect the position of the mid-frequency dip in the NMRD profile is determined by the anisotropy energy (ΔE), the difference in energy between spins aligned parallel to or anti-parallel to B_0. The amplitude of this dip is influenced by both ΔE and the nanoparticle diameter. The anisotropy energy for a single-domain particle is proportional to its volume, will therefore increase with an increase in particle diameter.

The overall amplitude of the profiles is determined by the saturation magnetisation (M_s), or the maximum magnetisation achieved in a magnetic field, meaning that highly crystalline particles will have a larger r_1 signal than their less crystalline counterparts across the entire profile.

Our Group have established the use of NMRD for evaluating magnetic order in intact suspensions of dispersed NPs or of 'soft' NP assemblies, effectively using the ^1H of the solvent as a probe of the nanostructure[23,24].

1.3. Magnetic Resonance Imaging

As in a standard NMR setup, a typical MRI scanner for human patients comprises of a superconducting magnet, to generate B_0, and an RF coil that can be used to both generate the RF pulse and detect the M_{XY} signal. Amplifiers close to the receiver coil are used to boost the signal. Two additional orthogonal gradient coils placed inside the magnet are also used, these are necessary to encode spatial information, in the perpendicular plane, into the NMR signal, as shown in Figure 1. 9: Diagram illustrating the position of the functional components of MRI within the scanner25..

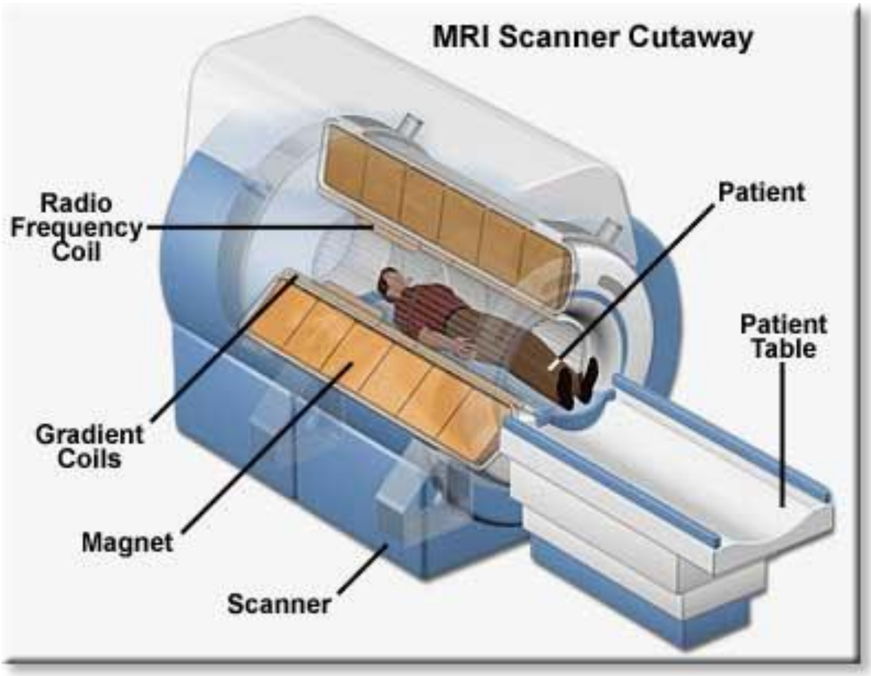

Figure 1. 9: Diagram illustrating the position of the functional components of MRI within the scanner[25].

Spatial encoding of the NMR signal is accomplished using a time-varying linear magnetic field gradient. In clinical systems the maximum achievable field gradient is 20-25 $mT.m^{-1}$ and the time taken for the field to change from 0 to the maximum gradient is in the region of 300-500 µs[1].

The first step in MRI is the localization of the RF excitation to a plane using a frequency selective excitation in conjunction with a slice selection gradient, G_{SS}[11]. By selection of the excitation frequency an interval in the xy-plane along the z axis (slice) can be selectively excited. The thickness of this slice can also be selected by adjustment of either the B_1 field bandwidth (reducing the range of frequencies transmitted results in a thinner slice), or of the gradient G_{SS}, (a stronger gradient results in a thinner slice)[16]. This G_{SS} field is shown clearly in Figure 1. 10.

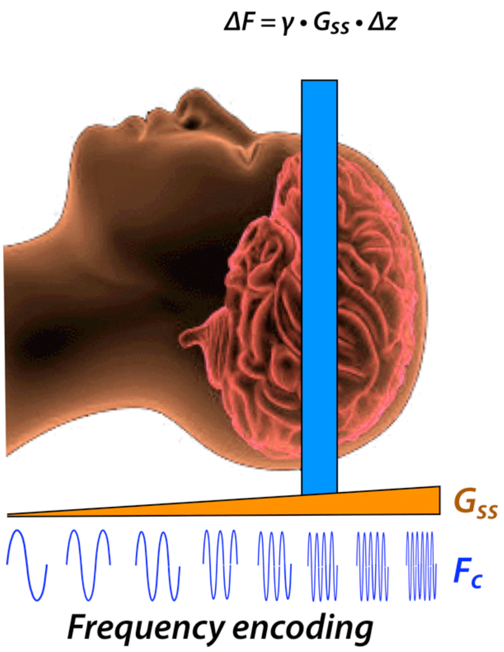

Figure 1. 10: Illustration of the slice selection process showing the field gradient and the associated resonant frequencies of each slice[26]

Following excitation, the net magnetization M_0 within the slice is oriented perpendicular to B_0, the detection of a signal at this stage would result in a single Larmor frequency. To obtain an image, two further gradients are required, and these are applied orthogonally to G_{SS}. This results in a 2-dimensional map of the selected slice, where each volume unit (voxel) has a unique phase shift proportional to its field and hence to its position along x or y, as shown in Figure 1.11.

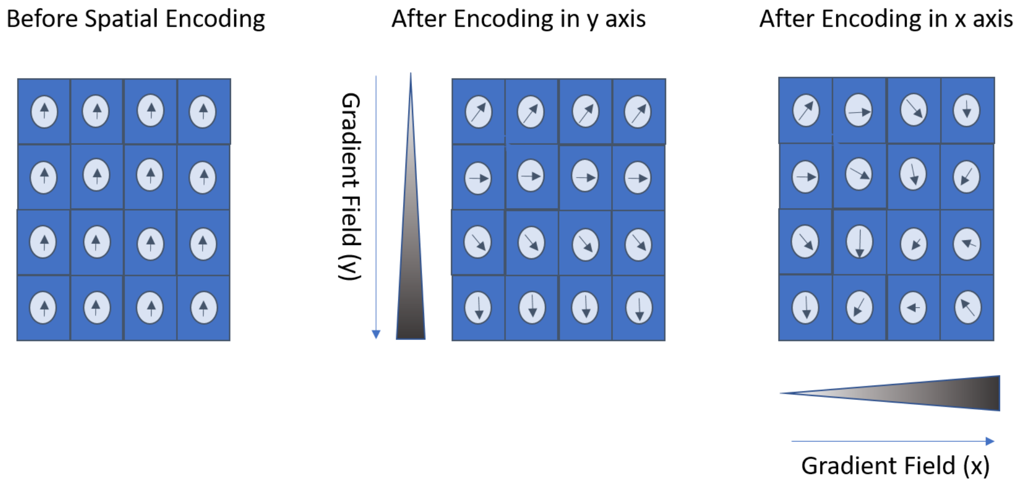

Figure 1. 11: Illustration demonstrating the mechanism of frequency and phase encoding in Magnetic Resonance Imaging

Following detection of the spatially encoded MR signal a raw data matrix is generated, this is a grid of points with the readout direction displayed horizontally and the phase encoded direction displayed vertically. All the information required to reconstruct an image is contained within this data matrix. The image data matrix is obtained by the 2-D Fourier transformation of this data. The image matrix is a frequency map of the ^{1}H signal intensity from a volume element (voxel) weighted by either the T_1 or T_2 values of the tissues contained with the sample volume[11], depending on the imaging sequence used.

1.3.1. T_1 - Weighted Magnetic Resonance Imaging

In MRI, the B_1 pulse, gradient field application and data acquisition must be performed a number of times for a given slice, in order for an accurate, high resolution image to be formed. The recovery time between scans is therefore very important. If a long recovery time (TR) is selected, all spins, regardless of location and local magnetic environment, will have sufficient time to fully recover all magnetization in the z direction. If a short recovery time is chosen, spins with a short T_1 will recover more magnetization along z than spins with a longer T_1 value (as shown in Figure 1. 12, below). This results in contrast between areas of slow T_1 and fast $T_{1,}$ where areas containing ^{1}H nuclei with fast T_1 relaxation appear brighter than the surrounding tissues. As the T_1 of ^{1}H nuclei is dependent on the local magnetic environment, contrast can be seen between ^{1}H nuclei contained in lipid cells, bone, muscle and other tissue types, and can be influenced by the presence of magnetic material[27].

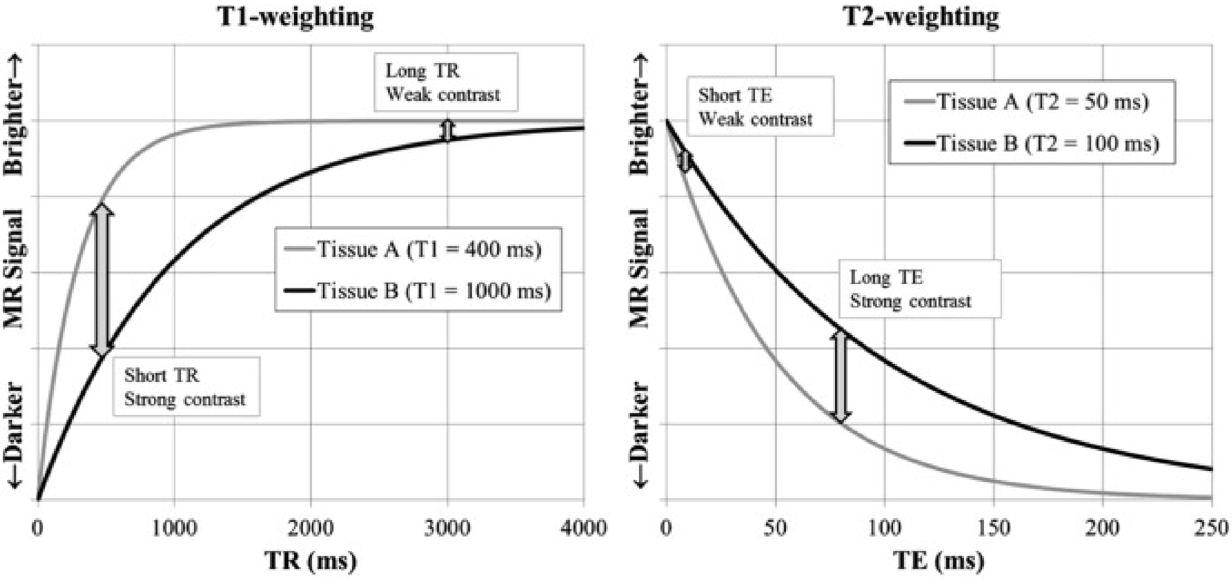

Figure 1. 12: (Left) Graphical representation of the effect of TR (recovery time between consecutive scans) on tissue samples with short (Tissue A) and long (Tissue B) T_1. Highlighting the effect of using a short (TR) to maximize contrast between these tissue types in MRI. (Right) Graphical representation of the effect of the choice of TE (Echo Time) on MR signal in T_2 weighted MRI. A short TE results in poor contrast between the Tissue samples while a longer TE (~80 ms) shows maximum contrast between the samples.[28]

1.3.2. T_2 – Weighted Magnetic Resonance Imaging

In MRI acquisition gradient fields are applied to the sample to encode spatial information into the data. However, these gradient fields can also contribute to spin dephasing. To combat this issue, a refocusing pulse is applied to the field following the $\frac{\pi}{2}$ pulse. This refocusing pulse results in a restoration of phase coherence, which maximizes the possible signal, this process is known as a spin echo[27]. The echo time (TE) is responsible for the difference in contrast. As T_2 is measured in the xy plane, it is a decay process. When a short TE is used, contrast is poor as ^{1}H nuclei from different tissue types have not yet had the opportunity to dephase. At longer TE, the difference between tissue types with different T_2 values becomes much more apparent, as shown in Figure 1. 12, with the signal for the short T_2 component selectively suppressed.

The use of Magnetic Nanoparticles as Contrast Agents for MRI

Contrast agents are chemicals, or nanoparticle suspensions that improve the contrast of an imaging technique. In MRI, contrast agents are used to alter the T_1 or T_2 response in a particular tissue type, resulting in an increase in the contrast observed in that region. T_1 agents typically reduce the T_1 of ^1H nuclei in the tissue of interest through interactions between the individual NPs and the tissue, generating positive contrast under T_1 – weighting conditions. In the case of T_2 contrast agents, magnetic NP clusters cause inhomogeneities in the local magnetic field of the ^1H nuclei of interest, increasing the rate of spin dephasing, thus reducing $T_{2,}$ generating negative contrast under T_2 weighting conditions. Note that if T_2 is strongly reduced the T_1 effect cannot be observed.

1.4. Magnetic Fluid Hyperthermia (MFH)

Superparamagnetic particles exposed to an alternating field can be used to induce the production of heat within a tissue. This heat is caused by either physical rotation of the particle (Brownian motion) or the movement of the magnetic moment within the particle, not necessarily accompanied by particle movement (the Néel effect). In theory, an alternating magnetic (or electrical) field will cause the magnetic moments of the particles to flip, aligning with the magnetic field. Heating of the particles occurs due to hysteretic losses from this flipping of the magnetic moments within the particles[29] and due to frictional losses due to the rotation of the particle[30]. The first reported use of magnetic NPs to heat tissues was in 1957 by Gilchrist et al[31]. The specific absorption rate (SAR), is the mass-normalized rate of energy absorption, and is used in assessing the viability of materials as potential hyperthermic agents. The SAR is calculated from the initial rate of temperature rise measured during heating and the specific heat capacity of the substrate (kcal kg^{-1} K^{-1})[32]. Superparamagnetic NPs have a much higher specific absorption rate compared to larger multi-domain particles (micron scale) of the same material and are the obvious choice in the further development of this field[33]. Hyperthermia is extremely useful in the treatment of cancers as tumour cells are highly susceptible to elevated temperatures.

1.5. Targeted Drug Delivery

The largest failing of the majority of chemotherapeutic agents is their relative non-specificity and potential side effects to healthy tissues. Targeted drug delivery offers an alternative to traditional therapies. Two types of targeting are possible, passive and active targeting. Both routes utilize the attachment of a therapeutic drug to a nanoparticle forming a drug-NP conjugate. One advantage of these drug-NPs is their high surface area-to-volume ratio which allows a large number of therapeutic molecules to be attached to each individual NP. In the case of magnetic NPs the nanoparticles may also be used to provide simultaneous monitoring of the biodistribution through MRI[12].

Passive targeting involves the accumulation of therapeutic agents due to their size in tumour sites. In tumours poorly organized vascular beds (leaky vasculature) can restrict lymphatic drainage, causing non-specific accumulation of NPs and therefore drug-NPs within the tumour, this accumulation is due to the size of the NPs, with smaller NPs able to freely move into and out of the tumour site, while NPs of ~100nm in diameter will freely enter the tumour and become trapped, thus accumulating in the site of interest. Active targeting on the other hand relies on an additional factor to bring the drug NPs to the area of interest. By utilizing the attraction of magnetic NPs to an external magnetic field, therapeutic agents can be directed to the site of interest using an external magnet. Generally this is done by intravenous injection of the drug-NP conjugates near the site of interest and further direction to the site of interest by the application of a field gradient followed by the controlled release of the drug[12]. Other approaches for active accumulation of drug-NP conjugates in diseased tissue involve the addition of targeting molecules to the drug-NPs. Potential targeting molecules include monoclonal antibodies, proteins, peptides and other small molecules. In some cases, these targeting molecules can also facilitate internalization of the nanoparticle into cells by receptor mediated endocytosis. The use of smaller molecules and short peptides in place of larger proteins as targeting agents may allow for increased binding affinity through multivalent attachment.

Finally, the most important step in any type of targeted drug delivery is the release of the drug at the correct site. Several mechanisms for this have been investigated including receptor mediated endocytosis, using pH responsive linking molecules or using the disintegration of temperature sensitive linking molecules via MFH[12]. In Chapter 4, some preliminary investigation into the potential for polymer mediated assemblies of nanoparticles as magnetically driven, targeted delivery agents has been described.

1.6. Preparation of Superparamagnetic Iron Oxide Nanoparticles

Magnetic nanoparticles may be synthesized by a number of routes including; co-precipitation of salts in the presence of a surfactant or surfactants, thermal decomposition of organic precursors, microwave assisted preparation, chemical vapour deposition, laser pyrolysis, sonochemical techniques and combustion synthesis[34], each having their own distinct advantages and disadvantages. Due to the novel nature of some of these techniques and other difficulties the methods still most commonly used are the thermal decomposition and co-precipitation.

1.6.1. Co-precipitation of Fe^{2+} and Fe^{3+} Salts

The most common method for the preparation of colloidally stable aqueous suspensions of iron oxide is through the co-precipitation of iron salts by the addition of hydroxides[35] as reported by Massart et al.[36,37], and Shen et al.[38]. A typical synthesis of iron oxide NPs by co-precipitation involves the mixing of ferric and ferrous ions in a 1:2 molar ratio in highly basic solutions at room temperature or elevated temperature. The physical properties of the NPs formed depend on the type of salt used, the ratio of ferric to ferrous ions, temperature, pH, ionic strength of the media, stirring rate etc[39] meaning that the reproducible synthesis of highly monodisperse nanoparticles by this method is difficult. Other issues arising from this synthesis route include poor crystallinity in the final material and high polydispersity[40].

1.6.2. Surfactant Assisted Thermal Decomposition of Metallorganic Iron Precursors

Thermal decomposition of organic precursors in the presence of surfactants counteracts these disadvantages by producing highly crystalline, highly monodisperse crystals of iron oxide. Sun and Zheng have reported a general approach for the preparation of highly monodisperse 6 nm NPs by thermal decomposition of Iron acetylacetonate, $Fe(acac)_3$, in the presence of oleic acid (OA) and oleylamine (OAm). These nanoparticles can also be used in a seed-mediated growth process to prepare larger nanoparticles without the need for a size selection process[41]. Similarly, Hyeon et al. reported the synthesis of γFe_2O_3 nanoparticles by the thermal decomposition of $Fe(CO)_5$, OA and trimethylamine oxide in octyl ether[42]. Other strategies involve the dissolution and subsequent thermal decomposition of ferromagnetic particles of iron oxide in the presence of surfactants[40].

1.6.3. Surfactant Free Thermal Decomposition of Metallorganic Iron Precursors

Although the surfactant assisted thermal decomposition methods outlined above yield highly monodisperse, highly crystalline materials, there is a major disadvantage as these particles are generally only colloidally stable in organic solvents. Phase transfer protocols have been reported however the ligand exchange process is difficult, grafting density is low and the original surfactants may still be present in unknown quantities. A practical alternative in the form of a surfactant-free thermal decomposition of $Fe(acac)_3$ has been proposed by Pinna and Niederberger using benzyl alcohol (BA) as both solvent and ligand for the synthesis[43,44]. BA is an environmentally friendly solvent and had previously been proven effective as a “soft” ligand for the synthesis of NPs. The NPs produced by this method are crystalline and NP size can be controlled. The advantages of approach include the freedom to selectively stabilize the NPs in any of a number of surfactants, they are colloidally stable in both aqueous and organic media following stabilization, the yield of the reaction is high (95%) and the particles can be stored in BA under N_2 for 6-12 months with no degradation to the NP shape or crystallinity[43]. NP shape is of increased interest to current research due to its effect on the magnetic response of the material. Chapters 5 and 6 focus on cubic iron oxide nanoparticles and a review of the current literature on the control of NP morphology can be found in Chapter 5.

1.7. Preparation of Superparamagnetic Nanoparticle Clusters

As previously outlined, magnetic nanoparticles are useful in biomedical applications as MRI contrast agents, drug delivery systems and hyperthermia mediators, however their application is largely dependent on their size, as above a certain size (~25 nm for iron oxide) multi domain behaviour is observed causing particles to have a permanent dipole, which can lead to uncontrollable particle aggregation. Alternatively, as particle size decreases, the observable magnetization also decreases. This behaviour is due to the increased surface area to volume ratio. It is believed that the outermost layer of spins within a magnetic particle are not-magnetically active, or may be “spin canted”[45]. For smaller particles the surface layer, which is not magnetically active, accounts for an increasing fraction of the total volume of the particle. While biological systems could potentially handle particles of ~100 nm in size, the tendency to aggregation of magnetic nanoparticles becomes too large for particle of size 20-30 nm. The other major issue with magnetic nanoparticles for use in bioapplications is the hydrophobicity of many surfactants used in the stabilization process.

An alternative to using larger particles to increase the magnetic response is the controlled assembly of nanoparticles into clusters (NPCs) using surfactants, ligands or polymers. These clustering agents are multi-functional as they are vital in the structural stabilisation of the cluster with respect to further aggregation, and also act to modulate the interparticle interactions, separating the NPs from each other spatially within the cluster. This prevents the formation of a cluster moment at zero field (superparamagnetism) increasing colloidal stability. Careful selection of the ligands/polymers used can further improve the usefulness of NPCs. Heat sensitive polymers with an LCST (lower critical solution temperature) of ~40^{O}C can be used with NPs as hyperthermia induced drug delivery system[46]. The polymers may increase the blood circulation time, hiding them from the immune system in vivo [47]. There is also the potential to further modify the surface of the NPC which may allow for specific targeting of certain organs in the body or even specific targeting of individual tumours allowing for directed hyperthermia treatment or enhanced localized imaging.

It has recently been observed that magnetic nanoparticles can be used as artificial atoms for the preparation of supramolecular structures. These structures have the capacity to combine the size and shape dependant properties of the magnetic nanoparticles by taking advantages of their electromagnetic properties. The forces involved in nanoparticle clustering can be tailored by changing the solvents, surfactants and/or the temperature of the assembly process; this allows a certain amount of control over the geometric configurations of clusters and the desired functions of the clusters as demonstrated in Figure 1. 13. Clustering has successfully been performed by direct solution growth and self-assembly methods[48].

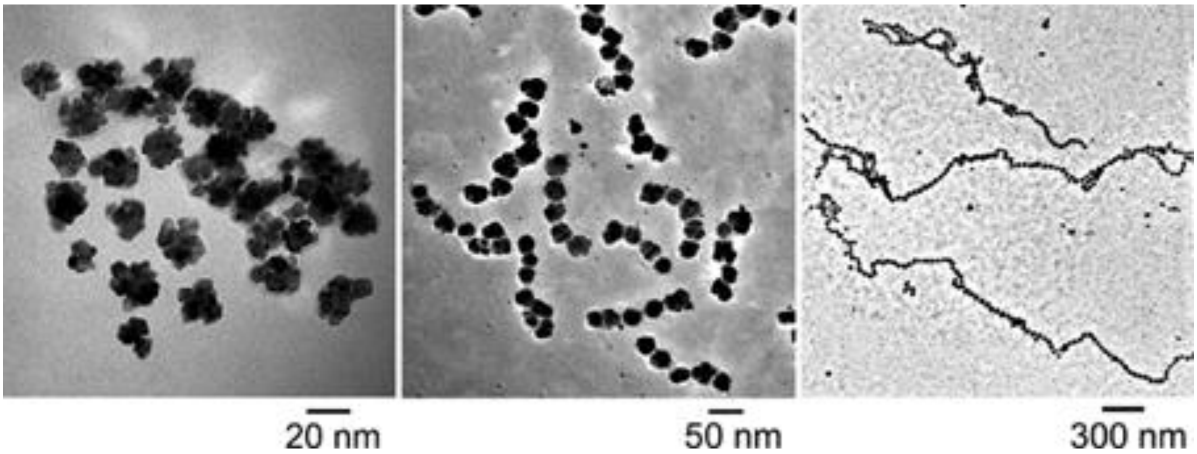

Figure 1. 13: TEM Images of Iron Oxide Nanoparticle Clusters with various superstructures[49]

Direct synthesis of nanoparticle clusters may be performed through many different single step techniques including thermolysis, solvothermal and microwave methods. Self-assembly techniques on the other hand involve the clustering of pre-synthesized nanoparticles. These techniques can be grouped further into evaporation-induced self-assembly techniques (EISA) techniques, layer-by-layer techniques and liquid-liquid interface assemblies[48]. Some examples are detailed in the introduction to Chapter 3.

One step reactions have obvious advantages in that they are more convenient, save time and are less prone to contamination effects than multi-step reactions. However, multi-step nanoparticle clustering is much more robust (can be applied to more NP types and different polymers) and as new nanoparticles are being developed every year with increasingly more tailored effects, multi-step clustering of nanoparticles is opening up as a huge field of interest as there is the potential to develop nanoparticle clusters with highly tailored composition, size, shape and properties[48]. Multi-step processes offer excellent versatility in the design, synthesis and characterization of the respective components and allow some insight into the physical processes involved in their clustering[50].

It is also possible to prepare multifunctional nanoparticle clusters by using two or more NP types in the preparation. For example some work has been performed in the clustering of iron oxide nanoparticles and quantum dots together to prepare materials that produce stronger signals in both MRI and optical imaging[48]. Clusters may also facilitate further surface modification such as ligand attachment, silica encapsulation or polymer coating[48].

There are also some issues associated with colloidal nanoparticle clusters; it is currently very difficult to position specific nanoparticles in desired locations within the clusters, robust methods have not yet been developed that enable reproducible size or shape control of nanoparticle clusters, it can be difficult to obtain uniform distribution of the nanoparticles within nanoparticle clusters throughout the sample batch, and the interaction processes that could potentially be used to manipulate the shape, size or composition of these superstructures and not well established[48]. The assembly of NPs into controlled assemblies is a major focus of this thesis and a review of relevant literature has been included in Chapter 3.

1.8. Thesis Aims

The aims of this work were to produce highly controlled assemblies of iron oxide nanoparticles using PMA. Preparation methods were developed and optimized for careful size-control of the assembly, and the NPCs produced were monodisperse, non-toxic, reproducible, scalable and had improved magnetic resonance properties compared to the primary NPs. The effect of preparation conditions on assembly was investigated and experiments to further the understanding of assembly kinetics were performed. Another aim was to determine the efficacy of these materials as potential theranostic agents through NMRD analysis, tracking experiments, and surface modification of the NPCs. Finally we aimed to improve the reproducibility of cubic NP preparation methods and to apply PMA to these cubic NPs, a feat that had yet to be reported.

Chapter 2: Experimental Techniques

2.1. Objectives

The purpose of this chapter is to outline the experimental techniques that are used frequently throughout this thesis. For each technique, when applicable, the relevant theory, typical experimental conditions used, and practical considerations to be made when using the techniques will be discussed.

2.2. Nuclear Magnetic Relaxation Dispersion Spectroscopy (NMRD)

2.2.1. Theory

Fast field cycling nuclear magnetic relaxometry (FFC-NMR) is a technique used for the determination of the field dependent relaxation properties of materials. The longitudinal relaxation time (T_1) is measured over a range of magnetic fields typically ranging from 10^{-6} T to 1 T. The upper limit is determined by technical limitations such as magnet field strength, and the time that the magnet can be maintained at high field without overheating, the lower limit is determined by local magnetic fields, in particular the magnetic field of the Earth[1]. While it is possible in theory to run a field dependence relaxation experiment using a variable electromagnet, or a series of standard magnets, it quickly becomes impractical due to the time involved[2]. FFC-NMR avoids these disadvantages using a highly reproducible variable field pulse generator and a low reluctance fast switching, 16 MHz/ms, magnet.

FFC-NMR experiments consist of 3 distinct stages:

1. Polarization
2. Relaxation
3. Acquisition

Each of which will be discussed in more detail below.

The control of magnetic field strength is of great importance to the FFC-NMR experiment as relaxation of magnetic moments is a fast process and the instrument must come to a stable field before any measurements can be made. This is done in practice by the use of current controlled systems instead of a direct magnetic field control[3], allowing for the stabilization of the magnetic field on a time-scale of a few µs. The magnetic recovery curve at a given field strength can be obtained by two types of experiment: non-polarized scan (NP/S) and pre-polarized scan (PP/S)

2.2.1.1. PP/S

A pre-polarized scan is the typical scan used in FFC-NMR; strong ^1H magnetisation is generated in the sample, i.e. the sample is polarized at a reasonably high magnetic field, so that all of the magnetic moments within the system are aligned either with or against the field (due to Heisenberg's uncertainty principle, the individual magnetic moments cannot be truly aligned with or against the field; however, the net magnetic moment in each case will lie along the field). At equilibrium at the polarizing field, there is a bulk magnetisation along the positive Z axis, i.e. along the magnetic field. The magnetisation is allowed to evolve at this polarization field B_{POL} for $4*T_1$ to achieve a high value. Following polarization, the magnetic field is switched to the field of interest, known as the relaxation field (B_{RLX}) and held for a variable time τ. Finally, the magnetic field is switched to the acquisition field (B_{ACQ}). At $B_{ACQ,}$ the sample is subjected to an RF π/2 pulse (B_1), at a frequency $\upsilon_{acq.}$ This rotates the magnetisation into the X-Y plane, when B_1 is switched off the magnetic moments within the sample will begin to precess in the xy plane and are subject to T_1 (spin lattice) and T_2 (spin spin) processes. The decaying signal, the free induction decay (FID) is recorded. Following data acquisition, a relaxation delay, that is a period of time between measurements typically $5*T_1$ at zero field, is included to allow the magnet some time to cool to room temperature before beginning the next experiment. This can significantly increase the lifespan of the NMRD instrument. The value of τ is varied from long τ values to short, ranging from a maximum of 4 times T_{1MAX} , where T_{1MAX} is the highest T_1 value recorded across the range of frequencies for a given sample, this value is determined by a probing study of 6 frequencies over the experimental range to a minimum of 1 ms. In a standard field cycling experiment this procedure is performed a number of times using different τ values, the strength of the FID is recorded for each tau value and a plot is generated in the form of a magnetisation recovery curve as seen in Figure 2. 1, below. The plot is fitted with a monoexponential function and if successful T_1 is defined as the time constant of the monoexponential fit.

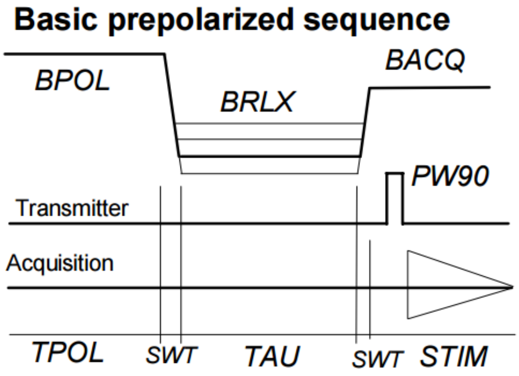

Figure 2. 1: The basic pre-polarized scan. SWT refers to the switching time of the instrument which is typically 2-3 ms. The multiple lines at B_{RLX} indicate the variable nature of this field whereas B_{POL} and B_{ACQ} are fixed.

2.2.1.2. NP/S

When the frequency of the relaxation field approaches that of the polarisation field (typically > 10 MHz), it is preferable to use a non-polarised (NP) sequence, as shown in Figure 2. 2. In this experiment magnetisation is allowed to evolve from a value of zero in the relaxation field of interest, as the difference in magnetization between B = 0 and the B_{RLX} is greater than the difference between any usable B_{POL} and B_{RLX}. Maximising the difference in the sample magnetisation at short and long τ values, provides a more accurate value for T_1. In the case of NP, the magnetisation recovery curve is an exponential growth and is fitted with a monoexponential function where T_1 is defined as the time constant of the monoexponential fit[2].

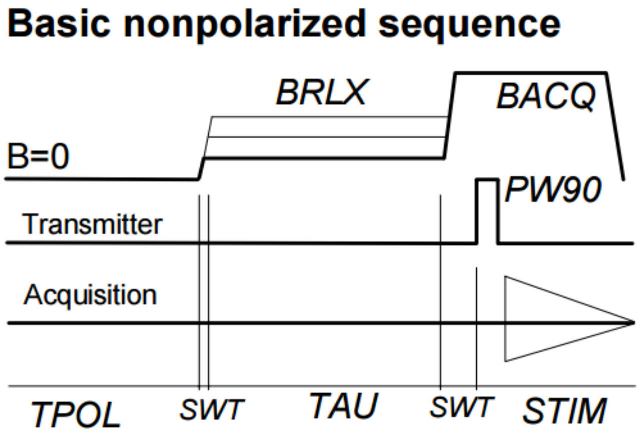

Figure 2. 2: Basic Non-Polarized sequence, the polarization in this case is performed at zero field and the magnetization allowed to grow to the relaxation field.

T_1 is only one of two relaxation mechanisms that can occur with magnetic moments in the presence of a magnetic field. As outlined in Chapter 1 dephasing of the magnetic spin can also occur in two ways T_2 and T_2*. To measure the true T_2 (also known as the spin-spin relaxation time) a different type of pulse sequence using a fixed field is used, this sequence is known as the Carr-Purcell-Meiboom-Gill Sequence (CPMG).

CPMG is a variation on the spin echo delay pulse sequence; first magnetization is rotated to the x-y plane using a standard $\pi/2$ pulse at the system frequency of the instrument. After a time τ, a 180^o pulse is applied, this inverts the magnetisation and also reverses any dephasing due to T_2*effects, but will not reverse T_2 effects as they are random. After inversion, the T_2* dephasing, refocuses the signal momentarily at a time 2τ, before dephasing again i.e. creating an echo. As this process is repeated the total magnetization (intensity of successive echoes) decays due to true T_2 processes rather than T_2* processes, by fitting the decay of the maximum signal achieved with each spin echo to an exponential function, a value for T_2 can be extracted, as shown in Figure 2. 3.

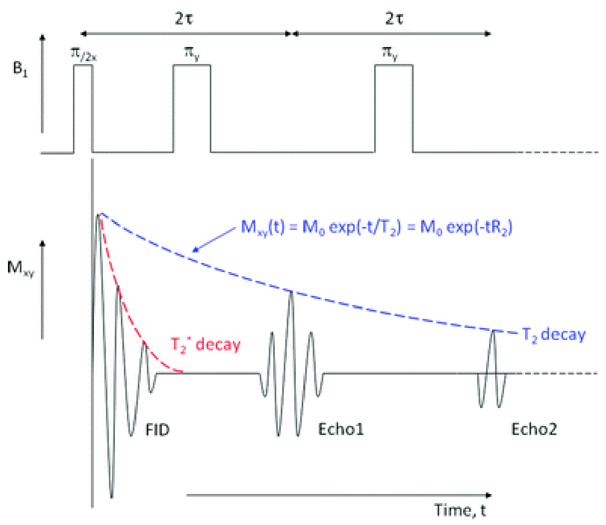

Figure 2. 3: Schematic representation of outlining the process of extracting a T_2 value from a CPMG experiment[51]

2.2.2. Experimental Limitations

The primary limitations with the field cycling NMR experiment are magnet heating caused by maintaining the sample at an elevated magnetic field for an extended period of time. Excessive heating causes degradation of the electromagnet over time; limiting the maximum time at high field. For NP and NPC suspensions this limitation can be overcome by increasing the concentration of the sample as this decreases the value of T_1. For very concentrated samples the switching time of the instrument (of the order of 1-3 ms) becomes an issue, as quickly relaxing species may have completely or mostly relaxed before the field settles, preventing measurement, this limitation may be overcome by dilution of a suspension of NPs or NPCs.

Another limitation of the field cycling NMR experiment is T_2* effects caused by magnet inhomogeneity. As T_2* effects can be very pronounced and cause rapid dephasing of the magnetic relaxation processes within the sample, care must be taken to minimize the effects of magnet field strength inhomogeneity. This limits the resolution of the instrument.

2.2.3. Experimental Setup

In this Thesis NMRD analyses were used to assess NP and NPC suspensions for their magnetic resonance properties. NMRD profiles recording the frequency dependence of the ^{1}H relaxation for NP and NPC suspensions was recorded over the frequency range 0.01–40 MHz using a Spinmaster FFC-2000 Fast Field Cycling NMR Relaxometer (Stelar SRL, Mede, Italy).

A standard NP/S sequence was used for frequencies above 10 MHz, below this value a PP/S sequence was used with a polarization field of 25 MHz, the polarization time was $4*T_{1MAX}$. A frequency B_{ACQ} of 16.3 MHz was used for ^{1}H detection, and the ($\pi/2$) pulse length was determined individually for each sample based on an angle scan to maximize the signal to noise ratio of the measurement, typically 10-20 ms. The temperature of the samples was maintained at $25^o \pm 1$ ^{o}C using a thermostatic airflow system.

To measure T_1 at frequencies higher than 40 MHz, a fixed field NMR Spectrometer, WP80 variable field magnet (Bruker, Massachusetts, USA) was used. T_1 was measured at 40 MHz and 60 MHz using an Aperiodic-Pulse-Sequence Saturation Recovery (APSR/S) pulse sequence. All of the ^{1}H magnetization recovery curves were singly exponential within experimental error and the random errors in fitting T_1 were always less than 1%. T_2 was measured using a non-polarized CPMG pulse sequence at the system frequency of 16.3 MHz using the Spinmaster FFC-2000 NMR Relaxometer and at 60 MHz using the WP80 NMR Spectrometer.

2.3. Dynamic Light Scattering

2.3.1. Theory

Dynamic Light scattering (DLS) is a powerful tool in the analysis of nanoparticle suspensions. DLS is used to analyse the behaviour of light scattered by a sample (generally liquid) enabling a number of properties to be determined[4]. The primary process involved in DLS is Rayleigh scattering. This form of scattering is observed with particles that are small compared to the wavelength of incident light, i.e. their interaction does not dramatically change the phase or amplitude of the light wave. The solvent molecules are themselves Rayleigh scatterers however microscopic and nanosized suspended particles also fulfil the Rayleigh criterion[4].

Rayleigh showed that the scattered light intensity was proportional to the square of the particle diameter and inversely proportional to the fourth power of the wavelength of light. This means that if two particles are observed one of which is 1 order of magnitude larger than the other, the larger particle will scatter 100 times more light than the smaller particle[5]. This makes DLS a very powerful tool in the analysis of nanoparticle suspensions as aggregates of nanoparticles will scatter vastly more light than the nanoparticles themselves.

In classical Rayleigh theory, the molecules are treated as independent scatterers, thus the intensity of scattered light is the sum of the intensities of the individual parts. This does not work quite so well in static light scattering experiments however as the scattered light from individual particle contributions interact both constructively and destructively and this interference is not uniform or reproducible. This problem was solved by Smoluchowski and Einstein in the early 1900s by developing the fluctuation theory of light scattering[4].

In fluids, the molecules are constantly in Brownian motion, thus light scattered from these molecules will fluctuate in intensity. If we observe a volume element (ν) which is small enough to be considered microscopic but large enough to contain a sufficient number of molecules the thermal motion will cause the number density of these molecules to fluctuate in time. The paths and positions of the molecules do not need to be taken into account and macroscopic thermodynamic concepts such as density can be used to describe the fluctuations[4]. Depending on their mass suspended particles follow the thermal motion of fluid molecules in a dampened form, the speed of Brownian motion depends on both the particle size and the viscosity of the dispersant used[5]. DLS measures the time dependant fluctuations in the intensity of scattered light to determine the translational diffusion coefficient (D) of the particle, and subsequently the hydrodynamic diameter of the particle using the Stokes-Einstein equation[5]:

$$D = \frac{k_B T}{3\pi\eta d}$$

Equation 2. 1

Where k_B is Boltzmann's constant, T is the absolute temperature (in Kelvin), η is viscosity and d is the hydrodynamic diameter of the particle.

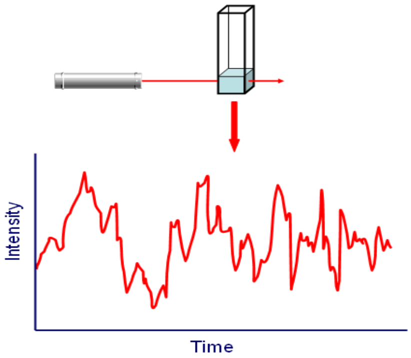

Figure 2. 4: An example of the intensity signal produced by a standard light scattering experiment[5].

A typical fluctuating signal is recorded by the instrument as shown in Figure 2. 4: An example of the intensity signal produced by a standard light scattering experiment5.Figure 2. 4 (above). Generally, at a certain time t_1 the mean signal will differ from the same signal a variable time τ later. If τ is chosen to be small the signal will not have changed by much during τ and the correlation between the two signals is high. If τ is increased the change is signal is more likely to increase and as τ tends towards infinity the correlation between the two signals approaches zero. A measure of this interdependence can be expressed in a correlation function G(τ). G(τ) is a measure of the mutual relationship in a signal. If the signal is completely random the correlation function G(τ) will remain flat, the signal is un-correlated. The generation process of the G(τ) function is shown in

Figure 2. 5. For non-periodic signals, such as those observed with liquid suspensions G(τ) is a decaying function as τ moves from 0 to ∞[4].

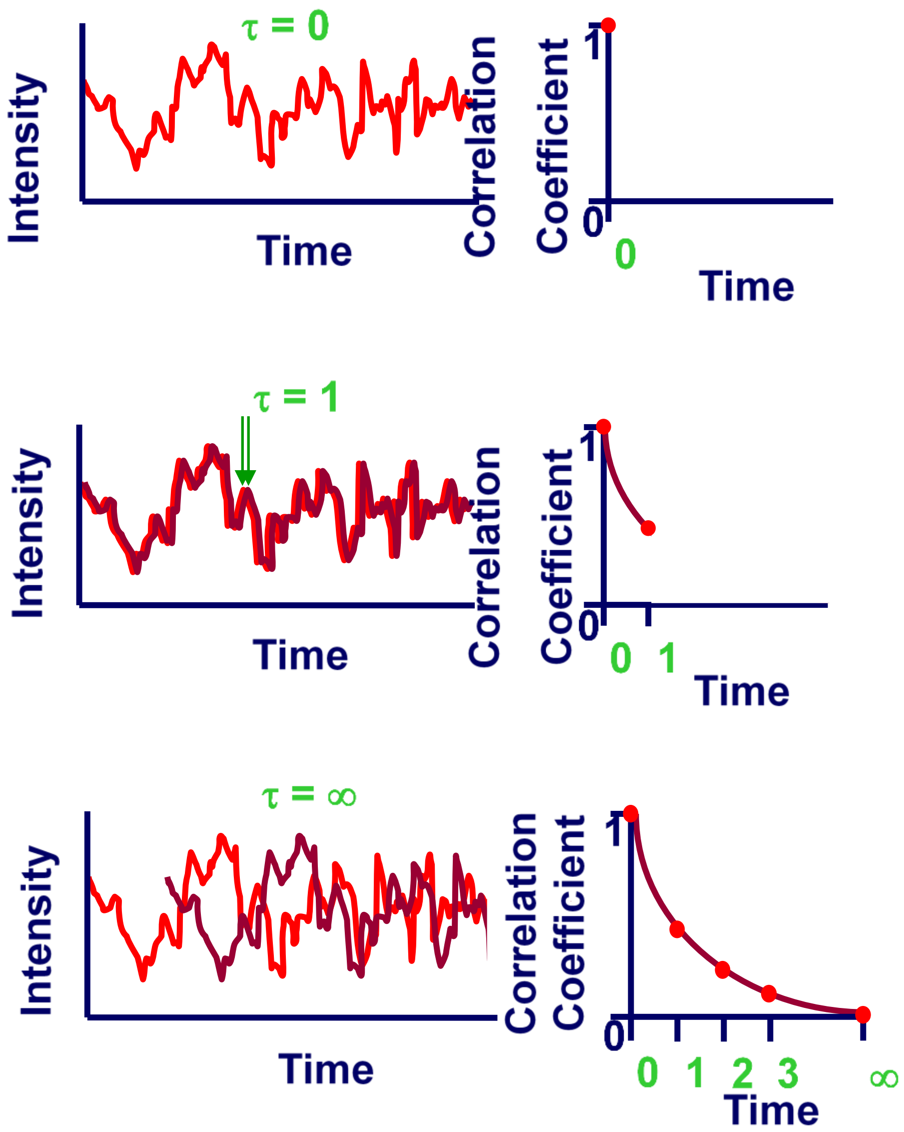

Figure 2. 5: Diagram demonstrating how the correlation function is formed by the autocorrelator in a typical DLS experiment[5].

In modern DLS this correlation function is determined using an autocorrelator. The correlator is designed to measure the degree of similarity between two signals (or one signal with itself at varying time intervals). If the particles are large the signal will be changing slowly so the correlation will persist for longer than for smaller particles. Looking at the correlogram from a measurement, such as in Figure 2. 6, can provide a lot of information about the sample. The point at which the correlation starts to decay rapidly indicates the mean size of the sample. The steepness of the curve indicates the polydispersity of the sample and the "flatness" of the baseline indicates the quality of the sample as large aggregates or dust samples will cause bumps to appear in the baseline[6].

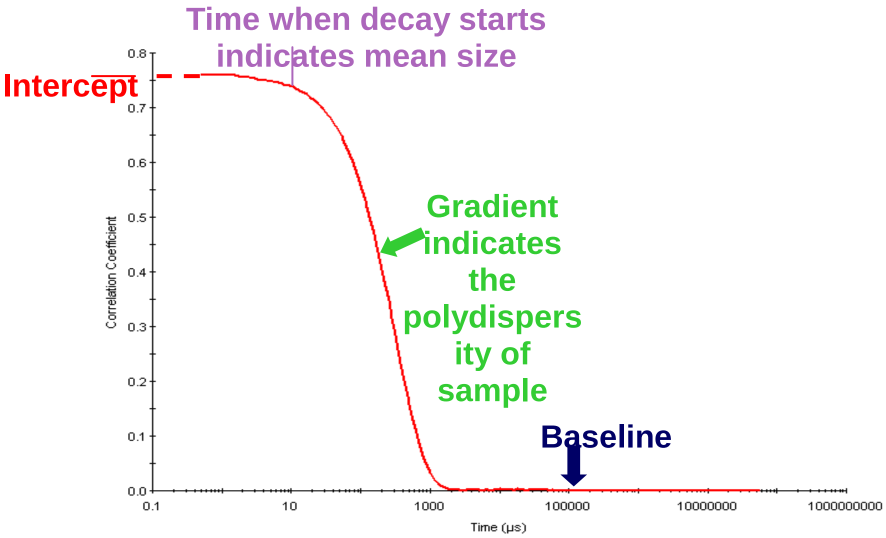

Figure 2. 6: Schematic demonstrating the features of a correlogram[6].

The rate of intensity fluctuation is dependent the translational diffusion of the particles in suspension (and thus the particle size) as can be seen in Equation 2. 2(below):

$$G(\tau) = B + A\sum e^{-2q^2D\tau}$$

Equation2.2

Where B is the plot baseline at t = ∞; A is the amplitude (or intercept) of the curve; q is the scattering vector = $(4\pi\, n/\lambda_o) * \sin(\theta/2)$, where n = dispersant refractive index, λ_o =

laser wavelength and θ = detection angle; D is the diffusion coefficient of the particle, and τ is the correlator delay time [5].

The diffusion coefficients are obtained by fitting the correlation with a suitable algorithm. Two methods are commonly used to do this:

1. Cumulants Analysis – Gives an average size (Z-average) and PDI
2. Distribution Analysis - Gives an actual size distribution from suitable data

Cumulants analysis is defined in the international standard on Dynamic Light Scattering ISO13321 (1996) and the only parameters required for analysis are the refractive index and viscosity of the dispersant. Cumulants analysis provides an intensity weighted mean hydrodynamic diameter (d_{hyd}) and a polydispersity index (PDI). Distribution analysis on the other hand uses a form of non-negative least squares (NNLS) analysis to fit the correlation function to a multiple exponential model to obtain the distribution of diffusion coefficients and hence d_{hyd}. As the Z-average is intensity weighted it is extremely sensitive to aggregates or dust particles, so it can be said that if a sample is truly monodisperse the values obtained from both methods will correlate well with each other[5].

Data produced in DLS experiments can be displayed in 3 different ways intensity distribution, volume distribution and number distribution; of these the intensity distribution is the most reliable indicator of sample quality due to the nature of light scattering as previously discussed. The volume distribution is analogous to the mass distribution of particles in separate peaks whereas the number distribution indicates the number of particles of a given size in each peak[5]. The volume and number distributions are both calculated from the intensity distribution using Mie theory and require knowledge of the particle refractive index and absorption values. This transformation also makes several assumptions:

- Particles are spherical
- Particles have a heterogenous and equivalent density
- Optical properties are known

Due to these assumptions DLS tends to overestimate the width of the peaks in the distribution so it is advised that the volume and number distributions are used only for the estimation of the relative amounts of material in separate peaks[5].

Traditionally frequency stabilized argon-ion lasers are often used as light sources in light scattering experiments due to their high stability and output power. When increasing the light intensity of the incident beam the signal to noise ratio is increased, however there are two major reasons why the light intensity should be kept at minimal levels:

1. Unwanted convection in the sample should be avoided
2. Spurious light from the cell and glass window surfaces should be minimized

For experiments with large scattering intensities such as those involving light scattered off particles or those investigating the critical region of fluids lower light levels of a few milliwatts is sufficient. In nanoscale particle sizers the most common light sources are He-Ne lasers[4].

2.3.2. Practical Considerations

As DLS is a real-time monitoring experiment the sample should consist of well-dispersed particles in a liquid medium as sedimentation will cause inconsistent results between measurements. Ideally, the dispersant should be transparent, it must have a different refractive index from the particles, its refractive index and viscosity should be known with high accuracy and it should be compatible with the sample (i.e. not cause swelling, dissolution or aggregation). Disposable cuvettes should be kept in a sealed storage container to minimize dust contamination, and glass cuvettes should be acid washed to ensure that there is no contamination from previous samples and should be stored capped to minimize dust contamination. The concentration of samples should also be considered as if a sample is too concentrated multiple scattering of light can occur and if the concentration is too low there might not be enough light scattered to produce a reliable signal.

A major disadvantage of DLS is that it assumes that all particles are spherical. The measured d_{hyd} of a non-spherical particle suspension is the diameter of a sphere that has the same average translational diffusion coefficient of the particle. This is a problem in particular with elongated (rod-shaped) particles as the diffusion coefficient of the particle may change based on the orientation of the particle, above a certain aspect ratio, two diffusion coefficients will be obtained. Particle size should then be verified using alternative methods such as microscopy.

2.3.3. Experimental setup

In this Thesis DLS measurements were performed to assess colloidal stability of NP suspensions and the d_{hyd} of NP and NPC suspensions. Measurements were also performed prior to and immediately following NMRD experiments to determine the stability of the suspensions to a 1 T magnetic field.

DLS measurements were carried out on a Zetasizer NanoZS (Malvern Sciences, UK). The light source used was a He-Ne laser with a wavelength of 633nm and a maximum power output of 4mW. Samples were measured using cuvettes with a path length of 1 cm, (aqueous samples were analysed using disposable plastic cuvettes (VWR, Ireland), and all samples suspended in organic solvents were analysed using glass cuvettes. A thermal equilibration time of 30 seconds at 25°C was used prior to all measurements ensuring reproducible testing conditions. Light intensity was detected at 173° to the incident beam, (backscatter detection). If dust was observed in the sample results, the sample was removed from the instrument, filtered using a 0.1 µm PTFE syringe filter (Whatman PLC, UK) and placed into a clean cuvette prior to analysis. Each sample was measured in triplicate to ensure that the sample was not sedimenting over time.

In this work, unless otherwise outlined, DLS results are plotted graphically as the average of 3 sequential measurements (mean d_{hyd} (nm)) , with error bars representing the standard deviation in the recorded d_{hyd} (nm) of these measurements, n=3, hereafter denoted as σ.

2.4. Electron Microscopy

2.4.1. Theory

Electron microscopy is an exceptionally powerful tool in the analysis of nanomaterials. It may be used to characterize the crystalline structure of NPs and determine the internal ordering of NPCs. Transmission electron microscopy (TEM) has in recent years become the first choice for the micro-structural characterization of materials. Image formation on a TEM requires the focusing of electrons using magnetic lenses, in particular the objective lens immediately below or around the specimen[7].

Most TEMs have thermionic electron guns which can accelerate electrons through a specific, user-defined potential energy difference between 40 and 200 kV. Below the electron gun is a series of two or more condenser lenses, these demagnify the electron beam and control its diameter as it hits the sample. This allows the operator to control the area of sample that is hit by the beam and the intensity of illumination on a given area of the sample. An aperture is present between the two condenser lenses which can be used to control the convergence angle of the beam[8].

The specimen chamber lies immediately below the condenser, generally samples are introduced into the specimen chamber using a side-entry specimen rod which holds a 3 mm diameter sample or grid, these are introduced into the system via an airlock and may be moved up to 2 mm in both the x and y directions to locate the area of interest[8].

The objective lens forms the first intermediate image and diffraction pattern, one of which is selected and enlarged by the subsequent series of projector lenses[8]. Not all of the rays in the back focal plane are required to form an image, by positioning an objective aperture (typically 0.5 – 20 µm in diameter) at a specific location, an image can be formed using only those electrons that have been diffracted by a specific angle[7]:

- When the aperture is positioned so that only the transmitted electrons are allowed through a bright-field image is formed
- When the aperture is positioned so that only some of the diffracted electrons are allowed to pass through a dark-field image is formed[7].
- The diameter of the objective aperture controls the ultimate resolution of the image formed.

Projector lenses each provide up to 20 times magnification, so a series of 4-5 lenses can easily achieve up to 1,000,000 times magnification of the sample. The final image is formed when the magnified electron beam strikes a viewing screen, usually a layer of electron-fluorescent material viewed through a lead glass window. The camera for a TEM system is located below this screen[8].

The scanning electron microscope (SEM) is similar to the TEM in that both instruments utilize an electron beam directed at the sample to generate an image; because of this it is not a surprise that the optics of both instruments are similar, the SEM also contains an electron source condenser lenses and a high vacuum system, the SEM however does not require the use of projector lenses as images are generated and magnified by a different method. The typical gun column setup for both TEM and SEM can be seen in Figure 2. 7, a comparison with light microscopy is also shown.

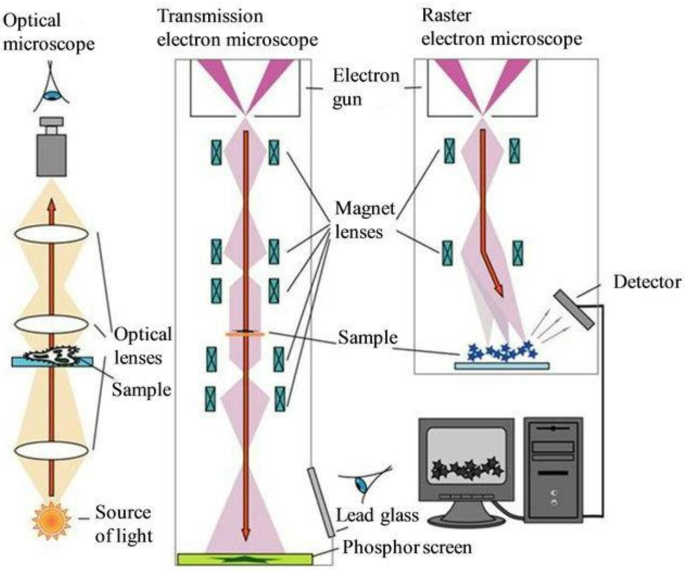

Figure 2. 7: Schematic outlining the differences between light microscopy, TEM and SEM[9].

There are two modes of analysis available with the SEM, secondary electron (SE) detection and backscattered electron detection (BSE). Secondary electrons are electrons released from the surface of the sample due to atom excitation. When the electron beam from the instrument strikes the surface of the sample energy is transferred into the sample, the excited atoms may release electrons if the sample energy is sufficient. Backscattered electrons on the other hand are incident electrons from the beam which are reflected or refracted on impact with the sample surface[8].

In SEM, a few types of electron source are routinely used, the most common of which is a tungsten filament, these filaments are sufficient in the imaging of biological and inorganic samples in the size range 0.2 – 20 µm, to reliably image nanoparticles a field emission electron source is required. Electrons are accelerated to an energy in the region 1 keV-30 keV (much lower than required for TEM). The electron beam is then demagnetized until it has a diameter of only 2 – 10 nm by the condenser lenses. This fine beam of electrons then scans across the sample in a raster pattern while a detector counts the number of low energy secondary electrons (or backscattered electrons) given off from each point of the sample, this signal is then digitized and displayed on the computer screen[8]. The brightness of each pixel in the image is determined by the amplification of the current received from the detector. This detection system is much simpler than that of a TEM and thus SEM instruments can be less expensive.

In recent years' manufacturers of both SEM and TEM systems have been moving towards a technique called scanning transmission electron microscopy (STEM). As the name suggests this method utilizes aspects of both the TEM and SEM. STEM uses a fine, focused electron beam(typically less than 1 nm in diameter), formed by a probe-forming (condenser) lens before the thin specimen to address each pixel in series, using a fast raster as in SEM, forming a sequential image as the probe is scanned across the image[10]. Two intensities are usually recorded at each point, small angle scattered electrons (bright field - BF) and high angle incoherently scattered electrons (high-angle annular dark-field – HAADF). In STEM the resolution of the scanned image is determined by the diameter of the electron beam as formed by the condenser lens system. STEM bright field images have the same contrast mechanisms as conventional TEM systems, whereas HAADF images are strongly sensitive to atomic number of the material being observed, if the sample is uniformly thick the HAADF intensity can be directly related to the average atomic number in the column at each pixel[10]. The use of field emission electron sources has greatly reduced the difference in resolution between STEM and conventional TEM instruments[8]. An FE-SEM equipped with a STEM detector therefore appears to offer the best of both worlds allowing for good resolution and versatility of analysis.

2.4.2. Practical Considerations

For any type of transmission microscopy (TEM or STEM) sample thickness must be very thin in order for the high electrons from the electron source to transmit through the sample, as such the concentration of samples deposited onto grids must be considered to avoid sample layering across the grid surface, in contrast if the concentration of nanoparticles is too low it becomes difficult to quantitatively determine the average NP size and size distribution.

In both TEM and SEM careful beam alignment must be performed to insure the clearest images and the best resolution. This must be performed at a high magnification (~100 kX magnification), imaging is then performed at magnifications between 80 kX and 1000 kX. Unfortunately, at high magnification sample burn can become a problem, sample images become less defined over time, practically this means that there is a limited window of time during which samples can be imaged. One method of combating this sample burn is by carbon coating using a sputter coater, this allows more time for the analyst to focus and capture an image, there are also disadvantages to this method, in the case of NPs in STEM mode the coating of carbon alters the observable size of the NP and in BSE and SE modes the coating of carbon can be seen covering the samples, Figure 2. 8.

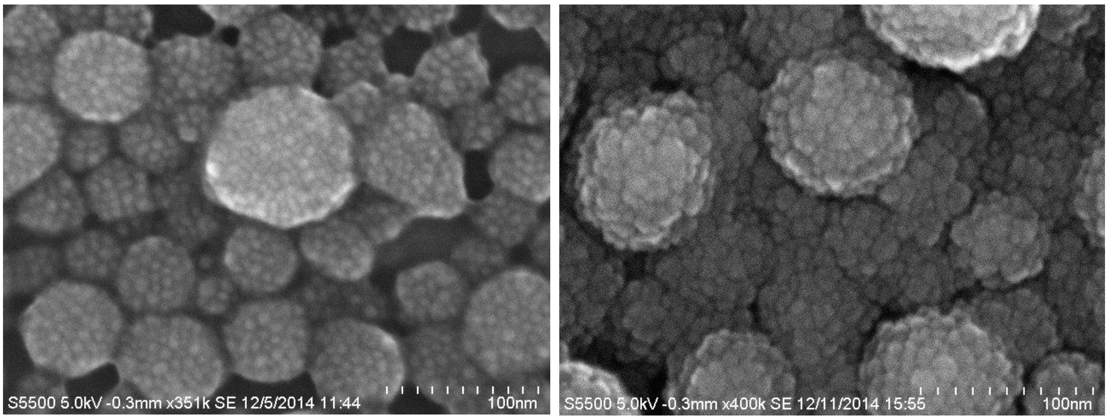

Figure 2. 8: Nanoparticle clusters imaged without (left) and with (right) carbon coating

2.4.3. Experimental Setup

TEM images were obtained using a FEI Tecnai G2 20 Twin, with variable accelerating voltage up to 200 kV for samples deposited on formvar coated 400 mesh copper grids (Agar Scientific, UK). Access to this instrument was granted courtesy of the Electron Microscopy Laboratory at the Conway Institute, University College Dublin. Samples were prepared by depositing a drop (6 µL for water-based suspensions; 2 x 3 µL for samples suspended in organic solvents) of the diluted (DLS concentration) sample onto the grid and allowing the solvent to evaporate overnight, samples covered with a clock glass to minimize dust interference, prior to imaging.

SEM images, BSE mode and SE mode, and STEM images were obtained using a Hitachi S5500 Field Emission Scanning Electron Microscope, with variable accelerating voltage up to 30 kV. Samples analysed in STEM mode were prepared as for TEM analysis as outlined above, for BSE and SE modes samples were prepared by deposition of the relevant sample (6 µL) to the surface of a 11mm x 5.5mm x 4mm Type 1 FESEM Mount (Agar Scientific, UK) and evaporation of the solvent prior to imaging.

2.5. Inductively Coupled Plasma-Atomic Emission Spectrometry (ICP-AES)

2.5.1. Theory

Atomic emission spectroscopy (AES) is one of the oldest spectroscopy techniques still in use today. In AES, the energy emitted from an excited atom as it returns to a lower energy state is used in the determination of qualitative or quantitative elemental composition for a given sample.

In AES emission is induced by first exciting the atoms in the solution. Excitation occurs by the addition of energy to an atom. This energy may be added in the form of heat (flame), light (hollow cathode lamps), electricity, or radio waves (ICP). Atomic theory states that atoms can only absorb discrete energy packets (quanta) and that these quanta can only be absorbed or emitted between precisely defined energy levels[11]. The energy difference between these energy levels is well defined and unique to each element. Energy released by an excited atom can be observed experimentally in the form of light of a highly specific wavelength. The wavelength of light produced is determined by the following equation:

$$\Delta E = h\nu$$

Where h = Planck's constant and ν= wavelength[11].

Equation 2. 2

Emission spectra are far more complex than their respective absorption spectra produced by today's technology. Absorption only occurs from the ground state of an atom to excited states, however in emission spectrometry; energy can be released not only in a fall of energy to the ground state of the atom, but also to a wide variety of intermediate energy levels, as shown in Figure 2. 9. As there is a much wider variety of wavelengths at which elements may emit light, spectral overlap can become an issue in AES, however as there are multiple analysis wavelengths an appropriate, interference free, wavelength is usually available. Wavelength selection therefore is a highly important part of method development when performing any type of AES[12].

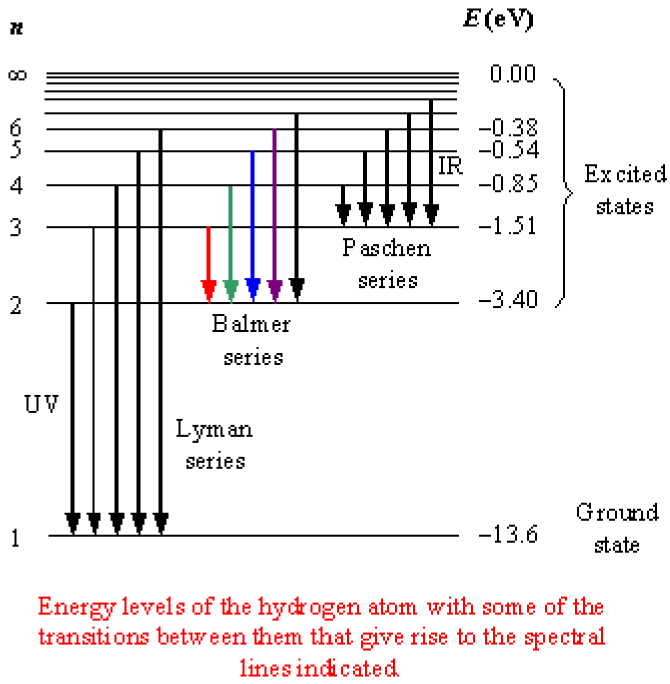

Figure 2. 9: Schematic showing the Energy levels of the hydrogen atom indicating the some of the possible transitions of energy levels[52]

Unlike atomic absorption spectrometry, which is used to quantitatively determine the concentration of a given element based on the absorption of light with a single specific wavelength, atomic emission spectrometry may be used to determine the presence of multiple elements simultaneously as the spectrum of light analysed is generated by the entire sample. In principle atomic emission spectrometry may be used for multi-element analysis of materials in solid, powdered, liquid, or gaseous form with minimal preparation of samples[11].

The major advantages of AES include the capability for multi-element analysis to be performed quickly and effectively, the lack of dependence on an external excitation source and the ability to avoid matrix interference effects by selecting an appropriate wavelength for analysis. The major disadvantage to AES is cost, as well as the potential for spectral overlapping to occur.

The process of atomic emission spectrometry involves 4 discrete stages, excitation, dispersion, detection and data processing. The means by which these stages are performed is largely dependent on the instrumentation used for analysis.

ICP-AES utilizes a high temperature plasma source to both atomize and excite the atoms within a sample. The inductively coupled plasma (ICP) is formed when energy is transferred to a gas via an induction coil[11]. The torch assembly consists of 3 concentric coaxial tubes, typically made of quartz, surrounded by a water cooled copper coil. This copper coil is connected to a radio frequency generator and is used to induce plasma formation. An electromagnetic field is passed through the copper coil inducing a magnetic field in the local environment; this causes charged particles (ions and electrons) to accelerate, the gas may be “seeded” with electrons via a spark to facilitate this acceleration. Due to the increased acceleration collisions of particles occur and sufficient energy to further ionize the gas is produced. Subsequent collisions with further gaseous atoms continue this cycle resulting in a self-sustaining plasma almost instantaneously. Two gas flows (typically argon) flow tangentially through the outer tubes of the ICP torch which cause the plasma to rotate. As a result the plasma also has a “weak spot” through which the sample to be analysed can be introduced[13].

Samples are typically introduced to the system by means of an aerosol using a pneumatic nebulizer. The solution to be nebulised is pumped into the nebulizer using a peristaltic pump and the resulting aerosols are then directed through a spray chamber. This allows for a size selection of droplets formed, as larger droplets may cause plasma flicker and thus data imprecision, smaller droplets are favoured for ICP-AES analysis. On exciting the spray chamber the remaining sample is directed into the base of the ICP, once here the sample is rapidly desolvated, decomposed and atomized. The resulting atoms are subsequently ionized and excited by the plasma.

Atomic emission from the plasma is then focused onto the entrance slit of a monochromator using lenses or a concave mirror. A monochromator is simply used to isolate a narrow range of wavelengths anywhere in a comparatively wide spectral range. The signal allowed to pass through the monochromator is then detected usually using a photomultiplier tube which is used to convert the photon flux into electron pulses which are then amplified and interpreted using a computer[13].

2.5.2. Experimental Setup

In the following work, ICP-AES was routinely used to determine the concentration of iron in NP and NPC suspensions. This was performed by preparation of a linear calibration curve in the concentration range 0.05 – 10 ppm Fe by diluting a commercially available Iron standard solution (Merck Chemicals, Germany) in 1M Nitric Acid.

The NP and NPC samples were prepared for analysis using a standard digestion protocol. 100 µL of sample was transferred into a clean, acid washed, 100 mL conical flask. 1.5 mL of concentrated HCl (~ 37% Fischer Chemicals Ltd, Dublin, Ireland) and 1 mL of deionised water were then added to the flask. The flask was then heated on a flat-bed hotplate until the sample volume reduced to approximately 100 µL. A further 1 mL of deionised water was added to the flask slowly and the solution heated to boiling. The solution was then removed and allowed to cool to room temperature before qualitative transfer to a 50 mL volumetric flask using 1M Nitric Acid (prepared in lab by dilution of concentrated Nitric acid, 70% Fischer Chemicals Ltd, Dublin, Ireland).

The solutions were then analysed using a Liberty 220 ICP Emission Spectrometer (Varian Inc, Agilent Technologies, Santa Clara, USA). An RF power of 1.1 kW was used and premium argon (Air products, Dublin, Ireland) was used as the plasma gas.

2.6. Kymography

A kymograph is a 2D graphical representation of a 1D movement over time, and is typically used in biology for instance, for tracking the movement of vocal chords during speech to assess voice disorders[53], tracking patient movement during sleep[54], monitoring cell division[55], or in the observation of protein transport by the flagella of algae[56]. The 2D graph produced typically shows lateral movement on the x axis and time on the y axis. In analogue systems, such as those used in patient movement tracking, a kymograph is produced by the response of a pen in contact with a record sheet, where the vertical position of the pen is directly related to fluctuations in the monitored variable. The record sheet is moved under the pen at a controlled rate, by a drum revolving at a constant velocity[55]. The resulting graph, such as in Figure 2. 10, provides information directly related to time. If both the measured variable and the time scale are known this information can be extracted, *e.g.* as L s^{-1} or mm h^{-1}. In this case while volume is a 3-dimensional property it is important to note that changes in it can be represented in a single dimension, such as the vertical movement of a piston in a collection vessel, such as a syringe, under constant pressure.

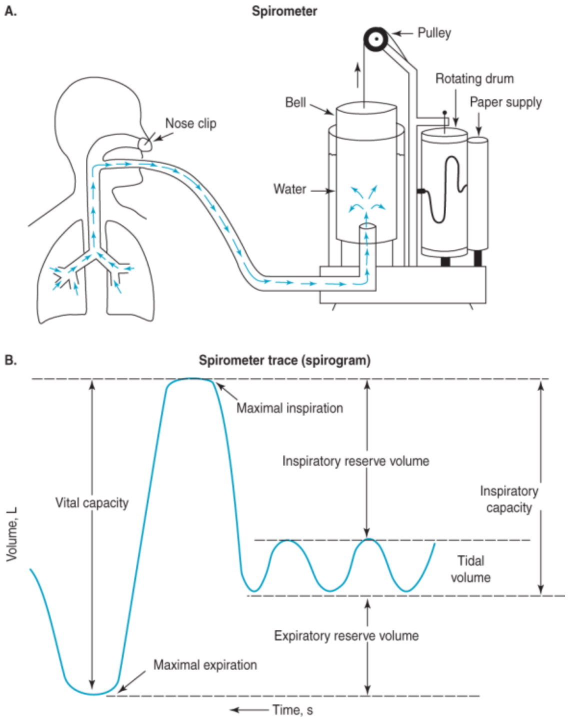

Source: Levitzky MG: *Pulmonary Physiology, Eighth Edition*: www.accessmedicine.com
Copyright © The McGraw-Hill Companies, Inc. All rights reserved.

Figure 2. 10: Typical Example of a Standard Analogue Kymograph, in this case 1 dimensional movement of the bell (up/down) can be directly correlated with internal gaseous volume, thus, a measurement of volume over time can be made.[57]

Digital kymography, is an interesting and useful development, utilizing modern image analysis techniques and algorithms to handle large data sets. A region of interest (ROI) is identified, the lateral movement of which is monitored by comparing consecutive images of a fixed area. High frame rate video allows for the capture of a large data set over a short time period, potentially up to thousands of frames per second, allowing for high resolution particle tracking. Freeware programs are now widely available to interpret images and produce a kymograph containing particle tracking for hundreds of particles simultaneously[55]. If the area of interest is fixed, the scale is known, and the frame rate of the video is known, an accurate measurement for lateral velocity can be extracted. Figure 2. 11, below demonstrates the fundamentals of this technique

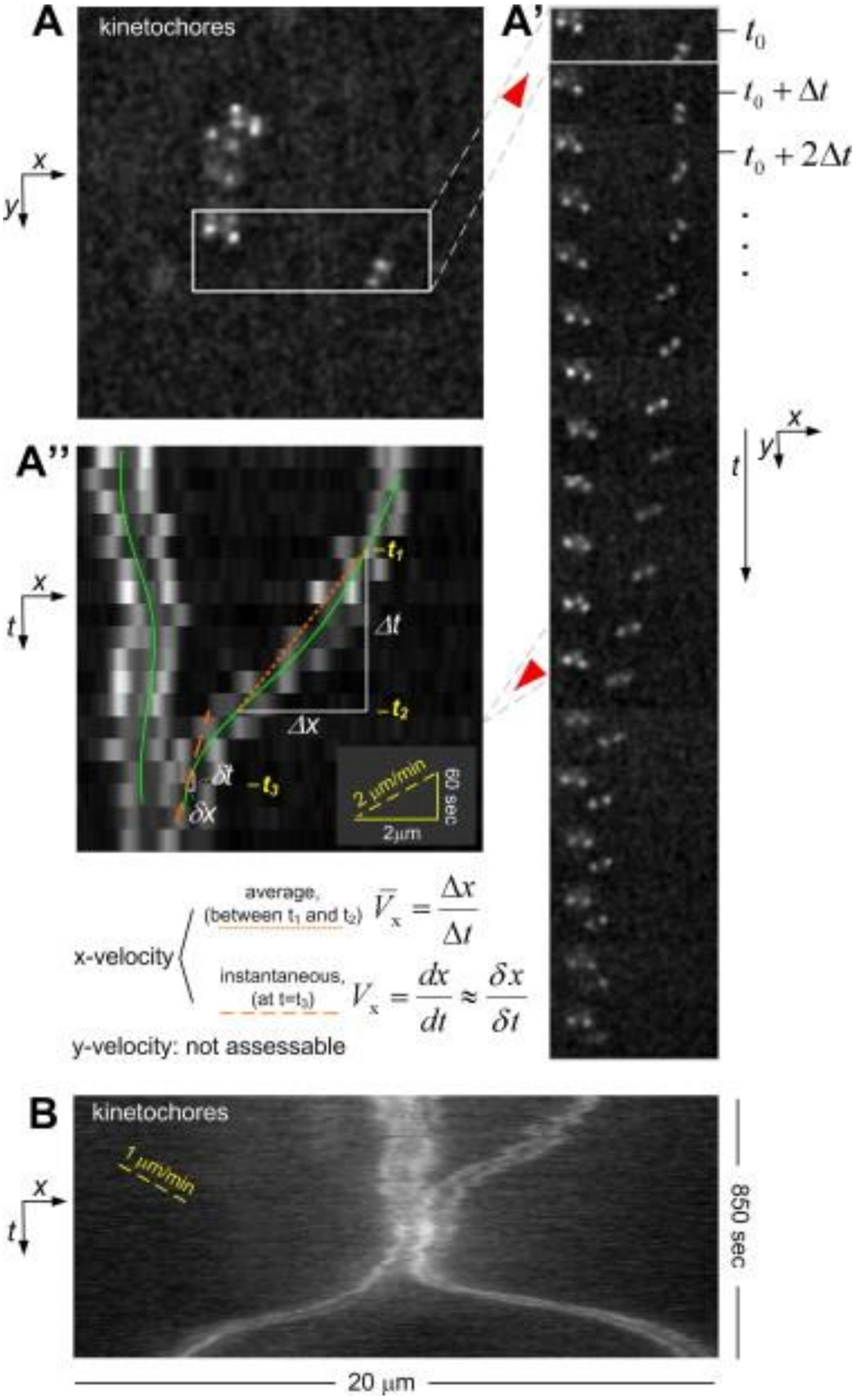

Figure 2. 11: Kymograph generation. (A) Kinetochore imaging during metaphase plate formation. The ROI defines the image window to be extracted for kymograph generation. (A') The same ROI is extracted from all sequential images, which are stacked up along the y-dimension. In this configuration, the y-axis of the kymograph is both spatial and temporal. (A'') Projected kymograph from A', where each pixel column in each ROI is replaced by a single representative pixel value (in this case, the maximum pixel value). Average velocity between t1 and t2 corresponds to the slope of the line connecting the track at these time-points (short-dashed line). Instantaneous velocity is the slope of the line tangent to the track at that time-point (long-dashed line). (B) Example of a projected kymograph derived from metaphase–anaphase sequential imaging of kinetochores. In this case, the defined ROI encloses the whole set of kinetochores[55].

Kymography is limited to the study of movement in one direction only, tracking magnetic nanoparticles in the presence of an external magnetic field gradient is potentially a suitable, and applications relevant, problem. It should also be noted that motions with a geometric shift of 10° from the axis of interest, will underestimate velocity values by less than 3%[55], thus slight deviations in the path of movement from the axis of interest will not dramatically affect the extracted velocities. The z-axis can be disregarded in these experiments as the depth of focus is quite small, if NPCs are moving vertically in the place they move out of focus and are no longer tracked by the kymography software, the main requirement is that sufficient particles remain in the field of view (FOV) for a statistically significant analysis of the dynamic NPC suspensions. There is also the potential to investigate the NPC properties. Hollow NPCs should have a lower magnetisation per nm^2 than densely packed NPCs, and thus should be attracted to a lesser degree. Hence kymography is of interest both to study the potential of NPCs for direct localization using an external magnet, and as a possible test of NPC density.

2.6.1. Experimental Protocol

In a typical experiment, the sample of interest was added to one channel of a 1 µ-Slide VI $^{0.4}$ ibiTreat Microscopy Chamber (ibidi GmbH, Martinsried, Germany) and placed into the microscope, Zeiss Axiovert 200M Inverted fluorescence microscope, with a 100x lens, 100x/1.4 Planapo Ph3 ∞/0.17, and the image focused. A small neodymium magnet, (Q-10-10-05-N, Supermagnete, Gottmadingen, Germany) was then placed in alignment with the channel in the microscopy chamber as demonstrated in Figure 2. 12, below. The image was then quickly refocused, due to magnetic interference, and a video sequence captured over 30 seconds with a frame rate of ~10 frames per second (fps), with inbuilt camera, AxioCam HR (Zeiss) and software, AxioVision SE64 Rel. 4.9.1 (Zeiss).

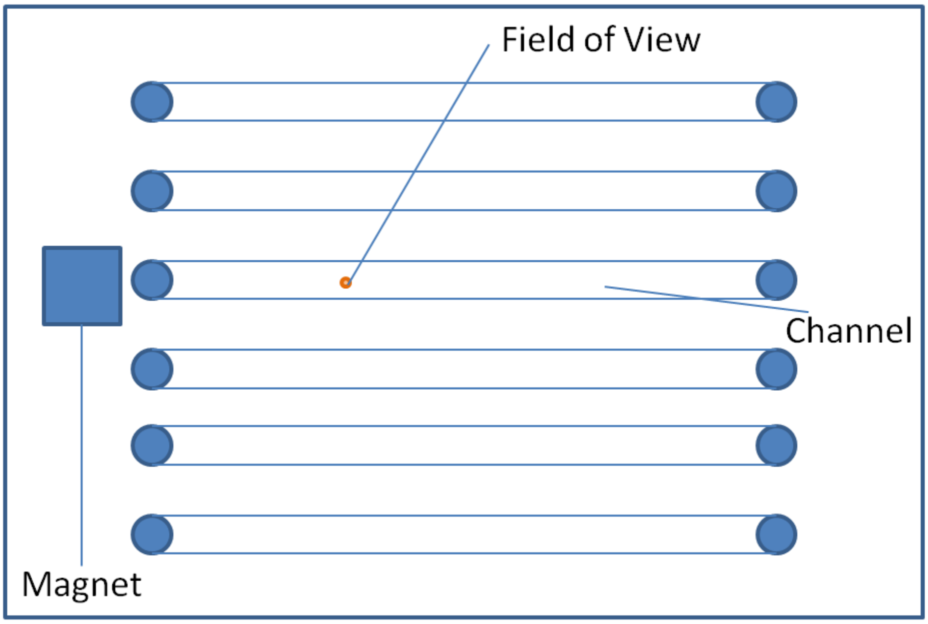

Figure 2. 12: Simplified schematic of the imaging setup from overhead. The microscope and camera in these experiments is directly above the FOV, multiple channels in the slide allows for multiple experiments to be run consecutively. The slide can be moved in all directions allowing for the selection of a field of view in any channel and the magnet was not fixed permanently in one place, but placed a constant distance from the nearest sample well in each experiment, 5 mm.

The images were recorded in transmission mode, as there was sufficient contrast between the NPCs and the solvent to be measured without the use of additional fluorescent labels. The NPCs measured were below the resolution of the microscope used, however due to the dynamic nature of the experiment changes in the suspension could be observed despite NPCs being < 1 px in diameter. The acquired video was then exported as a .tiff stack to ImageJ software, as part of the ICY software package. A freeware add-on, kymography tracker, was then used in ICY, to generate a kymograph, like that in Figure 2. 13. This kymograph was then converted to 16-bit for final analysis. The 16-bit image is then opened in ImageJ, and the diagonal lines are assessed to determine their slope. From these slope values, velocity, in pixels/frame can be derived. From this relative velocity, true velocity can be calculated when pixel scale and frame rate are known. The mean velocity and standard deviation were then calculated using a lognormal fit of the experimental data, for a minimum of 200 particles per sample.

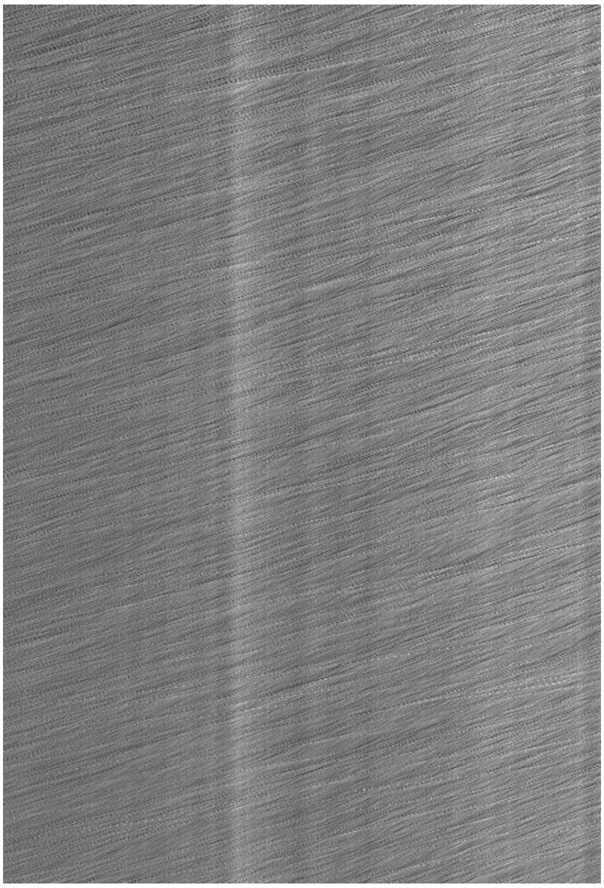

Figure 2. 13: Typical Kymograph produced by the analysis of magnetic tracking data as outlined in section 2.6.1. The sample observed in this kymograph is a PMA-NPC with d_{hyd} = 99 nm and PDI = 0.12.

Chapter 3: Polymer Mediated Assembly of Spherical Iron Oxide Nanoparticles

3.1. Introduction

As outlined in Chapter 1, there are significant benefits to the controlled assembly of superparamagnetic nanoparticles, increased total magnetic susceptibility, increased in-vivo circulation times, increased “stealth” from the immune system, and lower risk of uncontrolled agglomeration compared with individual magnetic NPs of similar total volume. In this chapter a polymer mediated approach to nanoparticle assembly will be presented, which includes method development to systematic study of the effects of assembly on the NPCs produced.

The aims of this study include the preparation of size-controlled assemblies of nanoparticles, the development of a robust, highly reproducible method for the preparation of these size-controlled NPCs with low polydispersity (PDI) with the possibility of significant scale up, potentially to the industrially relevant scale. A series of experiments were performed and successfully used to achieve these aims. Size controlled assembly was determined within the size range 50-200 nm, with high dispersible yields and low polydispersity. The method was found to be highly reproducible (σ <10%) and could be scaled from a 2 mL lab scale, to a 100 mL scale with no effect on the d_{hyd} of the NPCs prepared (σ <10%) and a decrease in the PDI as sample size increased (PDI = 0.103 at 2 mL scale, PDI = 0.025 at 50 mL scale). In the first half of this chapter the focus will be on the preparation of size-controlled, scalable assemblies with low polydispersity, then in the second half the effect of assembly parameters on the cluster formation will be discussed.

3.1.1. Single-Step Routes for Preparation of NPCs

Many research groups have reported the successful synthesis of stabilized nanoparticle clusters by single step reactions. These can largely be subdivided into two reaction techniques, co-precipitation reactions and thermal decomposition in a polymer matrix. In general, co-precipitation techniques involve the preparation of magnetic nanoparticles from iron salts in the presence of a polymer and a reducing agent which, under optimised conditions, produces water-soluble magnetic colloidal nanoparticle clusters which are suitable for further surface modification[58], magnetic separations[59] and biomedical sensing applications[60].

The work from Ditsch et al[61] was one of the first reported successful preparations of colloidal nanoparticle clusters by co-precipitation in the presence of a polymer and reducing agent. Aqueous solutions of iron salts were mixed vigorously with polymer and ammonium hydroxide at 80°C for an hour, producing magnetic colloidal nanoparticle clusters. This report also details the effect of polymer molecular weight on the cluster size, the effect of polymer concentration on cluster stability, the effect of attachment group density and further surface modification techniques to produce tailored macromolecular structure. From the work displayed it was concluded that the two most important factors in the design of purpose-built clusters are optimising the molecular weight (as this can affect cluster stability) and the amount of polymer used in the preparation.

A similar approach was taken by Corr et al[62]. In this report polysodium-4-styrene was used to produce stable magnetic nanowire structures. $FeCl_3.6H_2O$ and $FeCl_2.4H_2O$ were dissolved in water. Polymer solutions in water were then added in controlled volumes to the iron solutions prior to the introduction of aqueous ammonia until a pH of 9 was achieved. The resulting suspensions of nanoparticle clusters form extended assemblies on drying. When dried in the earths' magnetic field, some sample aggregation is observed, however when an external magnetic field is applied the particles were found to form macroscale chains or "nanowires", TEM shown in Figure 3. 1. It was reported that the negatively charged polymer was responsible both for NP stabilization and as a template for the nanowire assembly as neighbouring particles may be cross-linked by the polymer molecules due to interpenetration of the polymer shells. It was also found that increasing the polymer ratio had a direct effect on the width of these nanowire assemblies[62].

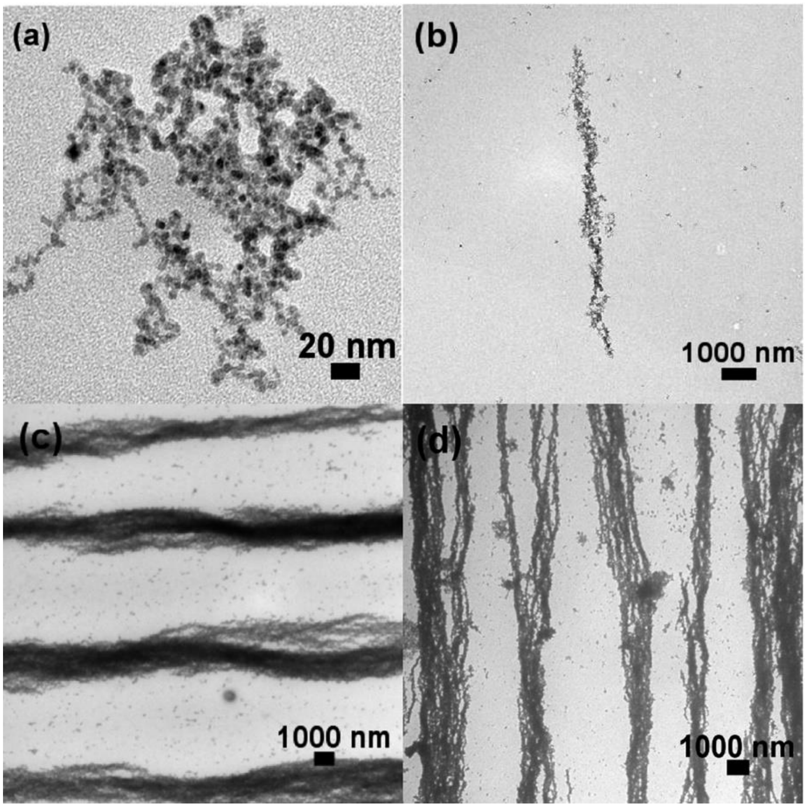

Figure 3. 1: Nanowire assemblies produced by drying in the presence of an external 1.5 T Magnetic field[62]. (a) shows NPs produced by the same procedure, dried in the absence of an external magnetic field.

In the method outlined by Luo et al[58], colloidal nanoparticle clusters were produced by means of a modified solvothermal reaction. Iron (III) chloride is dissolved in ethylene glycol in the presence of sodium acetate at 160°C for 1 h then heated in an autoclave to 200°C for 6 to 12 hours. By changing the duration of autoclaving the size of clusters produced can be controlled from 90-260nm with prolonged heating producing larger clusters. The polydispersity of these cluster formations was relatively low, with Dynamic Light Scattering (DLS) analysis showing a value for the poly dispersity index (PDI) of 0.173 for clusters of 223 nm. It should be noted however that upon further functionalization of these nanoparticle clusters (silica coating with a cross-linked poly(N-isopropylacrylamide) shell) the reported polydispersity is reduced to a value of 0.015 (with a cluster size of 759 nm). The sizes and polydispersities reported are consistent between sizing methods, TEM and DLS.

The method outlined by Ge et al[60] alternatively, employs a high temperature thermolysis reaction in the synthesis of polymer stabilized clusters. Iron (III) Chloride and poly (acrylic acid) are dissolved in diethylene glycol at 210°C and stirred vigorously. A sodium hydroxide stock solution in diethylene glycol is then added to the hot mixture, producing water and increasing the pH within the reaction system allowing the hydrolysis of iron chloride. Under optimized conditions the magnetite nanoparticles formed produce stable three-dimensional clusters that can be size controlled from 30 nm to 80 nm by varying the amount of sodium hydroxide introduced into the system. While the cause of size control is not known it is believed that minute differences in the pH change induced in the system may cause the size dependence of clustering as demonstrated in electron microscopy images, Figure 3. 2.

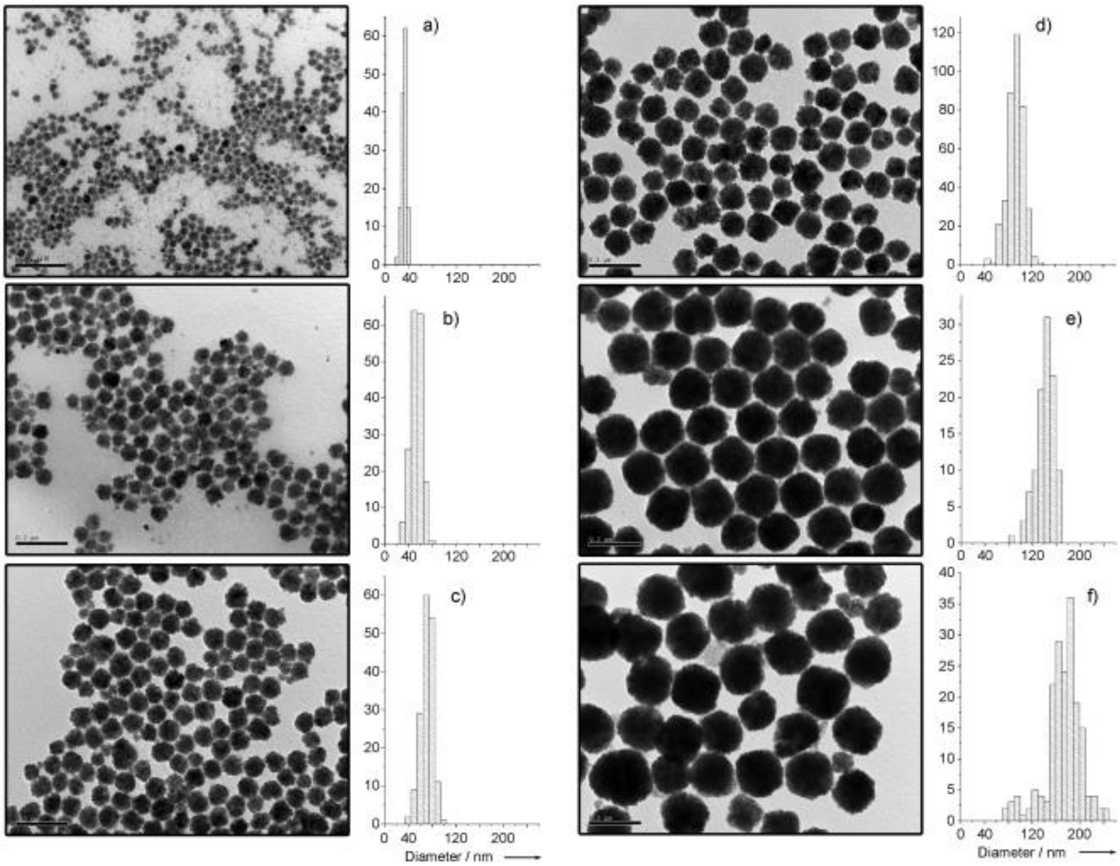

Figure 3. 2: Nanoparticle Clusters as Prepared by the Ge Method[60]. In this experiment the NPC size is determined by the amount of sodium hydroxide/polymer stock used in the synthesis, with increased NaOH resulting in larger NPCs. In this case volumes of stock of 1.6, 1.65, 1.7, 1.75, 1.8, 1.85 mL correspond to NPC sizes of 31, 53, 71, 93, 141, and 174 nm respectively.

Xia et al[59] outlined a method involving iron chloride salts and a 5% w/w solution of a polymer in water. This mixture was stirred vigorously under nitrogen, and ammonium hydroxide along with 5 mM α-cyclodextrin was added. Stirring was continued at room temperature for a further 90 minutes and it was reported that all aspects of cluster size, morphology, shape and solubility are tuneable by altering the synthetic parameters.

Similarly the method outlined by Sondjaja[63] involves the mixing of iron salts, polymer and ammonium hydroxide in water at room temperature, albeit without the use of cyclodextrin as a solubilising agent for the magnetite crystals formed. This method yields clusters which are tuneable in size by adjusting the molar ratio of iron to polymer. It should be noted however that in this report polydispersity was not accurately controllable, particularly for larger cluster sizes.

Another method for single step preparation of colloidal nanoparticle clusters involves the mixing of an inorganic precursor into a polymeric suspension which is then heated to initiate both precursor decomposition and cluster formation. The Tannenbaum group have outlined a successful method for this "polymer melt" one step synthesis in their publications[64,65] in which an appropriate polymer is dissolved in dried solvent at room temperature, iron pentacarbonyl is then added slowly and the resultant mixture, film-cast onto glass and the solvent allowed to evaporate. Thermal decomposition is then initiated by heating in a temperature controlled vacuum oven. Typically, this procedure yields polymer stabilized nanoparticles however when the metal volume fraction is above a specific critical value (polymer dependant), clustering is induced by attractive inter-particle Van der Waals interactions. This method of nanoparticle cluster formation is advantageous in so far as it produces low polydispersity, however thus far it has only been successfully reported for non-polar polymers meaning that further surface modification would be necessary in order for these particles to be suitable for use in biomedical applications. Nanoparticle clusters produced by co-precipitation methods on the other hand are usually stable in water.

3.1.2. Multi-step Synthesis Techniques for the Preparation of NPCs

Multi-step synthesis techniques for the preparation of magnetic colloidal nanoparticle clusters are the more popular route employed by research groups for a number of reasons: primary particles may be prepared by a number of methods enabling the tuning of emergent cluster properties, through control over primary NP and cluster size. Co-clusters of different particles can also be prepared, and a much broader selection of stabilizing ligands are available. In the following sections selected multi-step synthesis routes will be discussed including surface ligand polymerization, direct mixing techniques, phase transfer, micelle-mediated solvophobic clustering and self-assembly of Janus nanoparticles.

3.1.2.1. Surface Ligand Polymerization Techniques for the Preparation of NPCs

Surface ligand polymerization techniques have been reported by both the Hatton[66] and Tian[67] groups, and involve the exchange of surface stabilizing ligands of pre-synthesized nanoparticles and consequent polymerization of the new reactive surface ligands by techniques such as: (i) Ring-opening polymerisation (ii) Esterification of hydroxyl groups by acetylation. It was shown that by selecting appropriate ligands in the initial exchange step, desired properties such as water solubility may be obtained. Both of these processes generally produce polymer stabilized nanoparticles, however, it was reported that by utilizing specific pH responsive polymers reversible clustering may be obtained, however these clusters are only stable in acidic conditions[66].

3.1.2.2. Electrostatic Assembly Techniques for the Preparation of NPCs

The direct mixing of poly (electrolyte-neutral) block copolymers with oppositely charged species in aqueous solutions has led to spontaneous formation of stable core-shell complexes by electrostatic interactions. The general protocol for this type of reaction involves surface ligand modification of the NP with a charged species and the mixing of these charged nanoparticles with polymer solutions, in which at least part of the polymer has the opposing charge.

A significant number of the publications in this area of polymer mediated assembly have been from researchers Jean-François Berret and Jerome Fresnais[68–70]. Iron oxide nanoparticles prepared by co-precipitation techniques[36] were surface modified with citrate ions giving them a negatively charged surface. The polymer used as an assembly stabilizer was poly (trimethylammonium ethylacrylate methylsulfate)-b-poly (acrylamide) (PTEA-b-PAM). In this polymer the PTEA portion of the block co-polymer has a positive charge and the PAM portion is neutral, thus when introduced to the nanoparticle stock in solution the PTEA interacts directly with the citrate ions electrostatically and the neutral PAM provides steric repulsion which limits the overall cluster size. By varying the chain length of both PTEA and PAM clusters of various shapes and sizes may be produced. This method of nanoparticle clustering was also successfully employed with nanoceria (CeO_2) nanoparticles instead of iron oxide. A major short coming of this technique for the preparation of magnetic colloidal superstructures is wide polydispersity, with samples ranging in size from 20-100 nm by TEM with polydispersities ranging between 0.1 and 0.25 for DLS measurements, the morphology of these aggregates is also not fixed with spheres, cylinders and branched structures appearing in each preparation. In the method outlined by both the Chiu group[71] and the Gong group[72] a free radical polymerization step is used following the formation of core-shell or magneto-micelles by electrostatic assembly to induce cross-linking in the internal hydrophilic portions of the polymer leading to a much higher in vivo stability. Both of these reports describe the use of a photoinitiator to induce the polymerization step, which is later removed from the NPCs by dialysis.

3.1.2.3. Self-Assembly of Janus Nanoparticles

One type of Janus nanoparticles is those with two or more distinct surface coating regions. By selectively modifying the surface properties of nanoparticles in this way the Hatton group has shown that self-induced clustering may be performed[73,74]. Fe_3O_4 nanoparticles that were initially stabilized with poly (acrylic acid) were immobilized on functionalized silica masking a portion of the nanoparticle's face. The exposed portions of the nanoparticle are then allowed to interact with a second polymer (either poly (sodium styrenesulfonate) or Poly (N-isopropylacrylamide)). This secondary polymer acts as the stabilizing ligand for the colloidal nanoparticle clusters. By increasing the pH of the solution, the charge of silica is reversed, releasing the Janus nanoparticles. This mechanism is outlined graphically in Figure 3. 3. Nanoparticle clustering was driven by the Poly (acrylic acid) portions of the particles shielding themselves from the solution environment. It was also shown that the assembly process was controllable by careful adjustment of either pH or temperature, and that in some cases the clustering was reversible. It was also demonstrated that cluster size could be controlled by increasing the molecular weight of the grafting polymer, or reducing the available grafting area on the nanoparticle surface, both processes resulting in larger assemblies.

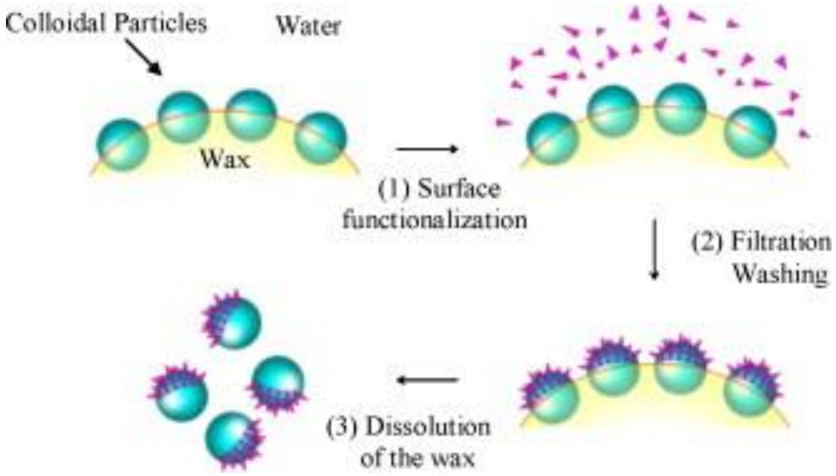

Figure 3. 3: Illustration outlining the preparation method of Janus nanoparticles[75]. By selective coating of part of the NP with hydrophilic material thermodynamically driven assembly can be induced.

3.1.2.4. Competitive Stabilizer Desorption (CSD)

Recently a new method for the preparation of NPCs from a non-aqueous suspension of colloidally stable iron oxide nanoparticles has been reported by our group[76]. In general OA stabilized nanoparticles in an organic solvent (heptane or $CHCl_3$) are placed into a cuvette with a polar solid liquid interface of cyanopropyl-modified silica particles and self-assemble over time.

In a stable suspension of OA stabilized iron oxide NPs an amount of free OA is available in the organic medium and this will exchange with surface-bound OA, in an equilibrium process. When a polar interface is introduced to this suspension the free OA molecules in the suspension will irreversibly bind, this triggers the slow release of OA molecules from the surface of the NPs, destabilizing the NPs (NP*s), in order to stay colloidally stable in suspension the NP*s will begin to associate with one another to form monodisperse clusters of size determined by the timing of removal of the polar interface.

3.1.2.5. Phase Transfer Techniques for the Preparation of NPCs

The reported techniques rely on solvophobic interactions to induce NP assembly. Usually a stabilized nanoparticle stock is prepared in an organic solvent such as $CHCl_3$ and is mixed with an aqueous solution of polymer, the organic solvent is then allowed to evaporate. The polymers used in this technique are therefore amphiphilic di- or tri-block co-polymers. As the organic solvent is removed the hydrophobic blocks of polymer interact with the organic layer on the surface of the nanoparticle leaving the hydrophilic blocks pointing outward to stabilise the particle in the now polar solvent. This procedure has been documented by the Weller group[77,78], who have shown that it is suitable for all manner of nanoparticles from cadmium/selenium core shell nanoparticle structures to iron oxide. At high concentrations of polymer, stabilized magnetic particles are formed however as the concentration of polymer is reduced the primary nanoparticles are found to cluster together in a thermodynamically driven self-assembly process.

Other techniques utilize the injection of a polar solvent, usually deionised water, into a non-polar solution of polymer and pre-stabilized nanoparticles inducing self-assembly of micelles. Preparations of this type have been reported by both the Park group[79] and the Liu group[80]. In the report from the Liu group hydrophilic pre-stabilized superparamagnetic iron oxide nanoparticles were incorporated into pre-formed micelles of polymer by stirring for 12 hours (the polymers used in this preparation were di-block co-polymers with distinct hydrophobic and hydrophilic regions). It was observed that the nanoparticles do not enter the hydrophobic Poly(ε-caprolactone) [PCL] core, rather they are stabilized in the micellar corona due to the presence of poly(glycerol monomethacrylate) [PGMA] by TEM[80].

Alternatively, the Park group reported the co-micelle formation by first mixing polymer and iron oxide nanoparticles in a co-solvent then slow addition of water to induce self-assembly of micelles. It was observed that by changing the initial co-solvent different types of superstructure could be prepared due to the difference in polymer surface area, a function of the polymer-solvent interactions and the dielectric constants of the respective solvent systems. It was also demonstrated in this work that the incorporation of nanoparticles interferes with micelle formation. This interference was attributed to the induced change in the relative volume of hydrophilic and hydrophobic chains within the polymer, as the incorporation of nanoparticles increases the effective volume taken up by the hydrophobic portion. A few examples of achievable NPC configurations are depicted in Figure 3. 4, below.

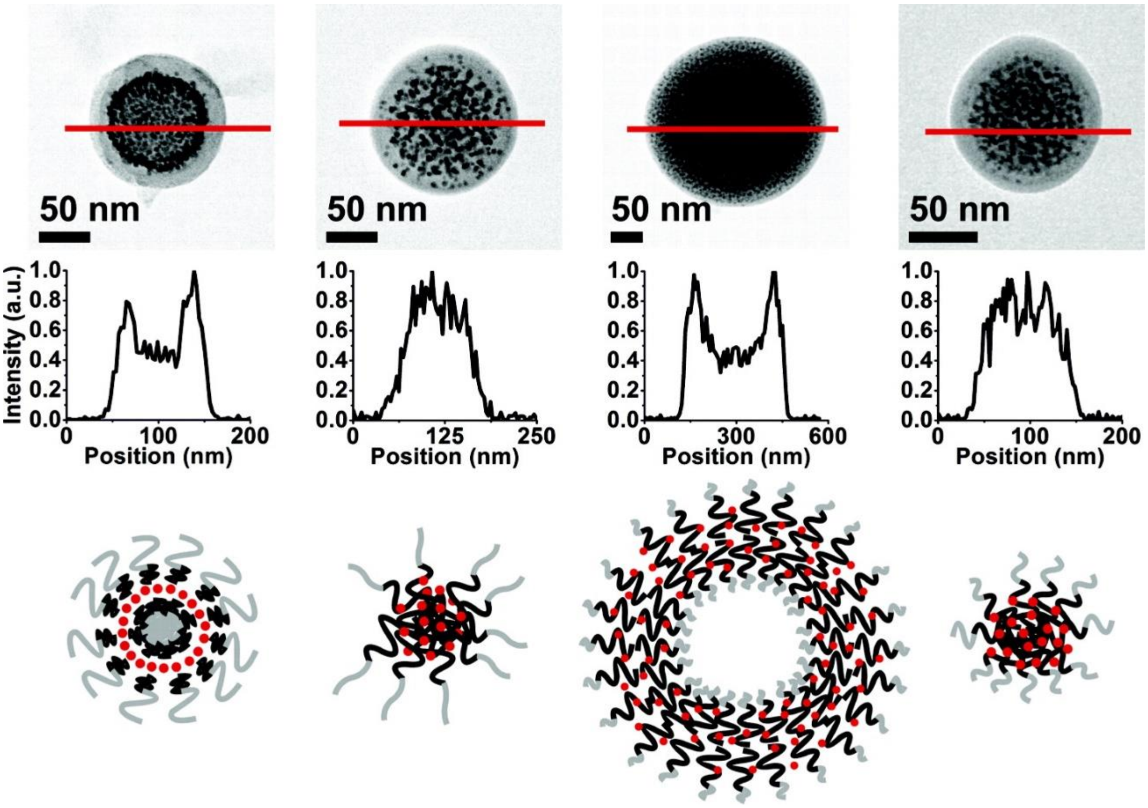

Figure 3. 4: Self-assembly of iron oxide Nanoparticles and Block Co-Polymers, Effect of Co-Solvent on Micelle Formation. The STEM images provided highlight some of the different internal structures which can be achieved. Also shown are the Fe intensity maps (from EDS analysis) of the image and an artistic representation of the materials' structures. Adapted from Hickey et. al[79]. The red dots represent NPs, black lines represent the hydrophobic polymer blocks and the grey lines represent the hydrophilic copolymer blocks.

It had previously been reported that solvent polymer interactions are an important factor in the self-assembly processes of amphiphilic co-polymers however in this report identified, that for the formulations used at least, the incorporation of nanoparticles drastically affects the self-assembly structure by modifying the relative volume ratio of hydrophilic to hydrophobic blocks[79]. One shortcoming of this extraordinary report however was the lack of demonstration of size control of the assemblies. Also, it was unclear whether ordered structures are present in all of the clusters formed.

Another method, outlined by the Cao group[81,82] uses water soluble Fe_3O_4 single NP containing micelles as precursors for polymer stabilized nanoparticle cluster assemblies, formed by solvophobic interactions. An aqueous solution of stabilised single nanoparticle containing micelles was first prepared using dodecyltrimethylammonium bromide (DTAB) as a stabilizing ligand. These water-soluble micelles were then transferred into an ethylene glycol solution. This causes the decomposition of the micelle structures as some DTAB is lost to the ethylene glycol, inducing solvophobic interactions between the stabilizing ligands and ethylene glycol resulting in nanoparticle aggregation. The initial report of this method[81] showed stabilized clusters with a diameter of 190 nm and a standard deviation of 15%, however, further investigations showed that by fine tuning the solvophobic interactions some control of the size of colloidal superstructures formed is possible. Nanoparticle precursors with a weaker affinity for the new solvent (caused by reducing the molar ratio of stabilizing ligand to nanoparticle) may lead to the generation of larger nanoparticle clusters and vice versa[82]. This results in a highly ordered structure, but the outcome is very sensitive to the starting conditions, which are not described in detail in the publications.

3.1.2.6. Interface Free Phase Transfer Techniques for Preparation of NPCs

As outlined in section 3.1.2.4, the presence of an interface can lead to surfactant desorption. As such, when looking at the assembly mechanics of standard phase-transfer based assembly process, involving a biphasic solvent system, more than one process may be influential in the preparation of highly monodisperse, size-controlled assemblies. In this Chapter we will address this by demonstrating the effectiveness of a monophasic, interface free phase transfer assembly method using tri-block copolymers from the Pluronics® range, as shown schematically in Figure 3. 5.

Pluronics® are a range of commercially available tri-block copolymers of poly (ethylene glycol)-poly (propylene glycol)-poly (ethylene glycol) that are FDA approved for some biological applications, and are common ingredients in cosmetics and contact lens cleaning solution. F127 has been used as a carrier for most routes of drug administration including oral, topical, intranasal, vaginal, rectal, ocular, and parenteral routes and is reported to be the least toxic of all commercially available co-polymers[83].

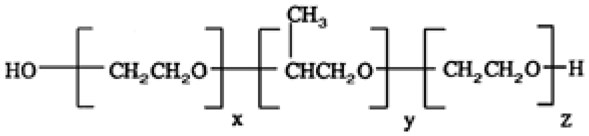

$HO-[CH_2CH_2O]_x-[CH(CH_3)CH_2O]_y-[CH_2CH_2O]_z-H$

Figure 3. 5: General molecular formula of the pluronic range of tri-block copolymers[84] where x and z are hydrophilic and y is hydrophobic.

These amphiphilic polymers interact with organic surfactants on the surface of the NPs and act as a further surfactant, stabilizing the NPs in organic media. Table 3. 1: Physical Characteristics of Pluronic Tri-block Copolymers, the hydrophobic chain length refers to section y in Figure 3. 5 (above) and the hydrophilic chain length refers to the combined length of both x and z chains. Table 3. 1 (below) outlines some of the properties of the Pluronics polymers that will be used in this thesis. It has been found that the polymer properties have an effect on the properties of the NPCs produced indicating that this method has the potential to be used for the large-scale production of tailored NPCs where specific NPC attributes can be selected.

Table 3. 1: Physical Characteristics of Pluronic Tri-block Copolymers, the hydrophobic chain length refers to section y in Figure 3. 5 (above) and the hydrophilic chain length refers to the combined length of both x and z chains.

Polymer	**Total Mw (Da)**	**% Hydrophobicity**	**Hydrophobic Chain Length (Da)**	**Hydrophilic Chain Length (Da)**	**CMC (mg/L)**	**CMC (μM)**
F127	12600	30	3780	8820	800	64
F108	14600	20	2920	11680	730	50
F68	8350	20	1670	6680	334	40
F123	5800	70	4060	1740	440	76

The interface-free preparation of NPCs using pluronics utilizes solvophobic interactions to prepare micelles within which NPs stabilized with an organic surfactant can be encapsulated. This mechanism is illustrated in Figure 3. 6, below. THF is used as a solvent for this process, as it can fully disperse suspensions of nanoparticles stabilized with organic surfactants; it is fully miscible with water and has a low boiling temperature which allows for evaporation processes to occur at room temperature, resulting in an aqueous suspension without drying the colloid or requiring a transfer across a phase boundary.

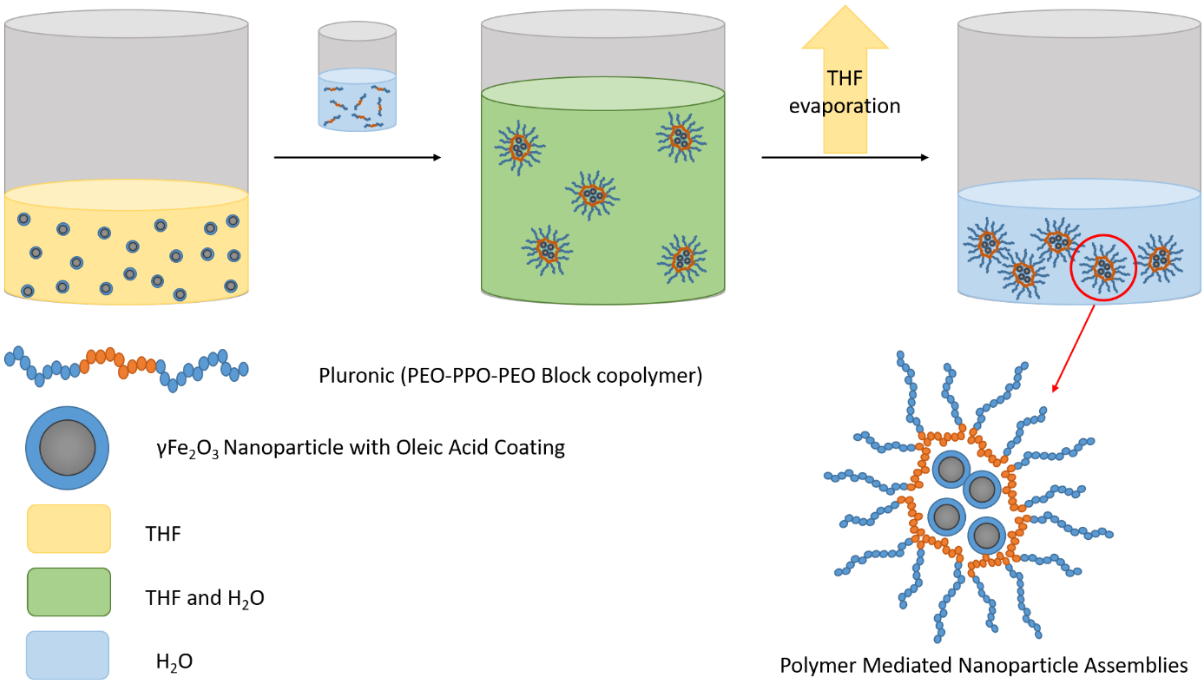

Figure 3. 6: Schematic of the assembly process involved in IF-PMA, a suspension of oleic acid stabilized NPs in THF and an aqueous solution of polymer were mixed thoroughly then allowed to tumble uncovered in a vented environment for 48 h to allow the complete evaporation of THF resulting in an aqueous suspension of NPCs

In this Chapter this interface free polymer mediated assembly of spherical γ-Fe_2O_3 NPs will be studied. The method development and optimization of the assembly protocol will be discussed, as will the effect of assembly parameters on the emergent properties of the clusters. The potential of these materials as theranostic agents will be addressed further in Chapter 4. In the final Chapter of this thesis the application of this polymer mediated assembly approach to cubic iron oxide nanoparticles will be investigated.

3.2. Experimental

3.2.1. Reagents

Iron (III) acetylacetonate (>99.9%), benzyl alcohol (>99%), oleic acid (99%), (3-Aminopropyl) triethoxysilane (99%) and Pluronics F127, P123, F68 and F108 were obtained from Sigma Aldrich and used without further purification. All remaining solvents were obtained from Brenntag UK Ltd and used without further purification.

3.2.2. Preparation of Iron Oxide Nanoparticles

3.2.2.1. Surfactant Free Thermal Decomposition of Iron (III) Acetylacetonate

Surfactant free thermal decomposition was performed using an adaptation of the process outlined by Pinna and Niederberger for the preparation of IONPs[44]. 1 g (2.8 mmol) of iron (III) acetylacetonate [Fe(acac)$_3$] was added to 20 mL of benzyl alcohol (BA) in a 3-necked round bottomed flask as illustrated in Figure 3. 7. The reaction mixture was degassed with N_2 for 15 min prior to heating to reflux temperature (~200^oC) and remaining at this temperature for 7 h. The resulting black liquor was allowed to cool to room temperature before transferring to a Duran bottle for storage, under an N_2 blanket. The particles formed in this reaction were found to be 8.52 nm ± 2.50 nm and the procedure was found to be scalable by a factor of 10; 10 g of precursor in 200 mL of BA; with no change in particle size (8.47 nm ± 2.44 nm, TEM) or colloidal stability of the resulting suspension. This method may also be adapted for other acetylacetonate complexes, such as cobalt and manganese, to produce metal oxide and mixed ferrite oxide NPs. As the NP suspensions are stable in BA under N_2 for up to 6 months, no workup is necessary at this stage.

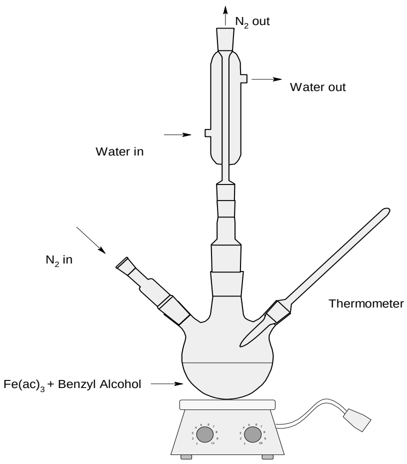

Figure 3. 7: Standard reflux setup used in the preparation of NPs by surfactant free thermal decomposition of Fe(acac)3

3.2.2.2. Core@Shell Synthesis of Fe_2O_3@ Fe_2O_3 Nanoparticles

Core@shell nanoparticles were prepared using an adaptation of the process outlined in section 3.2.2.1, a seed-mediated approach was taken to create larger NPs using the same synthesis method. 1 g (2.8 mmol) of Iron Acetylacetonate ($Fe(acac)_3$) was added to 20 mL of benzyl alcohol (BA) in a 3-necked round bottomed flask. The reaction mixture was degassed with N_2 for 15 min prior to heating to reflux temperature (~200^{o}C) are held at this temperature for 7 h. The resulting black liquor was allowed to cool to room temperature. When cooled the sample was precipitated over a magnet and the supernatant removed. The particles were then washed once with clean BA (20 mL) before resuspension in 10 mL of BA.

To this suspension of NPs in BA a further 1 g (2.8 mmol) of $Fe(acac)_3$, and a further 10 mL of BA was added. The reaction mixture was degassed with N_2 for 15 min prior to heating to reflux temperature (~200^{o}C) are held at this temperature for 7 h. The resulting black liquor was allowed to cool to room temperature before transferring to a Duran bottle for storage. The particles formed in this reaction were found to be 12.3 nm ± 3.1 nm.

Particles of size 10.5 ± 3.3 nm were also prepared by this core-shell method, in this case the second reflux step was extended to a 12 h hold at reflux.

3.2.2.3. Oleic Acid Stabilization of Iron Oxide Nanoparticles in Organic Solvents

15 mL of an NP suspension in BA (0.14 ± 0.005 M) were centrifuged for 5 min at 16,100 rcf and the supernatant removed, the resulting pellet was then washed twice with acetone before being redispersed in 7.5 mL of $CHCl_3$. 50 µL of OA (>99% Sigma Aldrich) was then added, the container was vortexed for 1 min to ensure homogeneity. The resulting dispersion was then tumbled for 2 hours at 400 rpm (Orbital Shaker HS 260 basic, IKA, Germany) to allow the surface stabilization reaction to go to completion.

3.2.2.4. (3-Aminopropyl) triethoxysilane stabilization of Iron Oxide Nanoparticles in H_2O

1.5 mL of an NP suspension in BA ((0.14 ± 0.005 M) was centrifuged for 5 min at 16,100 rcf and the supernatant removed, the resulting pellet was then washed twice with acetone and once with $CHCL_3$ before being redispersed in 1.5 mL of $CHCl_3$. 37 µL of (3-Aminopropyl) triethoxysilane (APTES) (>99% Sigma Aldrich) was added and the container was vortexed for 1 min to ensure homogeneity. The resulting dispersion was then tumbled overnight on a rotary shaker at 400 rpm, to allow the surface stabilization reaction to go to completion.

The APTES stabilized NPs in $CHCl_3$ were then precipitated out of solution by the addition of acetone and subsequent placement on a magnet, the supernatant was removed, and the sample was redispersed in 1.5 mL of deionised water (diH_2O). 50 µL of 1M HCl was then added and the sample was vortexed for 1 min to ensure homogeneity. The resulting dispersion was then tumbled for 1 hr, or a rotary shaker at 400 rpm to ensure that the aqueous stabilization step had gone to completion.

3.2.3. Polymer Mediated Assembly of Iron Oxide Nanoparticles – Method Development

The standard procedure utilized in this report involves the dispersion of standard NPs in an organic solvent (C_7H_{16}, $CHCl_3$) using Oleic Acid (OA) as a stabilizing ligand. This stable dispersion is then redispersed in THF and phase transferred to water using commercially available tri-block copolymers of poly (ethylene glycol)-poly (propylene glycol)-poly (ethylene glycol): pluronic F127, F68, F108, and F123. The polymer used in each case is outlined within the experimental methods.

3.2.3.1. Effect of Iron to Polymer Ratio on the Size and Polydispersity of NPCs Formed

7.5 mL of Oleic Acid Stabilized NPs (OA. NPs) in $CHCl_3$ were taken and centrifuged for 10 min at 16,100 rcf to remove aggregates; the supernatant was removed and precipitated on a magnet using acetone. The particles were then washed twice with acetone, and then redispersed in 30 mL of THF. Separately 1 L of a 64 µM solution of Pluronic F127 was prepared in water. In a standard preparation, 2 mL of polymer stock in water was added to a 7 mL glass vial; to this a volume of iron oxide stock in THF was added (varied between 1 mL and 5 mL, according to Table 3. 2).

Table 3. 2: Mass of iron in each sample of a standard preparation to investigate the effect of NP concentration on NPC cluster formation as determined by ICP-AES

Sample	Volume of NPs in THF (mL)	Amount of iron in sample (mmol)
1	1	0.08
2	1.5	0.11
3	2	0.15
4	2.5	0.19
5	3	0.23
6	3.5	0.27
7	4	0.31
8	4.5	0.34
9	5	0.38

This mixture was then vortexed for 1 min to ensure homogeneity then tumbled, uncovered, for 48 hours to allow the THF to evaporate, inducing cluster formation.

3.2.3.2. Effect of Centrifugation Speed on the Size and Polydispersity of NPCs Formed

A series of samples was prepared as outlined above. From each of these samples, a series of aliquots were taken for analysis. These aliquots were prepared by 1:10 dilution in deionised water and centrifugation for 5 minutes at 800, 3200, 5600, 8000, 10400, 12800, 15200 and 16100 rcf respectively. A comparison sample was also prepared as a 1:10 dilution of clusters in water with no centrifugation performed.

3.2.3.3. Investigation into the Reproducibility of the PMA Experiment

Following some preliminary experiments, a series of samples was prepared as outlined above, in triplicate. From each of these samples, three aliquots were prepared for DLS analysis by performing a 1:10 dilution in water followed by centrifugation at 0.8 rcf for 5 min.

3.2.3.4. Investigation into the Effect of Scale Up on the PMA Experiment

A series of 5 samples was prepared at 3 different scales. A standard scale experiment using 2 mL of 64 µM F127 in a 7 mL glass vial, a 3 times scale using 6 mL of 64 µM F127 in a 21 mL glass vial, and a 25 times scale using 50 mL of 64 µM F127 in a 250 mL glass Duran bottle. In this experiment, due to space constraints, the samples were allowed to evaporate uncovered in the fumehood, no shaking was applied. This resulted in a slower evaporation stage in particular for the large volume samples. The NPC samples produced were analysed by DLS following a cleaning step of a 1:10 dilution in water followed by centrifugation at 0.8 RCF for 5 min.

3.2.3.5. Continuous Monitoring of the Assembly Process

Three sample points were chosen from Table 3.2, and 36 replicates prepared. Each of these samples was weighed using an analytical balance prior to being placed on the rotary shaker and each sample was allowed to shake for a specific amount of time. At each time point a sample was removed from the shaker, weighed and then prepared for DLS by dilution in deionised water (1:10), and centrifugation for 5 min at 0.8 rcf. Samples were analysed at the following intervals: 10, 20, 30, 40, 50, 60, 70, 80, 90, 100, 110, 120, 140, 160, 180, 210, 240, 280, 300, 330, 360, 390, 420, 450, 480, 510, 540, 570, 600, 630, 660, 690 and 720 min.

3.2.4. Systematic Studies on the Effect of Assembly Conditions on the Size and Polydispersity of NPCs Formed by PMA.

3.2.4.1. Effect of Oleic Acid Concentration on NPC Formation

In this experiment the effect of oleic acid concentration on NPC formation was investigated by changing the concentration of oleic acid used in the first stabilization step. All other parameters were kept constant. The concentration of oleic acid used is reported as equivalents, this is a relative term where 1 equivalent is the volume of oleic acid required to completely cover the surface of every nanoparticle in the suspension. As the footprint of OA (the space required per ligand) is well reported as 48 Å^2, [85] and the surface area of the nanoparticles can be determined (assuming that the NPs are monodisperse and spherical) using the diameter of the NP as determined by TEM. 1 equivalent of OA can be calculated as the surface area of the NP in m^2, divided by the footprint of OA in m^2 (4.8 x 10^{-19} m^2).

As the surface of NPs is not perfectly spherical and the suspension of NPs is not uniformly monodisperse, an equivalency of 2.5 is generally required as a minimum to ensure total coverage of the NP surface. In suspensions with a large excess of surfactant, surfactant molecules can be either chemisorbed onto the NP, physisorbed into the stabilization sphere of the NP or free to diffuse throughout the solvent. In this experiment series were at 2.5, 5, 7.5 and 10 equivalents of OA per NP, as there is extensive washing between the OA stabilization and NPC formation steps it is believed that any effect on the size of NPCs formed, as a result of higher OA concentrations, is due to a larger stabilization sphere of physisorbed material surrounding the NPs. In the following experiments the amount of OA used in the initial stabilisation of NPs is reported as the volume (in µL) of OA per mL of NP stock suspension, where 10 µL/mL of NPs is equivalent to 5 surface equivalent volumes. This relative volume is reported as the syntheses can be scaled from 0.2 to 50 mL scale. It should also be noted that all graphs in the coming sections, unless otherwise reported are plotted as d_{hyd} vs iron concentration per mL of polymer stock used. This is again due to the fact that syntheses can be scaled, and to allow for direct comparison of results.

3.2.4.2. Effect of Polymer Concentration on Size and Polydispersity of NPCs

In this experiment 7 series of samples were prepared as outlined above using different polymer concentrations. In the case of F127 these concentrations were 4, 8, 16, 64, 256, 512 and 1024 µM respectively. These concentrations were selected as 64 µM is close to the literature value of critical micelle concentration (CMC) of pluronic F127 in water; 69 µM [86]. This experiment was also performed using 3 series of each of the pluronics, F108, F68 and F123 at concentrations approximately equal to 0.25, 1 and 4 times the CMC in each case.

3.2.4.3. Effect of Polymer Chain Length on NPC Formation

A series of samples was prepared as outlined above, using 10 µL /mL of NPs of oleic acid and polymer at the CMC for each of the pluronics F68 and F108. These pluronics were chosen as they contain the same ratio of hydrophobic material to hydrophilic material yet have different total molecular mass (8,350 and 14,300 respectively). These samples were prepared for DLS analysis by dilution (1:10) with deionised water and centrifugation for 5 min at 0.8 rcf.

3.2.4.4. Effect of Polymer Chain Ratio on NPC Formation

A series of samples was prepared as outlined above, using 10 µL per mL of NPs of oleic acid, and polymer at the CMC for each of the pluronics F127 and P123. These pluronics were chosen as they have the same amount of hydrophobic material however the hydrophobic chain accounts for 70% of the total mass of F127 and only 30% of the total mass of F123. These samples were prepared for DLS analysis by dilution (1:10) with deionised water and centrifugation at 0.8 rcf for 5 min.

3.2.4.5. Effect of NP Size on NPC Formation

A series of samples was prepared using standard spherical NPs prepared by thermal decomposition of iron acetylacetonate as outlined in section 3.2.2.1 with an oleic acid excess of 5 and 64 µM pluronic F127. Another series of samples was prepared using FeO@FeO core@shell NPs prepared by sequential thermal decomposition experiments and seed mediated growth experiments, used as received from a lab member. These particles were determined to have an average approximate surface area of 309 nm^2 and as such the same excess of oleic acid was used for the stabilization of these NPs. Following cluster formation, the samples were prepared for DLS analysis by dilution (1:10) with deionised water and centrifugation at 0.8 rcf for 5 min. In all cases unless otherwise specified, NPC size is plotted against the concentration of iron per mL of polymer stock solution as determined by ICP-AES analysis.

3.3. Results and Discussion

3.3.1.1. Effect of Iron to Polymer Ratio on the Size and Polydispersity of NPCs

As outlined in section 3.2.3.1, a series of samples was prepared varying the ratio of Fe to polymer in the clustering experiment, the results of which are shown below. Note that unless otherwise stated in the figure caption, in all following graphs, the concentration of iron is represented as [Fe] per mL of polymer stock solution (64 µM pluronic F127).

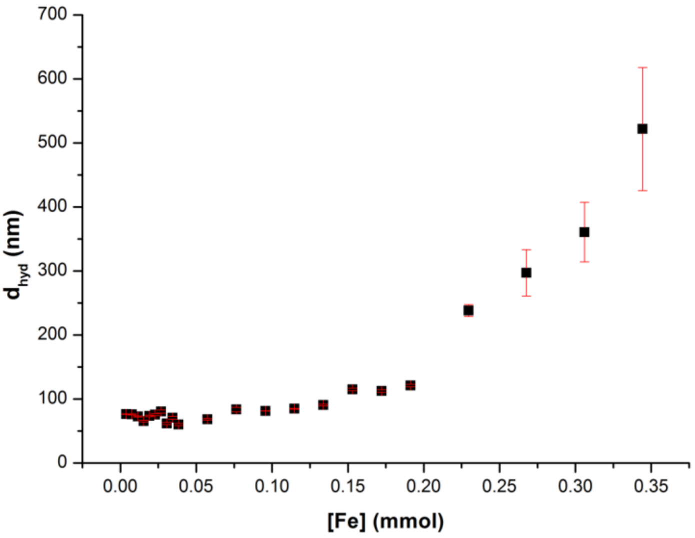

Figure 3. 8: The effect of iron to polymer ratio on the formation of NPCs was investigated over a concentration range of 0.008 mmol to 0.35 mmol iron. The polymer used was F127 at 64 µM and 2 mL of polymer stock was used in the preparation of each sample. NPC size increases with iron concentration however 3 distinct regimes are observed in the data. All samples were prepared as outlined in section 3.2.3.1., and were analysed as 1:10 dilutions of as prepared samples in diH2O. It was found that NPCs with a d_{hyd} *larger than 250 nm were not colloidally stable and did not survive the work-up procedure with a final dispersible yield of <1%. The data points and error bars correspond to the mean and standard deviation of 3 consecutive measurements.*

It can be seen from Figure 3. 8, that below a concentration of 0.05 mmol of NPs per mL of polymer stock, the size of cluster formed is not controlled but rather fluctuates around 80 nm, above this concentration the size of the NPCs formed increase almost linearly (R^2 = 0.93), as the concentration of iron in the final suspension is increased. Above a concentration of iron of 0.25 mmol per mL of polymer the clustering process begins to form large clusters leading to an apparent exponential size dependence (R^2 =

0.97). It should be noted that while there is still a visible increase in size as expected, the concentration of DLS ready samples produced above an iron concentration of 0.25 mmol is exceptionally low with a dispersible yield of material typically <1%, and the suspensions are not colloidally stable. NPCs of a size greater than 200 nm are found to be much less colloidally stable, probably due to their large size, and the centrifugation cleaning process reduces the dispersible yield of material to <1%. In this study we are interested primarily with stable NPC suspensions in the size range of 60-200 nm as these are the most relevant materials for use in biological applications.

It was initially hypothesized that the NPC formation is driven by solvophobic interactions and micelle formation. If that is the case, the implication is that the introduction of the nanoparticle suspension in THF induces micelle formation of F127, by reducing the CMC of the polymer. Note that this experiment, when repeated in the absence of NPs, was found to produce micelles with a size of 100-110 nm by DLS for F127 at 64 µM. Interestingly, the clusters formed at very low concentrations of Fe are approximately 80 nm, indicating that the NPs themselves (or the surfactant associated with them) interfere with micelle formation. It should also be noted that at 64 µM F127 does not contain micelles prior to the introduction of the organic solvent, with or without NPs. In this scenario there are two possible mechanisms at play which induce cluster formation. In scenario 1 the NPs in suspension collapse on introduction to the aqueous environment followed by a stabilization with polymer, previously free in suspension. In scenario 2 both the NP suspension and polymer solution collapse simultaneously. As the Fe concentration is increased, it is expected that the NP suspension would collapse first, this could correlate to the ‘kink’ in the response, Figure 3. 8; as the iron concentration is increased, larger and larger non- or-partially stabilized NPCs are forming initially, with NPs being added to the cluster faster than the polymer. At lower concentrations of Fe, this dependence is much weaker, probably due to the lower volume of THF that is being introduced into the polymer solution. It is likely that the NPC samples prepared with less than 0.05 mmol of iron are in the form of polymer micelles with NPs encapsulated in the hydrophobic core as the size of the “clusters” formed is not altered by the ratio of iron to polymer below this threshold concentration. This hypothesis is supported by the fact that at low concentrations of Fe the clusters formed are less dense than those formed at higher Fe concentrations, at least as suggested by FE-SEM images (Figure 3. 9).

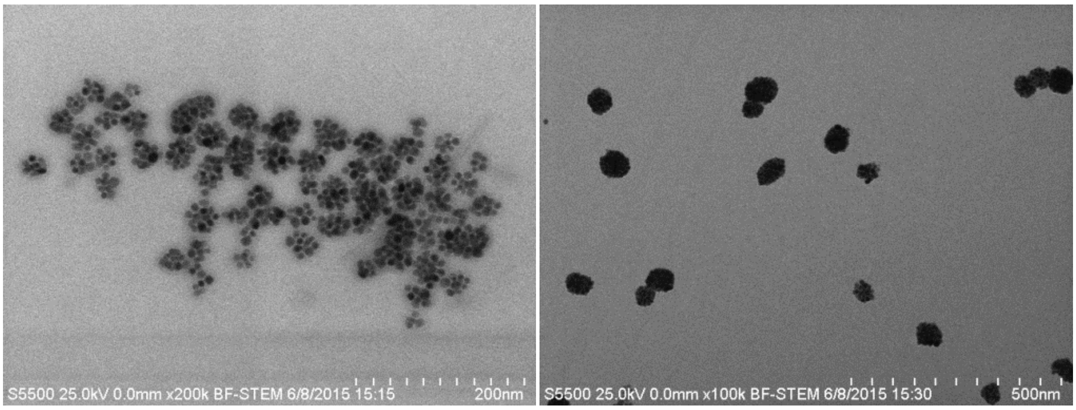

Figure 3. 9: Image illustrating the difference in NP loading density between NPCs prepared with low Fe concentration (0.024 mmol) and high Fe concentration (0.18 mmol)

Our interpretation is that at an Fe concentration of greater than 0.05 mmol per mL of polymer, the total number of NPs captured per NPC require a volume larger than that of an empty micelle of the polymer as prepared under similar conditions. This results in the formation of larger, denser NPCs than those observed at a lower Fe concentration. The NPC structure is no longer dependant on the micelle size of the polymer, but rather the number of NPs occupying the NPC. This can be observed using EM techniques as in Figure 3. 10, below. NPCs containing sufficient NPs to completely fill an F127 micelle grow in size as the concentration of Fe increases, while the distribution of NPs within the NPC is homogenous, and the loading density appears uniform.

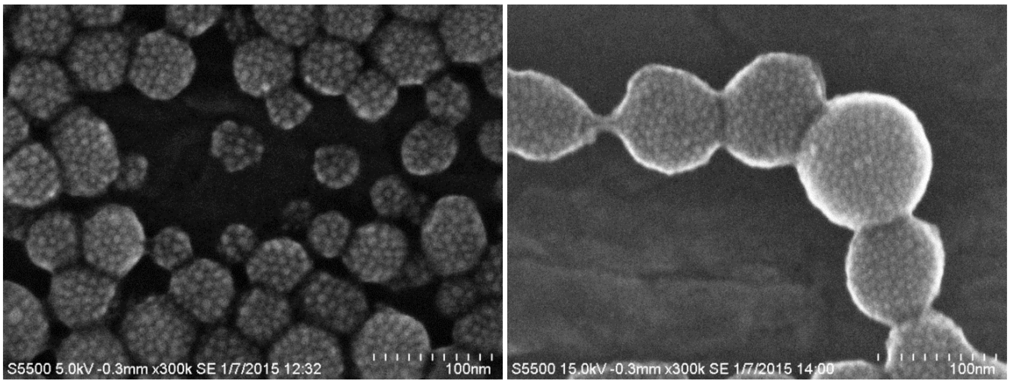

Figure 3. 10: SEM images showing the presence of spherical NPCs containing homogenous distributions of spherical NPs throughout. Both images were taken at a magnification of 300kX. Image 1 (left) shows clusters of 58 ± 3 nm and image 2 (right) shows clusters of 102 ± 5 nm. (d_{hyd} = 64 nm and 121 nm respectively)

Experiments performed in Chapter 4 further investigate the structure and internal ordering of the PMA-NPCs.

3.3.1.2. Effect of Centrifugation Speed on the Size and Polydispersity of NPCs Formed

The effect of centrifugation speed in determining the final size and PDI of NPCs was studied as we found that centrifugation greatly improves the PDI of NPC samples by removing some of the larger aggregates from the solution.

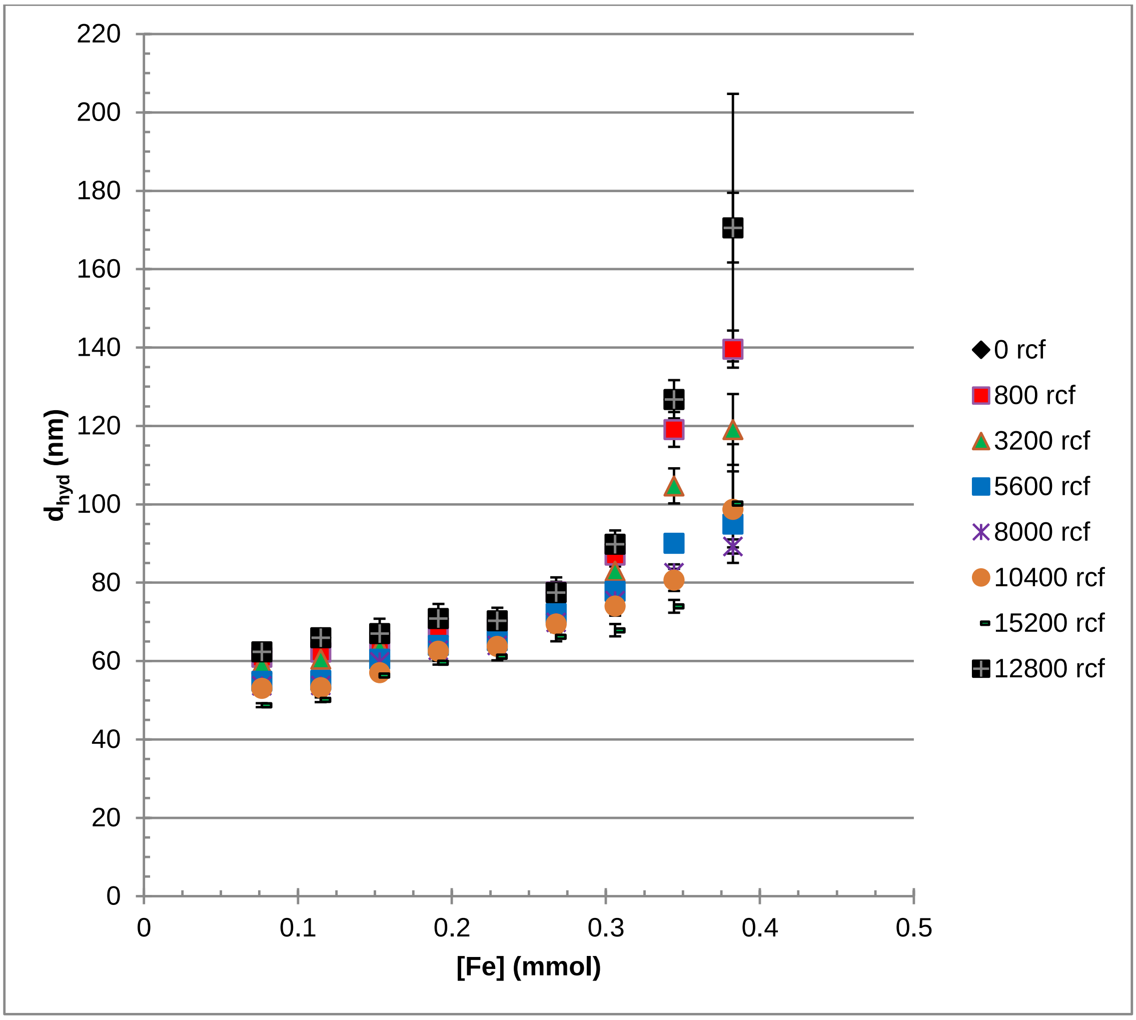

Figure 3. 11: The effect of centrifugation speed on size and PDI of NPCs. All data points for each concentration of iron were generated from the same stock solution of NPC and centrifuged for 5 min at the respective rcf. Increased centrifugation speed caused a decrease in both the size and PDI of the NPCs, the dispersible yield of NPCs was also reduced, as expected. All samples were prepared as outlined in section 3.2.3.1. (2 mL of 64 µM F127, and varied volumes of an NP stock suspension in THF, shaken uncovered over 48h on an orbital shaker) and were analysed as 1:10 dilutions of as prepared samples in diH$_2$O. The data points and error bars correspond to the mean and standard deviation of 3 consecutive measurements.

As can be seen from Figure 3. 11, increased centrifugation speed greatly impacts the size of the NPCs obtained at each concentration, and the range of NPC sizes obtained is drastically altered as the speed of centrifugation increases (60 – 180 nm when no centrifugation is applied as opposed to 40 – 100 nm after 5 min centrifugation at 15.2 rcf). It should be noted that the decrease in size was not systematic across the size range, or as the centrifugation speed was increased. In the case of each as-prepared NPC suspension, increasing the centrifugation speed decreases the amount of sample available for analysis. The larger aggregates are removed from the suspension as they are heavier, thus the yield of useable NPCs decreases. In Table 3.3, below, two samples at 3 centrifugation speeds are compared in terms of $d_{hyd,}$ PDI and dispersible yield. In both cases a decrease in dispersible yield is observed, as expected, as the centrifugation speed increases. This was found to be much more pronounced in higher Fe concentration samples (larger NPCs). PDI is also improved slightly with increased centrifugation as expected. The decrease in PDI is also much more apparent at higher iron to polymer ratios, for example at an iron concentration of 0.19 mmol Fe per mL of polymer the PDI is 0.177, with no centrifugation, reducing to 0.064 after 5 min at 5600 rcf. This is as compared to a change in PDI from 0.161 to 0.123 for the same change in centrifugation speed at the lowest Fe concentration.

It should be noted that the PDI is found to increase to 0.237 at much higher centrifugation speeds (12,800 rcf) at the highest Fe concentration. Our interpretation is that this is due to the extremely low concentration of available material for analysis following centrifugation at higher speeds, resulting in a perceived increase in polydispersity due to changes in the sample window during the analysis. It should be noted that all of the samples analysed fall within the tolerable limits for NMRD experiments (PDI < 0.2) prior to centrifugation.

Table 3. 3: A selection of data taken from the centrifugation speed experiment highlighting the effect of increased centrifugation speed on the size, PDI and dispersible yield of the as-prepared NPC samples

Sample Name	Centrifugation Speed (rcf)	d_{hyd} (nm)	PDI	Dispersible yield
0.04 mmol Fe	0	62.4	0.161	64%
0.04 mmol Fe	5600	54.8	0.123	63%
0.04 mmol Fe	12800	50.0	0.084	55%
0.019 mmol Fe	0	171	0.177	47%
0.019 mmol Fe	5600	95.0	0.064	12%
0.019 mmol Fe	12800	164	0.237	1.5%

All further experiments were evaluated using a 1:10 dilution of the sample (to bring the samples into the correct concentration range for DLS analysis) followed by 5 minutes centrifugation at 0.8 rcf as this allows for the most accurate representation of the as prepared samples, large aggregates or dust particulates are removed from the NPC suspensions while the NPC integrity is not compromised and the dispersible yield of material obtained is still relatively high.

3.3.1.3. Investigation into the Reproducibility of the PMA Experiment

As outlined in the experimental section the reproducibility study comprised of 3 sets of internal repeats (new assembly experiments from the same primary suspensions, labelled in the graphs below as 1,2,3) for each of 3 separately synthesised and suspended (THF) NP samples prepared (A, B, C). The graphs below demonstrate the reproducibility of the clustering process. The polydispersity of the samples produced is very low (typically 0.05 – 0.12), the highest recorded PDI value being ~0.17, well within the selected tolerable limits for analysis of, 0.20.

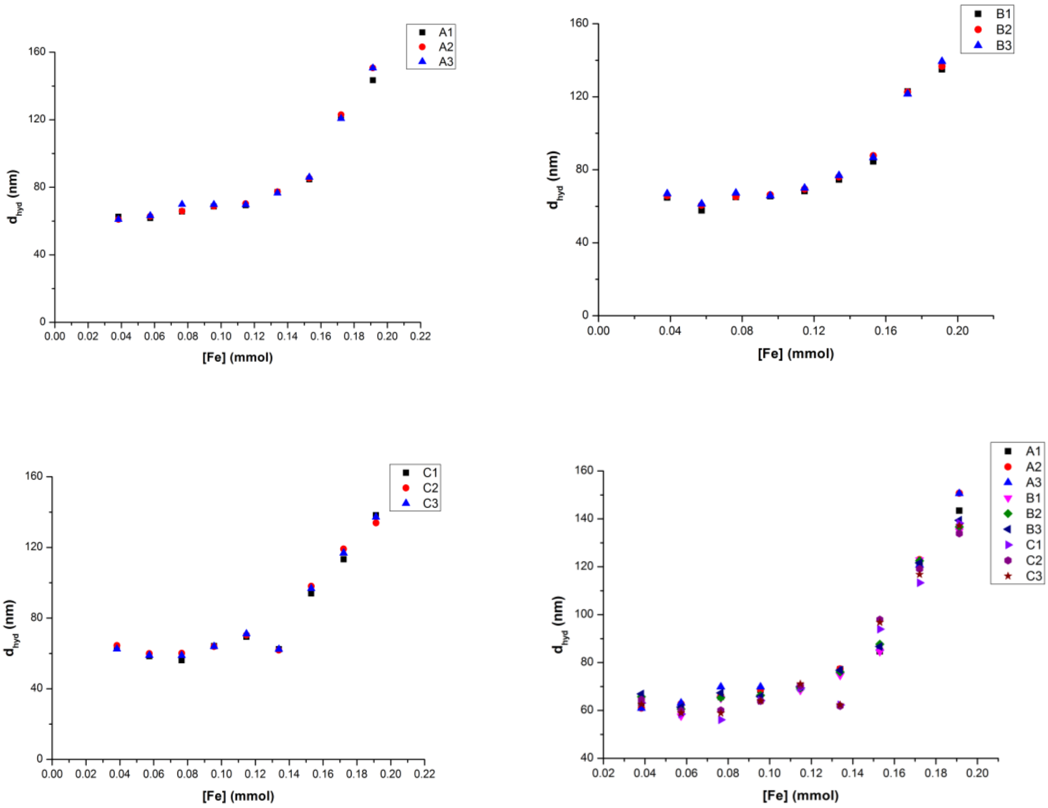

Figure 3. 12: Investigations into the reproducibility of the PMA experiment. Depicted above are 3 series of samples were prepared (A, B and C) and 3 internal repeats were prepared at each concentration point (1, 2, 3) these are plotted separately, demonstrating both the reproducibility of the work-up procedure and the homogeneity of the as prepared NPC suspensions. The final graph (bottom-right) shows all points graphed simultaneously demonstrating the reproducibility of the total experiment.

The demonstrated reproducibility implies that a change in size of the NPCs produced of approximately 5 nm, as the concentration of iron was increased can be assumed to be significant. A number of the relevant experimental parameters were then investigated to determine their role, if any, in the cluster formation process. The results of these experiments will be outlined in section 3.3.2. It should also be noted that above 0.018 mmol of Fe per mL of polymer, the DLS data obtained was not reproducible; successive measurements of these samples gave significantly larger and unstable d_{hyd} and PDI values, demonstrating that that samples are not colloidally stable in that concentration range.

3.3.1.4. Investigation into the Effect of Scale Up on the PMA Experiment

As outlined in section 3.2.3.4 a series of 5 samples was prepared at 3 different scales (standard, 3x and 25x, 2mL, 6 mL and 50 mL scale respectively). The results shown below demonstrate that the clustering experiment can be scaled up significantly without affecting the outcome. The size of NPCs formed is consistent as the scale increases and the dispersible yield of nanoparticles was also found to be comparable between the samples produced, with the exception of 0.075 mmol (as seen in Figure 3. 13)

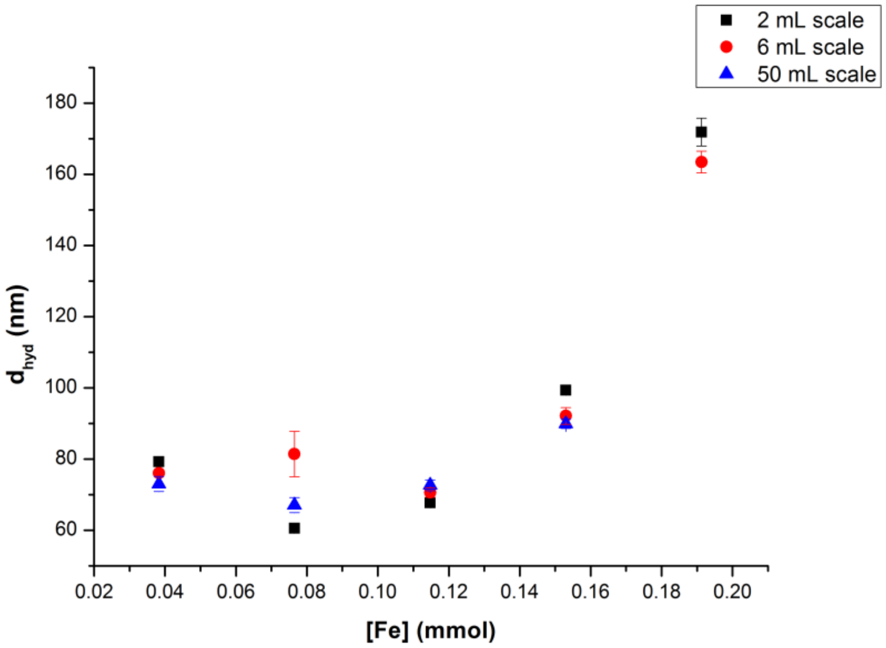

Figure 3. 13: Scale up experiment on the PMA method shown at 1x scale (final volume of NPCs per sample = 2mL); 3x scale (final volume = 6 mL) and 25x scale (final volume = 50 mL), as before, NPC size increases as iron concentration increases, the scale up procedure does not appear to impact significantly on the final NPC size at any ratio of iron to polymer within 10% error.

This result is promising as it indicates the potential to scale up the PMA method further which would be beneficial for the potential applications of NPCs. Feridex, a previously commercially available contrast agent based on iron oxide nanoparticles was administered at a dose of 0.56 mg/kg[87]. Assuming that the global BMI distribution is that of the USA, the average mass of an adult human patient is 74.6 kg[88]. This would imply that 41.8 mg Fe is required on average per patient. The NPC suspensions (0.04 mmol Fe per mL polymer solution at 64 µM) prepared and processed by 5 min centrifugation at 800 rcf have a concentration of 1308 mg/L or ≈31 doses/L at the same Fe concentration as Feridex.

To provide some context to the required scale; for MRI contrast agent application, the spin-spin relaxivity (r_2) of Feridex is given from the literature as 65 s^{-1} $mmol^{-1}$ at 1.5 T [22]. NPCs prepared at a concentration of 0.04 mmol Fe per mL polymer (d_{hyd} = 62 nm) have a ratio of 166 s^{-1} $mmol^{-1}$ at the same magnetic field, indicating that the NPCs could be used to either generate a much larger contrast effect, or alternatively provide the same effect at a lower dose. This would reduce the potential risk to patients, reduce side effects and be more cost effective as a larger number of doses per litre could be generated. This result will be discussed in further detail in Chapter 4.

A sample was also prepared at 50x scale (100 mL of 64 µM F127 in a 1 L Duran bottle) to demonstrate the potential for further scale up. The results are shown below, separately displayed as the assembly vessels (1L Duran bottles) were too large to place on the orbital shaker and thus were left uncovered in the fumehood during the evaporation stage. The decreased surface area of sample exposed to the air and the lack of agitation during the evaporation stage may both affect the rate of THF evaporation and hence the assembly kinetics.

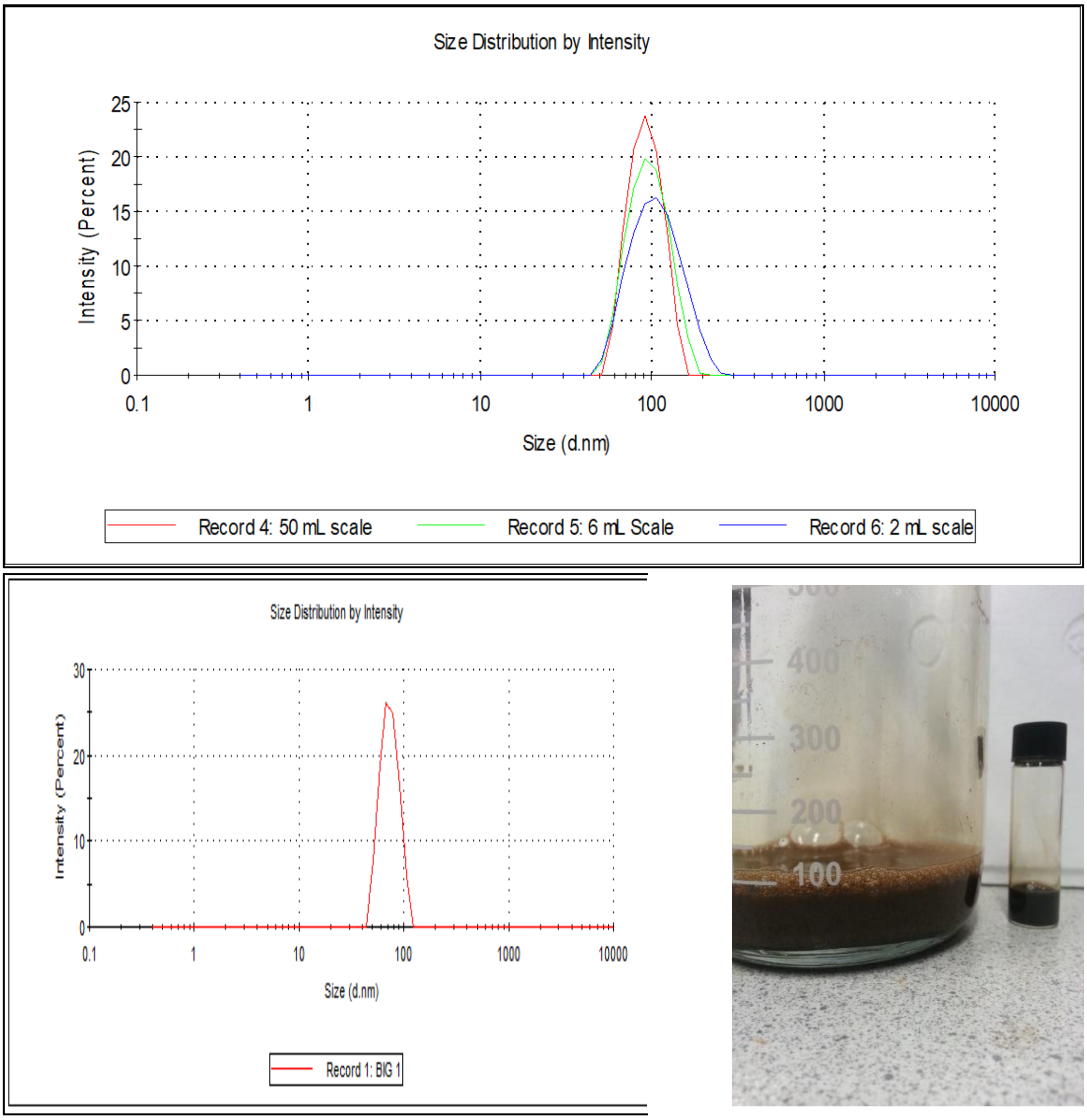

Figure 3. 14: DLS data demonstrating the size reproducibility of NPCs produced during the scale up experiment at a concentration of 0.17 mmol of iron per mL of polymer (64 µM F127). 2mL scale shown in blue, 6mL scale shown in green and 50 mL scale shown in red (Z-ave = 93 nm PDI = 0.06) [top left]. 50x scale up of the standard PMA experiment (final volume = 100 mL) demonstrating a monodisperse suspension of NPCs (Z-ave =82.5 nm, PDI = 0.111) [top right] (this figure is reported separately as the samples were too large to be placed on the orbital shaker during the assembly process, thus altering the assembly kinetics). Image [bottom] showing the difference in scale between the standard preparation method (2 mL scale) and a 50x scale up experiment (100 mL scale). All samples were prepared as outlined in section 3.2.1. and analysed as a 1:10 dilution of as prepared NPCs in diH$_2$O.

It can be seen from Figure 3. 14 above that the size of NPCs produced at each ratio of NP to polymer is unchanged as the process is scaled, interestingly, it was found that the polydispersity of the sample is reduced as the process is scaled up; 0.103 at 2 mL scale, 0.053 at 6 mL scale and 0.025 at 50 mL scale for the 0.17 mmol Fe per mL of polymer ratio.

3.3.1.5. Continuous Monitoring of the Assembly Process

In the case of interface-free phase-transfer mediated PMA of nanoparticles; there is almost no literature on the mechanism and kinetics of assembly. A continuous DLS monitoring experiment was devised to get insight into the characteristics of this preparation method. The work up of each sample involves dilution (1:10 NPC suspension in H_2O) prior to centrifugation and analysis. It was deemed acceptable to analyse the DLS results assuming the viscosity of pure water alone, as even at the highest concentration of THF; at 0 h; the maximum quantity of THF present would be 71 µL/mL of sample. When tested experimentally it was found that although additional THF at this concentration produces a significant difference in viscosity (1.01 mPa s^{-1} without THF and 1.10 mPa s^{-1} with THF) when the DLS measurements were evaluated with either viscosity, no significant difference in d_{hyd} or PDI was observed (< 10%), Figure 3. 15, and the change in viscosity over time is sufficiently low that the difference in viscosity between sequential measurements is not significant.

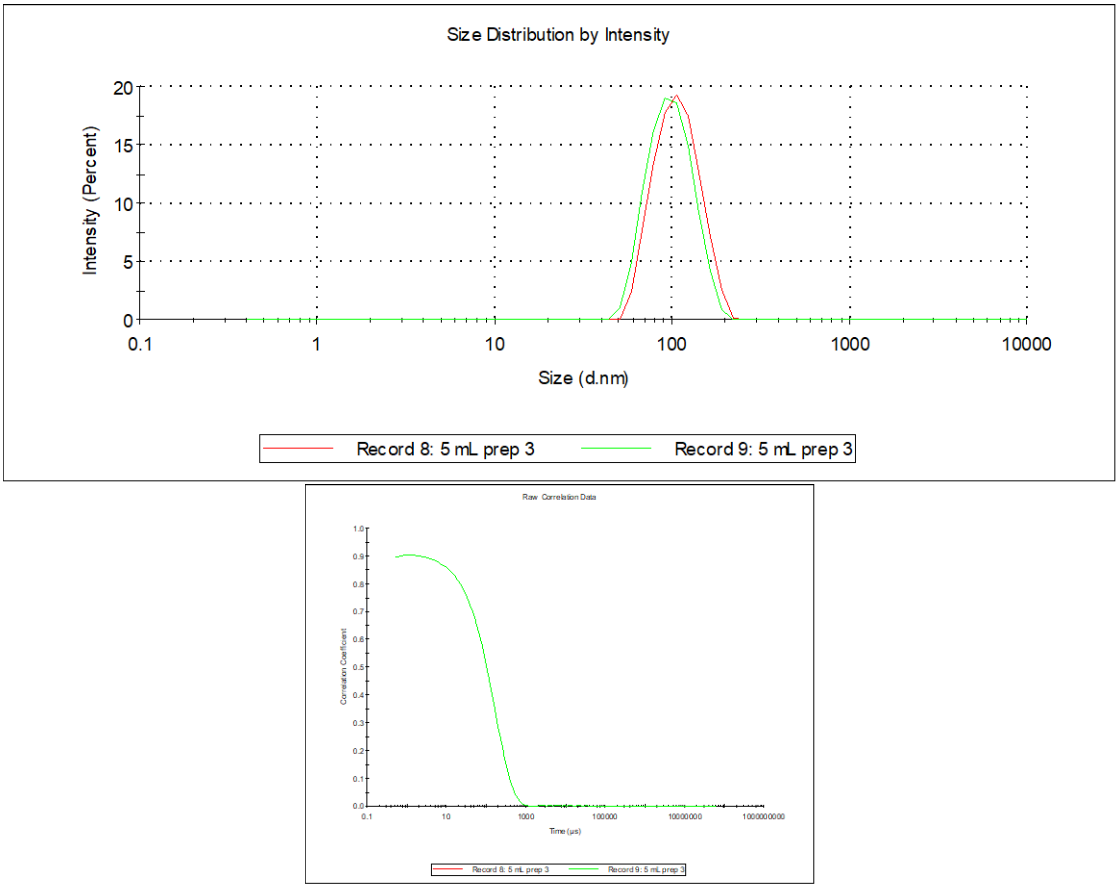

Figure 3. 15: Data interpreted using a viscosity value for F127 of 1.01 mP.s (red) and F127 with THF, 1.10 mP.s (green), the correlogram (right) shows a complete overlap of the data. As the difference in NPC size observed was not deemed significant, all subsequent samples were analysed assuming the viscosity of water

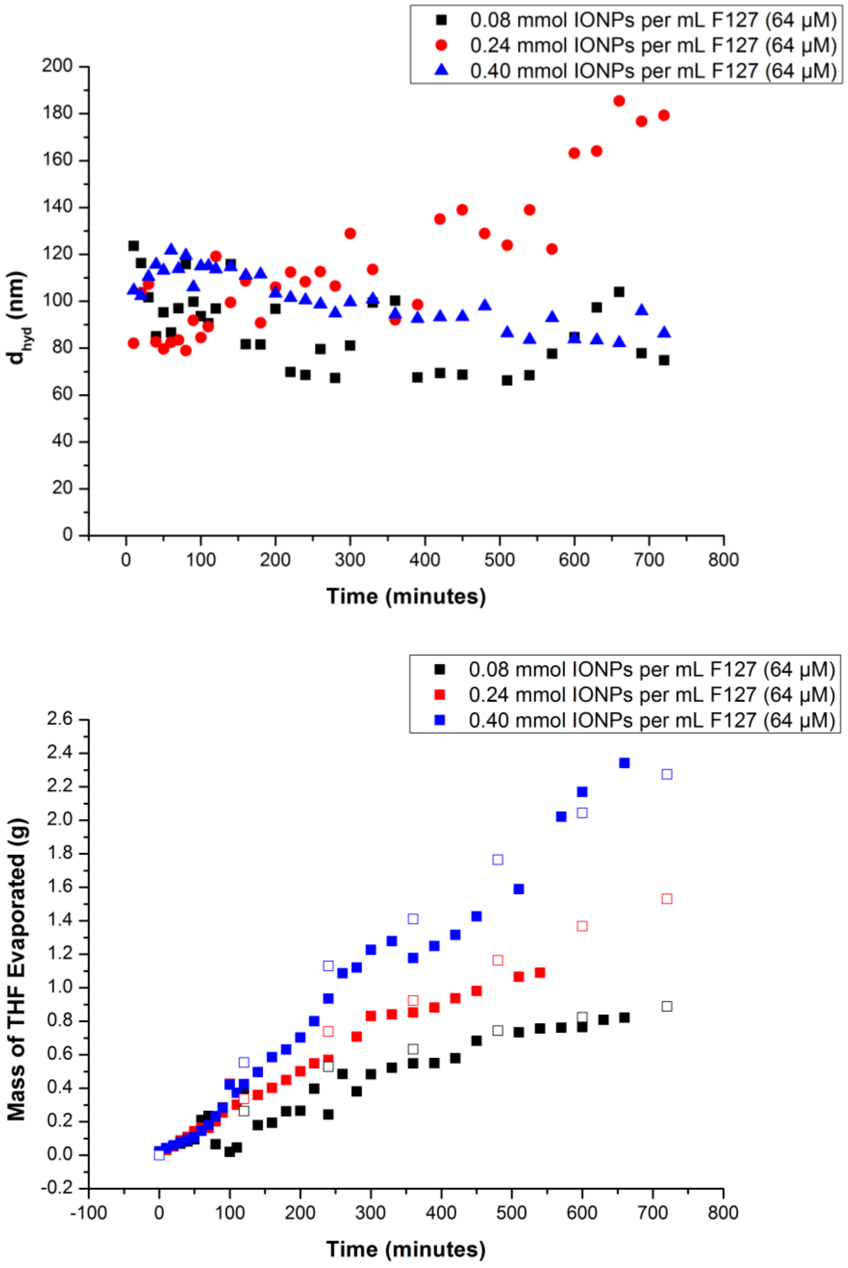

Figure 3. 16: Semi continuous monitoring of the PMA experiment (left). At each concentration of iron, 36 samples were prepared concurrently and at each time point one sample was removed, weighed to determine the rate of THF evaporation, and prepared for DLS analysis by dilution (1:10 in di H_2O) and centrifugation for 5 min at 0.8rcf. Determination of the rate of evaporation of THF from the continuous monitoring experiment (right). At t=0 the total volume of THF in each set of samples was 1 mL (0.89g) for 0.08 mmol Fe (black), 3 mL (2.67g) for 0.24 mmol Fe (red) and 5 mL (4.45g) for 0.40 mmol Fe. As the complete evaporation of THF takes 48 hr in all cases, the THF evaporation was only monitored for the first 12 hr of the experiment when it was expected that the evaporation rate is highest. The open squares correspond to polymer/H_2O/THF mixtures under the same conditions without the introduction of NPs. It can be seen that in the absence of NPs the rate of THF evaporation is slightly higher and is in the form of an exponential recovery curve (In the case of 1 mL THF the R^2 value for the exponential fit of the data is 0.9953) indicating that the presence of the NPs slows the evaporation of some THF potentially due to encapsulation within the polymer micelles.

Prior to mixing with polymer, the nanoparticle solution in THF has a typical d_{hyd} of 15 nm. As can be seen in Figure 3. 16, upon mixing clusters of 80-120 nm are rapidly formed. This indicates that micelles incorporating the NP stock solution are formed on mixing of the two solutions, as prior to mixing no micelles are present in the polymer stock solution.

In the case of the intermediate concentration of iron it appears that while initially these same processes are occurring, after an induction time of about 3 hours the NPCs start to grow to their final size. In the case of the highest concentration of Fe the NPCs formed on mixing are significantly larger than the NPCs observed after 12 hours (110-120 nm as compared to 80-90 nm). However, it is also interesting to note that the final size of these clusters is not the size observed after 12 hours. At a concentration of 0.04 mmol Fe NPCs produced following a 48 hr evaporation time are 65±1 nm. NPCs of 70 ± 1.7 nm are produced at the intermediate concentration of Fe, and 135 ± 2.4 nm at the highest concentration of Fe are also obtained. This indicates that the growth processes involved in the formation of large NPCs, particularly at higher concentrations of Fe occur on longer time scales than those measured in this experiment, growth of the NPCs is not observed during the continuous monitoring experiment, but the final NPC size indicates that growth has occurred in the remaining 36 h.

By weighing the samples at the start of the experiment and immediately prior to sampling for DLS analysis the rate of THF evaporation can be crudely determined. It can be seen that the rate of THF evaporation depends on the THF content of the original sample. The sample with most THF, loses THF at the fastest rate. In all cases the rate of THF evaporation appears quasi-linear in time, which corresponds to almost ‘ideal’ behaviour across the composition range, although there is a change in slope at around 240 min. This finding was confirmed by the repetition of the continuous monitoring experiment in the absence of NPs, 64 µM F127 was added to THF and allowed to tumble uncovered, the mass of the samples was recorded at 2 h intervals and plotted against the NP containing suspensions (open data points in Figure 3. 16). It was found that the samples prepared with no NPs present evaporated at a slightly faster rate and in a quasi-exponential manner (less ideal). Our interpretation of these observations is that in the case of NP containing suspensions, the first stage of evaporation corresponds to the loss of free THF, in the second stage, further loss is of THF initially associated with the NPCs. The d_{hyd} of the NPCs decreases continuously through the entire period except for the 0.24 mmol sample. This anomaly has yet to be explained.

The evaporation is performed over a 48 h period and this experiment represents the only first 25% of this time. To fully investigate the kinetics of NPC assembly points should be taken every 30 minutes for the entire 48 h period; however, this is impractical and impossible to achieve in the lab environment. Alternatively, a real-time in-situ monitoring experiment would be required however due to the need for sample processing (dilution, centrifugation etc.) prior to DLS measurement, the need for the samples to be shaking and the corrosive nature of THF to plastics a suitable setup for the proposed experiment could not be achieved thus far.

3.3.2. Systematic Studies on the Effect of Assembly Conditions on the Size and Polydispersity of NPCs Formed by PMA.

Having shown that the preparation of NPCs is a two-step process; initial stabilization of the NPs in organic solvent followed by phase transfer to water, a series of experiments was performed to investigate the effect of experimental conditions at each step of the of cluster formation on the final size and PDI of NPCs produced.

3.3.2.1. Effect of Oleic Acid Concentration on NPC Formation

In this experiment the effect of oleic acid concentration on NPC formation was investigated by changing the concentration of oleic acid used in the first stabilization step. All other parameters were kept constant and the experiments were performed using the same materials and at the same time. In Figure 3. 17 (below) the concentration of oleic acid used in the initial stabilization step of cluster formation, is reported as surface equivalents, this is a relative term where 1 surface equivalent is the volume of oleic acid required to completely cover the surface of every nanoparticle in the suspension. This value is calculated assuming that the particles are monodisperse spherical NPs, and the footprint of OA is 48 Å^2 [85] as outlined in section 3.2.2.3. Hence for 1 mL of a 60 mM Fe suspension, with a d_{TEM} of 8.6 nm, 6.2 µmoles of oleic acid are required for a single coating, this is considered 1 equivalent volume.

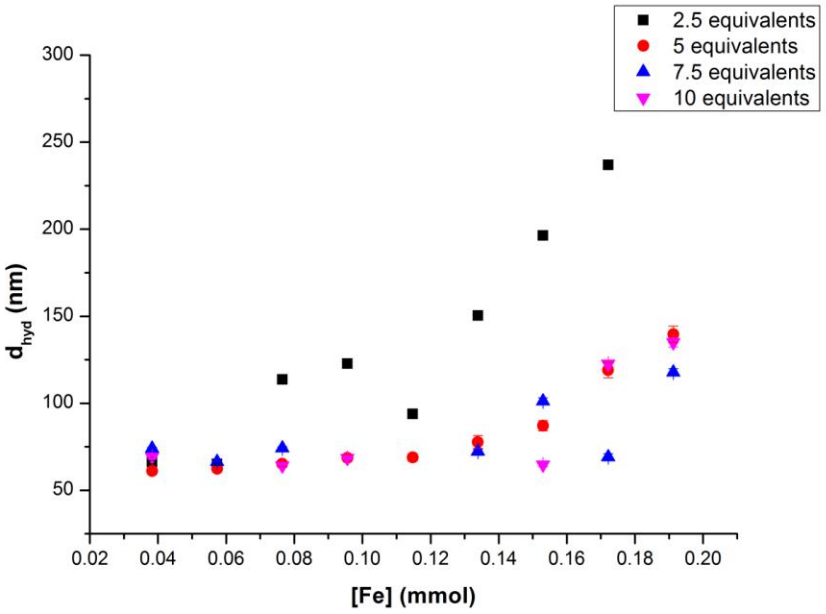

Figure 3. 17: Effect of Oleic Acid Concentration on the size and PDI of NPCs produced by PMA. As OA concentration increases the overall stability of NPCs is increased, higher yields and lower PDI, however the size of NPCs produced at large concentrations of iron is reduced as OA concentration increases. All samples were prepared as outlined in section 3.2.3.1. and were analysed as 1:10 dilutions of as prepared samples in diH$_2$O. Depicted above are samples prepared at 2.5, 5, 7.5 and 10 equivalents of OA (black, red, blue and pink respectively). As before NPC samples with a d_{hyd} larger than 200 nm were found not to be colloidally stable. NPC suspensions prepared at all other OA concentrations had good dispersible yields (> 50%) and low PDI. Samples prepared at an OA concentration of 2.5 equivalent volumes were found to be the least stable and NPC formation was not well controlled.

Prior to NP assembly the d_{hyd} and PDI of the OA.NP suspensions in THF are similar (Z-average = 19.0 nm PDI = 0.20 for 2.5 equivalents of OA; and Z-average = 18.9 nm and PDI = 0.20 at 10 equivalents of OA) and the dispersible yield is very similar (24.6 mM (87.7%) and 26.1 mM (93.1%) for 2.5 and 10 equivalents of OA, respectively). This strongly indicates that the additional OA in the suspensions is free within the solution and is not interacting directly with the NP surface via a physisorption mechanism (this would present as a slight increase (3-4 nm) in d_{hyd} which we do not observe). All of the OA.NP suspensions were stable when exposed to an external magnet, over a period of 48 h.

Despite our observations that increased OA concentration does not affect the stabilization of the NPs in organic media, it is clear from Figure 3. 17 that the concentration of oleic acid used in the initial stabilization step of cluster formation has a profound impact on the size of NPC produced. At the lowest concentration of OA (2.5 equivalent volumes) stable assembly of NPCs that is controllable over a range of sizes was not achieved, above a d_{hyd} of 200 nm the dispersible yield of NPCs was less than 5% and had high PDI values indicating that the NPCs produced were not colloidally stable. This can be observed particularly well at higher relative concentrations of Fe to polymer. At intermediate concentrations (5 surface equivalents), controlled assembly with good size control is observed. At extremely high concentrations of OA the effect of iron concentration on NPC size is dramatically reduced; in the samples prepared with 15 equivalent volumes of OA no significant change in size was observed for clusters containing 0.15 mmol and 0.3 mmol of Fe. This may be due to the free OA in suspension acting as a stabilizer for the cluster of NPs as well as the NPs themselves, limiting the upper size attained at close to the nominal polymer micelle size. Larger volumes of free OA may stabilize a larger number of smaller NPCs than lower quantities of free OA which may stabilize a smaller number of larger NPCs. It is also possible that the additional free OA is interacting with polymer alone, forming micelles with no incorporation of NPs, these micelles would be invisible in TEM due to low Z-contrast, while potentially dominating the DLS signal, which is consistent with the NPC size being close to the NP-free micelle size. An OA concentration of 5 equivalents was selected for all further experiments as this allowed us the widest range of size control, was reproducible and provided NPCs that were stable over a 3-month period, which had a low PDI and a high dispersible yield.

3.3.2.2. The Effect of Polymer Concentration on the Size and Polydispersity of NPCs

As outlined previously, it is apparent that cluster formation is induced initially by the formation of micelles. In the standard protocol the concentration of pluronic F127 used is 64 µM as this concentration is close to the literature value of the CMC (critical micelle concentration) of pluronic F127 in water at 25 °C, (69 µM [86]). A series of samples were prepared at polymer concentrations both above and below this value as it is believed that the introduction of nanoparticles may interfere with the micelle formation.

Polymer concentrations of 4, 8, 16, 64, 256, 512 and 1024 µM were prepared using F127 and a series of samples produced at each concentration using 2 mL of polymer solution in each case and the standard volumes of NP stock solution in THF. This experiment was also performed for each of the following pluronics: P123, F108, and F68 at concentrations of 16, 64 and 256 µM. DLS measurements were performed on the resulting suspensions, all samples were diluted 1:10 with distilled water and centrifuged for 5 minutes at 800 rcf prior to analysis.

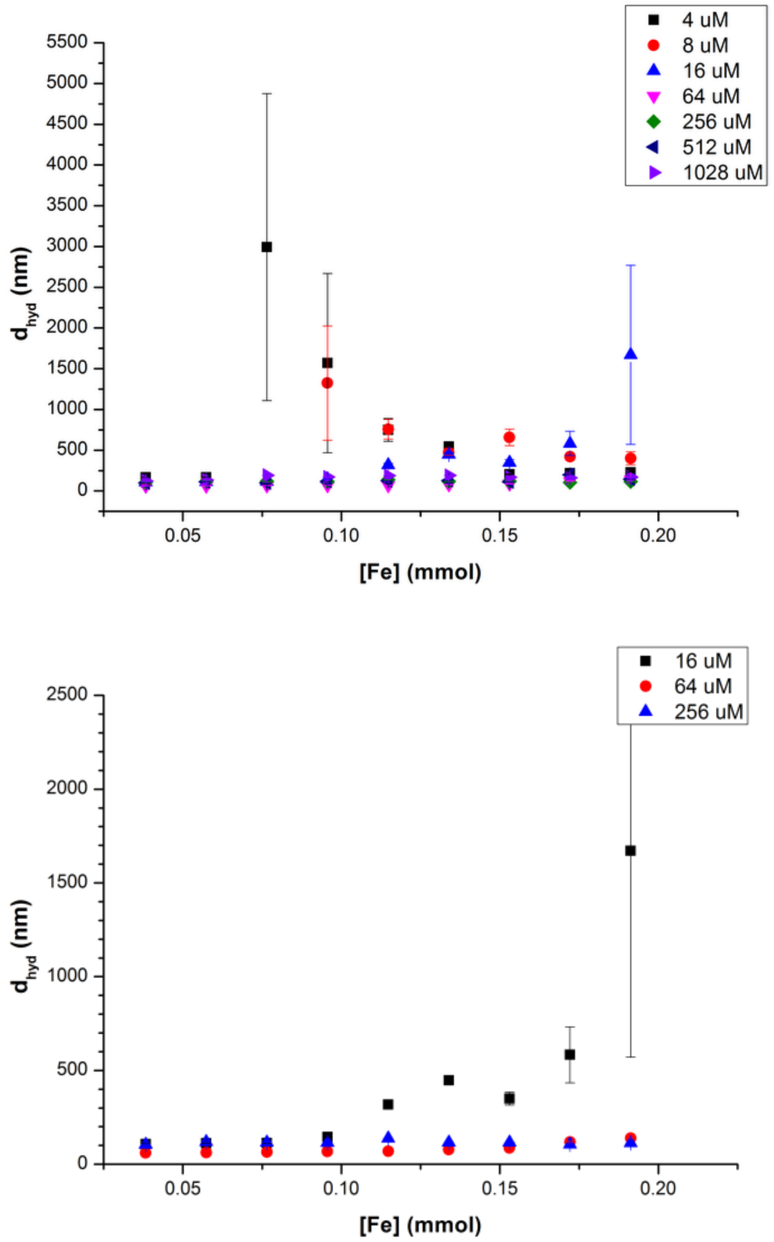

Figure 3. 18: The effect of polymer concentration on NPC formation (Pluronic F127). Samples were prepared using solutions of F127 ranging from 4 to 1028 µM (shown in left-hand graph). DLS data of NPCs prepared using polymer concentrations at 0.25*CMC, CMC and 4*CMC as shown in the second graph (right). All samples were prepared as outlined in section 3.2.1. and were analysed as 1:10 dilutions of as-prepared samples in diH$_2$O. It should be noted that the large error bars in the 16 µM data series are due to samples with very low yield and poor colloidal stability.

It is generally found that when the PDI is high the suspensions are not stable. In the case of the samples for which data is shown in Figure 3. 18, it is clear that not all of the samples produced in this experiment are colloidally stable; as evidenced by the large error bars associated with samples prepared with a polymer concentration much lower than the literature value for the CMC (of 65 - 70 µM). Samples prepared with lower polymer concentration were not colloidally stable, as evidenced by inconsistent NPC size between measurements. Whereas samples prepared at 4 times the polymer CMC are much closer to the micelle size of F127 in water (110 nm), and the size of NPCs produced was not appear affected by the NP concentration in the final NPC suspension.

In Figure 3. 18, lower graph, the data for polymer concentrations of 0.25*CMC, CMC and 4*CMC are shown (enlarged). It can be seen that for samples prepared with a polymer solution below the CMC, while some micelles appear to form at lower concentrations of Fe, cluster formation is not stable or controlled with aggregates larger than 300 nm forming. The average PDI of samples prepared with 16 µM was 0.378 also indicating that the samples are not monodisperse, whereas the average PDI of samples prepared with 64 and 256 µM was 0.102 and 0.109 respectively.

In Figure 3. 19 (below) the data obtained from samples prepared with a polymer concentration at or above the CMC is depicted. As the range of NPC sizes is smaller (60-200 nm) it is much easier to observe what is happening in this experiment.

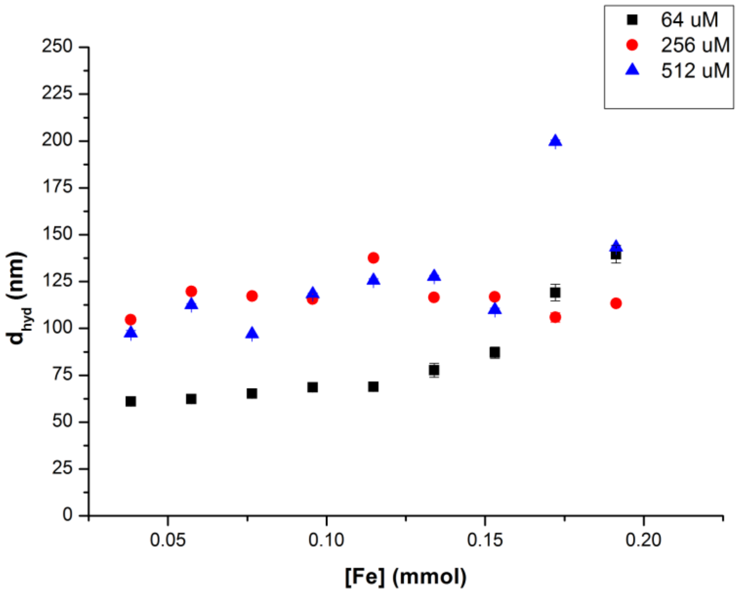

Figure 3. 19: The effect of polymer concentration on NPC formation, Pluronic F127 at and above the CMC of pluronic F127 in $H_2$0. Average PDI values were as follows (0.102 for 64 µM, 0.109 for 256 µM, and 0.160 for 512 µM) All samples were prepared as described in section 3.2.1. and were analysed as 1:10 dilutions of as prepared samples in diH_2O.

A gradual increase in size with composition that is quasi-linear in the range 0.04 – 0.14 mmol, is observed with a polymer (pluronic F127) concentration of 64 µM (just below the CMC of F127 in pure H_2O). Above a concentration of 0.14 mmol Fe the rate of change of size with respect to Fe concentration increases and the system moves into the range where control over the assembly is lost. TEM suggests that this size increase is consistent with additional NPs being incorporated into the NPCs, with no further change in ordering, as STEM analysis shows a closely packed NP layer of similar interparticle separation at the surface of the NPC, Figure 3. 10. Approaches to determining internal NPC ordering and density are discussed in Chapter 4. At concentrations above the CMC the samples typically form NPCs of 100-120 nm with no clear control over that value. Our interpretation is that this is caused by the DLS response being dominated by the presence of empty polymer micelles, as the micelle size of F127 prepared in these conditions without the introduction of NPs was found to be approximately 110 nm by DLS.

If this were the case, NPCs formed at concentrations of polymer much higher than the CMC would most likely be a broad distribution of magnetic and non-magnetic bodies, or, a broad distribution of clusters with variable loading, either way these suspensions are not useful for biological applications. Alternatively, extensive cleaning procedures such as magnetic chromatography could be employed to allow the determination of an accurate size and PDI of the magnetic NPCs produced by DLS measurement. Both of these processes are excessively time consuming, labour intensive and costly. Also, the extensive cleaning procedures would produce significant waste material. None of these issues are encountered when using a polymer concentration close to the CMC, making this the most suitable condition for NPC formation and the obvious choice for further investigation. It should be noted that the dispersible yield of NPs increased as the polymer concentration increased. For samples prepared with polymer concentration of 0.25*CMC the average dispersible yield was <1.5%, for samples prepared with polymer at the CMC the average dispersible yield was 53% and for samples prepared at 4*CMC the average dispersible yield was 61%. While the increased dispersible yield obtained at 4*CMC would be beneficial, the extensive cleaning procedures required for this material reduces its attractiveness.

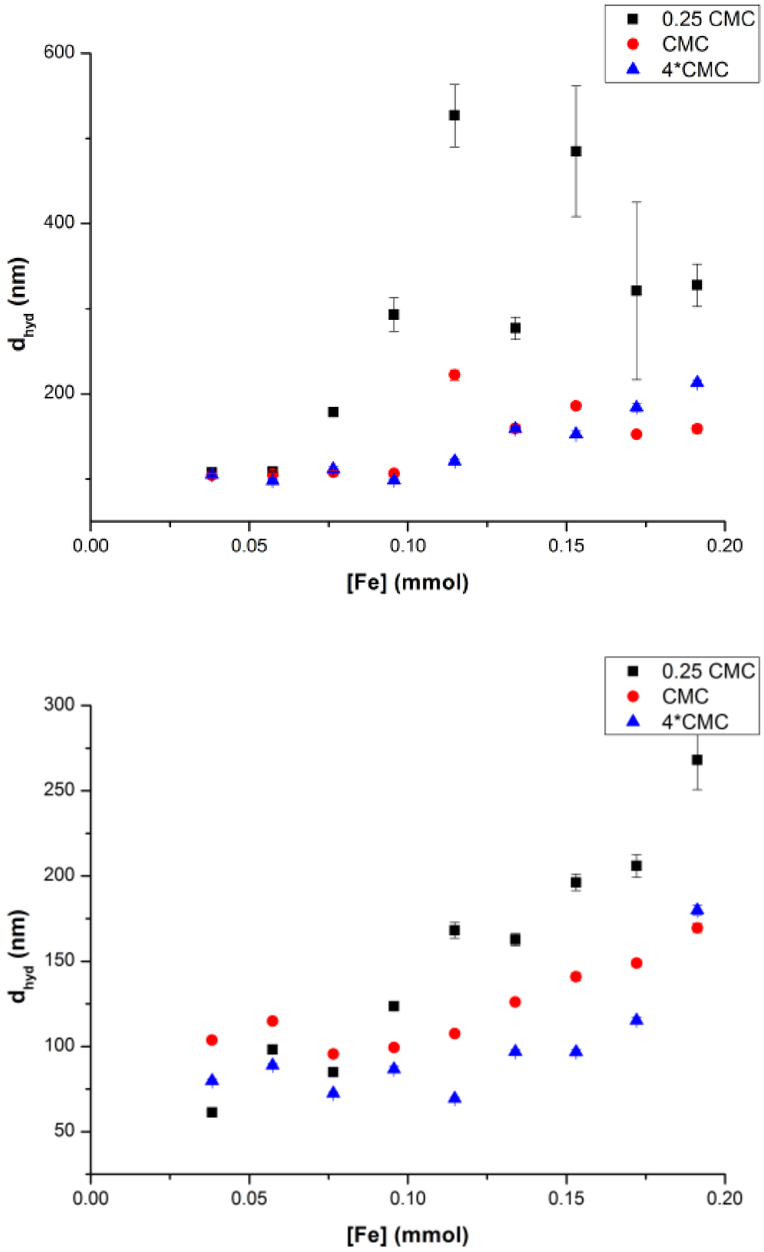

Figure 3. 20: Effect of polymer concentration on cluster formation, Pluronic F68 (left), and Pluronic F108 (right), as before samples were prepared at 0.25*CMC (black), CMC (red) and 4*CMC (blue).

Similar effects to those observed in for F127 (Figure 3. 18) was observed when using both Pluronic F68, and Pluronic F108, (Figure 3. 20) for PMA. In both cases the dispersible yield of sample increased as the polymer concentration increased, and the samples produced with a concentration below the CMC of the polymer were less optimal (no control over size, higher PDI and low dispersible yields) over the range of iron to polymer ratios. It is interesting to note that the NPCs formed at concentrations above the CMC of both polymers are as stable over time than those prepared using F127 at concentrations above the CMC, d_{hyd} and PDI are unchanged for 4 months. This is probably due to the increased hydrophilicity of the polymers, F127 is 70% hydrophilic, while F68 and F108 are both 80% hydrophilic. Note that all NPC samples prepared at the CMC and above for F127, F68 and F108 are stable for a period of at least 3 months with good PDI (<0.17).

It can be seen from Figure 3. 20 that even at a concentration of 4*CMC there is a degree of size control over the NPCs formed indicating that the DLS response is not dominated by micelle formation, unlike the case of F127. It is possible therefore that the relative hydrophilicity of the polymer could determine whether NPC formation is controllable. This hypothesis was tested using an alternative polymer P123, which has 30% hydrophilicity (w/w). It was found that regardless of polymer concentration that controlled assembly of NPs did not occur with P123. This indicates that the hypothesis may indeed be true, as the much lower hydrophilicity of P123 would make the micelles difficult to stabilize due to the much higher organic component. However, with such a large change in %hydrophilicity between F127 and P123 it is difficult to confirm whether controlled assembly of NPCs is dependent on the %hydrophilicity of the polymer. To confirm this hypothesis further study using alternative polymers of 30% with longer chain lengths could be used. Additionally, similar polymers with 50% hydrophilicity and 90% hydrophilicity could also be tested; however, such polymers are not currently commercially available.

3.3.2.3. Effect of Polymer Chain Length on Size and Polydispersity of NPCs

Samples of NPCs prepared using Pluronics F68 and F108 (both 80% hydrophilic) at their respective CMCs was compared to determine the effect of polymer chain length on NPC formation, size and PDI. Pluronics F68 and F108 have the same ratio of hydrophobic to hydrophilic material as each other however in the case of F108, both chains are longer. F68 has chain lengths of 1670 and 6680 Da, whereas F108 lengths of 2920 and 11680 Da; both for the hydrophobic and hydrophilic chains, respectively.

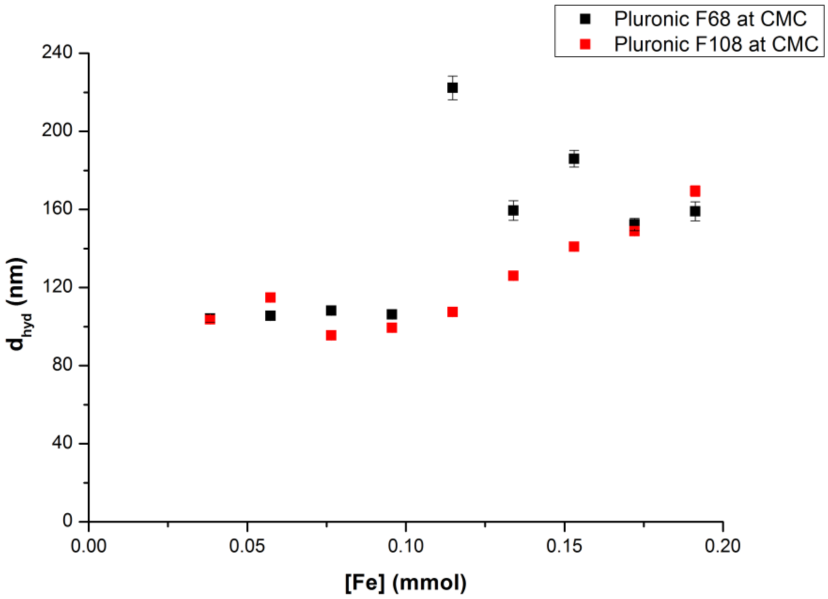

Figure 3. 21: Comparison of NPC formation by Pluronics F68 (black) and F108 (red) at their respective CMCs (F68 has a CMC of 334 g/L and F108 has a CMC of 730 g/L). The data suggests that NPC size and PDI, as Fe concentration is increased, is much more controllable when longer polymer chains are used in the clustering process, as indicated by the 3 bad data points in the F68 data, Samples prepared with F68 at concentrations of Fe greater than 0.075 mmol had an average dispersible yield of <10% and were more polydisperse (PDI >0.25) than the samples prepared with F108 (average dispersible yield of 64%, PDI <0.15)

The above data (Figure 3. 21) indicates that final NPC size is not affected by polymer chain length at any concentration of Fe. However, it is also apparent that samples prepared with a polymers of longer chain length show more controlled assembly, have a lower PDI, and were found to be more stable to the work up process. Further details of the differences in d_{hyd}, PDI and dispersible yield can be found in Table 3. 4, below.

Table 3. 4: A selection of data taken from the polymer chain length experiment highlighting the effects on the size, PDI and dispersible yield of the NPC samples produced

Polymer	**Fe Concentration (mmol)**	**d_{hyd} (nm)**	**PDI**	**Dispersible Yield (%)**
F68	0.04	104.2	0.175	64
F68	0.125	222.3	0.288	6
F108	0.04	103.7	0.091	66
F108	0.125	107.5	0.058	63

In conclusion it was determined that the size of the NPCs produced are not dependant on the length of the polymer chain used, however NPCs produced with longer polymer chains (total M_w >10,000 Da) are more stable in the aqueous environment, better tolerate the work-up procedures used (dilution in H_2O and centrifugation at 800 rcf for 5 min) and are more monodisperse than those produced with shorter chain lengths but the same ratio of hydrophilic to hydrophobic material.

3.3.2.4. Effect of Polymer Chain Ratio on Size and Polydispersity of NPCs

A further comparison was made to investigate the effect of polymer chain ratio, that is, the ratio of hydrophilic to hydrophobic material in the polymer, on cluster formation, size and PDI. In this case Pluronics F127 and P123 were compared. These polymers were chosen as the hydrophobic chain of both polymers is approximately the same length (3780 Da in F127 and 4060 in P123) however in F127 this chain accounts for 30% of the total molecular mass of the polymer whereas in P123 is accounts for 70%.

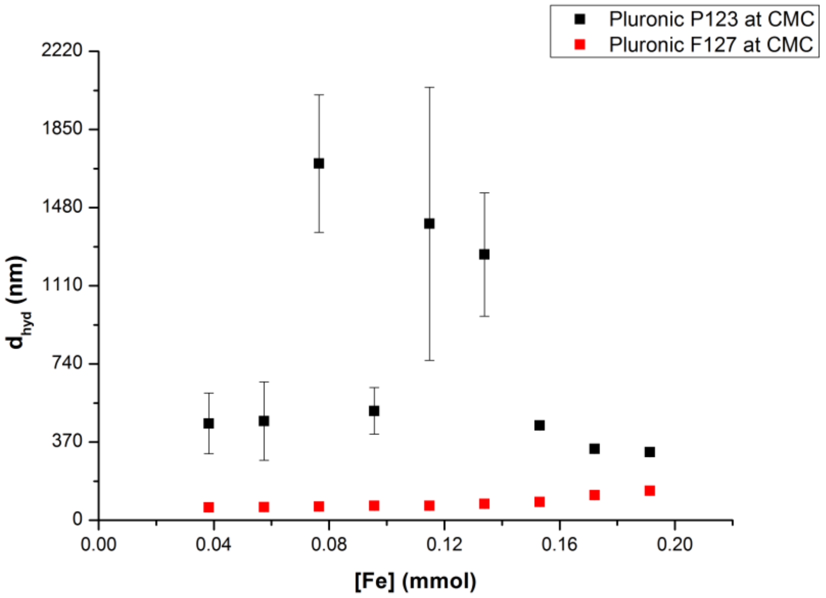

Figure 3. 22: Comparison of NPCs prepared using polymers with different polymer chain ratios, the polymers chosen were F127 and P123. These polymers have a hydrophobic chain length of approximately 4000 Da the difference between the polymers chosen is the length of the hydrophilic chains (8820 Da for F127 and 1740 Da for P123). It should also be noted that the F127 data reported here correlates well with the reproducibility data reported in section 3.3.1.3.

It can be seen from the above data Figure 3. 22 that clusters prepared using a hydrophobic polymer (P123) were not colloidally stable and uncontrolled aggregation was observed, also the dispersible yield of the NPCs produced across the series was between 1 and 5%. While it would be beneficial to extend this experiment to a wider range of polymers, that might for example have the same length PPO chain but a different ratio of PEO: PPO, such materials are not commercially available. So, the proposed comparison is difficult to make.

3.3.2.5. Effect of Nanoparticle Size on the Size and Polydispersity of NPCs

The effect of nanoparticle size on the size and PDI of NPCs formed by PMA was determined as outlined in section 3.2.4.5. The nanoparticles chosen for this experiment were analysed using TEM to determine an approximate surface area the volume of OA required in the stabilization of NPs in organic solvents was calculated, to maintain a coating of 5 surface equivalents. The Fe concentration as determined by ICP-AES was used to adjust the concentration of the NP suspensions so that in all cases the approximate number of NPs per mL of suspension was the same. The PMA experiment was then carried out as above, Figure 3. 23.

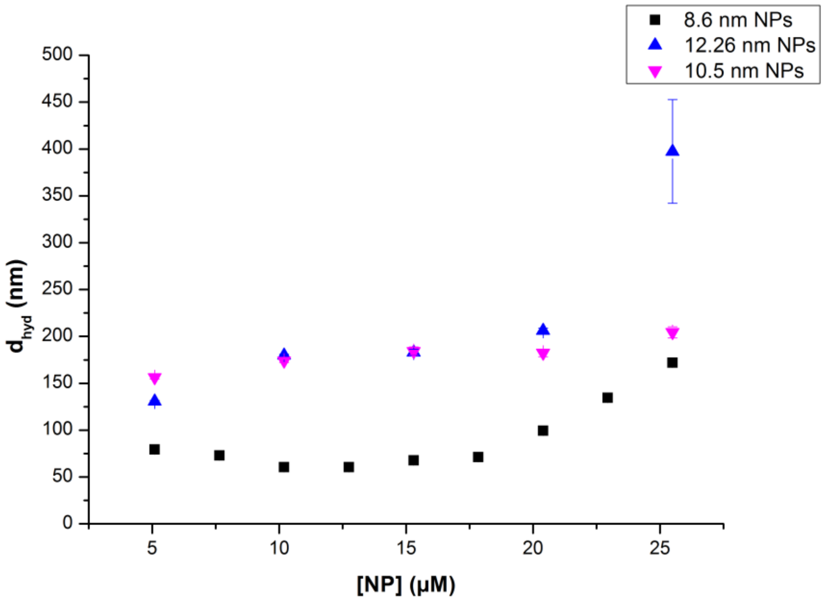

Figure 3. 23: Polymer mediated assembly of standard NPs (8.6 nm) and core-shell NPs (10.5 nm and 12.26 nm), the NP concentration was kept approximately equal between NP sizes (5.09 μM NPs) and the polymer used in each case was 64 μM Pluronic F127. The NPs were assessed by TEM to determine the d_{TEM} for the calculation of OA concentration required, this was also maintained between the samples at 5 equivalent volumes. Note that the 25 μM, 12.26 nm point had a dispersible yield of <5% and a high PDI, and is thus unreliable in the assessment of the overall trend.

It was found that in general larger NPs used produced larger NPCs, other considerations being equal. This may be due to the larger particles interfering less with micelle formation at lower concentrations of Fe, as the size of NPCs prepared with 10.5 and 12.3 nm particles did not have a significant difference in size or PDI at lower concentrations. Our interpretation is that the 8.6 nm particles interfere with the micellization process of F127 resulting in the formation of smaller micelles of F127 and hence smaller NPCs at low Fe concentrations. Above a threshold size, these interferences are no longer observed and the polymer micelles form as they would without the presence of NPs. This hypothesis could also be further tested using smaller NPs of iron oxide, a d_{TEM} *e.g.* of approximately 6 nm. It is believed that assemblies of these particles would be smaller again due to the increased volume to surface area ratio of the particles interacting more significantly with the polymers. Reproducible synthesis of 6 nm NPs by surfactant free thermal decomposition has not yet been achieved by methods that allow control over the surface ligand equivalents. In any case, reducing the size of the NP usually reduces its saturation magnetization significantly affecting applications performance[48].

As with previous experiments it was found that NPCs with d_{hyd} exceeding 250 nm were not colloidally stable and did not survive the work-up process at <1% dispersible yield. It is also clear from Figure 3. 23 that the increase in NP size does not have a proportional effect on the size of the NPCs produced; as, at intermediate concentrations of NPs, the NPCs produced using both 10 and by 12.3 nm NPs are the same size and have comparable PDI. This suggests that the size of the NPCs produced is largely determined by the number of NPs within the NPC as the Fe : polymer ratio is the same, so NPC size is determined solely by the number of NPs present.

A final experiment was performed to investigate the hypothesis that, for NPCs prepared using larger NPs, the formation of polymer micelles was not interrupted to the same extent by the presence of NPs in the suspensions. In this experiment NPs with a d_{hyd} of 12.3 nm were diluted to the same [Fe] as the standard preparation of 8.6 nm NPs, and the PMA procedure was performed as usual. It was found that the size of NPCs formed was less dependent on the relative concentration of Fe in the case of the larger NPs, Figure 3. 24.

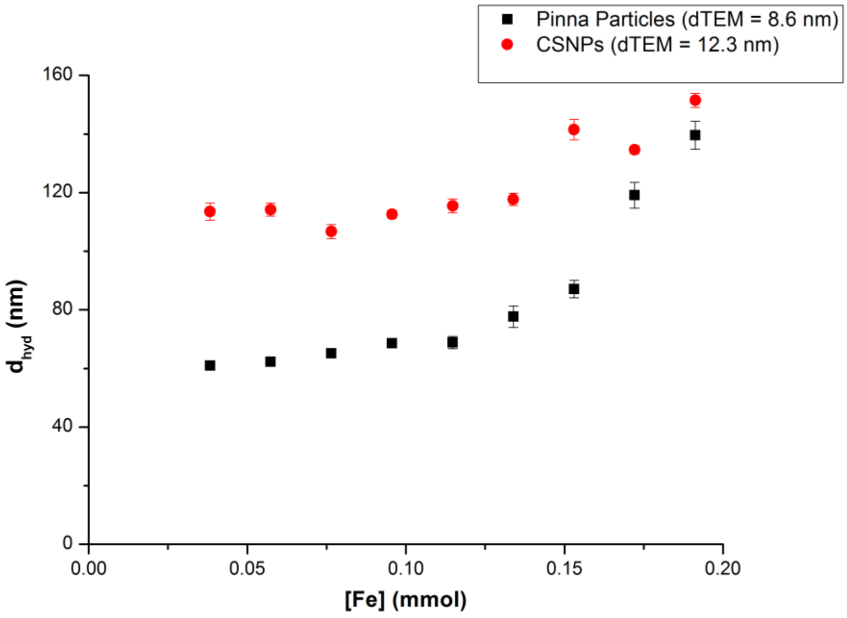

Figure 3. 24: Polymer mediated assembly of 12.3 nm and 8.6 nm NPs from stock suspensions at the same Fe concentration (74.5 mM). Both NP suspensions were prepared with 5 equivalents of OA, at 64 µM Pluronic F127. The relative number of NPs was 1.82 NPs (8.6nm) for every 12.3 nm NP.

This behaviour is similar to that observed in the original PMA experiment at very low iron concentrations, as demonstrated in Figure 3. 8. This indicates again that the final NPC size is largely dependent on the number of NPs in the NPC rather than the ratio of Fe to polymer which correlates with our previous findings (Figure 3. 8, Figure 3. 23). It is also apparent that smaller NPs (d_{TEM} <10 nm) have a greater effect on the production of polymer micelles. The NPC size in suspensions produced with 12.3 nm NPs, that appear to be unaffected by the increasing Fe concentration, are found to form NPCs at the same size as the micelles of F127 in H_2O. In NPCs prepared with smaller NPs the micelle size is reduced by 25%.

3.4. Conclusions

In this Chapter a successful method for the preparation of size controlled nanoparticle assemblies was presented, in the Fe concentration range 0.04 - 0.21 mmol at polymer concentrations around the CMC of the polymers Pluronic F127, F68 and F108. The effect of a number of assembly parameters on size and monodispersity was investigated, and the potential for scale-up to the application relevant range was also demonstrated. By careful control of individual assembly parameters, it was shown that a particular size of NPC could be targeted and selectively produced as high monodispersity suspensions reproducibly. Particular properties of NPCs could selectively targeted, *e.g.* NPCs with a high NP loading density (Figure 3. 9). The effect of polymer chain length and polymer chain ratio on NPC formation, PDI and stability were investigated.

It was found that the process is highly reproducible, and it can be scaled up to a 50 mL with no significant effect on the size of the NPCs produced, and to a 100 mL scale with a slight variation in the experimental setup. All samples produced are colloidally stable for a period of 3 months and the polydispersity of samples produced following a minimal work-up procedure are low (<0.18). All of the materials used in the preparation of these NPCs are widely commercially available at lost cost and high purity. They are non-toxic, and the polymers used have previously been FDA approved for selected bio-applications. These results show that at the time the study was completed a robust method for the reproducible preparation of NPCs over a size range 50-200 nm had been developed. It is important to note that multiple batches of NPs were used throughout this study and the response was highly reproducible. Since June 2016 the source of $Fe(acac)_3$ has changed and this reproducibility has no longer been possible.

It was determined that the optimal conditions for the production of colloidally stable NPC suspensions were using an Fe concentration between 0.04 and 0.19 mmol of Fe per mL of aqueous polymer solution at the CMC of the polymer (e.g. 64 µM F127). The polymer should be highly hydrophilic (>50%) and have relatively long polymer chains (total M_w >10,000 Da). The primary NPs should be stabilized with an intermediate amount of surfactant, 5 equivalents, to ensure complete chemisorption of OA to the NP, as this allows for optimal size control. The primary NPs must also be colloidally stable over a significant period of time, with an absolute minimum of 5 days, due to the length of time required for the assembly to occur.

The PMA method was also applied to larger nanoparticles and it was found that colloidally stable NPCs of d_{hyd} greater than was possible using smaller NPs, could successfully be prepared. This experiment was performed twice, using both the same Fe concentration (74.5 mM Fe) and, the same NP concentration (5 µM NPs) respectively. Our interpretations are that this increased stability at larger NPC size is probably due to increased magnetic interaction between individual NPs allowing larger NPCs to be more stable. If correct, this suggests that interparticle magnetic interactions are highly important in determining final NPC stability. Hence it may be that cubic NPs of iron oxide may also form larger NPCs during the PMA process than their spherical counterparts, due to the increased magnetic affinity (higher coercivity at the same volume) between cubic NPs in the superparamagnetic range than spherical NPs. Further experiments involving the preparation of NPCs from cubic NPs will be described in Chapter 6.

Chapter 4: Investigation into the Potential Theranostic Capabilities of Magnetic Nanoparticle Assemblies

4.1. Introduction

Theranostic agents as described in Chapter 1 are agents whose properties allow them to be used as both therapeutic and diagnostic agents. Nanoparticle based systems have huge potential as theranostic agents, due to their small size, high surface-to-volume ratio, they are easily functionalized, and easily tailored for desired purposes. As well as this, many nanoparticles have already been analysed for their diagnostic potential and their therapeutic potential separately. A theranostic approach to medical treatment is advantageous as it allows for real-time monitoring of a treatment as it is underway rather than before or after, it also reduces the total number of agents that a patient will be exposed to, minimizing the risk of unwanted drug interactions and side effects[89].

Nanoparticle based theranostic agents are an obvious route as many nanomaterials are already imaging agents: semiconductor quantum dots[90], carbon dots[91] and Au NP[92]s are all optically active; carbon nanotubes have some potential as Raman[93] and/or photoacoustic imaging[94] agents; and iron oxide and manganese NPs are useful MRI agents[95]. Nanoparticles must also be coated for biomedical applications, as they must be colloidally stable in an aqueous environment to prevent uncontrolled agglomeration in vivo. These surface coatings offer a route to functionalization with molecules of interest, such as drugs/antibodies, and to increased *in vivo* retention.

Magnetic nanoparticles, and nanoparticle clusters behave as contrast agents in MRI by inducing local magnetic field inhomogeneities which affect the NMR relaxation of the protons in the solvent. The interaction between magnetic NPs and solvent molecules can be described by an outer sphere spin–spin relaxation approximation, where the R_2 relaxation rate is determined by equation 4.1[96].

$$R_2 = \frac{\left(\frac{64\pi}{135000}\right)\gamma^2 N_A M \mu_C^2}{rD}$$

Equation 4. 1

Where N_A is Avogadro's number, M is the NP molarity (moles.L^{-1}), μ_C is the magnetic moment of the nanoparticle, r is the effective magnetic radius of the NP, and D is the diffusion coefficient of water molecules[97].

It is clear from Equation 4. 1 that the R_2 relaxation rate is directly proportional to the square of the magnetic moment and inversely proportional to the magnetic radius of the NPs. The magnetic moment of an NP is directly proportional to its volume, therefore the R_2 relaxation rate will increase with NP diameter[97]. However, a magnetically disordered surface layer is always present. As the diameter of a NP decreases, this outermost layer of atoms accounts for a higher fraction of the total volume of the NP. Thus, significantly reducing the effective magnetization of the NP[97].

Consideration of these effects suggests that for improved NMR (and thus MRI) response, larger iron oxide NPs should be used. However, as size increases Superparamagnetism is lost. Particles that display superparamagnetic properties do not typically exhibit a magnetic response in the absence of an external magnetic field. As the moments rapidly fluctuate they are only weakly attracted by one another allowing for the preparation of a highly stable colloidal solution of NPs. In the presence of a magnetic field, moments align with the magnetic field, on the removal of this external magnetic field, the net magnetization of the suspension returns to zero, thus the risk of aggregation is low. Ferromagnetic particles on the other hand have slowly fluctuating and strong moments even in the absence of an external magnetic field the magnetic moments align and "lock" resulting in increased probability of agglomeration of the NPs. *In Vitro*, this manifests as NPs becoming colloidally unstable and falling out of suspension, *In Vivo* however, this can manifest as a large agglomerate which could cause a blockage in the circulatory system, resulting in a stroke, embolism or coronary episode.

Controlled aggregation of superparamagnetic NPs allows for the retention of the valuable superparamagnetic properties of the NPs (low agglomeration risk, field switchable magnetic response) with the additional advantages of behaving as a larger single NP in the presence of an external magnetic field due to the alignment of the magnetic moments where the total magnetic moment of the NPC increases with NPC diameter. Controlled aggregation of magnetic NPs has been shown to significantly increase the T_2 weighted MRI response of the NPs[98], the challenges in realizing this are discussed in Chapter 3.

Magnetic fluid hyperthermia is a technique whereby nanoparticles in the presence of an external alternating magnetic field heat due to friction and hysteresis losses. Hence, NPs are currently under study as a potential treatment for solid tumours in cancer therapy, and as an approach for drug release when composited with thermally responsive polymers, and hydrogel matrices. As with NMR, the hyperthermic response of a material has been shown to be directly related to nanoparticle size, with a maximum hyperthermia response for iron oxide nanoparticles has been shown at ~12.5 nm[99] (Figure 4. 1) through simulations by Gonzales-Weimuller *et al*. The effect of assembly on the hyperthermia response of NPs prepared by thermal decomposition of iron acetylacetonate is not expected to be positive. There are two possibilities:

1. The NPs will still behave as individual 8.5 nm particles, and, as per Figure 4. 1 the SAR (specific absorption rate) will be unchanged
2. The NPC will behave as a single larger particle and the SAR will decrease as the motion of the moment is effectively stopped

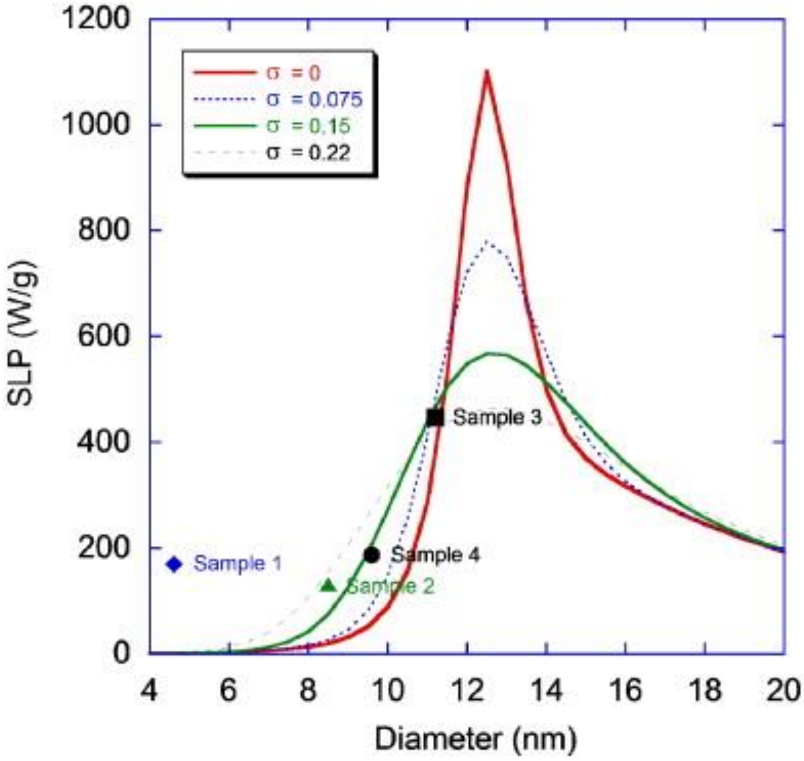

Figure 4. 1: Simulated hyperthermia response expressed as Specific Loss Power, SLP as a function of NP size for a magnetic field strength of 24.5 kA/m. Plots are calculated for various polydispersity indexes. In this figure σ represents the standard deviation of NP diameter (nm) in the theoretical samples. Additionally measured SLP values of 4 samples have been plotted for direct comparison with the theoretical data[100].

Another important characteristic of theranostic materials is their potential for targeted drug delivery. This takes two primary routes, active targeting either through the use of biological moieties such as proteins and antibodies or through physical properties of the materials such as magnetic distribution (using an external magnet to concentrate magnetic materials in a region of interest); and, passive targeting.

It is also known that tumours possess "leaky vasculature" which allows particles of a given size, generally between 10 and 100 nm to enter into the extra vascular space when the circulation times are sufficiently long[101]. This can result in retention within the tumour. Unprotected nanoparticles and poorly disguised NPs and NPCs are rapidly recognised by macrophages *in vivo* and transported to the liver to be broken down for excretion. This natural, non-specific response allows for the detailed study of the liver without the need for complex direct organ targeting NP or NPC design.

Active targeting is a much more complex route, as the NP/NPC sample must be sufficiently protected to avoid triggering the immune response, thus prolonging the circulation time *in vivo*. The use of proteins and monoclonal antibodies (mAbs) with targeted affinity for a specific cell type can then be used allowing for a higher degree of NP/NPC cell internalization, thus increasing the therapeutic efficiency of the NP/NPC sample[102]. However, targeting moieties generally decrease blood circulation times.

Drug delivery can also be performed by two methods, chemical binding to the NP or some part of the NPC and physical encapsulation within an NPC. Chemical binding can be performed using a number of chemistries such as click chemistry[103], and any method of surfactant characterization[104], whereas physical encapsulation requires no complex chemistry but rather is dependent on the intermolecular interactions involved in micelle/liposome/polymerosome formation[105,106].

In this Chapter the potential of NPCs prepared by PMA of NPs prepared by surfactant free thermal decomposition as future theranostic materials will be examined. Their magnetic resonance properties and the potential modification of the polymer for active targeting or drug delivery will be investigated. Preliminary studies on the active delivery through external magnetic fields and preliminary toxicological studies of the materials will be shown. These experiments are expected to show that the assembly of magnetic nanoparticles through PMA can provide a significant improvement as multimodal theranostic materials, as compared to dispersed nanoparticles.

4.2. Investigation into the Potential of NPCs prepared by PMA as MRI Contrast Agents

PMA-NPCs formed of dispersed iron oxide NPs prepared by surfactant free thermal decomposition of iron acetylacetonate, and assembled using Pluronic F127 were prepared as outlined in Chapter 3 and d_{hyd} was varied by careful control of the ratio of iron NPs to polymer. The r_1 relaxivity was measured for each sample as a function of Larmor frequency, in the range 100 kHz – 40 MHz, as outlined in Chapter 2, and the results are presented below in Figure 4. 2. Controlled assembly of nanoparticles results in suppression in the r_1; and an increase in the r_2 relaxivity. According to SPM theory[107], Chapter 1, a shift of r_1 max to lower frequency, peak broadening, and r_1 suppression are all expected as the size of the NPs increases. It can be seen in Figure 4. 2 that these trends are observed for NPCs prepared by PMA using Pluronic F127. Note that the samples were also shown to be stable to the magnetic field by DLS (Figure 4. 3).

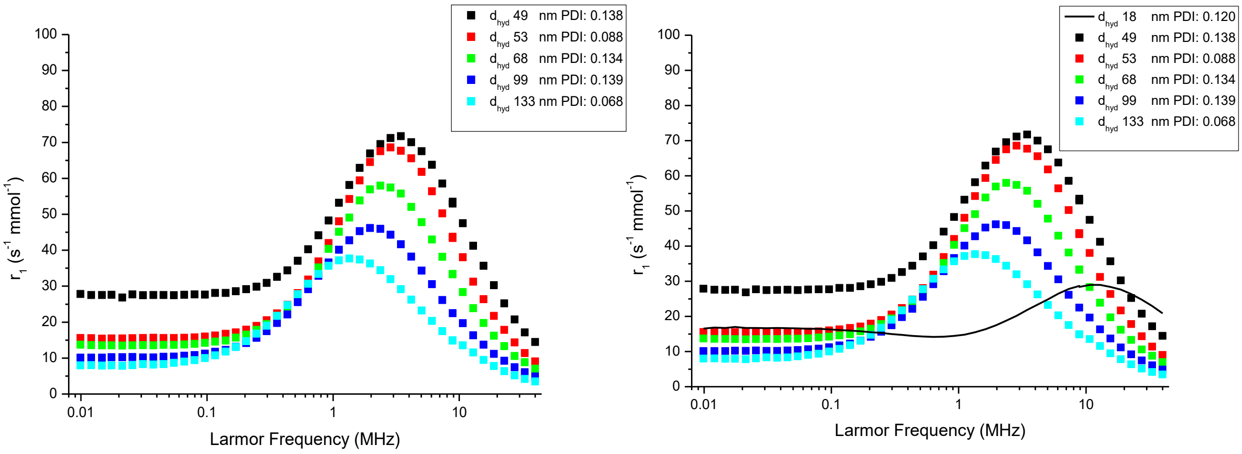

Figure 4. 2: FFC-NMR profile for NPCs (left) prepared using 8.5 nm IONPs assembled with Pluronic F127 over a frequency range of 100 kHz to 40 MHz. As expected there is a shift of r_1 max to lower field and increased r_1 suppression as the NPC diameter increases. Graph on the right shows this data, with dispersed NPs in water, also plotted on the same curve.

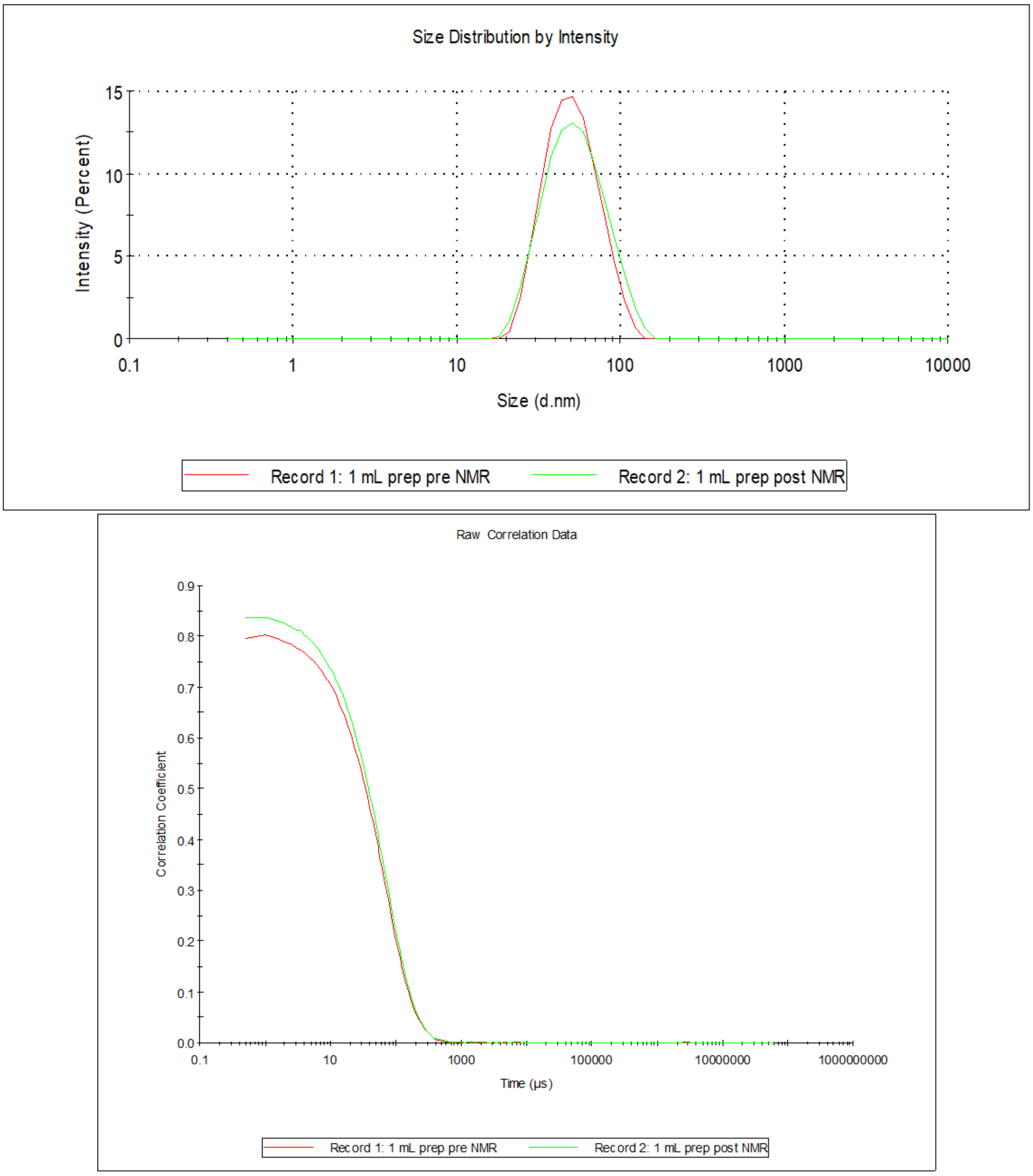

Figure 4. 3: DLS data of PMA-NPC sample (d_{hyd} = 47 nm) before (red)and after (green) exposure to the NMR fields. It can be seen both in the intensity curve and the correlation data that the size is unchanged, PDI remains low and that there is no indication of aggregation following exposure to the field.

The overall shape of the NMRD profiles recorded demonstrates an apparent convergence of the r_1 values at higher fields, and an $r_1 - d_{hyd}$ relationship at low field. The presence of an r_{1max} value at mid-high field (1-10 MHz) indicates that the assembly process has not affected the superparamagnetic nature of the material. If we directly compare the shape of the PMA-NPC profiles to those obtained for dispersed NPs prepared by thermal decomposition of iron acetylacetonate and stabilized in aqueous media (Figure 4. 4), it can be seen that while the overall shape of the curve is maintained, the r_1 minimum "dip" has been lost, indicating an increase in the magnetocrystalline anisotropy energy (activation energy for the reorientation of the moment). This is as expected, as NPs contained within a PMA-NPC are expected to have interparticle dipolar interactions. Hence, the dynamics of the cluster moment should be reduced as compared to dispersed NPs. Interestingly, the r_1 relaxivity profile of the dispersed NPs, if plotted with the PMA-NPC data, as shown in the insert of Figure 4. 2. demonstrates that the relaxivity at r_{1max} is higher for the NPCs than it is for the dispersed smaller particles. This is unusual, as it is expected that an increase in d_{hyd} would lead to an overall suppression of r_1, and a shift of r_{1max} to lower field.

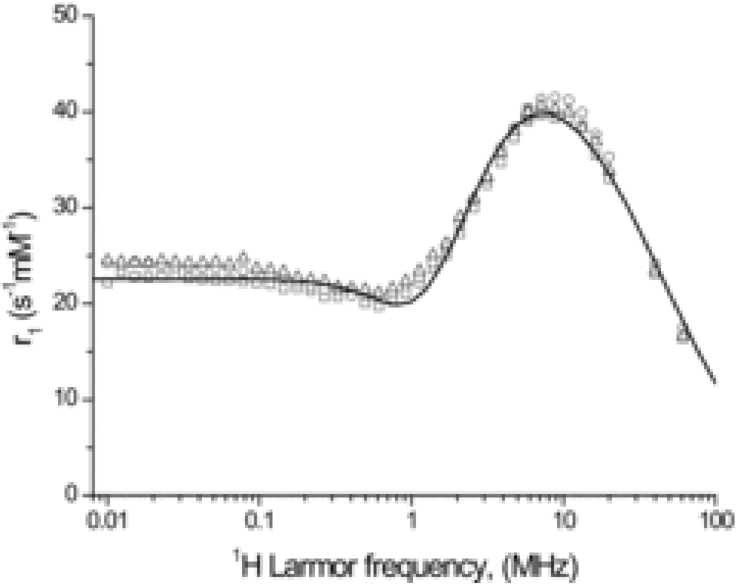

Figure 4. 4: NMR relaxivity profile of Primary NPs as prepared by the Surfactant Free Thermal Decomposition of iron (II) acetylacetonate, dispersed in water (APTES used as a stabilization ligand) and fit to the SPM model described by Muller[108], where the open circles and triangles represent the true r_1 values measured at a given frequency and the solid line represents the SPM fit..

If we consider the PMA-NPC profiles alone, it can be clearly seen that an increase in d_{hyd} corresponds to a shift of r_{1max} to lower frequency, and overall suppression in r_1 at lower frequencies. The response was simulated using the SPM model developed by Müller *et.al* for each PMA-NPC sample. It can be clearly seen in Figure 4. 5, below that the model can be manipulated to fit the data well, and some interesting material properties may be extracted,

Table 4. 1. These values can then be directly compared to those found by simulating the magnetic resonance response of primary nanoparticles. It can be clearly seen that there is a striking difference in the behaviour of the primary particles, prepared by surfactant free thermal decomposition of iron (II) acetylacetonate and stabilized with oleic acid in a heptane suspension. This indicates that the intact, soft assembly in suspension behaves as a single magnetic entity rather than a collection of primary particles. This is also suggested by the change in magnetic response observed over the range of NPC sizes.

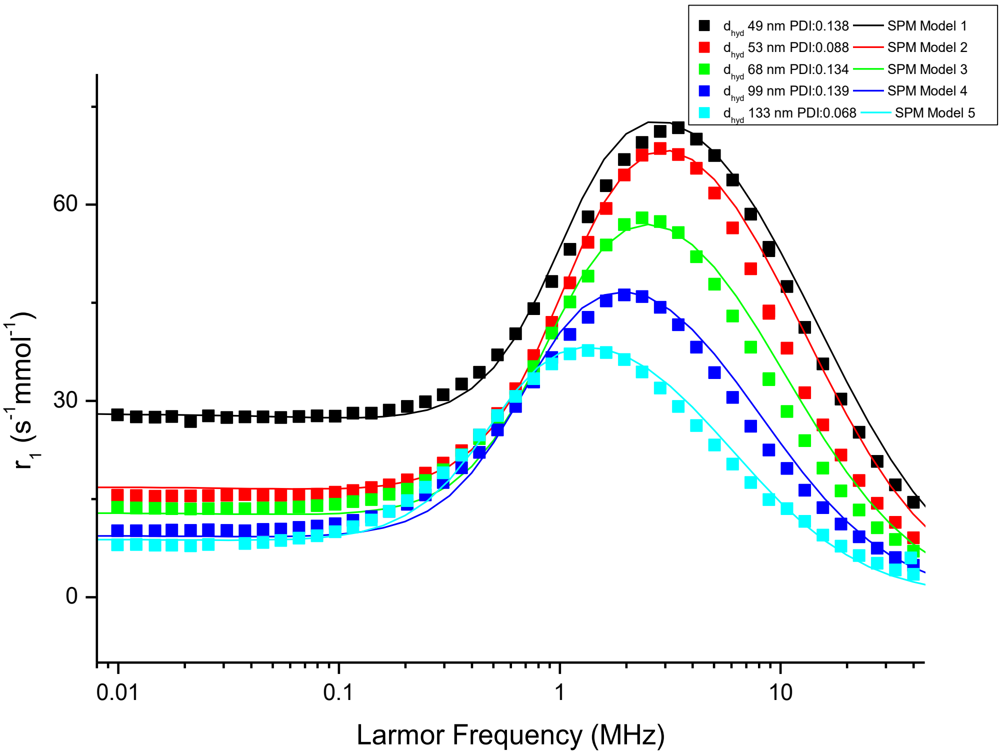

Figure 4. 5: Simulated fits of NMRD profiles of the PMA-NPC samples based on the SPM model developed by Müller et al.

Table 4. 1: Magnetic properties of primary NPs and NPCs extracted from the SPM fit of NMRD data recorded in H_2O. Primary NP data and fit have previously been reported for water stable NPs prepared by the surfactant free thermal decomposition method[108].Parameters extracted are magnetic diameter (d_{NMR}), saturation magnetization (M_s), Neél correlation time (τ_N), activation energy (ΔE), and diffusion coefficient of water surrounding the particle.

Sample	d_{NMR} (nm)	M_s (emu. g^{-1})	τ_N (ns)	Δ E (GHz)	Diffusion Coefficient ($cm^2. s^{-1}$)
Primary NPs	10	60	17	1	402000
49 nm NPC	6.5	45	7	4	150000
53 nm NPC	7	41	6	1.5	140000
68 nm NPC	7.8	34	6	1.5	140000
99 nm NPC	9	27	6	1.5	140000
133nm NPC	10.5	21	6	3	140000

The fit to the data produced using the parameters found in Table 4.1 above, is particularly interesting. If we consider the NPCs, separate to the dispersed NPC sample, it can be seen that the ‘magnetic diameter’ of the clusters increases with increased d_{hyd}, and that M_s decreases. This indicates that by the SPM model at least the overall magnetic response is lowered as d_{hyd} increases. This is consistent with the NPCs being hollow; with the magnetic percentage % decreasing with size, or with an increasing fraction of the NPCs being solvent inaccessible. If we directly compare the PMA-NPC parameters with those of the dispersed NPs (these are the actual primary NPs used in the NPC assembly, so the intrinsic magnetic properties of these particles are the same) it can be seen that assembly has a significant effect on the magnetic resonance properties. The most unexpected result, the relevant magnetic diameter (d_{NMR}) were found to be equal to or lower than that of the primary particles, which is counter intuitive. It was expected that the larger NPCs would behave magnetically as a single larger particle, however these low d_{NMR} values suggest that the correlation time for interaction of diffusing water with the magnetic entity is shorter than for NPs, see Chapter 1.

Indeed, to fit the data well the diffusion coefficient of the water around the NPC must be significantly lower than the diffusion coefficient of the water surrounding primary NPs in an aqueous suspension. While the literal interpretation of the parameters extracted from the SPM simulations is problematic, it is highly likely that they capture aspects of the dynamic ^{1}H-μ interactions not obtainable by other approaches, in this case local water appears to be more restricted for clusters, and there is discernible cluster size dependence to this restriction (as manifested in the d_{NMR} values).

When compared to the magnetic response of the primary NPs a significant increase in r_1 is observed at lower frequencies (low field) for 49 nm sized NPs. This is indicative of an increase in the magnetocrystalline anisotropy, confirming the presence of interparticle interactions (clustering). The r_1 values observed at low field decrease with increasing NPC size indicating: either that only surface NPs are sensed, i.e. water cannot diffuse easily throughout the NPC; or, that the NPCs are becoming less dense as the size increases, and so there is a larger distance between particles in the NPC, reducing intraparticle magnetic interactions.

A different response was observed for DHAA-stabilized nanoparticle assemblies (DHAA-NPCs) analysed within our research group in collaboration with Prof. Mathur, University of Cologne, Figure 4.6. These assemblies have a similar size range to the polymer mediated assemblies, so the comparison is interesting.

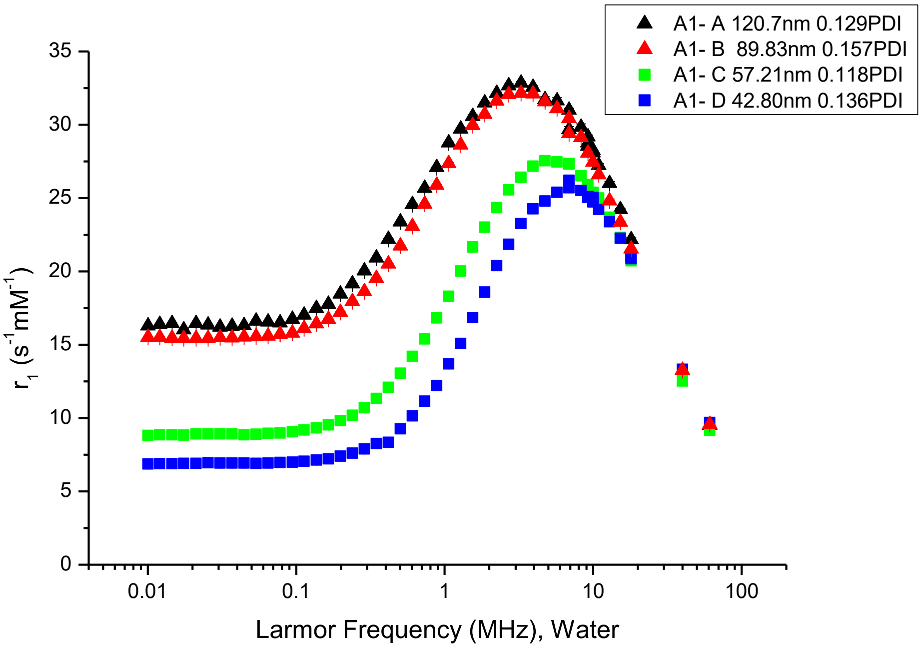

Figure 4. 6: NMRD profiles of dense nanoparticle assemblies of varying sizes, as prepared by a collaborator and analysed using FFC-NMR Relaxometer as outlined in Chapter 2

The main observations for DHAA-NPCs are that in the clinical MRI (~60 MHz; 1.5 T) range the r_1 values for differently sized assemblies are very similar, as was the case for PMA-NPCs; as d_{hyd} increases. The ν_{max} value was found to move to low frequency, as with PMA-NPCs, however unlike the PMA-NPCs a significant increase in r_1 is observed at lower frequency as d_{hyd} increases. The increased low frequency r_1 is consistent with higher magnetocrystalline anisotropy, due to increasing interparticle interactions in the NPCs, the opposite effect is seen for PMA-NPCs. A possible interpretation of this behaviour is that the DHAA-NPCs are fully H_2O permeable, indicating that all nanoparticles in these assemblies are sensed by the diffusing solvent

molecules and hence the effect of anisotropy dominates.

A further study of dense NP clusters; in this case NP containing liposomes (LNPCs) was performed within the research group which also yielded different size dependent behaviour. In this case a decrease in r_1 was observed with increasing d_{hyd}, and a linear dependence was found in the relationship between r_1 (ν_L = 0.01 MHz) and d_{hyd}, Figure 4.7, It was suggested that this effect arose due to surface area: volume (r^2 / r^3) considerations, *i.e.* the diffusing water only sensed the NPs at or close to the surface of the clusters; hence the linear dependence of r_1 on d_{hyd}. This hypothesis is consistent with the fact that the LNPCs contain a water impermeable layer of hydrophilic lipid molecules. In broad terms, the profile shape is largely unchanged suggesting similar interparticle interactions in all cases with the r_1 reducing with size at as a greater fraction of the NPs are embedded in the core.

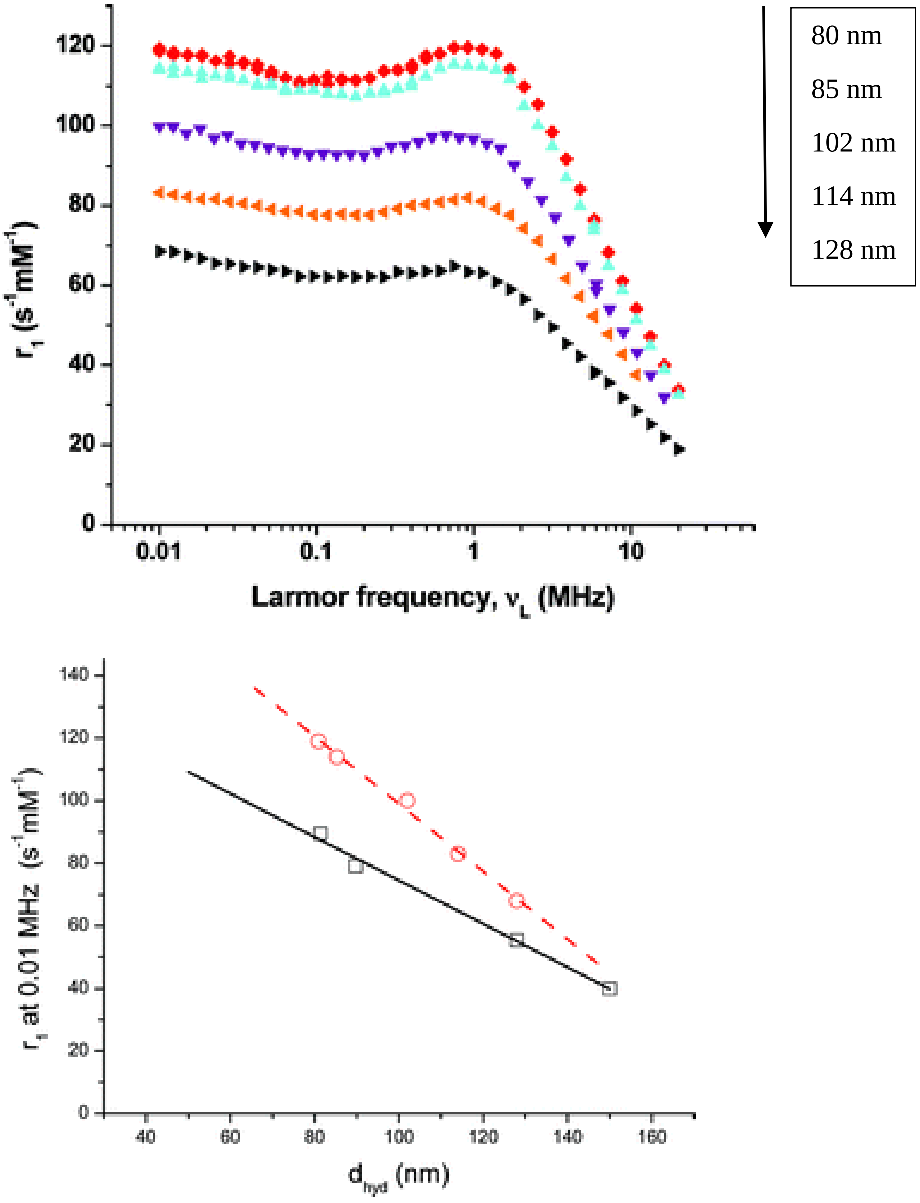

Figure 4. 7: NMRD relaxivity profiles of magnetoliposomes (Left) and a graphical representation of the relationship between r_1 at low field and the hydrodynamic diameter of the magnetoliposomes [109]

A similar linear dependence of the low frequency r_1 values was observed for PMA-NPCs with a good linear correlation (once the 49 nm sample is excluded), but with a much lower slope (Figure 4. 8)

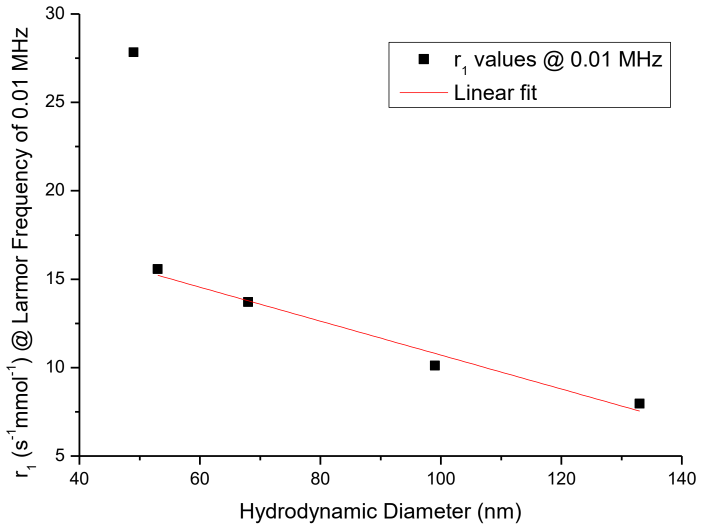

Figure 4. 8: Plot of r_1 relaxivity against hydrodynamic diameter, T_1 measurements performed at 60 MHz. Linear correlation (r^2= 0.956) observed when 49 nm data point is excluded.

This suggests a surface limiting behaviour for PMA-NPCs similar to the LNPC case. The retention of a clear r_1 max confirms that the magnetocrystalline anisotropy is much lower in this case. However, the behaviour of PMA-NPCs is unlike DHAA-NPCs for which r_1 increases with size. The implication is, that for PMA-NPCs there is increased magnetocrystalline anisotropy, but with the retention of permeability, unlike the other types of cluster.

As outlined in Chapter 1 and in the introduction to this Chapter, iron oxide nanoparticle assemblies are more commonly associated with T_2 – weighted MRI. In Figure 4. 9 the concentration independent r_2 relaxivities at clinical field (ν_L =60 MHz; ~1.5T) are graphed against d_{hyd}. If all NPC properties were constant with the exception of NPC diameter, it would be expected that a linear response would be observed, increased number of particles causing an increased magnetic response.

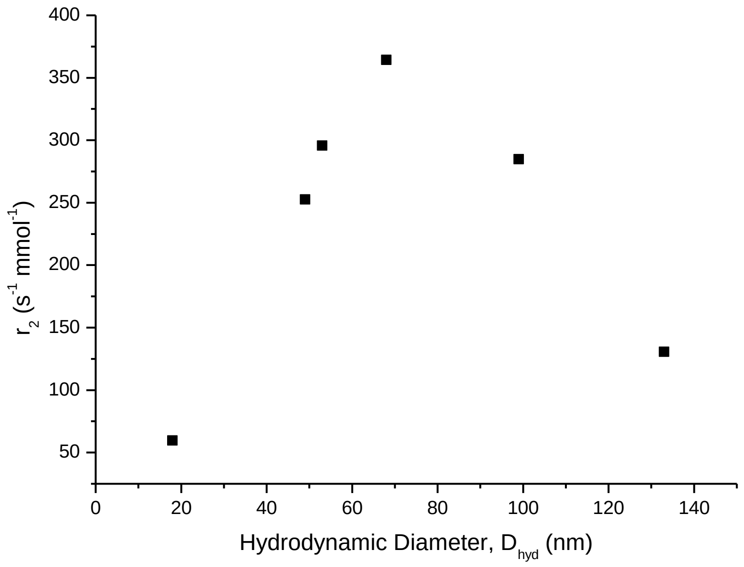

Figure 4. 9: r_2 relaxivity vs hydrodynamic diameter, measurements performed at clinical field, (1.5 T; 60 MHz)

For PMA-NPCs Figure 4. 9, two apparently linear regimes can be observed. It is interesting that the r_1 response changed smoothly and continuously over the complete size range, with no transition apparent at ~70 nm. The unusual r_2 behaviour might arise due to a change in the internal NPC structure at d_{hyd} values greater than 70 nm. It may also correspond to the transition between the MAR and SDR, to investigate this hypothesis, the r_2 values were obtained with an echo delay of 16, and an echo delay of 80 in all cases. There was no indication of an echo delay dependence for any of the samples in this study, typical results showed a T_2 values of 1.2×10^{-3} s for an echo delay of 16 ms, and 0.9×10^{-3} s when measured with an echo delay of 60 ms suggesting that all samples are in the MAR. Alternatively, larger PMA-NPCs may have regions of water permeability (folded gaps within a loosely packed cluster). Schematic representations of these NPC structures are shown in Figure 4. 10, below.

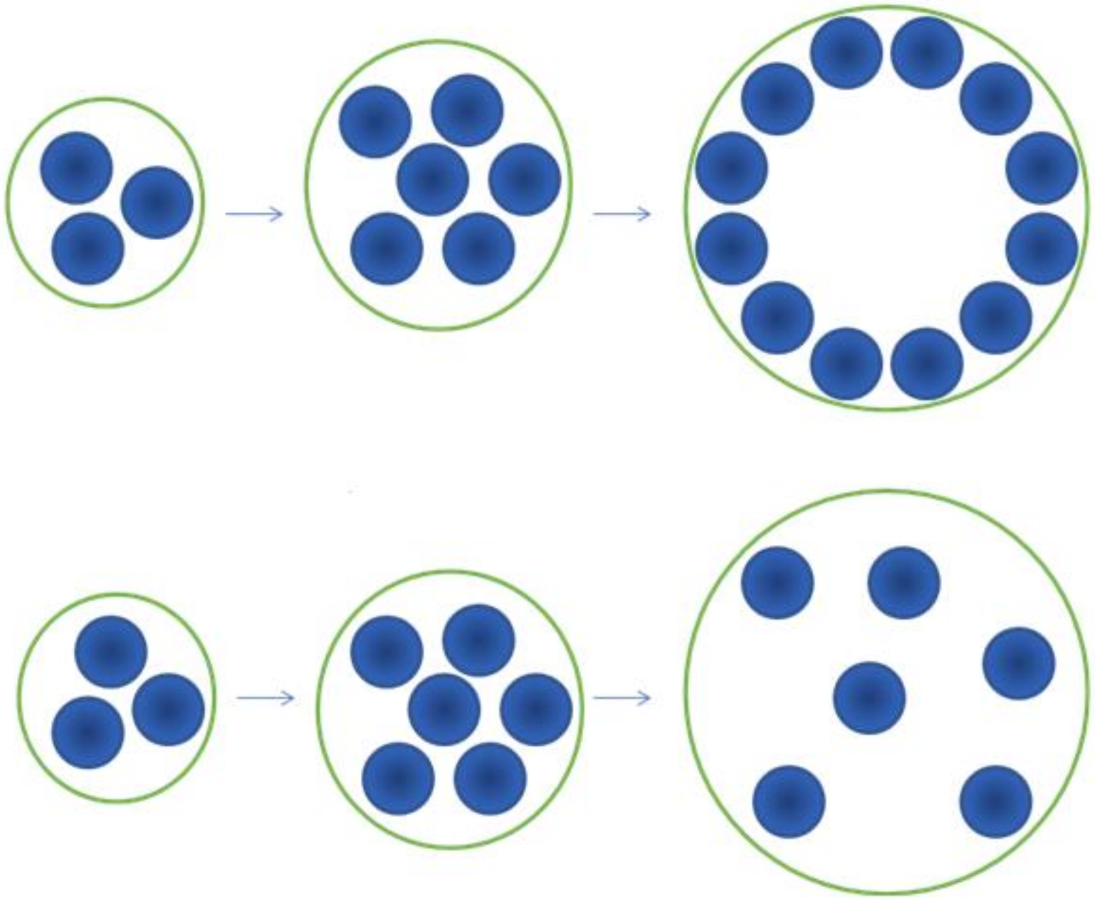

Figure 4. 10: Illustration of potential internal structure dependency of PMA-NPCs, upper structure, hollow spheres with a densely packed outer shell "surface NPCs"; lower, "plum pudding" type model where NPs are randomly distributed within the NPC, "embedded NPC"

A direct relationship between the packing density of a nanoparticle assembly, it's saturation magnetization and its size has recently been modelled and reported by the Sandre group[110]. The observed r_2 values, for a range of samples taken from multiple sources, at clinical field were scaled by $\frac{\varphi_{intra}}{{M_v}^2}$, where ϕ_{intra} is the internal magnetic volume fraction of the NPC and ${M_v}^2$ is the squared saturation magnetization value of the NPs in $A.m^{-1}$. In Sandre's report the scaled r_2 values (notated as r_2*, with units of s^{-1} mM^{-1} m^2 A^2) were found to be directly proportional to d_{hyd} for all samples, across a wide d_{hyd} range.

The r_2 data recorded for PMA-NPCs at clinical field was scaled as described by Sandre[110] assuming a hexagonally close packed NPC structure and an M_s value of 60 emu.g^{-1} (the value obtained from magnetometry of the dispersed primary NPs)[108]. It can be seen from Figure 4. 11, that using these assumptions, the PMA-NPC data (black squares) does not fit the Sandre Model.

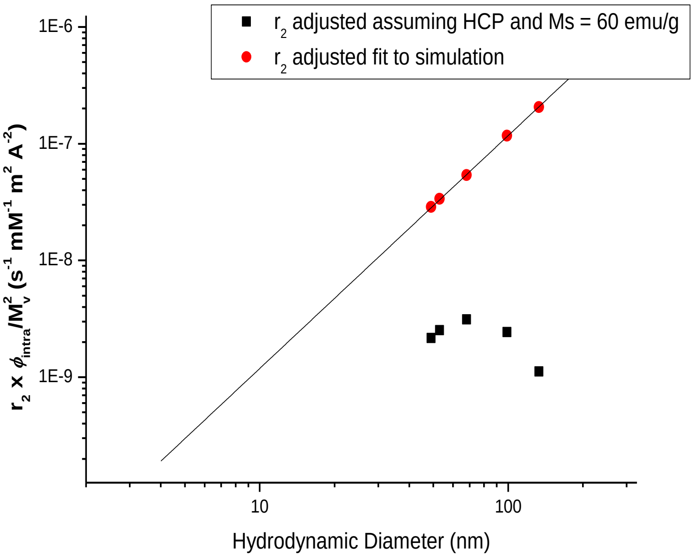

d_{hyd} (nm)	r_2*
49	2.78E-08
53	3.42E-08
68	5.69E-08
99	1.15E-07
133	2.19E-07

Figure 4. 11: Black data points represent the observed r_2 data adjusted assuming hexagonal close packing, and a saturation magnetization for the clusters of 60 emu/g (as this is the Ms of the primary nanoparticles). Red points have been fit to the simulation assuming hexagonal close packing. The table provided (right) gives the r_2^* values required to fit the data to the Sandre curve

The scaling factor $\frac{\varphi_{intra}}{{M_v}^2}$, can be recalculated in several ways to attempt to fit the data to the expected curve. In Table 4.2, the M_v value was fixed at 60 emu. g^{-1} and ϕ was adjusted to fit the data, within 1% error (red squares in Figure 4.11). It is immediately clear that this is not physically possible, as the magnetic volume fractions extracted are greater than 1. Furthermore, this approach indicates that ϕ must increase with $d_{hyd;}$ TEM analysis of PMA-NPCs, strongly suggests that ϕ either remains constant or decreases, (Figure 4.12), hence this approach is physically unrealistic.

Table 4. 2: r_2 relaxivity results adjusted to fit the Sandre model assuming M_s of 60 emu. g^{-1}

d_{hyd} (nm)	M_s ($A.m^{-1}$)	Packing density (φ)
49	294000	9.5
53	294000	10
68	294000	13.5
99	294000	35
133	294000	145

A second forced fitting of the data to the expected curve was performed where the packing density was assumed to be 0.74 (hexagonally close packing factor), and the M_s values were adjusted. It was found, Table 4.3, that in order to fit the data to the curve the M_s values must decrease with increasing NPC diameter. However, as the same primary NPs are used, M_s cannot change, so the model is unphysical. In fact, this model demands that M_v is constant for all d_{hyd} and therefore cannot accommodate a change in the response in the r_2* vs d_{hyd} plot. Therefore, the Sandre model cannot be applied to explain the relaxivity of PMA-NPCs.

Table 4. 3: r_2 relaxivity results adjusted to fit the Sandre model assuming a constant magnetic volume fraction of 0.74.

d_{hyd} (nm)	M_s ($A.m^{-1}$)	Packing density (φ)
49	6.50E+09	0.74
53	6.50E+09	0.74
68	5.00E+09	0.74
99	1.80E+09	0.74
133	4.70E+08	0.74

The model operates on the assumption of highly monodisperse, packed, water impermeable NPCs. Thus, PMA-NPCs are either permeable and/or have looser internal structures. STEM analysis (secondary electron detection mode) indicates dense NP packing on the NPC surface, this suggests that the embedded NPC model, (Figure 4. 10) is not appropriate. TEM, as expected shows significant numbers of overlapped objects, however, the transmission is not significantly increased towards the NPC centre suggesting that the clusters are not densely packed throughout. It should be noted that the image bottom-right of Figure 4.12 was taken at a much lower magnification and indicates that this behaviour is uniform throughout the sample. Hence, we suggest that PMA-NPCs are increasingly hollow as d_{hyd} increases and that the likely internal ordering is a densely packed shell surrounding a hollow centre. This may result in some water ingress, but further study (e.g. cryo-TEM) would be required to support that claim. A single sample was analysed by cryoTEM, however on microtoming the PMA-NPCs were found to collapse. It may be possible for a method to accurately assess these materials by cryo-TEM to be developed, however long-term access to this resource was not available.

We can conclude that the significant differences in the NMRD response for apparently similar NPCs (Figure 4.12) demonstrate the unique sensitivity of the technique to subtle differences in the organization in nanoparticle assemblies that cannot be obtained with any other approach.

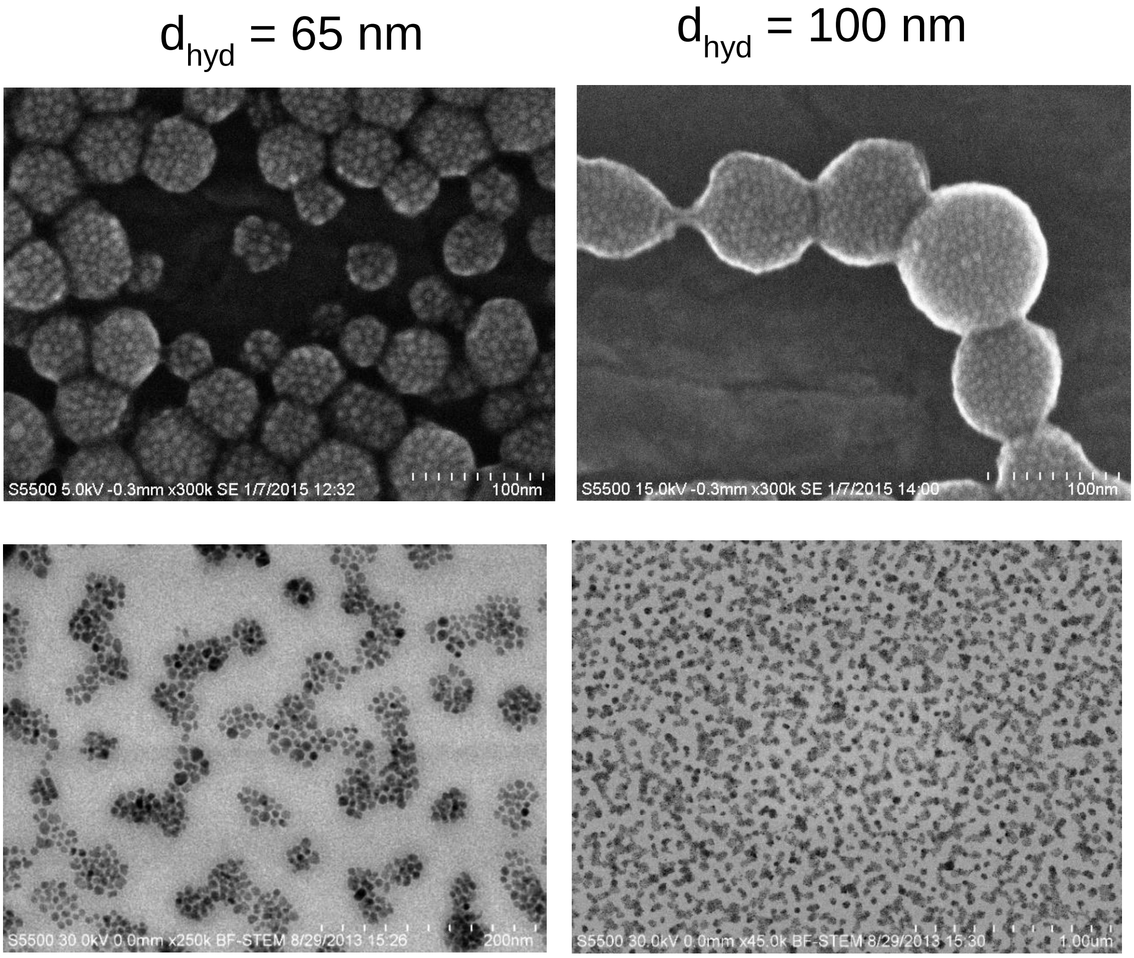

Figure 4. 12: Secondary Electron Images of PMA-NPCs, (top) 65 nm and 100 nm respectively. Both images were captured at a magnification of 300kX. It can be clearly seen that the packing density of the NPs at the surface of the NPC is unaffected by the increase in d_{hyd}. It can also clearly be seen that the NPCs are spherical in nature and are made up of smaller inorganic NPs. Scanning transmission electron microscopy (STEM), bottom shows that the NPC density does not appear to increase towards the centre of the NPC, indicating that the PMA-NPCs are not densely packed structures. The image bottom-right was taken at a much lower magnification and indicates that this behaviour is uniform throughout the sample.

Table 4. 4: NMR data at clinical field observed for a number of iron oxide nanoparticle assemblies including previously commercially available contrast agents[111]

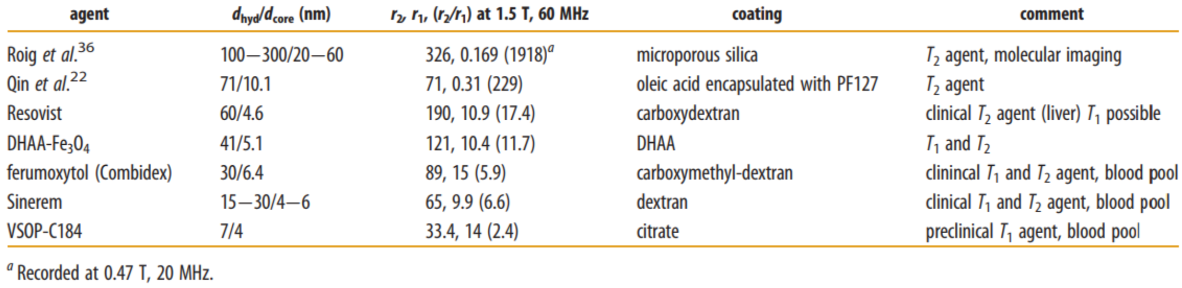

agent	d_{hyd}/d_{core} (nm)	r_2, r_1, (r_2/r_1) at 1.5 T, 60 MHz	coating	comment
Roig *et al.*[36]	100—300/20—60	326, 0.169 (1918)[a]	microporous silica	T_2 agent, molecular imaging
Qin *et al.*[22]	71/10.1	71, 0.31 (229)	oleic acid encapsulated with PF127	T_2 agent
Resovist	60/4.6	190, 10.9 (17.4)	carboxydextran	clinical T_2 agent (liver) T_1 possible
DHAA-Fe_3O_4	41/5.1	121, 10.4 (11.7)	DHAA	T_1 and T_2
ferumoxytol (Combidex)	30/6.4	89, 15 (5.9)	carboxymethyl-dextran	clinincal T_1 and T_2 agent, blood pool
Sinerem	15—30/4—6	65, 9.9 (6.6)	dextran	clinical T_1 and T_2 agent, blood pool
VSOP-C184	7/4	33.4, 14 (2.4)	citrate	preclinical T_1 agent, blood pool

[a] Recorded at 0.47 T, 20 MHz.

Table 4. 4, above, and Table 4. 5, below, show the r_1, r_2, and the r_2:r_1 ratio for a number of reported nanoparticle assemblies of iron oxide NPs, previously available commercial MRI contrast agent[112], and the data obtained for NPCs prepared by PMA all at clinical field, 60 MHz, ~1.5 T. It can be seen that the PMA-NPCs with d_{hyd} = 68 nm, have the highest reported r_2 values (364 s^{-1} $mmol^{-1}$ for the 68 nm PMA-NPCs, vs 326 s^{-1} $mmol^{-1}$ the highest reported materials prepared by Roig *et.al*) and thus have potential as T_2-weighted MRI contrast agents. It is also advantageous both that this PMA-NPC sample is in the ideal size range for indirect targeting of tumours through leaky vasculature (EPR effect).

Table 4. 5: NMR relaxivity data measured at clinical field (1.5 T; 60 MHz) for NPCs produced by PMA

Hydrodynamic Diameter (nm)	**r_1 (s^{-1} $mmol^{-1}$)**	**r_2 (s^{-1} $mmol^{-1}$)**	**r_2:r_1 ratio @ 60 MHz**	**r_2:r_1 ratio @ 16.3 MHz**
49	9.47	252.66	26.69	4.018
53	5.62	295.71	52.59	6.958
68	4.63	364.19	78.68	11.075
99	3.58	284.71	79.53	18.562
133	2.57	130.57	50.72	36.306

4.3. Kymography

In a typical experiment PMA-NPCs were recorded interacting with an external magnet (Block magnet 10 x 10 x 5 mm, NbFeB, Supermagnete GmbH, Germany) over a 30 second period, as outlined in Section 2.6.1. In Figure 4. 13, below 4 consecutive frames from one of these videos have been shown with a region of interest (ROI) highlighted with a red circle. It can clearly be seen that the ROI is moving in a right to left direction over the consecutive frames, imperfections in the imaging slide can also be seen (darker region of the images) which do not move relative to the frame. It is difficult to highlight a number of ROIs in these images as the NPCs are close to the limit of resolution of this particular microscope and thus the majority of ROIs are a single pixel in size. The lateral movement of these NPCs is clearly evident in the video recording, but does not translate to high quality still sequential images.

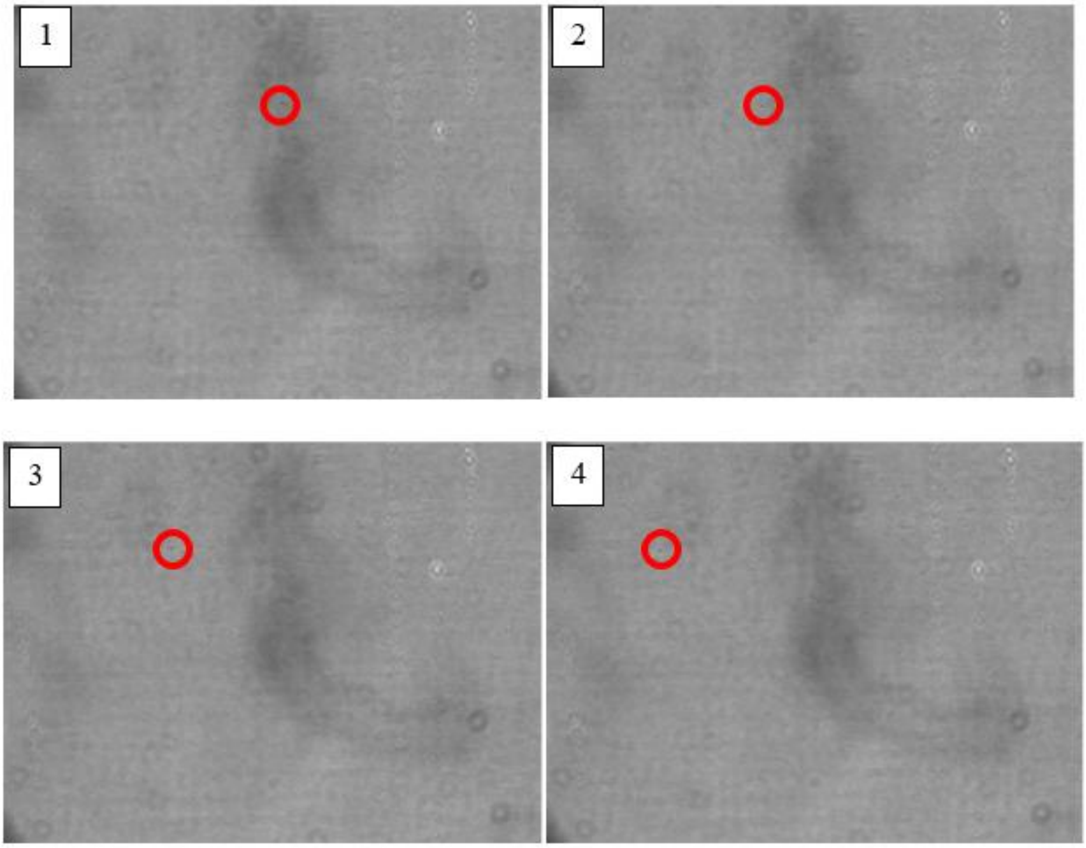

Figure 4. 13: A number of consecutive frames from video monitoring of the NPC colloidal suspension interacting with an external magnetic field. A single particle of interest has been highlighted demonstrating the potential for microscopic tracking of magnetic NPCs in real time. (d_{hyd} of PMA-NPC = 138 nm, primary NP size d_{TEM} = 10.4 nm)

Experiments were performed including with no external magnetic field, and where the magnetic field was removed then re-applied in a different position. In all cases the NPCs were found to move towards the magnet, when the magnet was removed, the NPCs did not move, and when a second magnetic field was applied in a different position, the NPCs in the vicinity were found to move towards the second magnet. The results indicate strongly that the PMA-NPCs can be directed to an area of interest by the application of an external magnetic field and that this process can be measured kymographically using transmission even though the NPCs are sub-pixel in size. Preliminary studies were performed on the largest stable PMA-NPCs available to investigate the potential use of light microscopes and kymography analysis for the tracking of magnetic clusters, and it can be seen from Figure 4.14, that velocities can indeed be extracted and directly compared. It should be noted that the PMA-NPC samples analysed in Figure 4. 14 are prepared with different primary NPs to those discussed earlier in this Chapter, as these were the largest stable PMA-NPCs available for analysis. It should also be noted that the values provided by the secondary axis in Figure 4. 14, are estimated, due to inconsistencies in the frame rate of the camera over the course of the measurement. These values have been calculated using the total time of measurement and the total number of frames recorded, so are approximately correct assuming the camera was stable over each measurement.

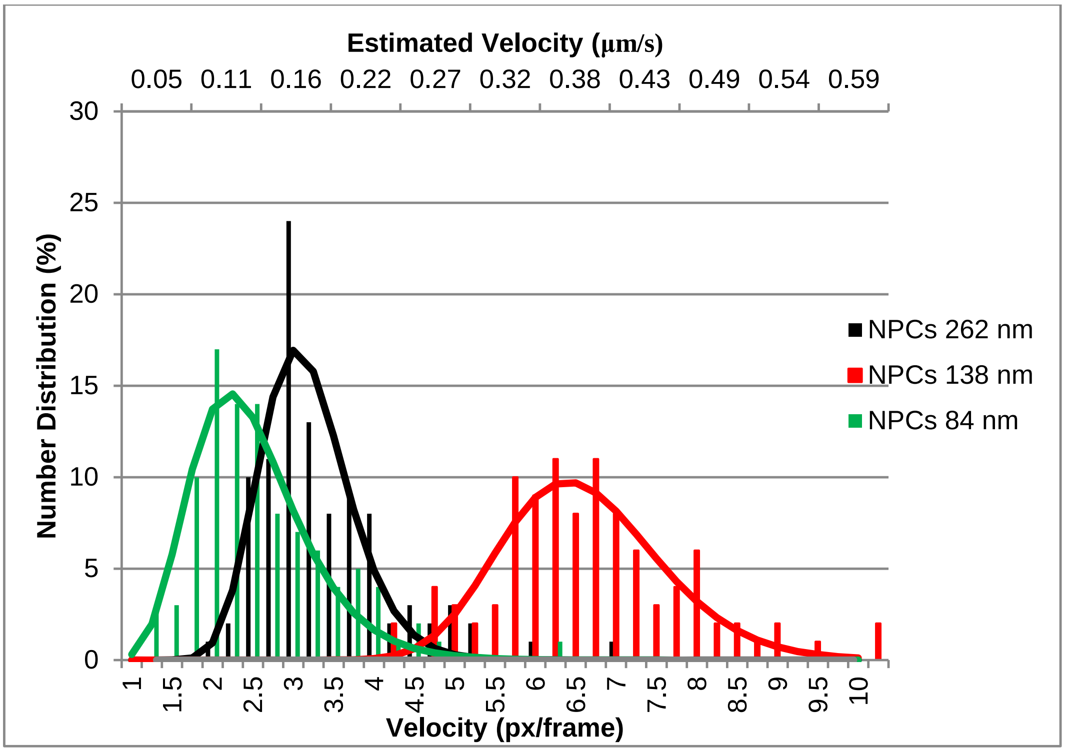

Figure 4. 14: Kymography results from the analysis of 3 samples. It can be clearly seen that there is a significant difference in PMA-NPC velocity from sample to sample. However, it can also be seen that there does not appear to be a direct correlation between PMA-NPC size and velocity. The secondary horizontal axis (above) shows the estimated velocity in μm per s. It should be noted that these samples are prepared with different primary NPs as these were the largest stable PMA-NPCs available for analysis.

Kymographic analysis of the NPC tracking experiments was then performed on a range of PMA-NPCs prepared with 8.5 nm NPs and pluronic F127 as the polymer, to investigate the effect of d_{hyd}. The results obtained from the primary analysis of the data were interesting but for different reasons than was expected. It can be seen in Figure 4. 15, below, that a change in particle velocity occurs (time is the vertical axis). On further analysis of the extracted video file it is clear that the velocity of the particle changes over the course of the measurement, slowing down over time, as demonstrated in Figure 4. 16. This observation was not expected as it was assumed that the magnetic field gradient is constant, therefore the magnetic force should remain unchanged over the course of the experiment. This behaviour might be due to: (1) While the NPC suspensions were highly monodisperse by DLS, there is still a small range of sizes (polydispersity width = 8 nm by DLS), perhaps the smaller NPCs move faster and as the measurement time increases fewer of these are seen in the field of view. (2) There are unknown factors involved that affect the velocity of the NPCs in the field of view, e.g. concentration effects, changes in the matrix, or complex non-laminar fluid dynamics.

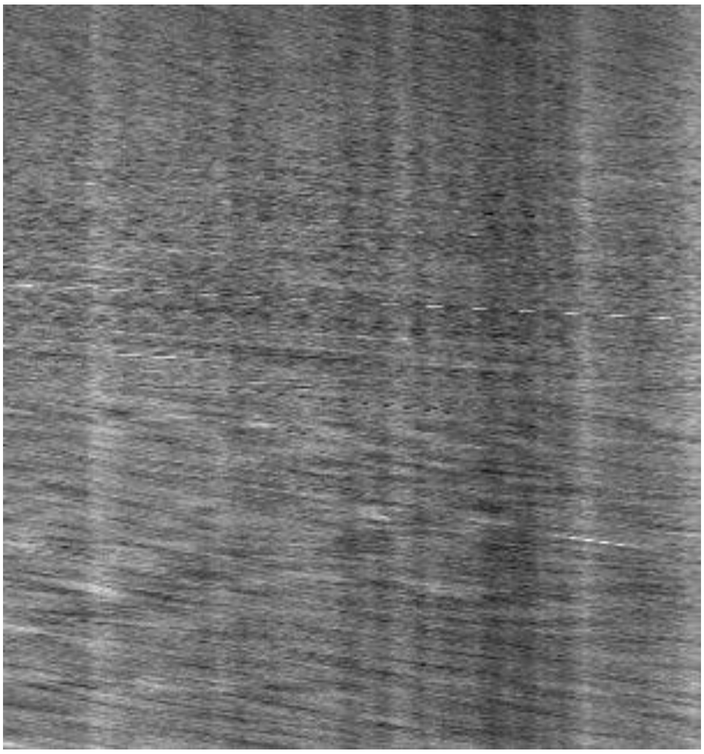

Figure 4. 15: Kymograph extracted from tracking experiment of PMA-NPCs, primary NP d_{TEM} = 8.5 nm, NPC d_{hyd} = 68 nm. It can be seen that there is a distinct change from the beginning of the experiment (top of kymograph) and the end of the experiment (bottom of the kymograph), experiment length 30 se

Hypothesis 1 seems probable as smaller NPCs with the same internal magnetic volume fraction should move faster than larger NPCs under the same conditions. This suggests that dynamics are determined by the frictional force. However, as discussed before, we anticipate that smaller NPCs to be more dense and therefore to be strongly magnetic. Note, the size distributions of these NPC samples are narrow, with a PDI < 0.12, by DLS. The magnetic force experienced by a magnetic nanoparticle in an external magnetic field gradient is described by Equation 4. 2:

$$f_m = M.\nabla B$$

Equation 4. 2

where M is the volumetric magnetization of the NP suspension and ∇B is the magnetic flux density gradient[113]. When the initial average velocity and final average velocity were calculated, as described in Chapter 2, the difference (as observed in Figure 4. 16) was too large (*e.g.* decrease from 25 px/frame to 2.5 px/frame over a 30 sec measurement) to be ascribed to differences in velocity from larger and smaller NPCs in the size distribution, given the high monodisperisty.

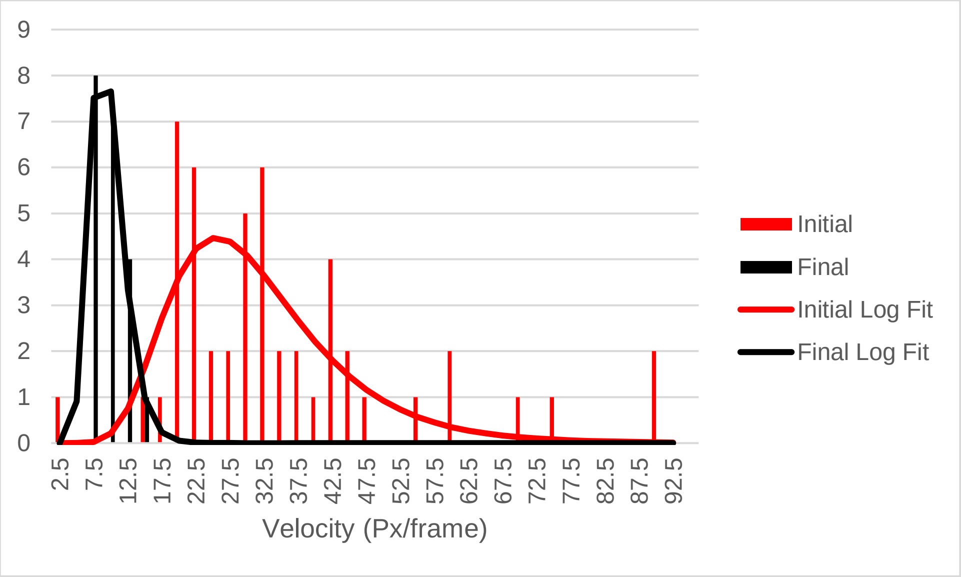

Figure 4. 16: Histogram illustrating the change in velocity measured at the start of a measurement, with the velocity at the end of the measurement. A significant change in velocity is observed over the 30 second measurement window.

To investigate hypothesis 2 a number of further experiments were performed using lower concentrations of nanoparticles, injecting a concentrated sample into a well on one side of the channel, and adjusting the position of the field of view along the channel. No significant improvement was found in these observations when compared with the initial study; in the majority of cases a decrease in velocity was observed with time, however this decrease was not systematic or reproducible, even on the analysis of multiple aliquots of the same sample. On lowering the concentration of NPCs (from 2 mM to 0.2 mM) it should be noted that there was insufficient contrast between the NPCs in suspension and the fluid, hence no data could be extracted from these experiments. In one experiment however unusual behaviour was observed, a portion of the suspension appeared to be flowing away from the magnet for the final 8-10 seconds of a 30 second measurement. This was observed when the field of view was close to the magnet and close to the channel walls. Subsequent analyses with different NPC samples, (larger d_{hyd}, PMA-NPC samples prepared with larger primary NPs) in the same region produced similar results. Our interpretation is that this is the result of complex fluid dynamics. Initially the NPCs are attracted to the magnet, as expected, and move towards it. This flow of NPCs drags some of the aqueous solvent along as it moves. As there is restricted space in the channel, this movement of liquid causes a convective circular flow. The pressure of this backwards flow and friction between the two streams causes the movement of the NPCs in suspension to slow dramatically over the analysis timeframe. It is expected that this effect could be avoided at a lower concentration, however the contrast is then lost. To conclude, it is probable that complex fluid dynamics limit the applicability of kymography as a tool to extract NPC magnetic density, however it is clear that kymography can be used to track the movement of magnetic NPCs in a fluid environment in the presence of an external magnetic field gradient, and that PMA-NPCs can be actively transported through liquid environments using an external magnetic force.

While the aim of these experiments was to investigate the possibility of rudimentary kymography for measuring relative density between PMA-NPCs of different sizes, it is clear from the above observations that the response is too complex under these conditions to extract meaningful data. Alternative methods for nanoscale density measurement are also challenging. Malvern have recently developed a new analysis system that can track single particles through the change in sample viscosity observed in a narrow channel (Archimedes). Unfortunately, this system, while promising has insufficient resolution to capture changes in density for particles with a hydrodynamic diameter of less than 500 nm.

Rough estimates for NPC density could potentially be determined using fractional centrifugation experiments, however the NPCs produced by PMA are not dense and are not rigid in nature, so tend to disintegrate under the centrifugal forces required to move them from one fraction to another. Similar issues have been found using magnetic chromatography, when the magnetic field used is sufficient to capture the NPCs, any flow of solvent around the NPCs contributes to PMA-NPC degradation. Furthermore, on elution from the magnetic chromatography column, the NPCs are found to have collapsed, resulting in a non-stable, precipitate of primary NPs.

An additional method for studying NPC density could be cryoTEM of cryo-ultramicrotomed samples. The NPC suspension would be frozen in liquid nitrogen, and thin slices (30-60 nm) of the sample would be taken for cryoTEM analysis by sectioning with a diamond knife. However, the issue of sample rigidity would again be a problem for PMA-NPCs. It is believed that water is free to diffuse into and out of the NPC so on introduction to the sample chamber of the TEM sample collapse would be highly likely due to the sublimation of frozen water in the presence of a vacuum. In a single experiment it was observed that the NPCs collapsed when subjected to this process. Unfortunately, it was not possible to secure long-term access to this resource. Environmental SEM could potentially overcome this issue; however, the resolution of environmental SEM is significantly less than TEM, and would be insufficient for NPCs of diameter ~100 nm. It would also be impossible to identify individual NPs with that technique.

Hence, unfortunately, while accurate measurement of the NPC density would be of interest for interpreting the magnetic resonance properties of PMA-NPCs, the soft nature of these materials means that accurate density measurements are highly challenging, which further explains the advantage of in situ solvent relaxation time measurements.

4.4. Fluorescent Labelling of F127 NP Assemblies

F127 is a tri-block copolymer of poly (ethylene oxide), poly (propylene oxide), poly (ethylene oxide) where both ends of the polymer are -OH terminated. As such there is a wide range of potential functionalization experiments that could be performed on this polymer. Functionalization of F127 is of interest to this work as it could potentially be used to actively target regions of interest in the body, (antibody or protein functionalization), allow for the coupling of other nanoparticles with optical properties (Au NPs or QD labelling) for further theranostic development, or it could be used to bind drug molecules to the NPC surface for targeted drug delivery. Bis-aminated polymers (e.g. F127-NH_2) are among the most useful for further reactions as they are highly reactive. In this work the NH_2 - NHS ester chemistry, as shown in Figure 4. 17, was used to generate a fluorescently labelled polymer to quickly assess the effects, if any, of polymer modification on NPC formation and stability. These experiments can provide insight into the potential effectiveness of this strategy for drug conjugation or further functionalization of the NPCs.

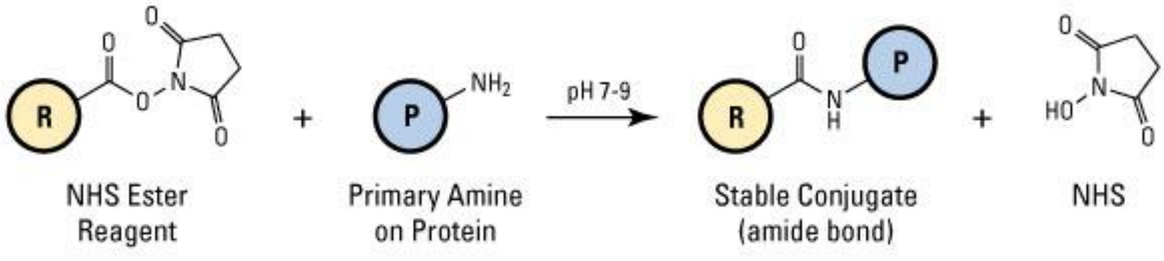

Figure 4. 17: Schematic of standard NHS Ester reaction with primary amines[114]

Bis-amine terminated F127 was synthesized based on a previously reported method by Suthiwangcharoen[115]. Initially CDI-functionalized F127 (F127-CDI) was prepared as follows. F127 (5.0 g; 0.4mmol) was dissolved in dry acetonitrile (7 mL) and added dropwise to a solution of N, N_0 -carbonyl diimidazole (CDI) (0.65 g; 4 mmol) in dry acetonitrile (7 mL) at room temperature under nitrogen. The reaction mixture was stirred overnight and concentrated using a rotary evaporator. The concentrated mixture was purified by precipitating in excess of cold diethyl ether while stirring. This process was repeated at least three times to ensure that the excess CDI was completely removed. The purified F127-CDI was dried under vacuum overnight at room temperature and collected as white powder.

Amine-terminated F127 (F127-NH_2) was then synthesized from the purified F127-CDI. A solution of F127-CDI (2.1 g; 0.16 mmol) in acetonitrile (2.5 mL) was added dropwise to 1,2-ethylenediamine (2 mL) at room temperature over 2 h. The reaction mixture was stirred overnight, and the excess 1,2-ethylenediamine was removed by rotary evaporation. The crude product was further purified by precipitating in excess cold diethyl ether. This process was repeated three times. The purified F127-NH_2 was dried under vacuum overnight at room temperature and collected as white powder.

Fluorescently tagged F127 was then prepared according to a standard protocol advised by the dye supplier, Thermo Scientific. A working standard of dye, NHS-functionalized Dylight550 (Thermo Scientific, Rockford IL, USA) was prepared at a concentration of 10 mg/mL (100 µL) in DMF, and a working standard of F127 – NH_2 was prepared at a concentration of 8 mg/mL in Phosphate Buffered Saline, 0.15M NaCl at pH 7.2-7.5.

100 µL of F127 – NH_2 was added to 66 µL of the dye solution, the mixture was vortexed, then incubated for 1 hour, on an orbital shaker, at room temperature. Following this reaction, excess unreacted dye was removed by dialysis (2500 MW cut-off). The dye labelled F127 was then made up to a volume of 1 mL (0.8 mg/mL). 3 series of NPCs were prepared as outlined in Chapter 3, with 0.1%, 0.5% and 1% dye loading (v/v dye labelled F127: unlabelled F127) respectively.

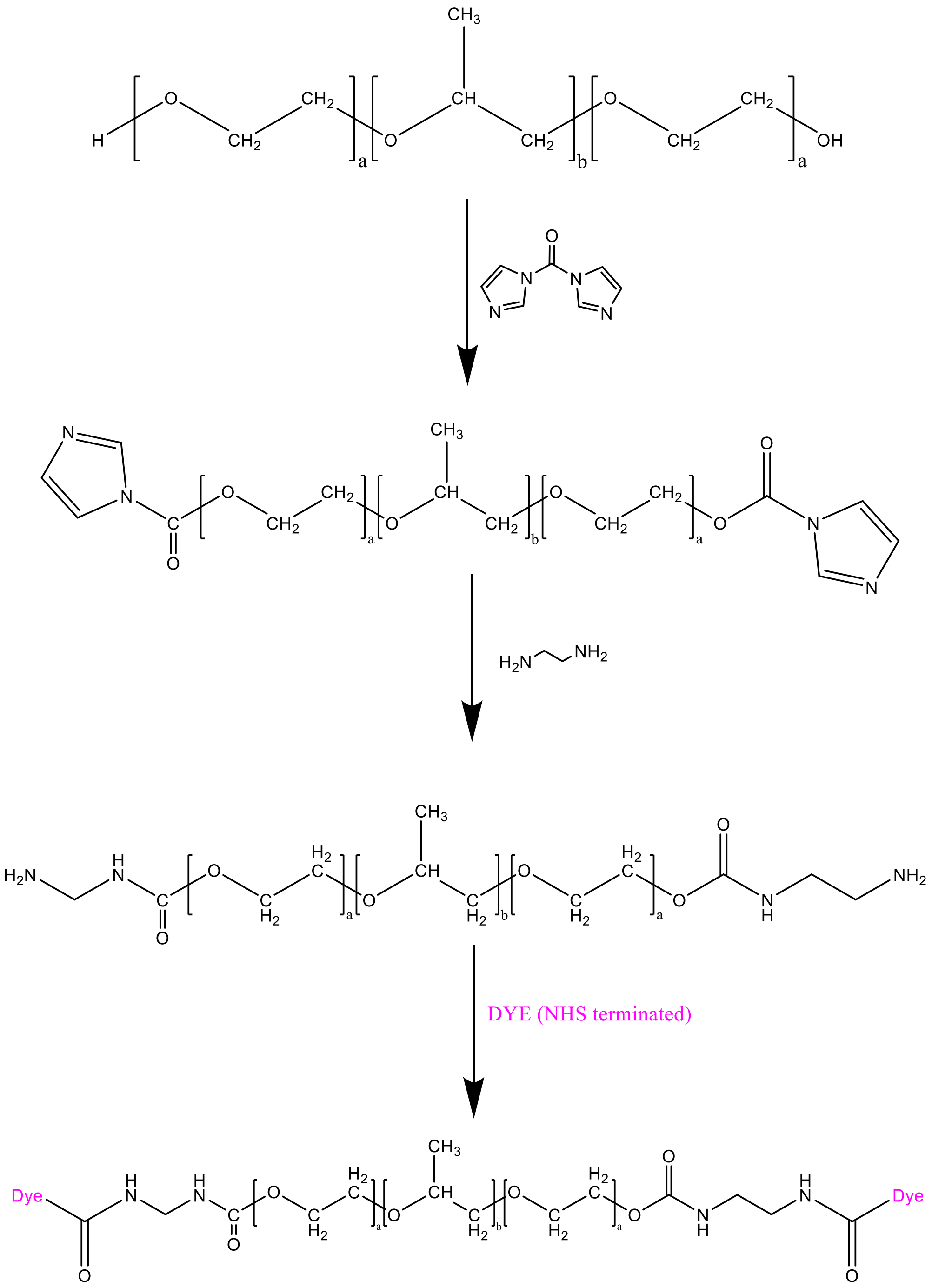

Figure 4. 18: Mechanism for the preparation of dye labelled Pluronic polymer.

Remaining dye labelled F127 and the labelled NPCs were then further assessed using IR, NMR, UV-Vis and Fluorescence measurements.

4.4.1. Characterization of F127-dye Conjugate

ATR-IR analysis was performed on the F127 pluronic, the intermediate compounds and the final dye labelled F127 conjugate. It can be seen from the spectra obtained, Figure 4. 19 that the reaction did go to completion. Following the initial modification of pluronic F127 with CDI a small peak at approximately 1750 cm^{-1} corresponding to a C=O bond, and a shallow broad peak at 3000 – 3200 cm^{-1} corresponding to an N-H bond can be observed alongside the strong peaks also observed with the pure, unmodified F127 sample. On completion of the second reaction with ethylenediamine, a significant increase in the broad N-H peak can be observed at 3000-3200 cm^{-1}. Additional peaks can also be observed in the region from 1500 – 1750 cm^{-1} which can be attributed to N-H bending (1550-1640 cm^{-1}).

On completion of the final dye conjugation a significant change in the IR spectrum is noted. The absence of the N-H peak observed at 3000-3200 cm^{-1} indicates that the conjugation reaction was successful and no trace of NH_2 terminated polymer remains. There is also a shift of the primary peak to higher wavenumbers indicating a modification of the overall vibration of the molecule, which can be attributed to the addition of a high molecular weight functional group.

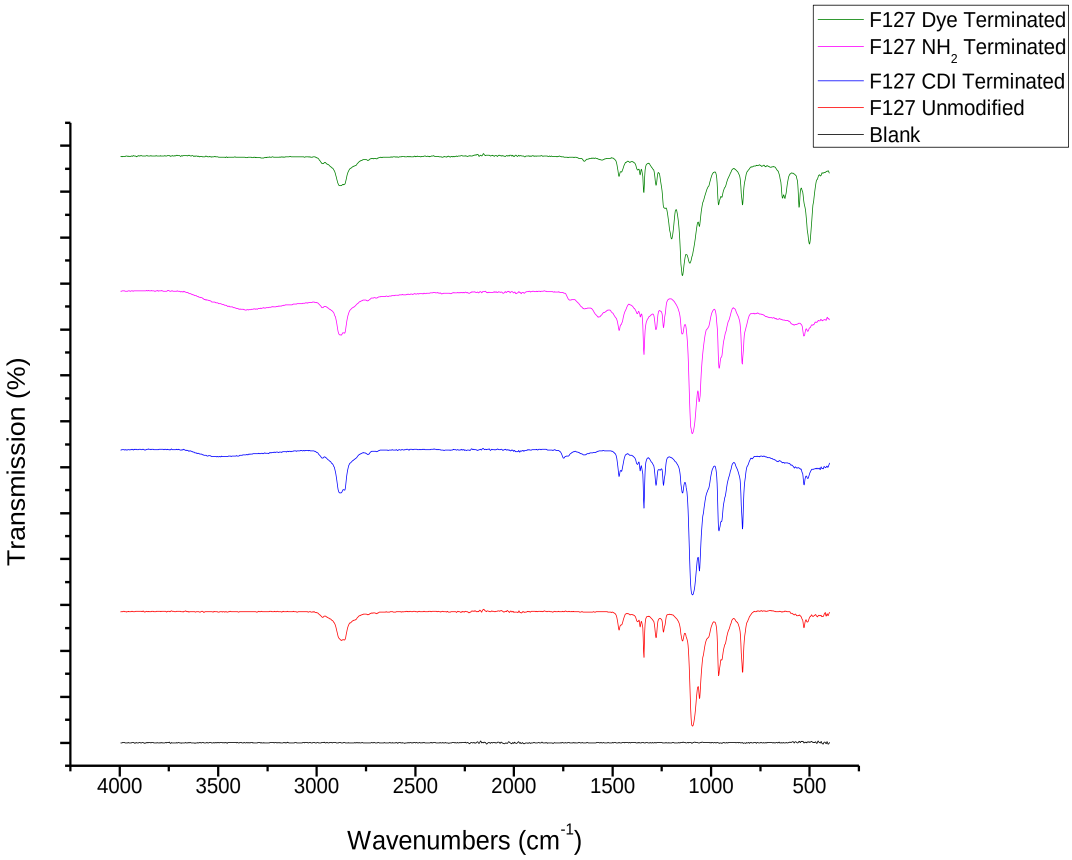

Figure 4. 19: Infra-red analysis of pluronic F127(red), intermediate products, CDI terminated (blue) and NH_2 Terminated F127 (pink), and the dye labelled F127 conjugate (green). Blank corresponds to the background corrected scan of air.

Fluorescence excitation and emission spectra were measured on both free dye and dye labeled polymer (post-dialysis). It can be seen that there is no significant shift in fluorescence caused by the dye-conjugation. There is also no evidence of quenching. Thus, it can be assumed that the conjugation of the dye molecule to the polymer has not affected the physical properties of the dye. This is promising as any modification of a drug molecule or of a protein, antibody or other biological moiety should be minimized to reduce the risk of unwanted, uncontrolled side reactions.

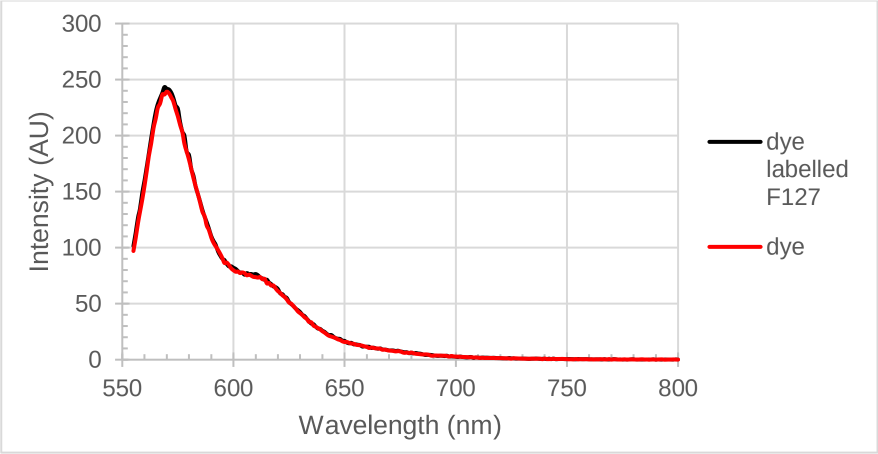

Figure 4. 20: Fluorescence measurement of unbound dye and dye-labelled polymer. It can be seen that dye conjugation has no impact on the fluorescence properties of the dye.

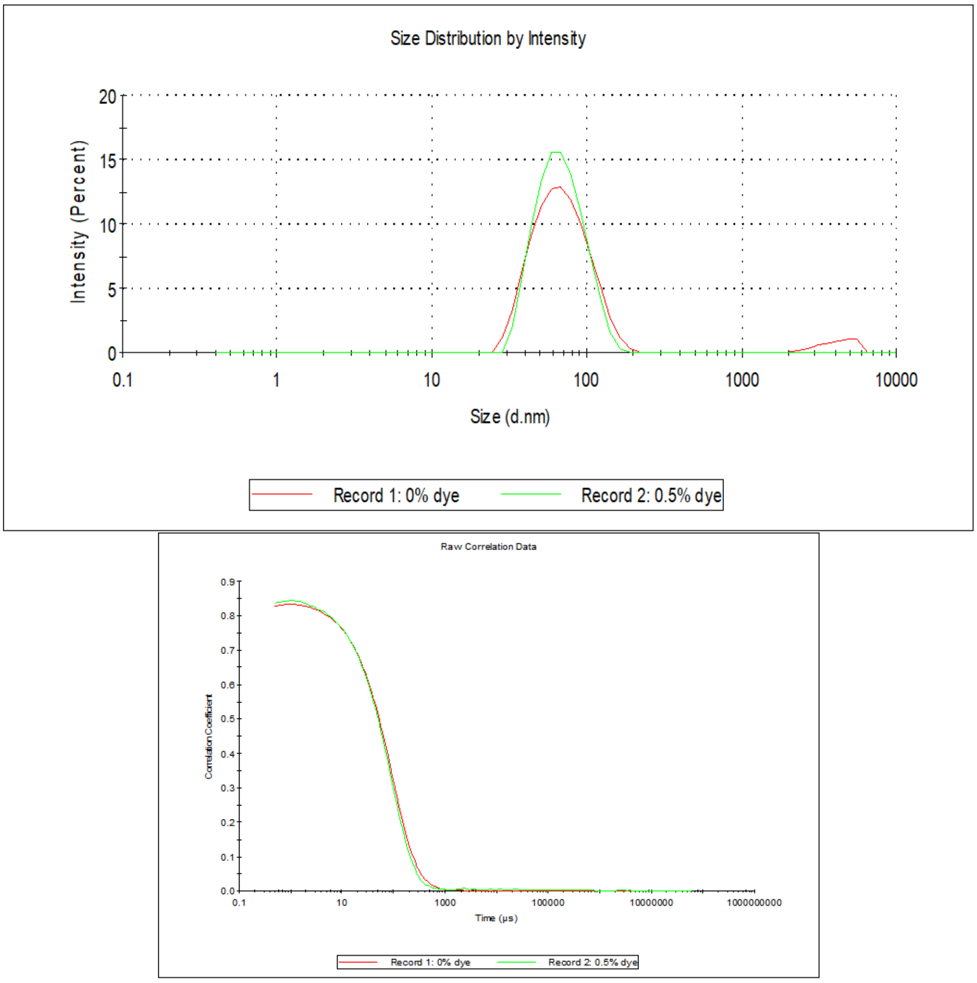

Figure 4. 21: DLS data demonstrating the reproducibility of size of NPCs produced with 0% dye labeled polymer (red) and 0.5% dye labeled polymer (green). The size determined was 66 nm and 62.5 nm respectively (z-average size) and the PDI of was 0.22 for unlabelled clusters (higher than usual due to the presence of dust in the measurement sample) and 0.12 for labeled NPCs. It can be seen from the correlogram data that both samples are similar in nature and no evidence of aggregation/sedimentation is shown.

The data demonstrated the successful dye-labelling of pluronic F127 with little evidence of any effect on the NPC size formed, Figure 4. 21, and concentration. The efficiency and efficacy of the NH_2 – NHS ester reaction opens up a broad range of possibilities for surface modification of the NPCs. The NH_2 terminated polymer can be easily reacted with any NHS ester. Proteins, sugars or antibodies would be ideal candidates for surface modification of the NPCs allowing for focused cell targeting, modification of the polymer with additional NPs such as gold NPs or quantum dots for optical imaging and modification of the polymer with small drug molecules could allow for simultaneous drug delivery and imaging, all possibilities for the use of PMA in the generation of multi-modal theranostic materials.

It should be noted that these dye-labeled materials are colloidally stable over the course of a DLS measurement and are found to be stable on exposure to a 1 T magnetic field (demonstrated both by DLS and NMRD, Figure 4. 22) Their colloidal stability is limited compared to those materials prepared without dye labelling. The un-labeled materials are colloidally stable over a period of six months, whereas the dye-labeled material has a colloidal shelf life of about 2 weeks.

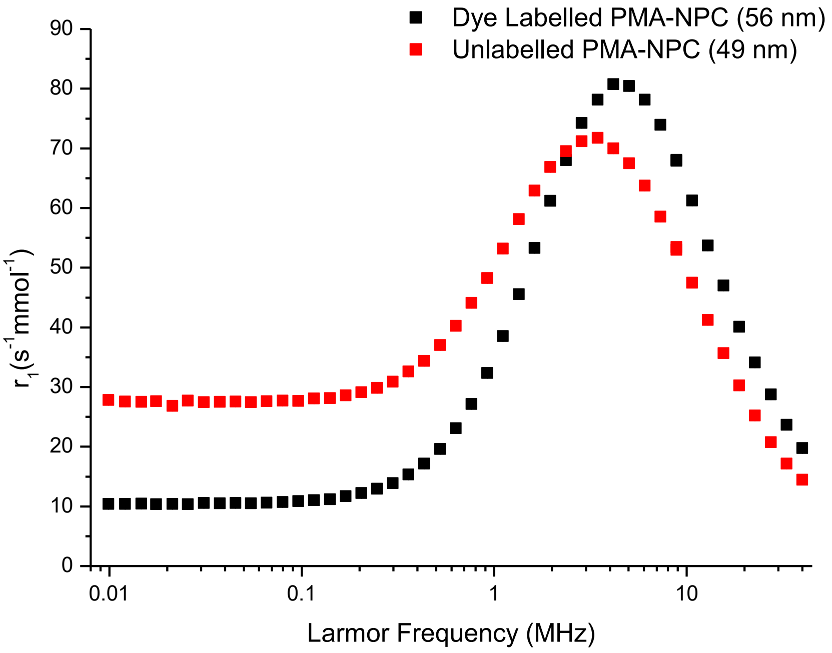

Figure 4. 22: NMRD Profile of NPCs prepared with 0.5% dye labeled polymer. The overall shape of the profile remains the same indicating that the superparamagnetic properties of the NPs have been retained, however the magnetic behaviour is altered slightly, likely due to the increase in hydrophobicity at the terminal ends of the dye labeled polymer. The size determined was 56 nm and 49 nm respectively (z-average size) and the PDI of was <0.15 in both cases.

NMRD analysis of the dye labeled NPCs was undertaken. It can be seen that the overall magnetic resonance behaviour of dye labeled NPCs in suspension are similar to unlabelled NPCs of very similar size, Figure 4. 22; the overall shape of the profile indicates that the particles still have superparamagnetic properties. The frequency of the r_1 max is shifted significantly compared to NPCs of a similar size (49 nm unlabelled NPCs, 56 nm labeled NPCs) prepared without dye labeled polymer, suggesting that the dye resulted in a change in NPC magnetic structure. However, any quenching of the dye, and the number of dye molecules per NP cannot be estimated as the fluorescence is compromised by the strong absorbance of the NPCs, (dark brown to black suspensions).

4.5. Toxicology Studies

Toxicology and cellular cytotoxicity studies are of utmost importance to the development of a theranostic agent. With NPs and NPCs, the small size of the materials can be a cause for concern as they are in the ideal size range for cellular uptake, it is important that healthy cells are not damaged by unloaded NPCs. From experiments performed by this research group previously, it was determined that PMA-NPCs are transported quickly to the liver, upon injection into the tail vein of a mouse model. Therefore, a number of cell lines were selected to evaluate the effect of NPCs during this process. Human monocyte cells, THP-1, were selected in order to evaluate toxicity and activation of the immune system. Hepatic toxicity was also accessed on human liver cell line, HepG2. Cellular uptake was also investigated by Prussian Blue staining.

4.5.1. Experimental Protocol

Suspensions of leukemic monocytes, THP-1, were cell grown in RPMI-1640 media supplemented with 10 % FBS and 0.05 mM 2-mercaptoethanol. Hep-G2, adherent carcinoma hepatocytes were grown in MEM with Earle's salts (Sigma, M4655) supplemented with 10 % FBS and 1 mM sodium pyruvate. Cultures were incubated in a humidified atmosphere at 37 ^{o}C and 5 % CO_2. The range of nanoparticles were tested in both cell lines and cellular proliferation was determined with AQ_{ueos} one solution cell proliferation assay containing MTS (3-(4,5-dimethyl-2-yl)-5-(3-carboxymethoxyphenyl)-2-(4-sulfophenyl)-2H-tetrazolium) (Promega G3581). Cells were seeded at $3x10^4$ cells in 100 µL complete media on 96-well plates 1 day prior to NP addition. NP dilutions were made in respective media and incubated for 24 and 72 h. After the exposure period, 20 µL MTS solution was added to 100 µL media and incubated at 37 ^{o}C for 3 h. Absorbance was measured at 490 nm on BioTek plate reader and normalised to non-treated samples by subtraction of background absorbance. Prussian blue staining suggested internalization of most of the Fe dose. NPCs stock solutions were quantified by ICP-AES in order to determine iron concentration in water and 2 mM working stock solutions were prepared. Test concentrations were based on iron molarity rather than NP weight per volume, in order to compare suspensions (due to the wide range of size distributions).

4.5.2. Experimental Results

It can be seen in Figure 4. 23, in the case of leukemic THP-1 monocytes, there is no observable toxicity in the first 24 hours. However, some toxicity is observed for the smallest NPC, with only 80% cell viability at an iron concentration of 100 μM over 72 hours.

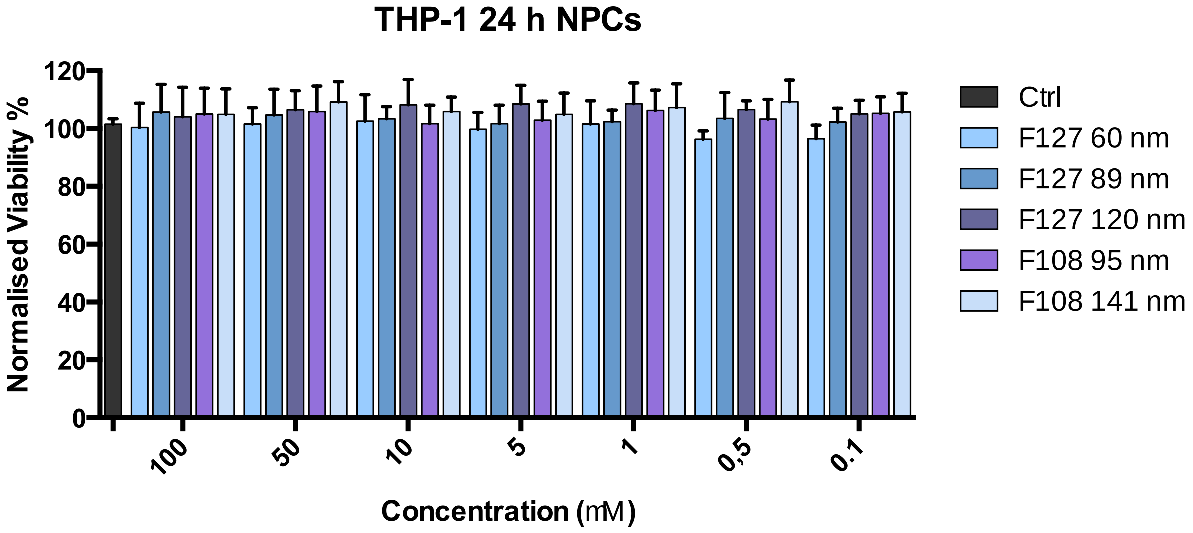

Figure 4. 23:Observed toxicology of NPCs prepared by a polymer mediated approach on THP-1 monocytes over a 24 hour period. 2 polymer types were assessed, and a range of NPC sizes were assessed. There was no observable toxicity under these conditions for each NPC sample at any NPC concentration.

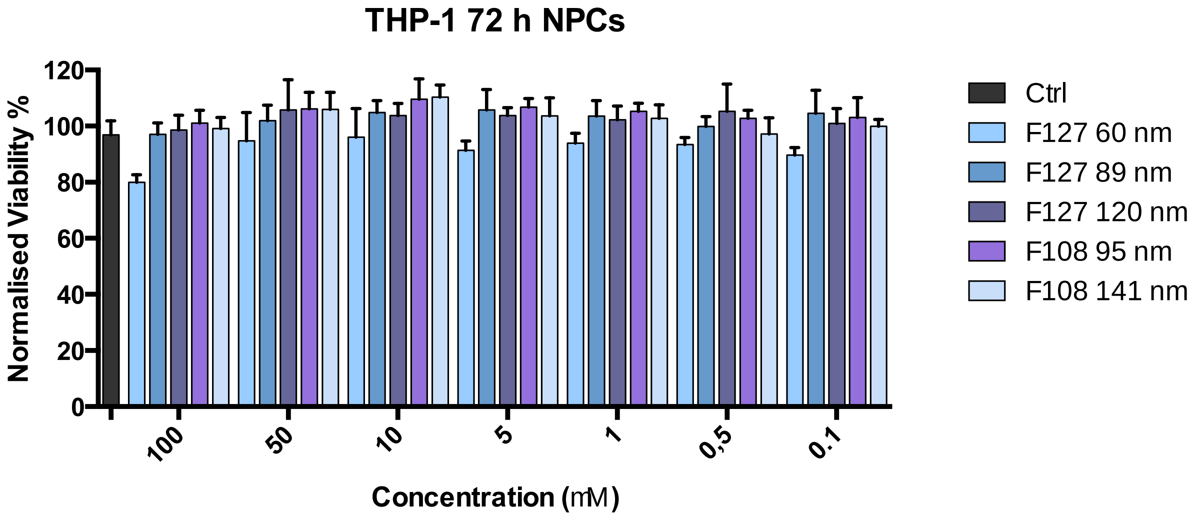

Figure 4. 24: Observed toxicology of NPCs prepared by a polymer mediated approach on THP-1 monocytes over a 72 hour period. 2 polymer types were assessed, and a range of NPC sizes were assessed. In this case toxicity was observed in the case of the smallest NPCs, however, this toxicity is still low with a maximum of 20% cell loss at the 100 µM concentration.

A further study was performed using the same NPC samples under identical conditions using the HepG2 hepatocyte cell line. It can be seen again that the sample containing the smallest NPCs show some degree of toxicity with 20% cell death following the first 24 hours. Interestingly, there does not appear to be a direct relationship between NPC concentration and cell viability in this case.

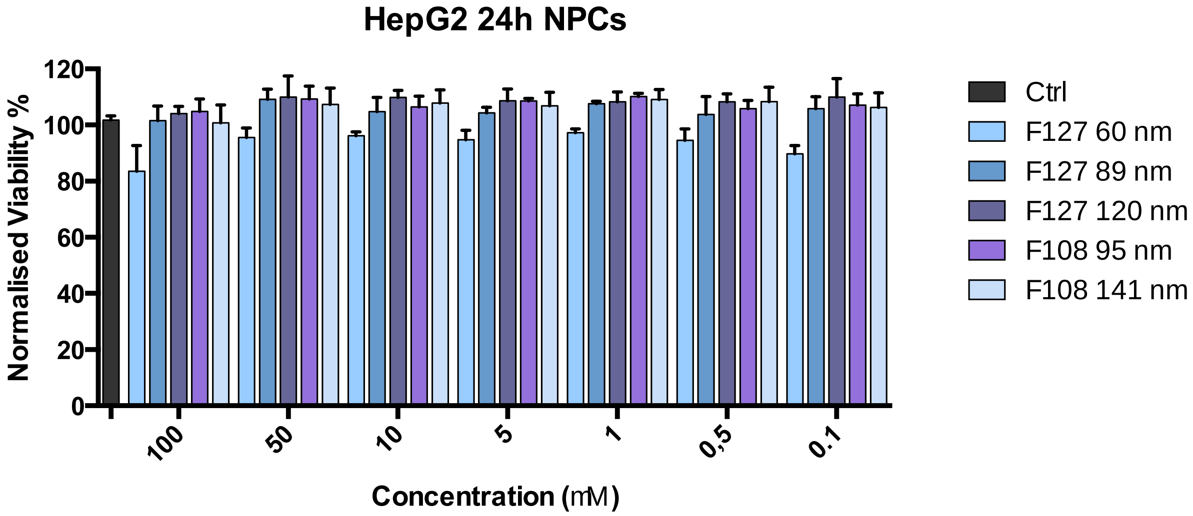

Figure 4. 25: Observed toxicology of NPCs prepared by a polymer mediated approach on HepG2 hepatocytes over a 24 hour period. 2 polymer types were assessed, and a range of NPC sizes were assessed. In this case toxicity was observed at the highest concentration of NPC loading, with 20% cell loss.

Table 4. 6: Measured IC_{50} values for a range of NPC sizes prepared with either F127 or F108 pluronics tri-block-copolymers.

IC_{50} (μM) for nanoparticles and clusters				
Nanoparticle	THP-1		HepG2	
	24h	72h	24h	72h
F127 60 nm	>100	>100	>100	>100
F127 89 nm	>100	>100	>100	>100
F127 120 nm	>100	>100	>100	>100
F108 95 nm	>100	>100	>100	>100
F108 141 nm	>100	>100	>100	>100

It is apparent therefore, that PMA-NPCs are non-toxic to monocytes and hepatocytes even up to very high Fe concentrations. The slight increase in viability relative to the control (non-treated cells) is due to the additional metabolic intake provided by the NPs. The use of a range of NP stabilizers gives rise to no additional toxic effects due to the stabilizers themselves of the chemical processes involved.

4.6. Conclusions

The work described in this chapter helps establish the potential of PMA-NPCs as multimeric theranostic materials. It has been shown that assembly of the iron oxide nanoparticles has a significant effect on the magnetic resonance properties of the suspensions and allows for the development of superior T_2 – weighted contrast agents for MRI.

It was determined by NMRD that the architecture of the PMA-NPCs is probably hollow spheres with a densely packed NP surface. This result correlates well with TEM and STEM of the PMA-NPCs which show a tightly packed surface (by secondary electron probing of the NPC surface) while also showing no indication of a dense core by transmission detection. It was also determined that the PMA-NPCs are permeable to H_2O as indicated by the r_1 response of these materials.

The kymography experiments performed clearly demonstrate that the NPCs can be moved in a targeted way by the application of an external magnetic field gradient, allowing for concentration of NPCs in a region of interest. The dye labelling experiment highlights the effectiveness of NH_2- NHS ester chemistry and the ease of modification and purification of the pluronic F127 polymer. It was also successfully demonstrated that the modification of the pluronic polymer had little effect on the size and PDI of PMA-NPCs and that the NMRD profiles changed only slightly with the addition of the dye. B Most importantly, initial toxicology studies show no obvious signs of toxicology for hepatic cells, or for human monocytes.

In ongoing work, the Group is attempting to further scale-up the PMA-NPC process and to evaluate the long-term stability of the suspensions. The application of the PMA method to a wider variety of materials is also of interest, particularly MnO NPs as they are known T_1 weighted contrast agents for MRI as dispersed primary NPs. $CoFe_2O_4$ are also of interest due to their known high capacity for heating by hyperthermia. Further improvements in MRI response and hyperthermia may be obtained by using the PMA approach to assemble more strongly magnetic NPs, such as γ-Fe_2O_3 nanocubes. Chapter 6 will describe some of this preliminary work.

Chapter 5: Formation and Properties of Monodisperse Cubic Iron Oxide Nanoparticles and Steps Towards Size Control

5.1. Shape Control of Iron Oxide Nanoparticle Synthesis

It has been reported that cubic iron oxide NPs have a higher degree of crystallinity when directly compared to spherical NPs of similar size[116]. This increased crystallinity is desired, as the higher the degree of crystallinity, the higher the saturation magnetization and thus the higher the efficacy of any contrast agents produced using cubic NPs. Additionally it has been reported that shape can significantly affect both surface reactivity and magnetocrystalline anisotropy[117,118].

Many different nanoparticle shapes have been reported for iron oxide, from cubes[1–3,5,116] and octahedra[118] to nanorods[117,119], and octapods[120,121].The vast majority of which have been prepared using a surfactant assisted thermal decomposition approach. It is widely hypothesized that the presence of a surfactant in the synthesis can act as a capping agent, influencing the growth mechanism, in some cases forcing the particles to grow along particular planes, {100} in the case of cubic NPs[122], allowing for highly monodisperse NPs, however there is little consensus on this point. Cubic NP synthesis by the thermal decomposition of organic iron precursors typically occurs in one of two methods; one pot reactions, either thermal decomposition of organic iron salts or in situ iron oleate formation and decomposition, where the iron oleate is formed by the decomposition of inorganic iron salts such as iron chloride and iron pentacarbonyl; or multistep synthesis where initially a precursor such as iron oleate is prepared and cleaned followed by a second reaction involving the thermal decomposition of that precursor.

5.1.1. One Pot Synthesis of Iron Oxide Nanocubes

One pot syntheses are gaining popularity as there is less waste produced and typically the reactions are more efficient in terms of time and energy. One approach uses bulk goethite powder (FeO(OH)) as a precursor[118] using oleic acid and tetraoctylammonium bromide as capping agents and 1-octadecene as a solvent. Goethite is an anti-ferromagnetic iron phase[123], thus displaying no magnetic properties in the presence of an external magnetic field. In work shown by Li *et al.* the high temperature reaction between FeO(OH) and oleic acid produces iron carboxylates which are then pyrolised leading to the formation of Fe_3O_4 [118]. The capping ligand and reaction times must be carefully controlled, as NPs of multiple shapes and sizes may be produced by this method.

Alternatively, iron acetylacetonate may be used as a precursor. Iron acetylacetonate is highly valued as a precursor as it is widely available, until 2016 was available in high purity (<20ppm impurities), it is crystalline, non-hydroscopic, stoichiometric, and readily decomposes at a much lower temperature than nanoparticle nucleation allowing mixtures to be homogenous prior to nanoparticle generation. Publications by the Hyeon group[3,5,124], Pellegrino group[1,125] and Batlle group[2,4] use this precursor to form iron oxide nanocubes. The key step, is believed to be the degassing stage of the reaction mixture, the mixture is raised to a temperature of ~100 ^{o}C and held for a period of time either under vacuum, or through nitrogen bubbling to remove volatiles. However, the evidence to support this claim is limited. It should also be noted that while some DLS measurements have been provided in the above listed publications, the data is presented as number distributions or as volume[3,5,125] distributions, which is discouraging as these distributions artificially remove any evidence of agglomeration which would be evident in intensity distributions, other publications only assess the NPs for size using TEM, which does not provide any confirmation of colloidal stability[2,124].

The Hyeon group synthesized cubic ferrimagnetic nanoparticles by thermal decomposition of iron acetylacetonate in the presence of oleic acid using benzyl ether as the solvent[124]. The materials produced are highly crystalline, highly monodisperse and highly magnetic. However, the size of nanoparticles produced is too high for our interests, the smallest documented particles are still very much in the ferromagnetic range at 22 nm; as such these particles are not ideal for biomedical applications as they may agglomerate *in vivo* or on exposure to an external magnetic field. The Pellegrino group and Batlle group use a modified version of the Hyeon experiment whereby iron acetylacetonate is thermally decomposed and the reflux temperature of the mixture was modified using alternative solvents such as squalene (~285 ^{o}C), octadecene (~314 ^{o}C) and phenyl ether (~258 ^{o}C). Related surfactants were also used such as decanoic acid[4].

The resulting cubic materials, have a much wider size range, including some sizes in the superparamagnetic range, ~12 nm edge length. It is highlighted in these works that in addition to the degassing phase, the heating ramp must be well controlled for reproducibility, typical values would be 0.5 ^{o}C/min, 2.5 ^{o}C/min and 7.5 ^{o}C/min.

5.1.2. Two-Step Synthesis Approach

The most common method for the synthesis of cubic NPs at present is the preparation of an iron oleate precursor from iron salts, followed by the reaction of this product in the presence of sodium oleate and oleic acid in high boiling solvents[116,122,126–128]. In all of these cases iron oleate was prepared by reacting iron chloride salts with sodium oleate in a biphasic mixture of water, hexane and ethanol. These reactants are stirred vigorously overnight and in the case of Shavel *et al*[127]. are then worked up immediately. In the other reports[116,122,126,128] following the overnight stirring the mixture is raised to reflux temperature where it is held for 4 hours. Following reflux, the oleate precursor is washed with water prior to any further reactions. This cleaning step allows for the removal of any unreacted reagents, which may interfere with the subsequent reactions.

The formation of cubic NPs is still somewhat of a mystery, facet formation in the growth phase of nanoparticle synthesis has been observed but the processes involved are not fully understood. Shavel *et al.* report the importance of sodium salts in the formation of the cubic NPs[127]. However, in the work produced by Zhen *et al.,* additional sodium oleate is not required for the preparation of cubic NPs[116]. An interesting report from the Dragnea group[129] highlights some of the difficulties with using iron oleate as a precursor, total decomposition of iron oleate occurs at an extremely high temperature ~380^{o}C, as such thermal decomposition methods with reflux temperatures of ~300^{o}C are highly dependent on the purity and homogeneity of the iron oleate precursor. The synthesis parameters, ratio of precursor to surfactant, reflux temperature, heat ramp etc, also influence the size, shape and polydispersity of the NPs produced. Pichon *et al.* reported that higher reflux temperatures produce larger NPs (growth phase dominates the NP synthesis), while faster heating rates produce smaller particles[126] (nucleation phase dominates the NP synthesis). The ratio of precursor to surfactant is also an issue that effects particle size, shape and polydispersity. A report from the Karty group highlights the effect of oleic acid; when excess oleic acid has been included NPs do not form. It appears that this excess further stabilizes the iron oleate and no reaction occurs[130]. This two –step method was the method adopted for our studies; the parameters affecting NP formation are explored in further detail in Section 5.3.

Despite the large number of reports, a reliable route for the preparation of highly crystalline, monodisperse, cubic, iron oxide nanomaterials with controlled size between 12 and 20 nm (edge length), was desired for further development of polymer mediated assemblies of magnetic nanoparticles. A number of the previously reported approaches were investigated as potential candidates, the surfactant assisted thermal decomposition of iron acetylacetonate in the presence of decanoic acid as described by Guardia et. al[1], and the surfactant assisted thermal decomposition of iron oleate as described by Shavel et al[127] were selected due to the previously reported high crystallinity, and high SAR values[1]. A further method was proposed for development, a surfactant free thermal decomposition of iron acetylacetonate in the presence of sodium salts, based on the surfactant free nanoparticle synthesis outlined in Chapter 3. This method was proposed due to the advantage of surfactant free particles, which allows for careful control over the stabilization conditions, and the ratio of nanoparticles to surfactant, a key factor in the control of assembly (as outlined in Chapter 3).

The synthesis methods were investigated for their reproducibility, and degree of size control, as well as the morphology of the nanoparticles produced. While many reports of monodisperse, cubic nanomaterials have been made, there is insufficient evidence of synthesis reproducibility, or control over particle size. There is also evidence of difficulties with the synthesis method, with reports indicating that multiple preparations must be combined in order to have sufficient material for even the most fundamental analyses. If a material is potentially destined for biological applications, process scalability is a must.

5.2. Surfactant Assisted Thermal Decomposition of Iron Acetylacetonate

Surfactant assisted thermal decomposition of iron acetylacetonate was performed based on a previously published method[1]. 0.353 g (1 mmol) of iron(III) acetylacetonate and 0.69 g (4 mmol) of decanoic acid were added to a 50 mL three-necked round-bottomed flask, with 25 mL of dibenzyl ether. The mixture was heated to 60 °C and degassed under vigorous N_2 flow with vigorous stirring (using a magnetic follower). The reaction vessel was then heated to 200 °C and held for 2.5 hours to allow all components to fully decompose. Finally, the solution was heated to reflux temperature and kept at this temperature for 1 h. The resulting black liquor was cooled to room temperature, and precipitated using 60 mL of ethanol and centrifuged at 16,100 rcf for 10 mins. The black precipitate was then redispersed in a small volume of chloroform and precipitated as before until the supernatant was clear. Finally, the collected particles were dispersed in 15 mL of chloroform, heptane or THF for further analysis and nanoparticle assembly. A series of samples were prepared using the above synthesis parameters and the resultant NPs can be observed below, Figure 5. 1. It can be seen that under identical synthesis conditions and parameters that the size and morphology of the NPs produced was not reproducible. It can also be observed that the degree of facet formation is low, with most particles appearing to maintain a quasi-spherical morphology

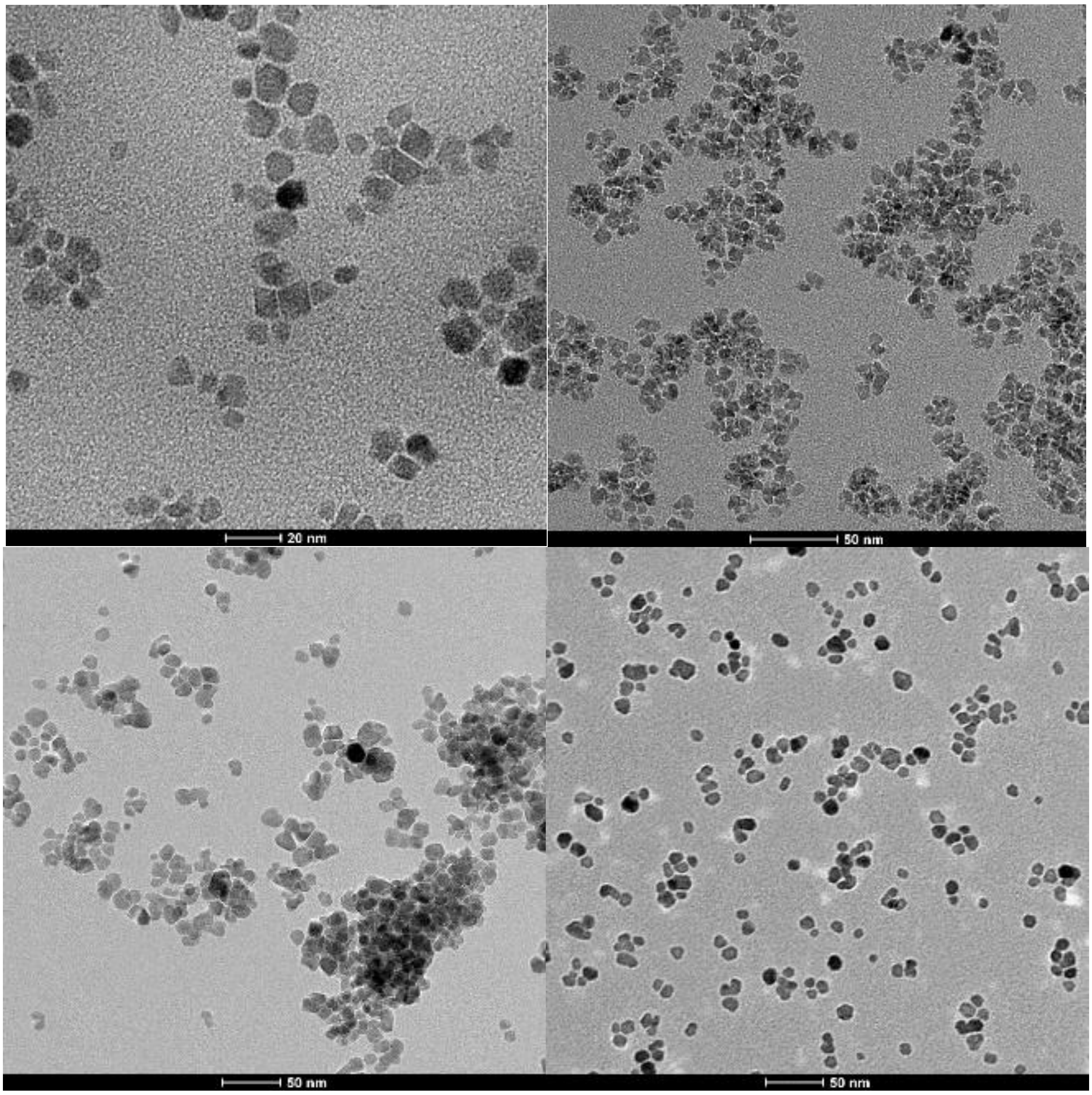

Figure 5. 1: A selection of TEM images of a variety of attempts to prepare cubic nanoparticles by thermal decomposition of iron acetylacetonate in the presence of decanoic acid, in each case the parameters were the same, (0.353g of iron acetylacetonate, 0.69g decanoic acid and 25 mL dibenzyl ether, heated to 200 °C for 2.5 hr, then heated to reflux for a further 30 min. It can clearly be seen that the synthesis method does not yield reproducible NPs, nor were the particles formed highly cubic. Scale bar in image 1 (top left) is 20 nm, all others are 50 nm.

It should also be noted that the outcome of this synthesis method was unpredictable, with particles forming less than 30% of the time. In the successful nanoparticle syntheses, no reproducibility in size was observed; every time that the experiment was successfully attempted, a different size of nanoparticle would be produced. In the initial work performed by the Pellegrino group, it was indicated that the rate of heating at each stage strongly influenced the eventual size of the nanoparticles formed. However, even under identical conditions, with a reproducible heating rate of 2.5 ^{o}C/min, using the same equipment on the same day, no two batches produced nanoparticles of the same size. Additionally, since June 2016, the iron (III) acetylacetonate source previously used was no longer available, and issues have arisen with any nanoparticles prepared using the new source, such as failure to stabilize under standard conditions, high polydispersity, a large degree of variability in the morphology of nanoparticles produced and a failure to assemble. Due to these reasons, this method was found to be both unreliable and not reproducible, and an alternative method was attempted.

5.3. Surfactant Assisted Thermal Decomposition of Iron Oleate

5.3.1. Synthesis of Iron Oleate

Iron oleate was prepared using an adaptation of a previously reported method[127]. In a standard synthesis 6.5 g (0.04 mol) of $FeCl_3$ (anhydrous, Sigma Aldrich), and 36.5 g (0.12 mol) of sodium oleate were added to a 500 mL three-necked round bottomed flask with a co-solvent mixture of ethanol (80 mL), water (60 mL) and heptane (140 mL). This mixture was stirred vigorously overnight by magnetic stirring, the mixture was then heated to reflux and held at this temperature for 7 hours. The resulting mixture was then allowed to cool and separate in a separating funnel, the aqueous layer was removed. The remaining black, organic layer was then washed with hot deionized water (~80 °C) a number of times, dried over magnesium sulphate, filtered, and then concentrated by rotary evaporation. Iron oleate was formed as a black-brown, highly viscous liquid at a yield of 83%.

Heptane was used in place of hexane in this synthesis for a number of reasons:

- It is less toxic to humans and the environment
- It has a higher boiling point which allows washing to be performed at higher temperatures (the importance of this will be outlined further in section 5.3.3)
- It has very similar physical properties to hexane
- While some previous publications do not include the reflux step, it was found that this step increased the yield of iron oleate and allowed for a quicker cleaning process.

5.3.2. Preparation of Cubic Nanomaterials by Thermal Decomposition of Iron Oleate

In a typical synthesis 1.5 g (1.67 mmol) of iron oleate, 250 mg (0.82 mmol) sodium oleate, 250 µL (0.80 mmol) of oleic acid, and 20 mL of squalene were added to a 3-necked, round bottomed flask. The flask was first heated to 120 °C under vigorous N_2 flow to degas the solution and allow all components of the reaction to mix well, it was held at this temperature for 2 hours. The flask was then heated to reflux and held at this temperature for 2 hours, before cooling to room temperature. The resulting black suspension was alternately solublized with heptane and washed with ethanol 3 times before suspension of the materials in heptane for analysis and imaging, or in tetrahydrofuran (THF) for assembly, as discussed in Chapter 6.

5.3.3. The Effect of Precursor Purity on Nanoparticle Formation

While many publications using iron oleate as a precursor for cubic iron oxide NPs suggest that the synthesized iron oleate precursor should be washed 3 times with water, it was observed that even on the third washing step the separation of the aqueous and organic layers takes a significant amount of time (~ 2 hours) and there is an emulsified “bubble” layer formed at the interface (as shown in Figure 5. 2). Hence, the effect of iron oleate purity on nanoparticle formation was investigated by preparing nanoparticles under identical conditions using iron oleate that had been washed 3, 12, 30 and 60 times with hot deionized water (~80 ^{o}C) respectively. It should be noted that with progressive washes the time required for phase separation decreased and the volume of the “bubble” layer also reduced. Following the washing step, the iron oleate in each case was dried over magnesium sulphate and concentrated as outlined in section 5.3.2.

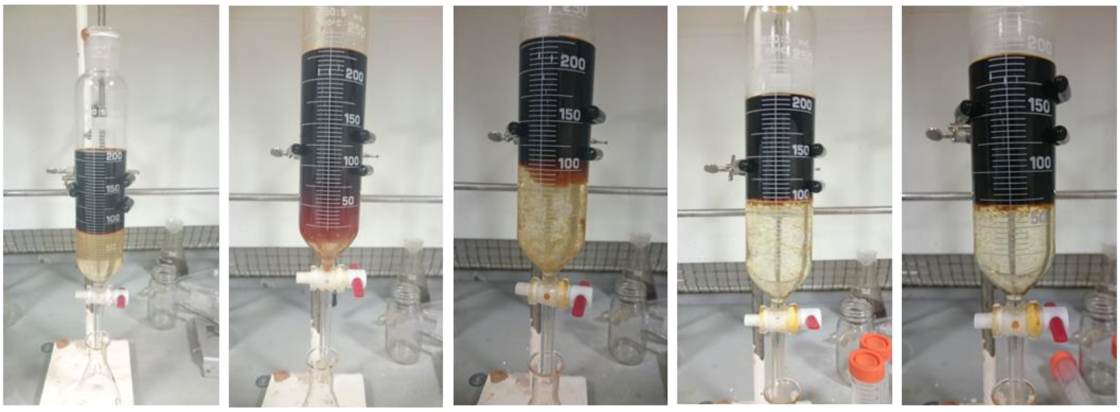

Figure 5. 2: Series of images indicating the emulsified "bubble layer" that forms during the oleate cleaning process. Image 1 (left) shows the initial separation observed immediately following the reflux step of iron oleate synthesis. As we move from left to right the number of washes performed increases, 3, 12, 30 and 60 washes respectively, with all images being taken approximately 1 hour after the washing procedure. It can be clearly seen that the emulsified bubble layer is greatly reduced on repeated washing and that the aqueous layer becomes clearer following repeated washing steps, indicating that the water-soluble impurities are being removed efficiently.

In each of the following syntheses, 0.3 g (0.3 mmol) of iron oleate (FeOL), 0.15 g of sodium oleate (NaOL) and 50 μL of oleic acid were added to a three-necked round bottomed flask with 10 mL of squalene as a solvent. The mixture was then heated to 200 °C under a vigorous N_2 flow and held at this temperature for 2 hr. The mixture was then further heated to reflux under an N_2 blanket and held at reflux for a further 2 hr. The resulting black suspension was washed by consecutive dispersion with 5 mL of heptane and precipitation with 40 mL of acetone (the dispersion and precipitation step was performed a number of times; 3, 12, 30, and 60, as outlined in the experimental text and figure captions below). The particles were then resuspended in heptane for TEM analysis. Figures 5.3-5.6 demonstrate the effect of iron oleate purity on the size, morphology, polydispersity, and shape quality of cubic NPs prepared by surfactant assisted thermal decomposition of iron oleate.

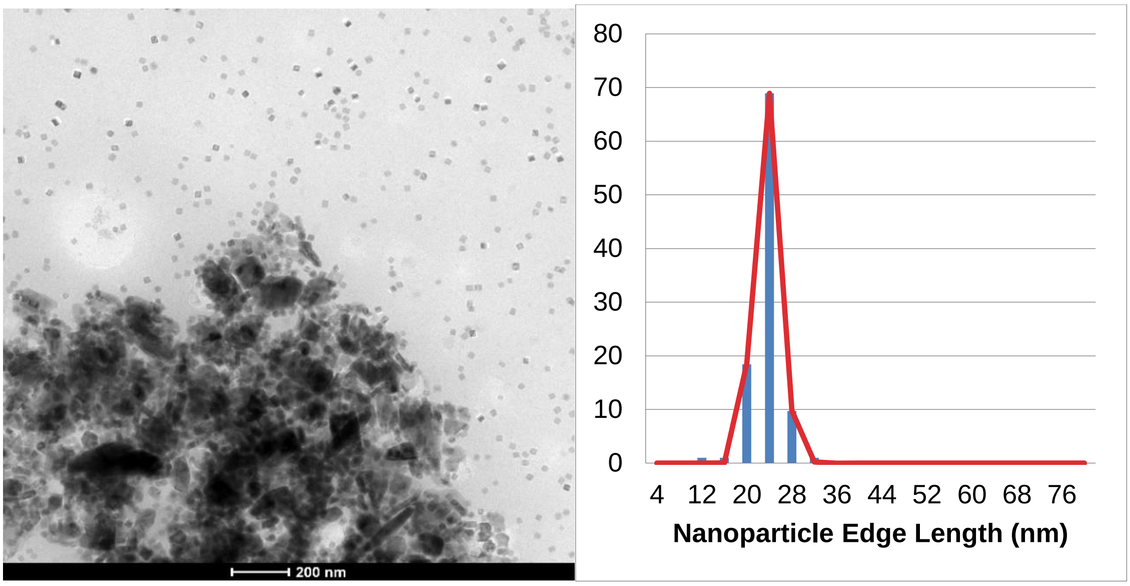

Figure 5. 3: Nanoparticles prepared from three times washed iron oleate precursor, it can be seen that a large proportion of materials produced are amorphous and there is no homogeneity of size, reasonably well dispersed cubic nanoparticles can also be observed on the grid, however these cubic materials appear truncated and rounded. (Edge length = 22.8 ± 1.6 nm)

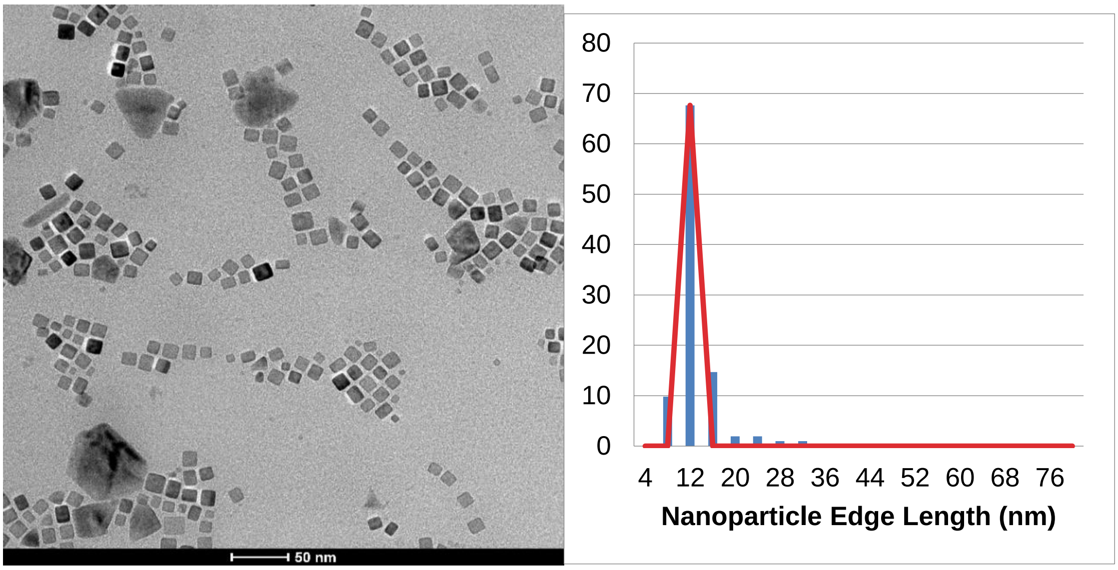

Figure 5. 4: Nanoparticles Prepared from 12 times washed iron oleate precursor. In this case cube like nanoparticle, formation has again occurred with significantly more defined edges and corners, however larger particles and particles with different morphology (triangular, hexagonal etc.) can still be observed. The NP size of all materials is more uniform, however there is still polydispersity in the sample. (Edge length = 11.2 ± 1.8 nm)

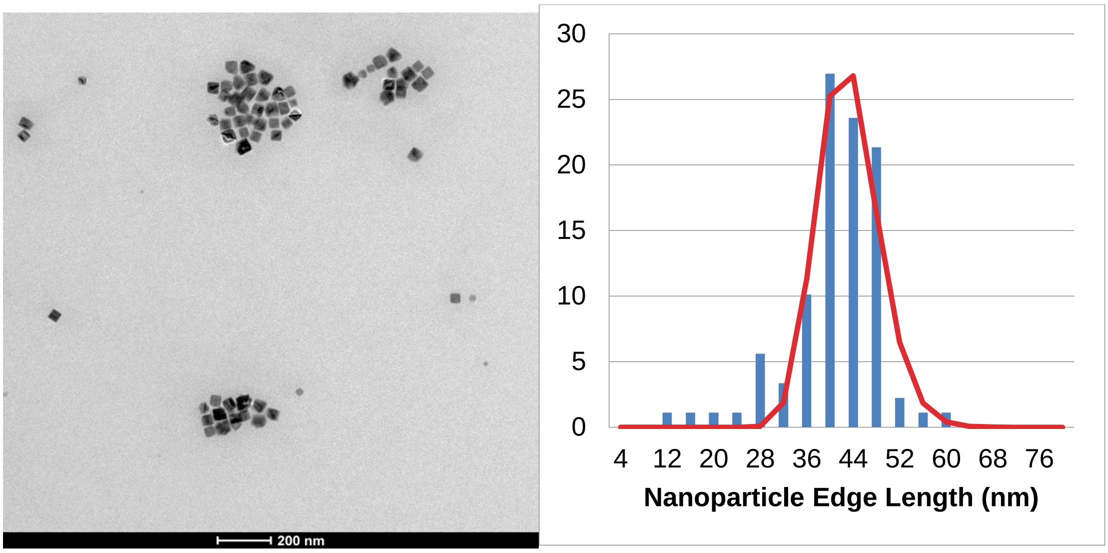

Figure 5. 5: Nanoparticles prepared from 30-times washed iron oleate. It is clear from this image that the materials produced from this synthesis are much more monodisperse and all have a cube like morphology. It can also be observed that the corners are somewhat less rounded than NPs prepared with less oleate washing. (Edge length = 43.3 ± 5.2 nm)

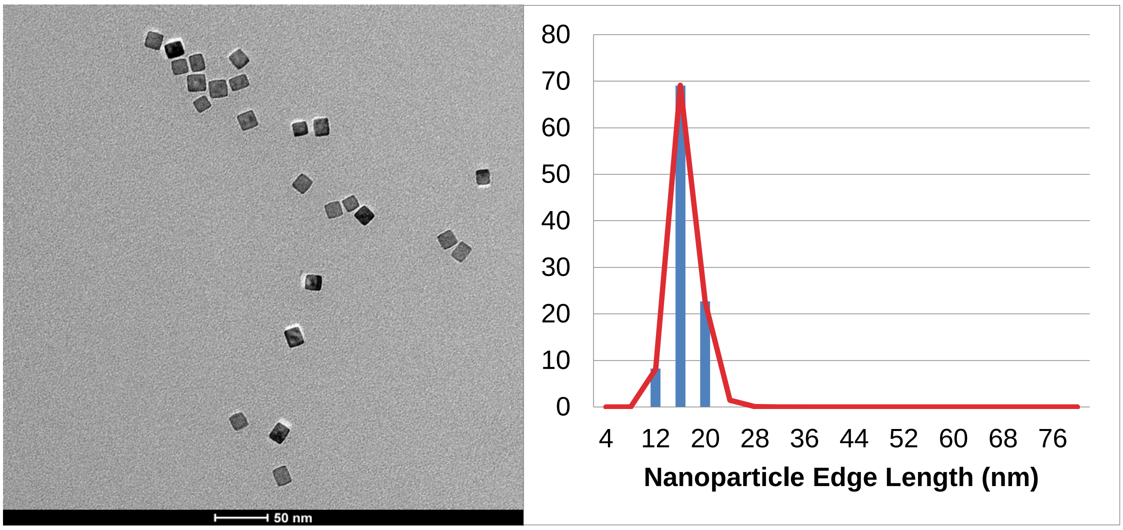

Figure 5. 6: Nanoparticles prepared from 60-times washed iron oleate. It is clear, that following extensive washing of the precursor that the edges and corners of the cubic materials have become more defined, the particles are more monodisperse and the morphology is more uniform. In this case there was no evidence of uncontrolled NP formation anywhere on the TEM grid. (Edge length = 16.5 ± 1.5 nm)

It can be seen from the above data (Figures 5.1 – 5.4) that by reducing the levels of water soluble impurities in the iron oleate precursor, through extensive cleaning, that some shape control can be observed. With more washing steps, the more monodisperse the nanomaterials produced become. The morphology of the materials produced also becomes more defined and more uniform. With less washing, a large percentage of the suspension prepared consists of sub-micron level amorphous particles, which are undesirable. The dispersible yield in all cases is >95%, and greater than 98% for NPs prepared with more than 12 times washed iron oleate. The washings are milky white initially and decreasingly so as the process continues. Iron salts are always strongly coloured, hence, it is probable that the majority of the impurities removed by this washing procedure are sodium salts due to the large excess of sodium oleate used in the synthesis of the iron oleate precursor It will be shown later (Section 5.3.6) that a controlled amount of sodium oleate is required for the formation of cubes in the thermal decomposition step. High field ^{1}H NMR analysis was performed on the prepared iron oleate stocks to investigate if impurities could be observed. It can be seen in Figure 5. 7, that there is a single peak observed which decreases in size with further cleaning. This peak appears at a chemical shift of 7.2 ppm. The relative height of this peak to the peak observed at 1.2 ppm was calculated and can be seen in Table 5. 1. Analytical determination of these impurities could not be performed due to the nature of iron oleate, as it is not a stochiometric material, multiple phases of Iron Oleate will exist in the same sample, (Fe, Fe^{2+}, Fe^{3+}) and as iron has magnetic properties, these states can contribute a change in the chemical shift which is not consistent from sample to sample, or batch to batch. As such, attribution of the individual peaks in the spectrum is difficult for this material, and comparative analysis of the same sample with further washing was used. It may be possible to identify these impurities by concentration and analysis of the washings; however, we do not believe that the nature of the impurities would be consistent from subsequent washings.

Table 5. 1: Relative height of the impurity peak to the peak observed at 1.2 ppm in the ^{1}H NMR spectrum of iron oleate at various stages of cleaning.

Number of Washing Steps Used	Relative Height of Impurity Peak
3	145.7%
12	5.4%
30	3.4%
60	2.7%

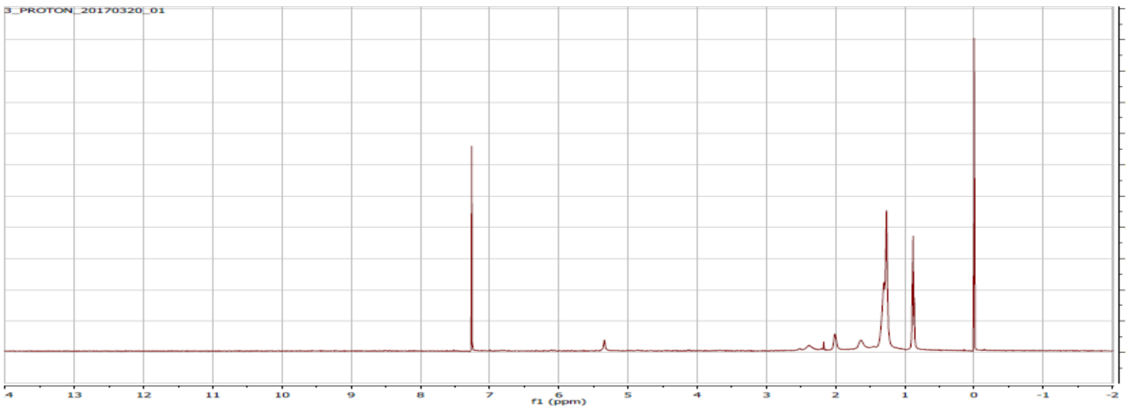
3_PROTON_20170320_01
f1 (ppm)
4
13
12
11
10
9
8
7
6
5
4
3
2
1
0
-1
-2
110
100
90
80
70
60
50
40
30
20
10
0

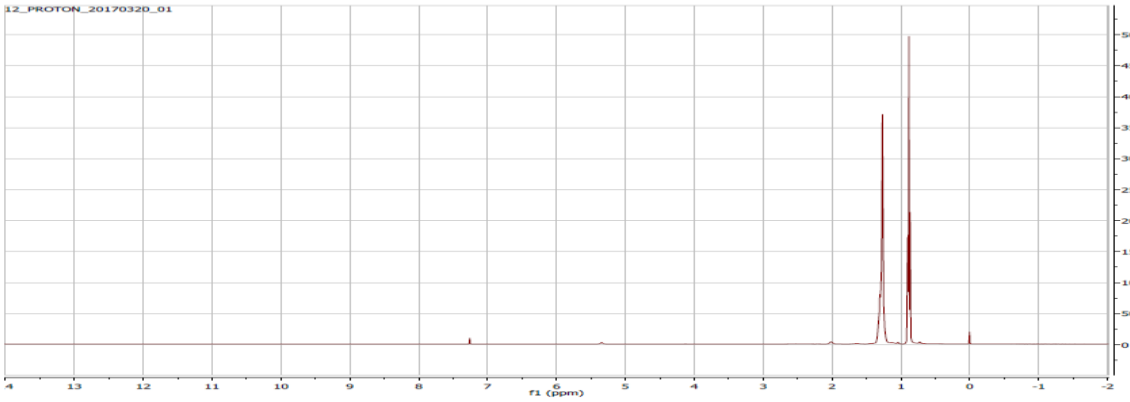
12_PROTON_20170320_01
f1 (ppm)
4
13
12
11
10
9
8
7
6
5
4
3
2
1
0
-1
-2
500
450
400
350
300
250
200
150
100
50
0

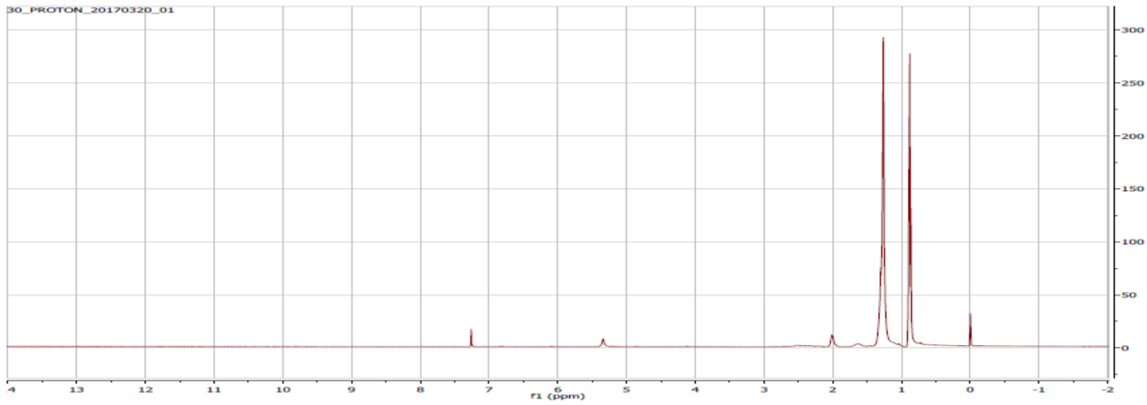
30_PROTON_20170320_01
f1 (ppm)
4
13
12
11
10
9
8
7
6
5
4
3
2
1
0
-1
-2
300
250
200
150
100
50
0

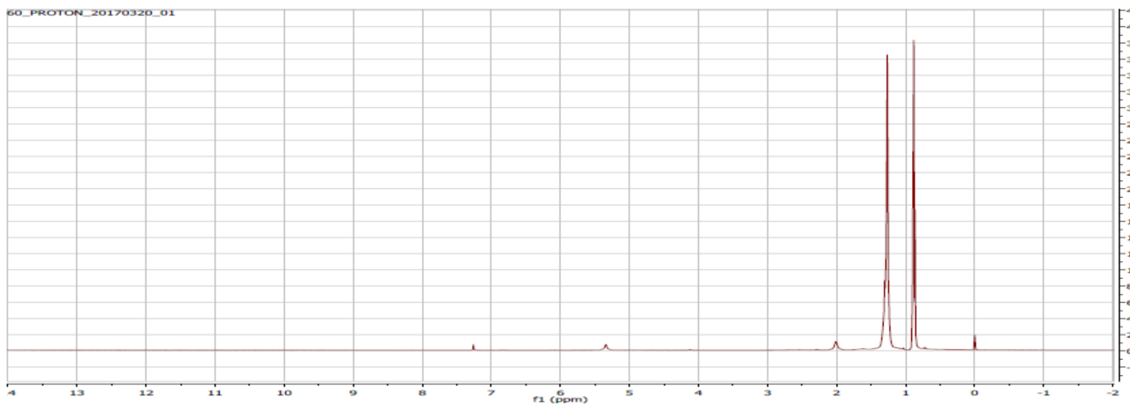
60_PROTON_20170320_01
f1 (ppm)
4
13
12
11
10
9
8
7
6
5
4
3
2
1
0
-1
-2
420
400
380
360
340
320
300
280
260
240
220
200
180
160
140
120
100
80
60
40
20
0
-20

Figure 5. 7: ^{1}H NMR analysis of the iron oleate precursor following 3 (top left), 12 (top right), 30 (bottom left), and 60 (bottom right),$CDCl_3$ was used as a solvent for these analyses.

5.3.4. Investigation into the Effect of Oleic Acid on Nanoparticle Formation

As this method is a surfactant assisted thermal decomposition method it is difficult to quantify the concentration of surfactant stabilizing the nanoparticles following standard work up procedures. It was intended that these materials be put forward for assembly by the PMA method previously outlined. As demonstrated in Chapter 3 the concentration of surfactant on the surface of the nanoparticles must be kept constant, in a specific range in order for size control during the assembly process. Therefore, the effect of the oleic acid surfactant on the final particle size was investigated. A series of syntheses were performed varying the amount of oleic acid used, Figures 5.8-5.13, all other parameters were kept constant at 0.3 g of iron oleate (60 times washed), 50 mg of sodium oleate and 10 mL of squalene. The reactions were heated to 200 °C and held at that temperature for 2 hours under vigorous N_2 flow, then heated to reflux (~300 °C) for a further 2 hours. All resulting NPs were then washed by consecutive dispersal in 5 mL of heptane and precipitation with 40 mL of Ethanol, before final dispersion in heptane for imaging, or THF for NP assembly.

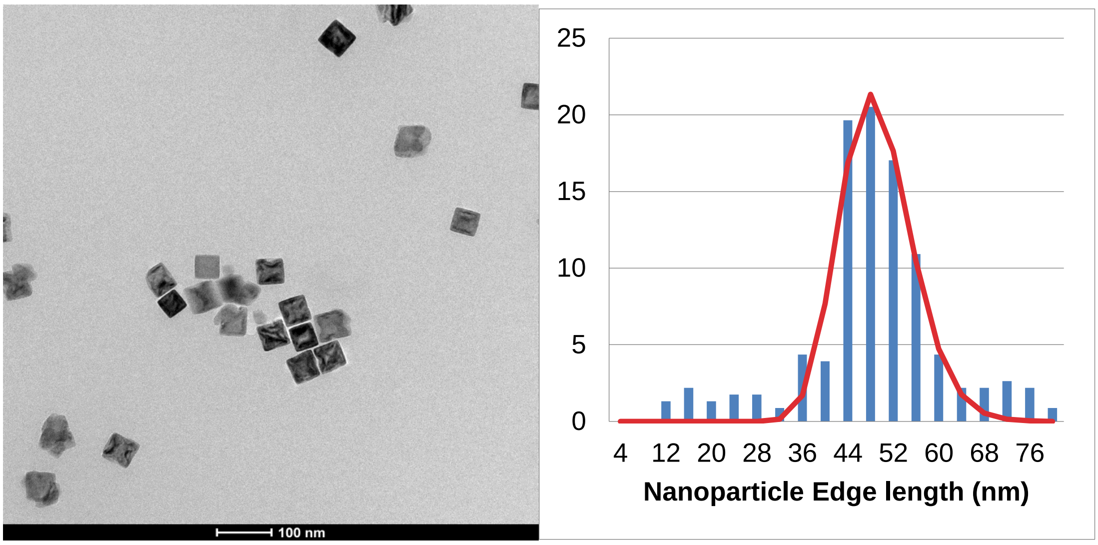

Figure 5. 8: Iron oxide nanocubes prepared by thermal decomposition of iron oleate (0.3 mmol) in the presence of sodium oleate (0.16 mmol) using squalene (10 mL) as a solvent. The NPs produced are highly cubic and expected to be ferromagnetic due to the high size (edge length = 49.2 ± 6.3nm. It can be seen that while a cubic morphology has emerged some nanoparticles have a concave edge and some NPs are slightly amorphous.

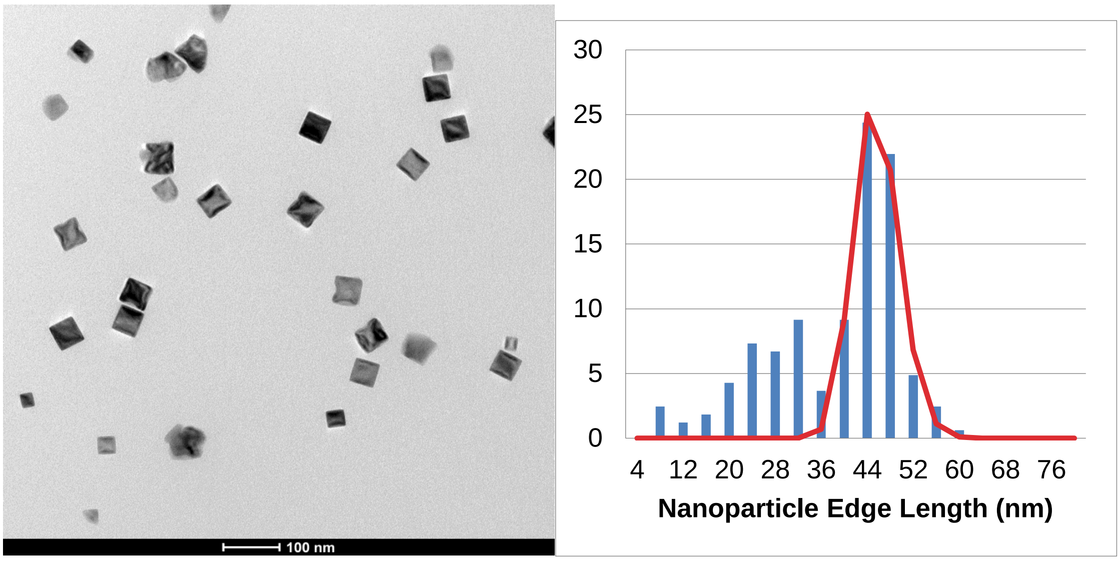

Figure 5. 9: Iron oxide nanocubes prepared by thermal decomposition of iron oleate (0.3 mmol) in the presence of sodium oleate (0.16 mmol) and oleic acid (0.03 mmol) using squalene (10 mL) as a solvent. The NPs produced are highly cubic and expected to be ferromagnetic due to the high size (edge length = 45.7 ± 3.9nm). It can be seen from the image that the concave edges observed in the sample prepared with no oleic acid are reduced, however some loss of morphology can be seen, also there appears to be a relatively broad size distribution as observed in the TEM size analysis.

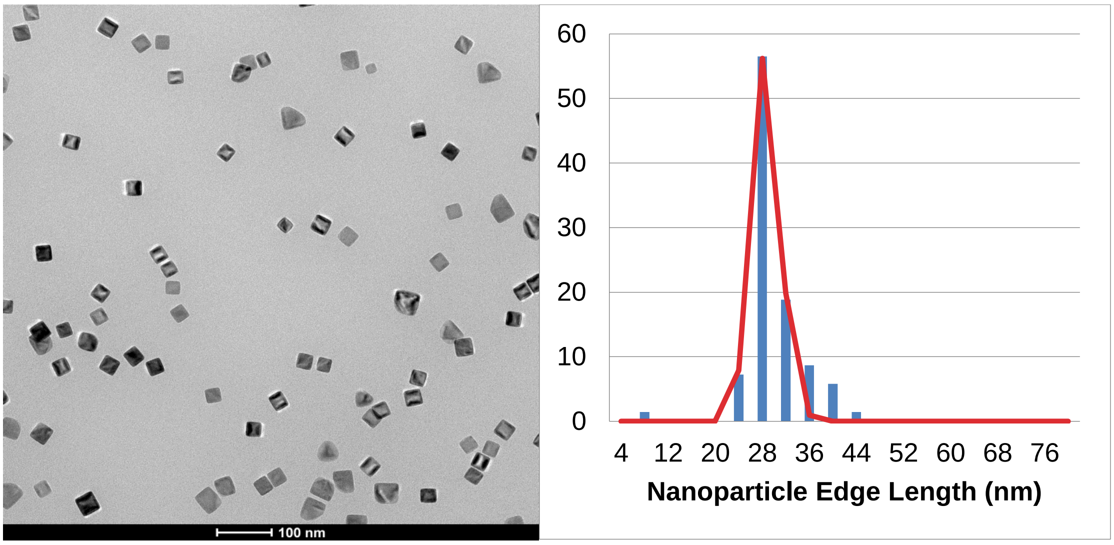

Figure 5. 10: Iron oxide nanocubes prepared by thermal decomposition of iron oleate (0.3 mmol) in the presence of sodium oleate (0.16 mmol) and oleic acid (0.06 mmol) using squalene (10 mL) as a solvent. The NPs produced are highly cubic, it can be seen that the concave edges are no longer apparent, however a number of NPs appear as triangular or cubic with a single corner truncation. The NP size is reduced, compared to samples with less oleic acid in the preparation (edge length 28.1 ± 2.3 nm)

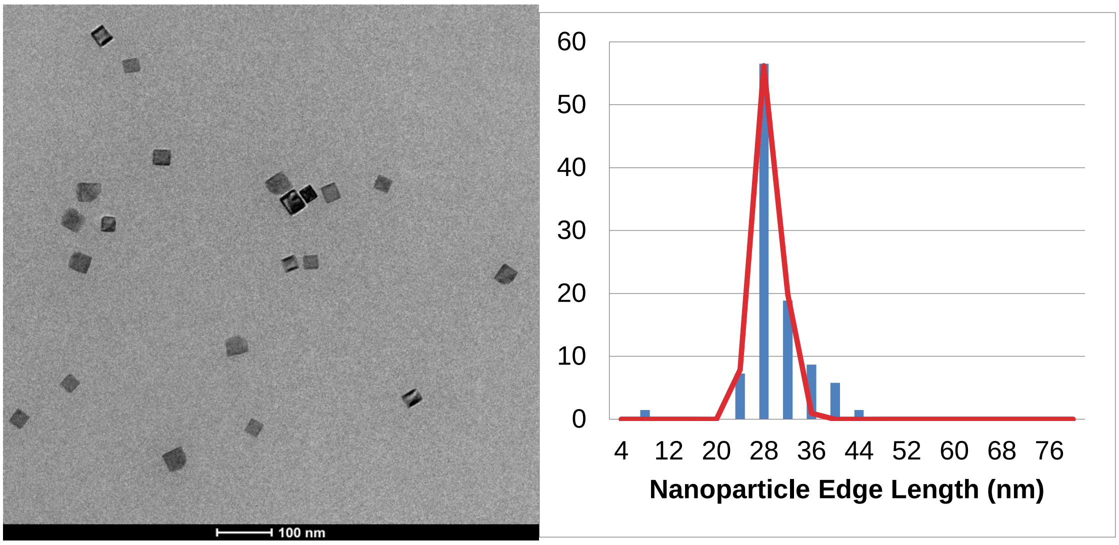

Figure 5. 11: Iron oxide nanocubes prepared by thermal decomposition of iron oleate (0.3 mmol) in the presence of sodium oleate (0.16 mmol) and oleic acid (0.09 mmol) using squalene (10 mL) as a solvent. In this case the nanoparticles produced are highly cubic, however a broad size distribution was found (edge length = 31.0 ± 6.0 nm).

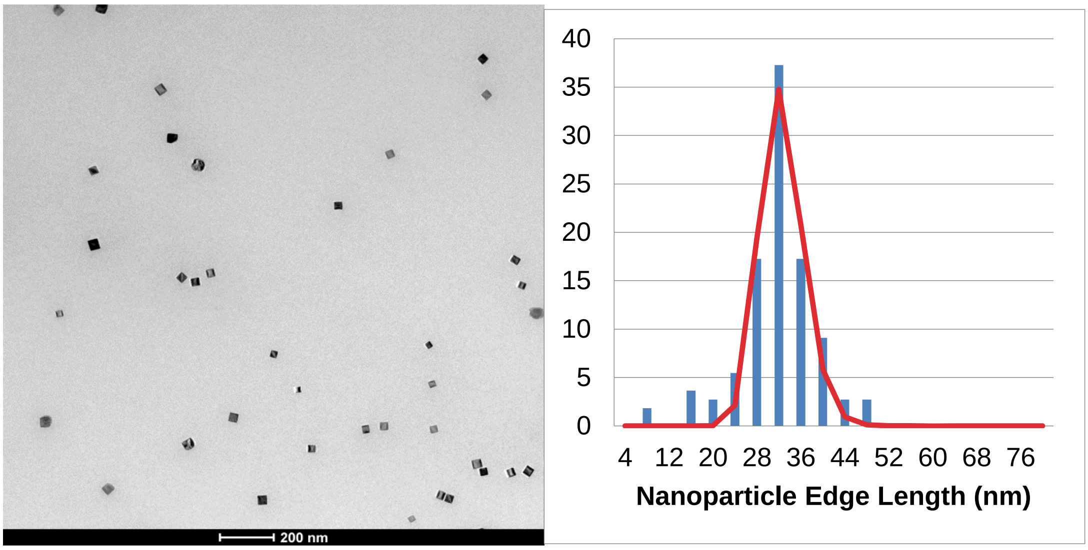

Figure 5. 12: Iron oxide nanocubes prepared by thermal decomposition of iron oleate (0.3 mmol) in the presence of sodium oleate (0.16 mmol) and oleic acid (0.12 mmol) using squalene (10 mL) as a solvent. In this case the nanoparticles produced are highly cubic, and the size distribution of NPs was found to be reduced compared to samples prepared with lower oleic acid concentration (edge length = 32.4 ± 4.4 nm).

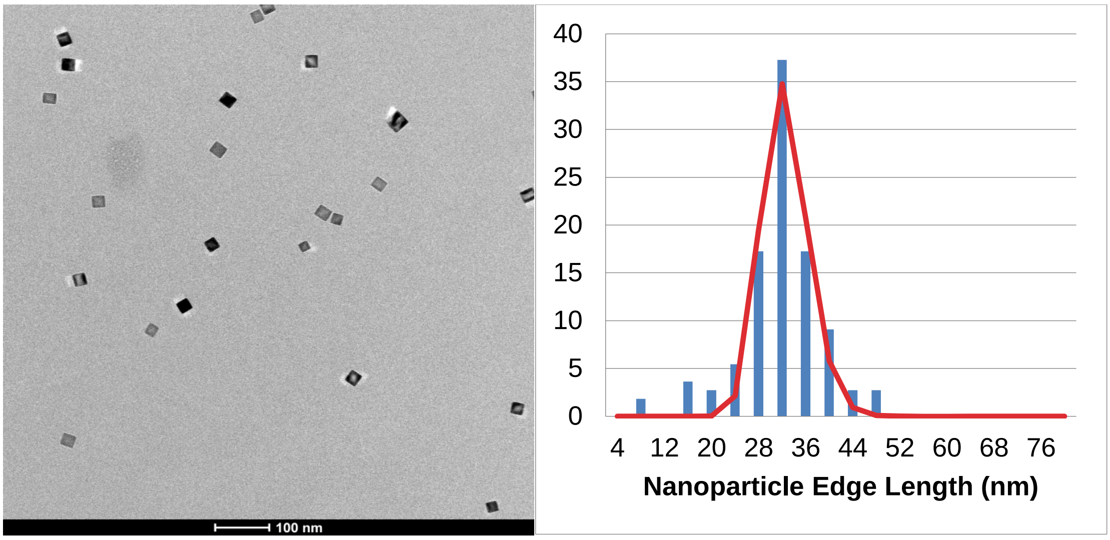

Figure 5. 13: Iron oxide nanocubes prepared by thermal decomposition of iron oleate (0.3 mmol) in the presence of sodium oleate (0.16 mmol) and oleic acid (0.15 mmol) using squalene (10 mL) as a solvent. In this case the nanoparticles produced are highly cubic, and the size distribution and polydispersity of NPs was found to be reduced compared to samples prepared with lower oleic acid concentration (edge length = 24.8 ± 2.5 nm).

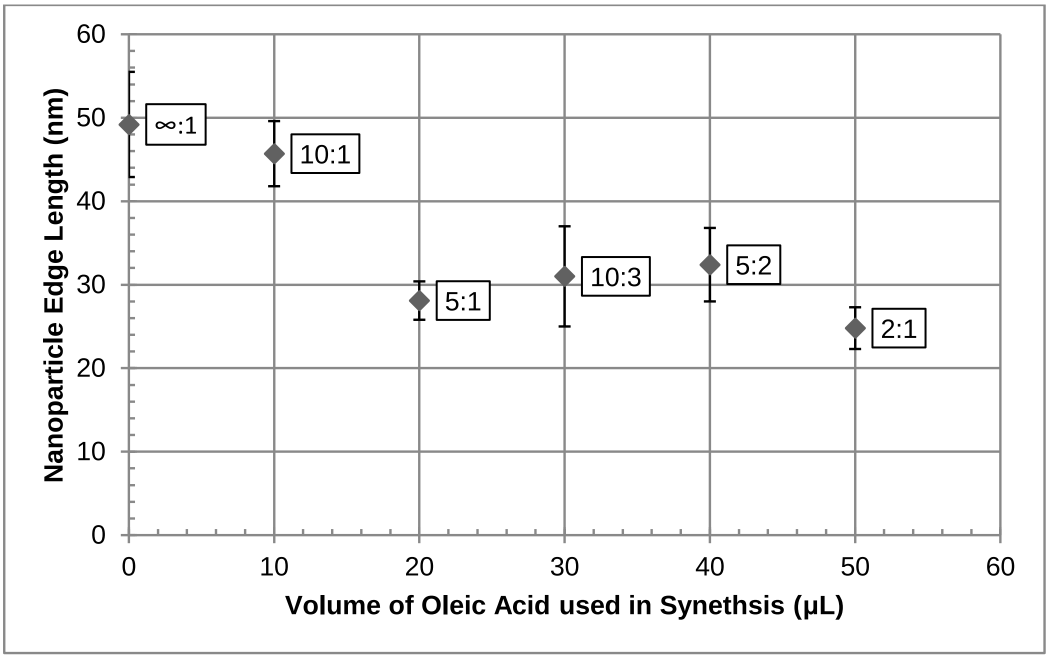

Figure 5. 14: NP edge length as a function of oleic acid content in the thermal decomposition. It can be seen that there is an overall downward trend as oleic acid content increases; however, this relationship is not linear. Error bars indicate ± σ as determined by TEM. Data labels represent the molar ratio of iron oleate to oleic acid. All samples have an aspect ratio of 0.9 – 1.1 as determined manually, no obvious systematic shift in shape has been observed.

It was found that adjusting the amount of oleic acid had no significant effect on nanoparticle morphology; however there did appear to be an effect on nanoparticle size at lower molar ratio of oleic acid, as seen in Figure 5. 14. Systematic behaviour is not observed, however, above a molar ratio of ~5:1 iron oleate to oleic acid, especially after NP polydispersity is accounted for, and it is believed that this is due to the non-stoichiometric nature of iron oleate as a precursor.

Iron oleate is a notoriously difficult material to work with, it resists cleaning, is non-stoichiometric, and its inconsistent decomposition will likely affect any attempt to observe systematic behaviour on nanoparticle formation. It is interesting to note however that at extremely high concentrations of oleic acid (1 mL in a 0.3g iron oleate decomposition, a molar ratio of 1:10, iron oleate: oleic acid) nanoparticles do not form even under extended reflux times. This may be due to free oleate being in such high abundance that iron oxide nuclei remain stabilized at sub critical sizes.

In summary, cubic nanoparticles in the 20-26 nm range are possible under the conditions described and that while the oleic acid concentration may contribute to the size and polydispersity of the nanomaterials, it is difficult to observe any systematic change. To investigate the hypothesis that nanoparticle size is not dominated by the molar ratio of oleic acid to iron oleate, a reproducibility study was performed in the absence of oleic acid.

5.3.5. Investigation into Synthesis Reproducibility

Having identified potential size control (if over a narrow range), three samples were prepared consecutively by thermal decomposition of iron oleate (0.3 g) in the presence of sodium oleate (50 mg) using 10 mL of squalene as a solvent, without the inclusion of oleic acid as a surfactant using the protocol outlined in section 5.3.5. This synthesis procedure was chosen to demonstrate that any inconsistencies observed in repeated syntheses were as a direct result of the iron oleate precursor, rather than the combination of oleate sources in the synthesis. In all cases the precursor used was washed 60 times prior to the thermal decomposition step.

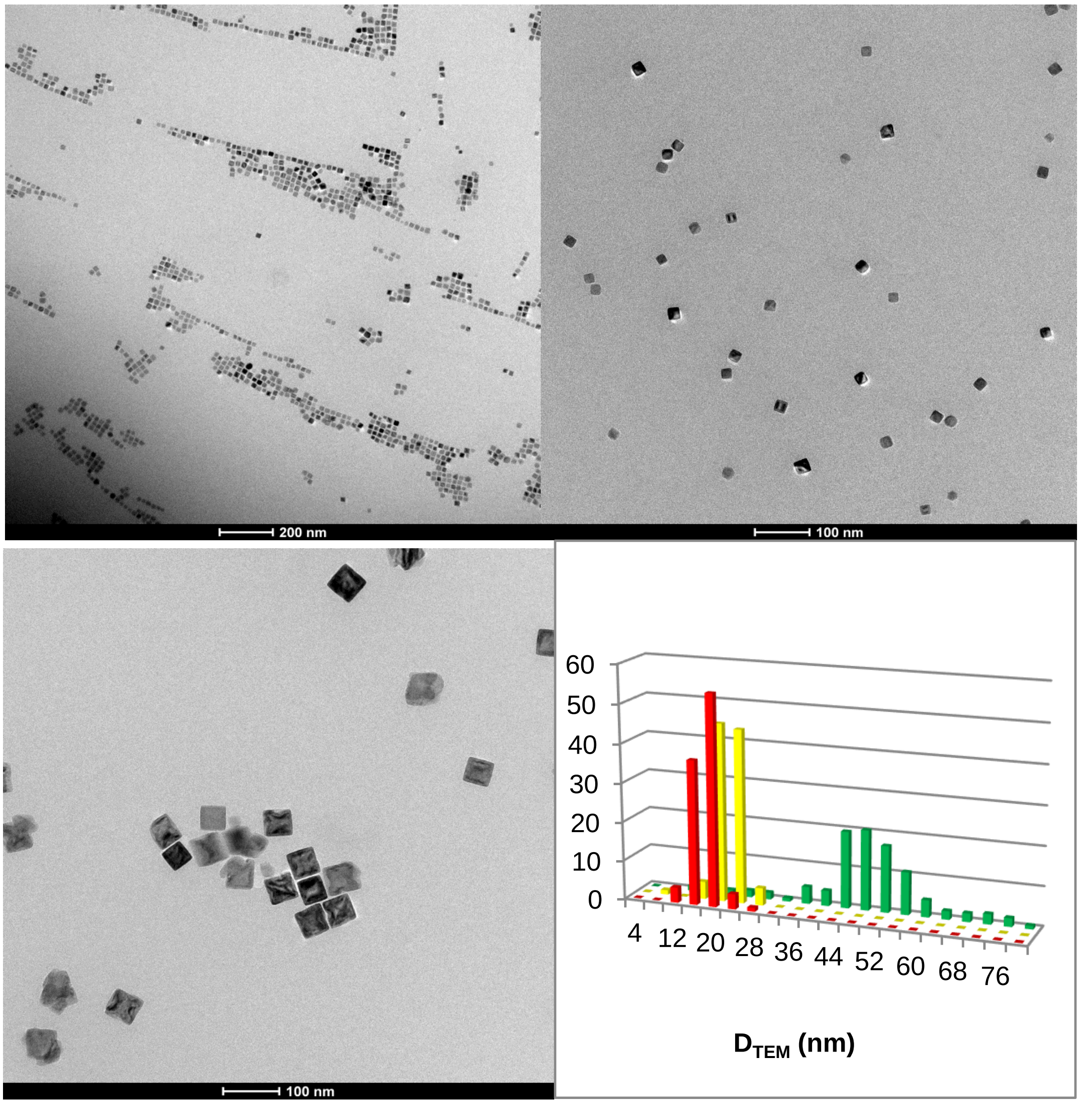

Figure 5. 15: Images captured of 3 consecutive syntheses under identical conditions. In each case 0.3 g of FeOL was added to 50 mg of NaOL and refluxed in 10 mL of squalene. It can be clearly seen from the histogram overlay plot that the synthesis does not produce NPs of consistent NP size from synthesis to synthesis. Edge lengths = 17.0 ± 1.7 nm, 22.3 ± 2.5 nm and 49.3 ± 6.3 nm

It can be clearly observed from the histogram overlay of the TEM image analysis that there are huge inconsistencies between NP syntheses performed under identical conditions suggesting that NP size control may be difficult if using iron oleate as a precursor. The 3 concurrent syntheses produced NPs of 18.6 ± 2.1 nm, 22.3 ± 2.5 nm, and 49.2 ± 6.3 nm respectively. The size of NPs produced is completely inconsistent from synthesis to synthesis, even when using the same equipment, glassware and precursor. Any potential trial at synthesis reproducibility between precursor batches would be futile if intra-batch reproducibility is poor. It is important to note that while publications have been made using materials prepared by a similar synthesis method to the one reported here, and synthesis conditions for the preparation of a specific size have been claimed, reproducibility studies are not reported. Furthermore, imaging of the particles prepared is generally restricted, only highlighting a few particles rather than a wide field of view. Additionally, it is rare to find any reports of DLS measurements, which suggests difficulty with colloidal stability and suspension monodispersity, both of which are needed for biomedical applications.

5.3.6. The Effect of Additional Sodium Oleate on Nanoparticle Formation

Inorganic sodium salts are believed to fully dissolve and dissociate during the thermal decomposition process, and the free Na^+ ions are believed to influence the promotion of nanoparticle growth along the {100} planes ((100), (010), and (001)), inducing the formation of facets on the particle surface. A series of experiments were performed varying the amount of pure sodium oleate added to the thermal decomposition of high purity (60 X washed) iron oleate, to investigate the effect of free Na^+ ions on the formation of the nanoparticles. In each case the mass of iron oleate, volume of oleic acid used, and the volume of squalene used was maintained at 0.3 g, 50 µL and 10 mL respectively.

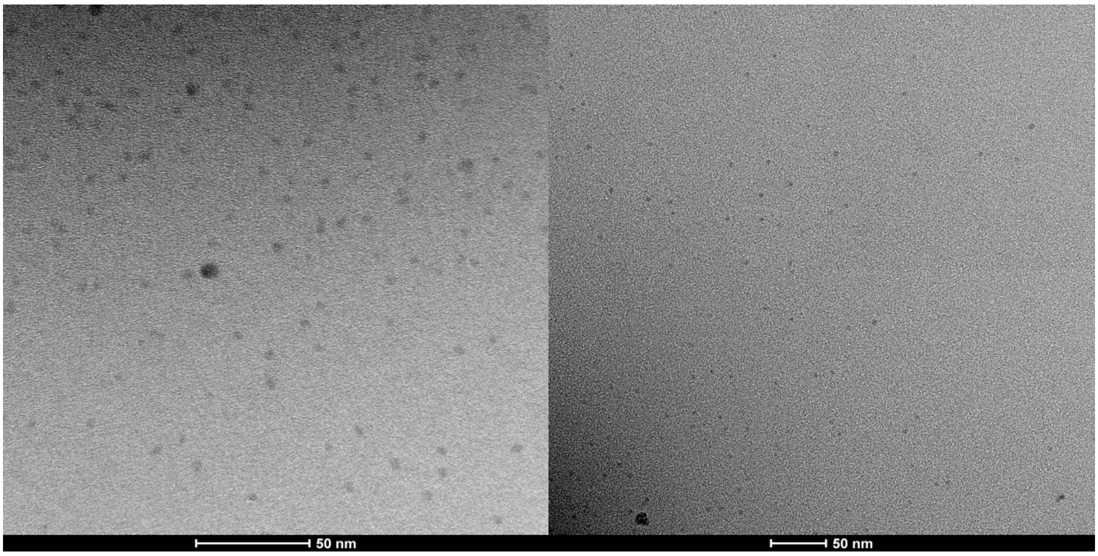

Figure 5. 16: Nanoparticles prepared by thermal decomposition of iron oleate in the absence of additional sodium oleate. (0.3 g FeOL, 50 µL OA, and 10 mL squalene, heated to 200 °C for 2 hr under vigorous N_2 flow, then to reflux for a further 2 hr under an N_2 blanket). An accurate size could not be determined due to poor image contrast; however, the NPs are spherical and small with an estimated diameter of 6 nm.

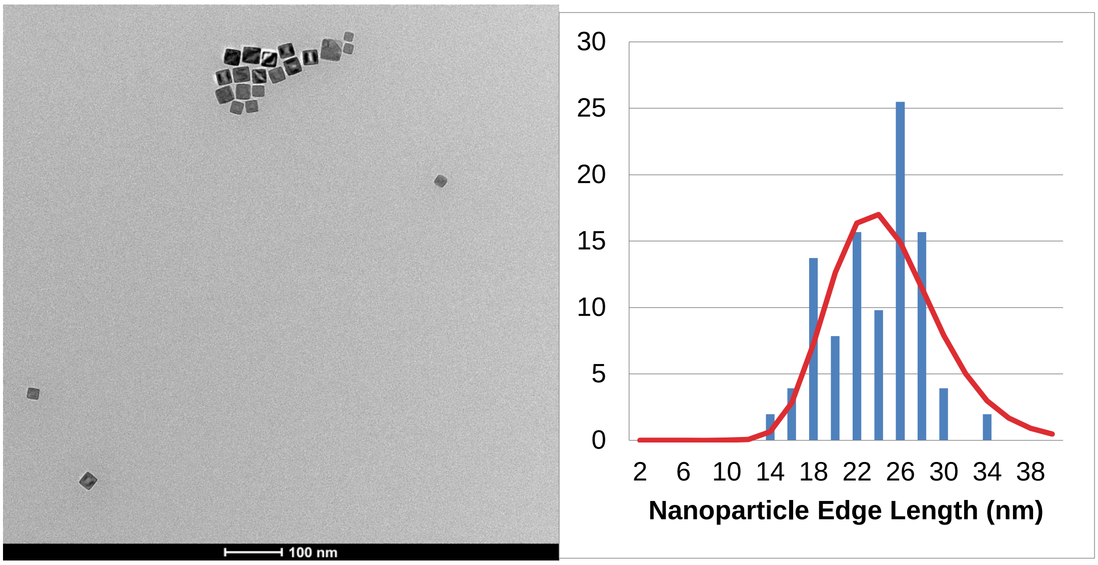

Figure 5. 17: Nanomaterials prepared by thermal decomposition of iron oleate in the presence of sodium oleate (molar ratio of iron oleate to sodium oleate = 2:1; 0.3 g FeOL, 50 mg NaOL, 50 µL OA, and 10 mL squalene, heated to 200 °C for 2 hr under vigorous N_2 flow, then to reflux for a further 2 hr under an N_2 blanket) Edge length = 24.8 ± 5.0 nm

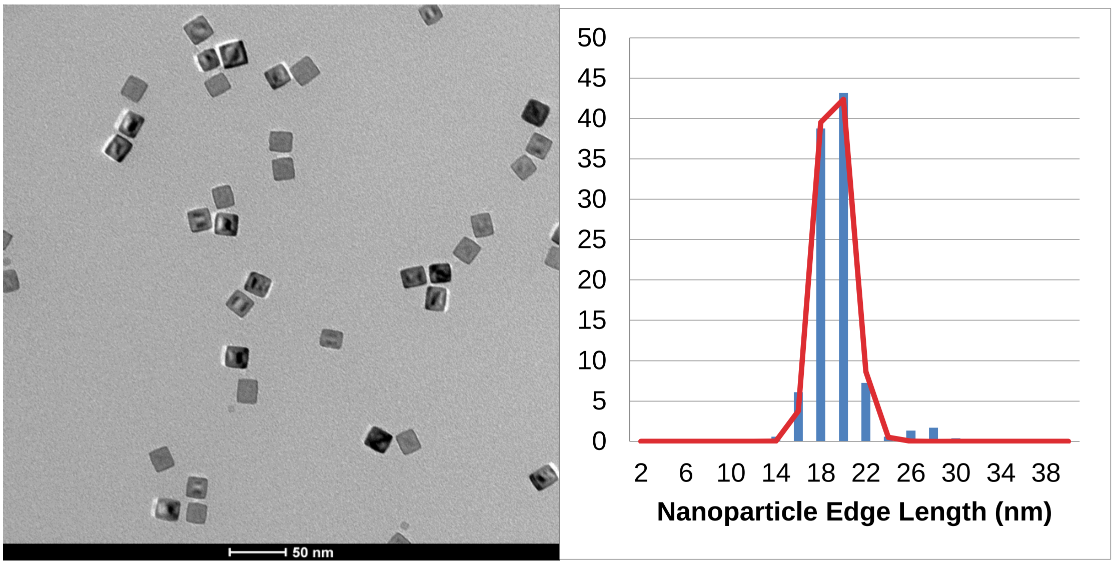

Figure 5. 18: Nanomaterials prepared by thermal decomposition of iron oleate in the presence of sodium oleate (molar ratio of iron oleate to sodium oleate = 1:1; 0.3 g FeOL, 100 mg NaOL, 50 µL OA, and 10 mL squalene, heated to 200 °C for 2 hr under vigorous N_2 flow, then to reflux for a further 2 hr under an N_2 blanket) Edge length = 19.2 ± 1.5 nm

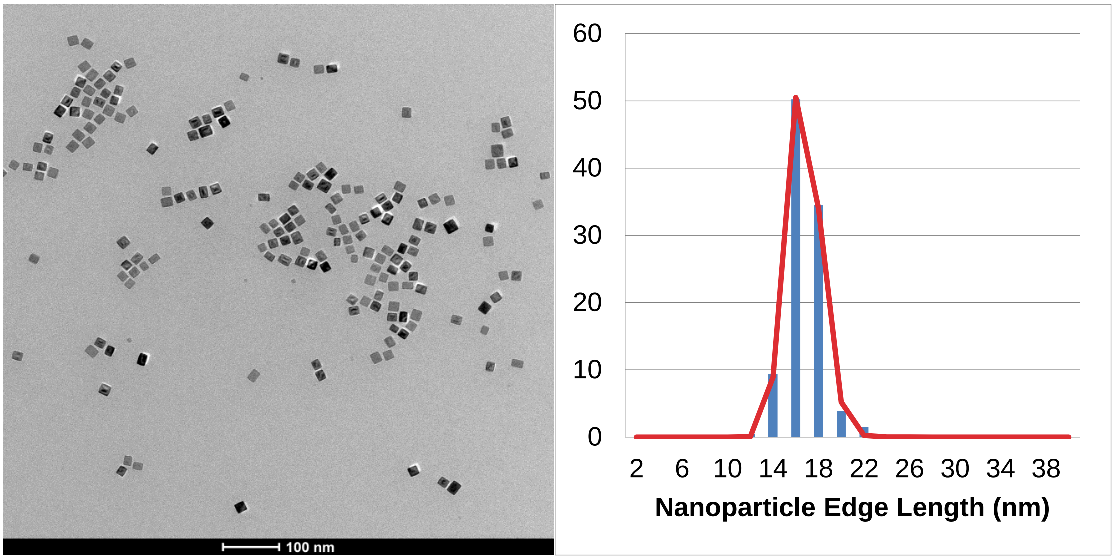

Figure 5. 19: Nanomaterials prepared by thermal decomposition of iron oleate in the presence of sodium oleate (ratio of iron oleate to sodium oleate = 1:2; 0.3 g FeOL, 200 mg NaOL, 50 µL OA, and 10 mL squalene, heated to 200 °C for 2 hr under vigorous N_2 flow, then to reflux for a further 2 hr under an N_2 blanket) Edge length = 16.7 ± 1.5 nm

It is evident from the above images that the presence of sodium oleate during thermal decomposition influences the promotion of growth in the {100} planes, promoting the cubic shape, during nanoparticle formation and growth. In the absence of additional sodium oleate, iron oxide nanoparticles with a spherical morphology can be synthesized. With added sodium oleate, it was found that cubic NPs in the desired size range were formed; the edges and corners of these materials did not appear to become more or less defined at higher concentrations of sodium oleate, indicating that the presence of Na^+ in the reaction vessel is the only requirement for the formation of cubic NPs rather than spherical. An excess of NaOL does not affect the shape of NPs, or impede the reaction, unlike our observations with excess oleic acid in the reaction, as described in 5.3.4.

These results are of interest as they are directly opposed to our findings described in section 5.3.3, where it was observed that cubic nanoparticles were more defined as fewer (sodium containing) impurities could be observed in the iron oleate complex. Further experiments were performed at very low concentrations of sodium oleate to determine if a minimum sodium concentration is required for cube formation (10:1

ratio of iron to sodium). Amorphous spiky NPs were found to form under these conditions, Figure 5. 20, indicating that a minimum Na^+ concentration is required for the formation of cubic iron oxide nanoparticles. Thus, in further experiments a minimum concentration of sodium oleate was used equivalent to a 2:1 molar ratio between iron oleate and sodium oleate.

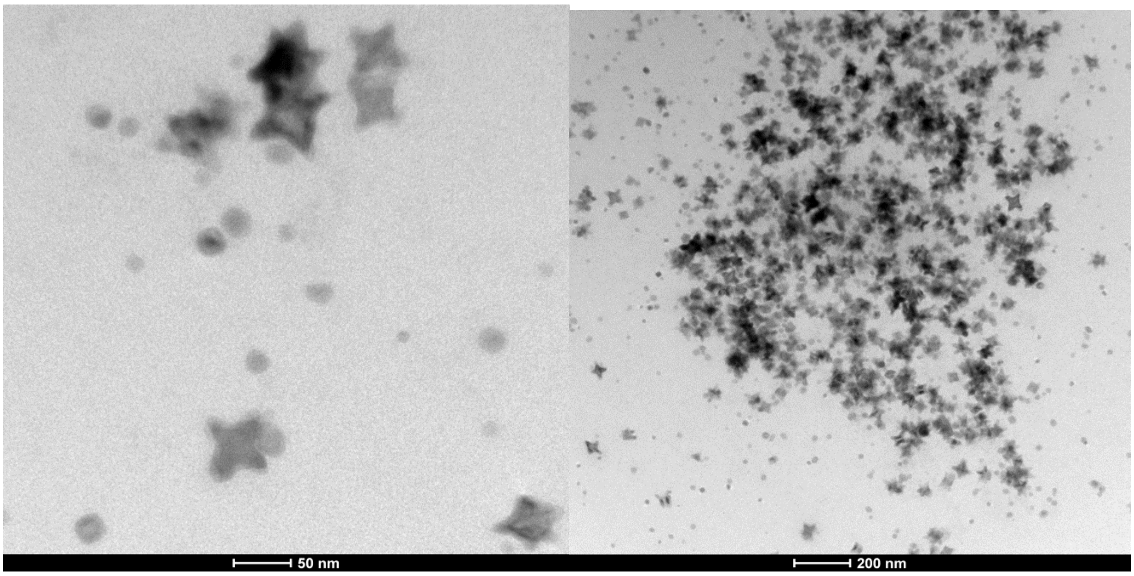

Figure 5. 20: Amorphous NPs produced by thermal decomposition of iron oleate in the presence of a small concentration of sodium oleate. (0.3 g FeOL, 15 mg NaOL, 50 µL OA, and 10 mL squalene, heated to 200 °C for 2 hr under vigorous N_2 flow, then to reflux for a further 2 hr under an N_2 blanket), an accurate size could not be determined due to poor contrast however the spiky NPs have a span of approximately 50 nm.

It should be noted here that while the data above, Figure 5. 17 -Figure 5. 19 display a downward trend in size, as with the previous experiments, the NP sizes were not reproducible between consecutive syntheses under identical conditions, the findings regarding NP shape were not affected by the irreproducibility of the synthesis.

5.3.7. Scale-up of Cubic Nanoparticle Preparation by Surfactant Assisted Thermal Decomposition of Iron Oleate

A series of scale-up experiments was performed to demonstrate that sufficient NPs for an assembly optimization series of experiments could be prepared in a single reaction without affecting the polydispersity or the cubic morphology of the NPs, using the protocol described in section 5.3.5., and relaxing the aspiration to size control. A five times scale up synthesis was performed using 1.5 g of iron oleate (60 times washed), 250 mg of sodium oleate, 250 µL of oleic acid decomposed and refluxed using 20 mL of squalene as a solvent. Note that the solvent (squalene) volume was only doubled, to allow for total precursor solubility, while reducing solvent waste. This increase in precursor concentration did not apparently further confound the irreproducibility to that experienced with this synthesis in general. The resulting particles were then cleaned by consecutive dispersion in heptane (5 mL) and precipitation in acetone (40 mL), three times before resuspension in heptane for image analysis.

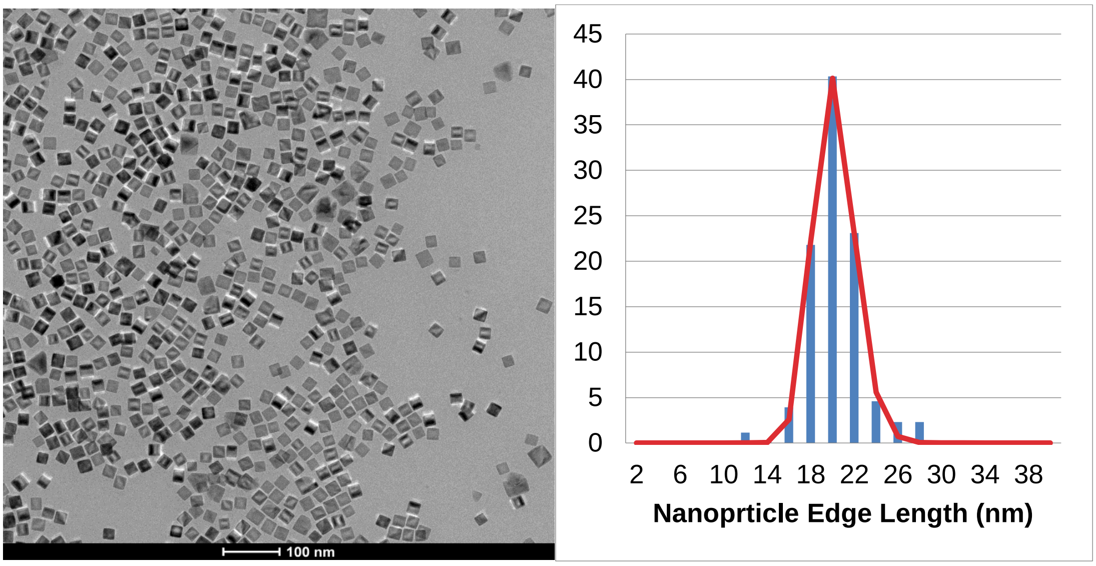

Figure 5. 21: TEM image and image analysis of Nanoparticles produced by a 5 x scale up of the standard thermal decomposition of iron oleate, (1.5 g FeOL, 250 mg NaOL, 250µL oleic acid and 20 mL of squalene as a solvent. It can be seen both from the image and the data analysis that the NPs produced are highly cubic and highly monodisperse, (NP edge length = 20.2 ± 1.9 nm)

It can be seen from the above image, that upscaling had little effect on the NP morphology, corner and edge definition and the monodispersity remain good. A further scale up was performed at 10 X the original scale (3.1 g of Iron oleate, 500 mg of sodium oleate, 500 µL of oleic acid, and 40 mL of squalene were heated to 120 ^{o}C under vigorous N_2 flow for 2 h, the solution was then heated to reflux (~300 ^{o}C) for a further 2 h, and it can be seen in Figure 5.22 below that again, scaling up the synthesis has had no effect on morphology and the size and polydispersity of the NPs produced is acceptable for use as biomedical probes, although as before, the NP size does vary.

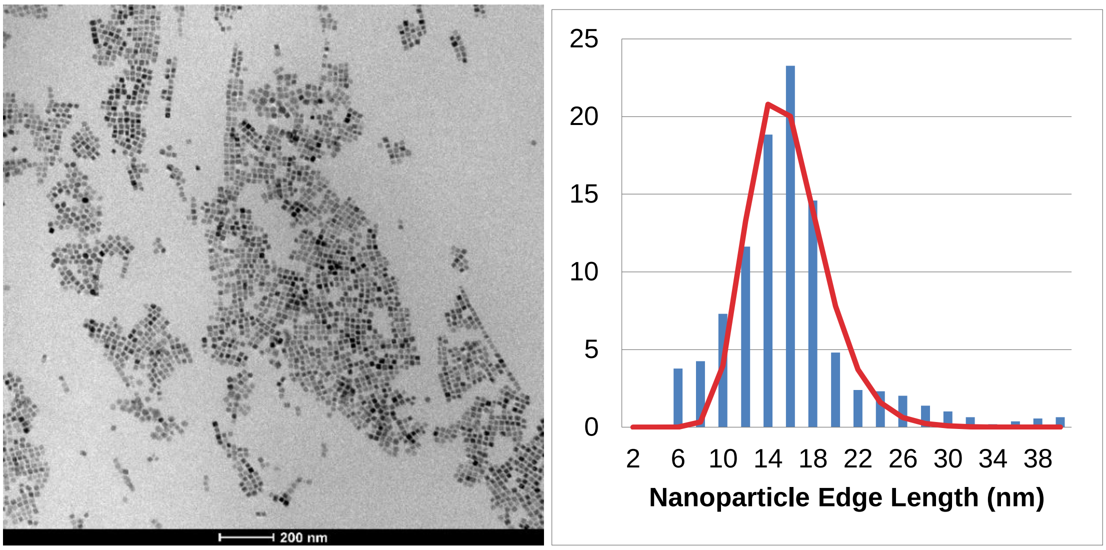

Figure 5. 22: TEM image and image analysis of Nanoparticles produced by a 10 x scale up of the standard thermal decomposition of iron oleate (3.1 g FeOL, 500 mg NaOL, 500 µL oleic acid and 40 mL of squalene as a solvent. It can be seen both from the image and the data analysis that the NPs produced are highly cubic and highly monodisperse, (NP edge length = 15.8 ± 3.4 nm)

5.4. Phase Transfer of the Cubic Nanomaterials to Aqueous Suspension

As outlined in Chapter 4 the greatest potential of these materials is in the field of biomedicine, applications which require all samples to be water (and indeed buffer) stable for use *in vivo*. As these cubic nanoparticles were prepared using a surfactant assisted thermal decomposition approach, a phase-transfer method must first be employed to allow for testing to be performed in an aqueous environment. The nanocubes were phase transferred using a ligand prepared elsewhere in the group, which will henceforth be referred to as ligand 1. This ligand was a polymer functionalized with a catechol group, see Figure 5. 23. It should be noted that in a fatty acid stabilized suspension the oleic acid interacts with the nanoparticles in two ways, through chemisorption to the NP surface, and through physisorption in a second shell around the NP. Neither chemisorption, or physisorption rely on irreversible covalent bonding and the oleic acid molecules are known to freely diffuse to and away from the NP in an equilibrium. Catechols are known to have a much stronger affinity for iron oxide nanoparticles than carboxylates, thus the catechol will preferentially interact with the particles displacing oleic acid. The secondary functionality if the ligand, in this case PEG, can confer water solubility.

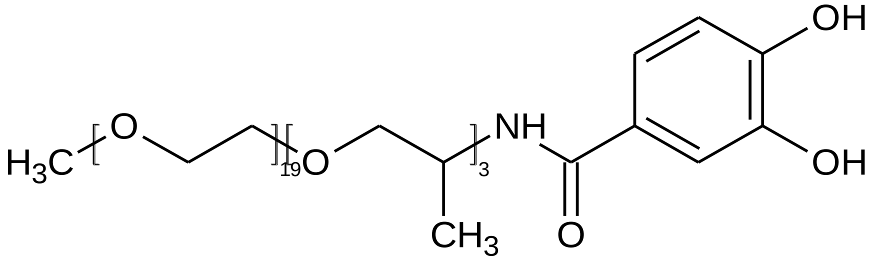

Figure 5. 23: Structure of catechol functionalized polymer, ligand 1.

To promote phase transfer, a suspension of iron oxide nanocubes in heptane (1 mL at a concentration of 0.2 mM) was precipitated with ethanol (10 mL) and the solvent removed, a solution of ligand 1 in ethanol (5 mL at a concentration of 0.01 mM, calculated as a 20 times surface equivalent volume using a surfactant footprint of 95 Å^2 [125]) was then added to the NPs, the particles were placed into an ultrasonic bath at room temperature for 5 minutes, and then placed onto a rotary shaker overnight to allow the ligand exchange to go to completion. The resulting dark brown suspension was then washed by consecutive precipitation with 10 mL of acetone and resuspension with 1 mL of ethanol 3 times. In the final washing step after the acetone was removed, the particles were resuspended in deionized water (1 mL) and vortexed for 1 min, the sample was then placed onto a rotary shaker for a further hour. Prior to analysis, this water-stabilized sample was diluted 1:5 with deionized water, placed into a centrifuge at 16,100 rcf for 5 mins to remove agglomerates, and DLS data shows that the final water stabilized suspension is monodisperse and has a hydrodynamic diameter in the expected range (~35 nm for cubes with an edge length of 16 nm by TEM analysis). This phase-transfer method is highly successful with dispersible yields in water of above 90% following phase transfer.

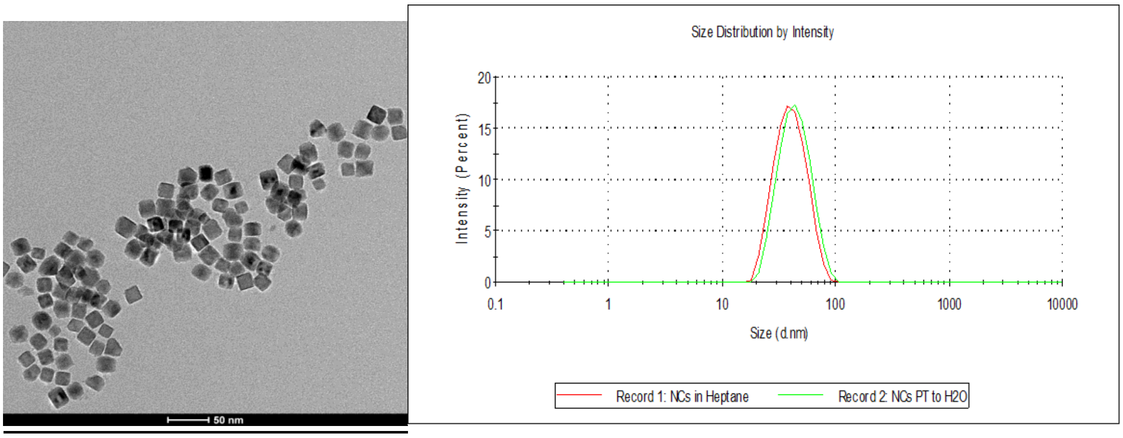

Figure 5. 24: TEM of Cubic NPs phase transferred to water using Ligand 1, there is no apparent agglomeration and no change in NP size observed by TEM. The samples were found to be colloidally stable in water for at least 3 months, d_{TEM} = 17.7 ± 0.5 nm (left), d_{hyd} =37.8 nm in heptane, d_{hyd} = 41.2 nm in H_2O, PDI < 0.1 for both samples (right).

TEM analysis of the phase-transferred NPs correlates well with the DLS results obtained, there was no indication of agglomeration on the TEM grid, NPs appear reasonably well dispersed and there was no obvious change in NP size or polydispersity, as compared to imaging before phase transfer.

5.5. Investigation into the Magnetic Resonance Response of Cubic Iron Oxide Nanoparticles

A sample of ultra-small iron oxide nanocubes was successfully prepared by thermal decomposition of iron oleate, (2.2 g of iron oleate, 100 mg of sodium oleate, 375 mg of oleic acid and 22.5 mL of squalene were degassed under vigorous N_2 flow for 2 hr at 120 ^oC, followed by 2 hr at reflux temp, ~300 ^oC). These NPs, as can be seen in Figure 5. 25, were not perfect cubes but rather truncated cubes or faceted spheres, and the shape is much less uniform across the sample compared to the larger cubes discussed in previous sections. It is our hypothesis that the cubic shape of the NPs is less energetically favourable at smaller sizes due to the high surface area: volume produced. However, despite the morphological variance within the sample, this sample was of interest in terms of its magnetic resonance properties as it has a similar d_{TEM} and d_{hyd} to NPs prepared by the surfactant free Pinna approach discussed in Chapter 3 (1 g of iron acetylacetonate, and 20 mL of benzyl alcohol, heated to reflux, ~200 ^oC, for 7 hr), i.e. d_{TEM} = 8.6 nm, d_{TEM} = 8.2 nm for spheres and cubes respectively.

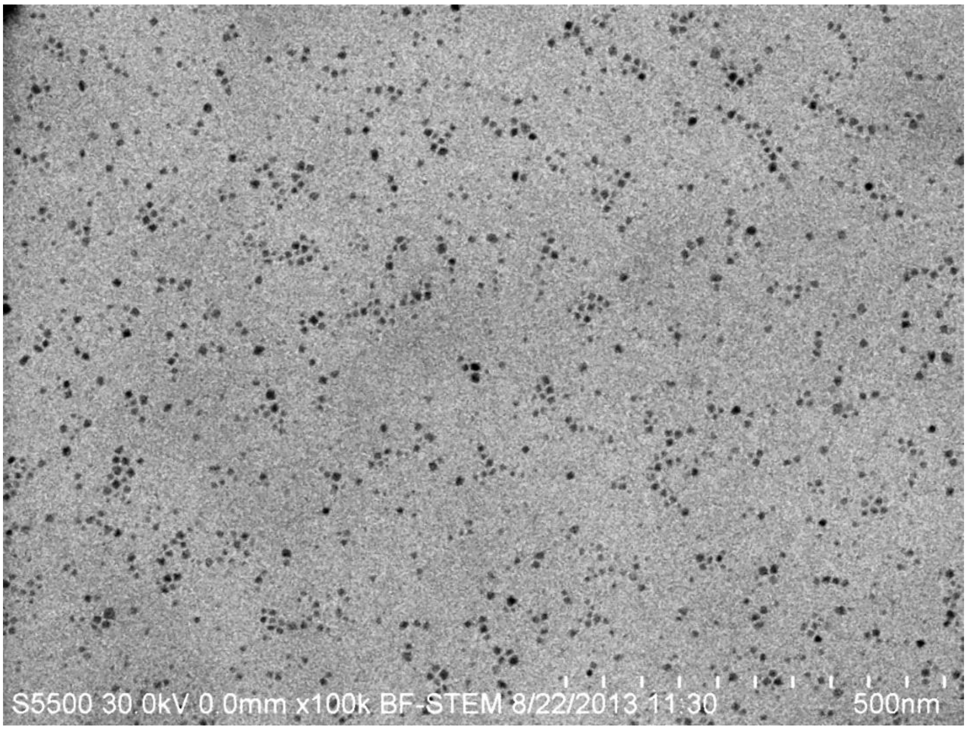

Figure 5. 25: Nanocubes prepared by surfactant assisted thermal decomposition of iron oleate (2.2 g of iron oleate, 100 mg of sodium oleate, 375 mg of oleic acid and 22.5 mL of squalene were degassed under vigorous N_2 flow for 2 hr at 120 °C, followed by 2 hr at reflux temp, ~300 °C), with a similar total volume to the NPs prepared by the Pinna Method. d_{TEM} = 8.2 ± 2.1 nm, (edge length = 5.8 nm, assuming perfect cubes).

Two samples were analysed by NMRD using the approach described in Chapter 2. A quasi-cubic NP sample prepared by surfactant assisted thermal decomposition of iron oleate in heptane (8.2 ± 2.1 nm); and a spherical NP sample prepared by surfactant free thermal decomposition of iron acetylacetonate and stabilized with oleic acid in heptane (8.6 ± 1.8 nm), both samples were analysed at a concentration of ~2 mM and a volume of 1 mL and were found to be stable to a 1 T magnetic field by both DLS and NMRD. T_1 analysis was performed over the range 100 kHz – 40 MHz with 45 frequencies analysed. T_2 analysis was performed at 16.3 MHz and at 60 MHz (equivalent to 1.5 T, in the clinical MRI range).

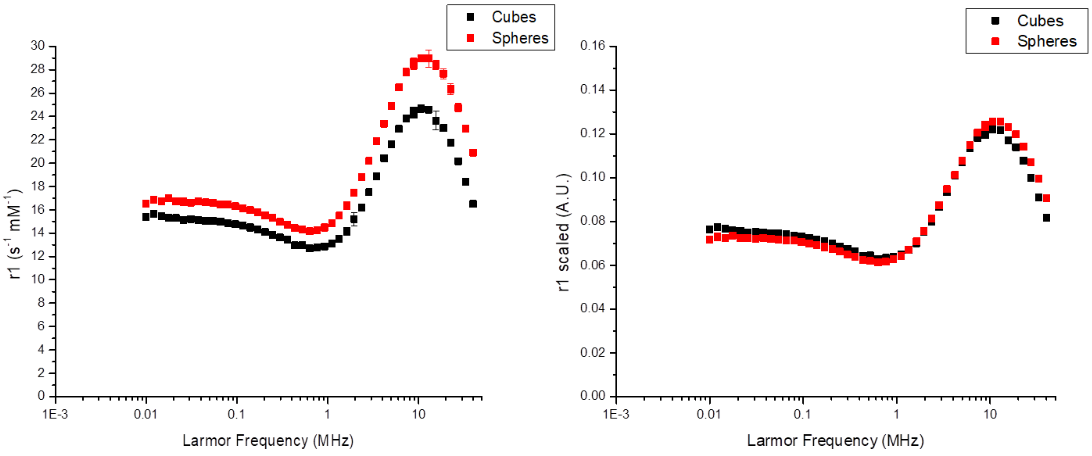

Figure 5. 26:   NMRD r_1 relaxivity profiles, comparison between spherical NPs prepared by surfactant free thermal decomposition of iron acetylacetonate (8.6 ± 1.8 nm), and quasi-cubic NPs prepared by surfactant assisted thermal decomposition of iron oleate (8.2 ± 2.1 nm) (left), [both in heptane]. (Right) the NMRD r_1 relaxivity profiles obtained were scaled by NP surface area (based on TEM diameter/edge length), it can be seen that the profiles overlay closely once scaled, indicating that the magnetic response of the magnetic materials is not directly related to either NP synthesis type, or NP shape. Both samples were found to be stable to the magnetic field by both NMRD and DLS analysis.

The overall shape of the recorded profiles indicates that these NPs are superparamagnetic, due to the presence of an r_{1max} and a “dip” in the profile at a slightly lower field to the r_1 max, the NP suspensions also demonstrate stability on exposure to the magnetic field (~1 T) further indicating the superparamagnetic nature of the suspensions. This stability is determined by the single frequency measurement point of

T_1 at a given Larmor frequency, in this case 40 MHz, prior to and immediately following profile acquisition. If sedimentation occurs during profile acquisition the T_1 value will increase. It should be noted that the sample was not removed from the instrument following profile acquisition until this stability check has been performed, to minimize agitation to the sample, and that the profile acquisition process takes 0.75 - 3 hr, at a range of fields up to 1T, depending on sample concentration. It can also be seen that the shape of the NPs does not appear to have a significant impact on the overall shape of the profile recorded. Also, the type of synthesis (surfactant free vs. surfactant assisted) used to prepare the nanoparticles does not appear to have impacted the profile obtained, suggesting a similar oxide phase. It can be seen in the left-hand plot that the overall shape of the NMRD profiles is unchanged, however there appears to be a suppression in r_1 for the cubic NPs over the whole profile. The right-hand graph is interesting, as the NMRD responses were scaled by the total surface area of the NPs (assuming perfect spheres and perfect cubes respectively) and it can be observed that the scaled signals directly overlap.

These results are surprising as they indicate, for this size of cubic NP at least, that the ΔE_{anis} is similar in both cases. This suggests that, contrary to expectation, the shape of the NPs (the presence of corners) has not significantly altered the dynamics of the magnetic moment. For cubes the availability of different “easy axes” is expected to dominate, but in fact only the total surface area appears to matter. This result is promising for the potential further assembly of the cubic NPs prepared by surfactant assisted thermal decomposition of iron oleate as it indicates that the magnetic response of the individual nanoparticles is not significantly different, the NPs are in the superparamagnetic regime and may not experience uncontrolled agglomeration due to increased interparticle interactions. Trials into the further assembly of nanocubes will be discussed in Chapter 6. It should be noted again that these NMRD measurements were performed in heptane, it remains to be seen whether this behaviour would also be observed in aqueous suspensions. Phase transfer of the materials has been completed, however the instrument is currently not accessible. Encouragingly, it has also been previously reported by the group, that the magnetic response of NPs prepared by surfactant free thermal decomposition (Pinna NPs) is largely unchanged when measured in aqueous suspensions compared to heptane, which was the fundamental reasoning for using heptane as the solvent for this analysis.

5.6. Surfactant Free Thermal Decomposition of Iron Acetylacetonate in the Presence of Sodium Salts

While NP synthesis by surfactant-assisted thermal decomposition has been shown to produce highly crystalline, nanoparticles with the desired cubic morphology, a surfactant-free approach to preparation of cubic nanoparticles would be better for the purposes of further stabilization and controlled assembly of the nanoparticles by PMA due to the difficulties in assessing oleic acid concentration on the surface of the NPs and need for controlling the ratio of oleic acid to polymer, as described in Chapter 3. To date, no such approach has been published.

A key factor in the preparation of cubic iron oxide appears to be the presence of Na^+ ions in the reaction vessel during thermal decomposition. It is believed that this encourages the growth of the particles in the {100} plane, forming facets and ultimately giving the particles their cubic morphology. There are a wide range of Na salts that could potentially be used, from simple NaCl and sodium citrate, to sodium oleate and sodium acrylate. Initially NaCl was chosen as Cl^- ions are very weakly binding and if at all, sodium oleate was avoided, along with any other potential ligand anions.

5.6.1.1. Preliminary Experiments

In a typical synthesis, 1.0 g (2.8 mmol) of iron (III) acetylacetonate, and 0.1 g (1.7 mmol) of NaCl were added to a three-necked round bottomed flask with 20 mL of benzyl alcohol. This mixture was degassed under N_2 for 15 min, and then heated to reflux temperature (~200 °C) where it was held for 7 hours. The resultant black suspension was allowed to cool and was stored as synthesized under N_2 until required. Further stabilization of the nanoparticles with oleic acid to prepare heptane suspensions, and with APTES to prepare water suspensions were performed following the method described in Chapter 3 for spherical NPs.

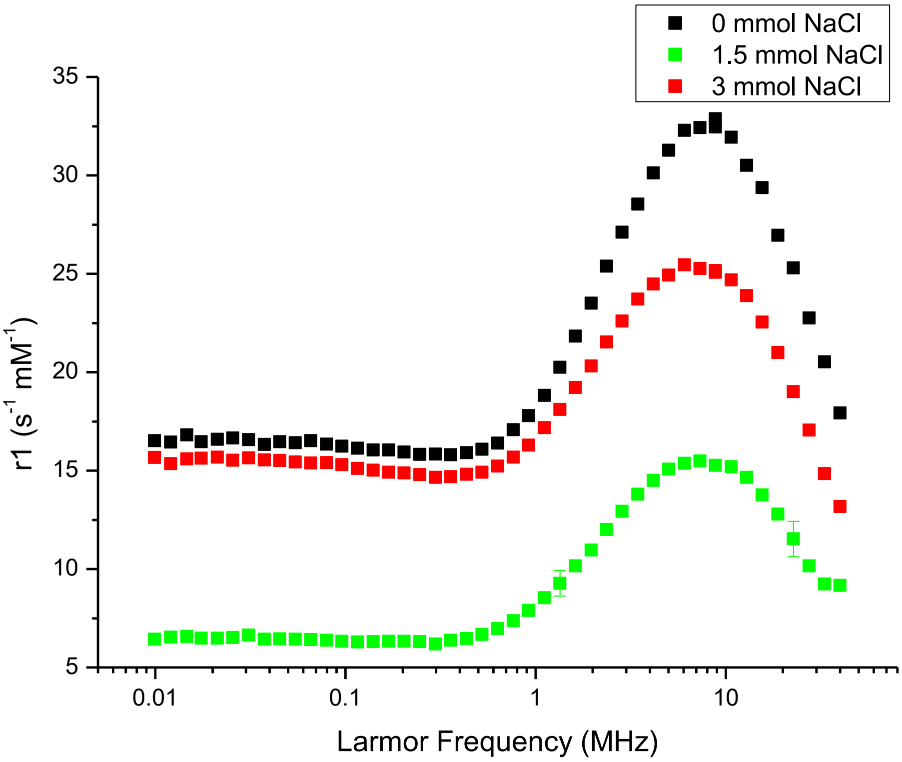

Figure 5. 27: NMRD profiles extracted from analysis of NPs, stabilized in heptane, prepared with 0 mmol, 1.5 mmol and 3 mmol NaCl added into a standard 1 g (2.8 mmol) iron acetylacetonate thermal decomposition reaction respectively. A distinct change in the profile is observed, however no simple trend is apparent.

Figure 5. 27, above, shows the NMRD profiles extracted from 3 samples prepared by thermal decomposition of iron acetylacetonate (1g) in 20 mL of benzyl alcohol. The profile in black represents these NPs, while the samples represented by green squares and red squares represent sample prepared with the addition of NaCl to the reaction mixtures prior to thermal decomposition, 0.09 g and 0.19 g respectively. The overall shape of the NMRD profile is as expected for NPs prepared by the Pinna method, there is a superparamagnetic response, an observable r_{1max} value and a convergence of the r_1 values at higher Larmor frequency. It is apparent that the NPs are well dispersed, and it should be noted that there was no indication of aggregation in the magnetic field by NMR and DLS. It is clear from the above NMR data that there is a distinct change in

the magnetic response of the materials prepared with the addition of NaCl in the thermal decomposition. However, it is not a simple scaling, the profile does change shape.

It is interesting to note that the NaCl added during the thermal decomposition stage did not fully dissolve during the reaction and could be observed in the washing steps as whole crystals. This is an issue for the thermal decomposition method, as any undissolved material present in the reaction vessel may act as a nucleation site for the nanoparticles, potentially leading to multimodal distributions of NPs, and as the NaCl crystals are not uniform in size or morphology this may contribute to a higher degree of polydispersity and differences in the NP morphology of produced materials. As the NaCl is not completely soluble in benzyl alcohol, the amount of free Na^+ ions in the reaction mixture may not be reproducible from batch to batch, (due to a changing total available surface area of NaCl crystals). The hypothesis that total available surface area of NaCl crystals results in a change in both the morphology and the magnetic resonance behaviour of the NP suspensions produced was investigated and is demonstrated by the following experiments.

5.6.1.2. Analysis of the Effect of NaCl Crystal Size on the Morphology and NMRD Response of NPs Prepared by Thermal Decomposition of Iron Acetylacetonate

A sample (~20g) of NaCl crystals were ground to a fine powder using a mortar and pestle, and stored for further syntheses. In each test, two syntheses were performed concurrently, one with the coarse NaCl crystals and the other with finely ground NaCl. In each synthesis 1 g (2.8 mmol) of iron acetylacetonate was dissolved in 20 mL of benzyl alcohol and the appropriate amount of NaCl was added (1 mmol, 2 mmol, 3 mmol). The mixtures were then heated to reflux (~200 ^{o}C) and held at this temperature for 7 hours. The resultant black liquor was washed by precipitation with acetone 3 times and then stabilized with oleic acid in heptane for further analysis. It can be seen from the data below, Figure 5. 28, Figure 5. 29, and Figure 5. 30, there is a significant difference in the outcomes of preparations with and without the addition of NaCl.

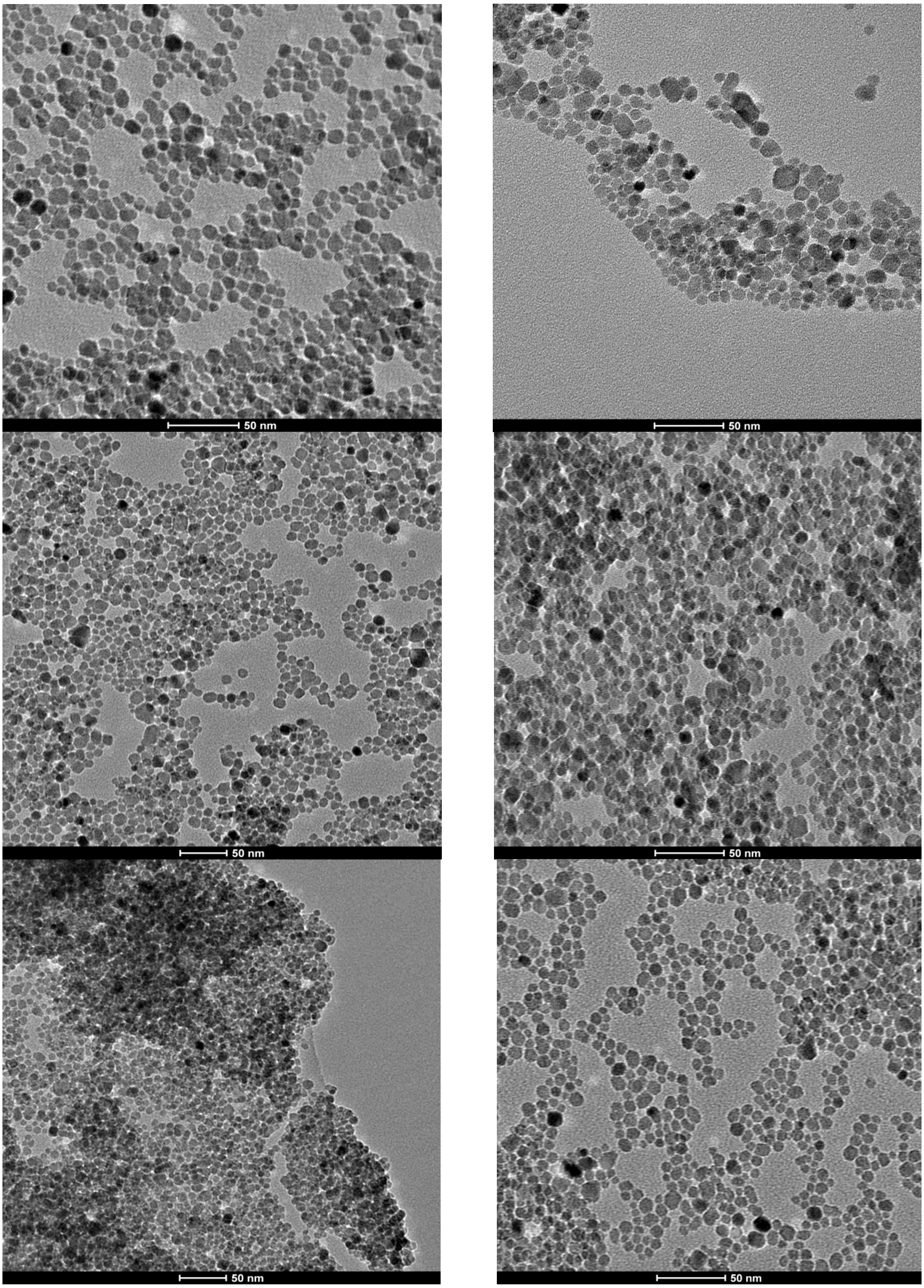

Figure 5. 28: TEM analysis of the NaCl Pinna syntheses, 1 mmol of coarse NaCl (top left), 1 mmol of fine NaCl (top right), 2 mmol of coarse NaCl (middle left), 2 mmol of fine NaCl (middle right), 3 mmol of coarse NaCl (bottom left), 3 mmol of fine NaCl (bottom right). It can be seen that the NPs are not cubic, however there is a higher degree of facet formation, if small, in all cases, when compared to the standard, surfactant free thermal decomposition approach.

The images produced by TEM analysis of the samples suggest that the approach is promising, while the overall shape of the NPs is not cubic, there is an increase in visible facet formation on the nanoparticle surface. There is also an increase in the polydispersity of the NPs, this may be related to the presence of extra (NaCl) surfaces. Additionally, in some cases the NP size (d_{TEM}) has changed significantly however there is no obvious correlation between preparation conditions and the NP sizes as indicated in Figure 5.29.

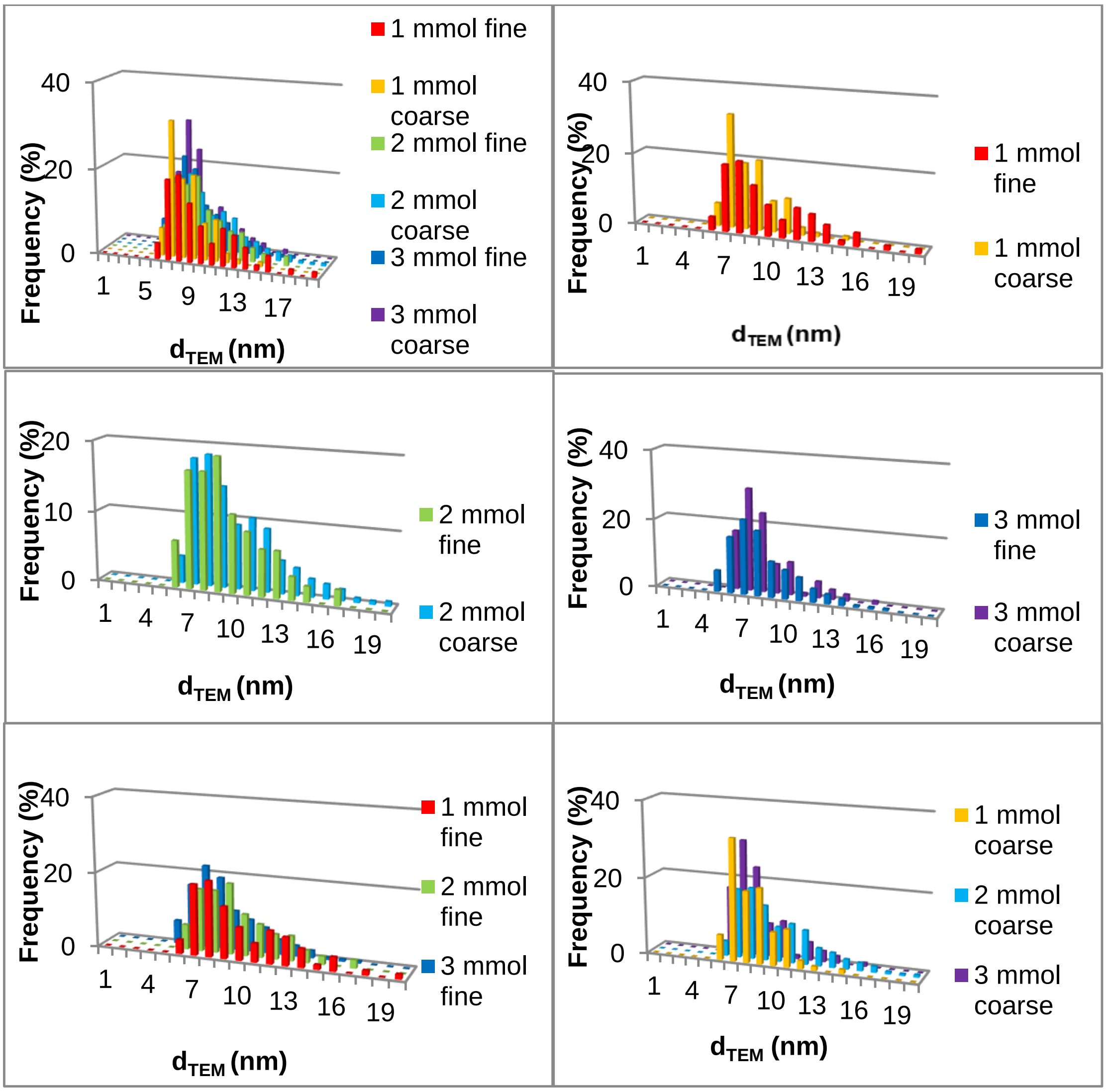

Figure 5. 29: Histogram depiction of NP diameters, as determined by TEM, produced by each of the NaCl Pinna reactions described above. It can be seen that the peak of the NP size distributions is not consistent between syntheses and that polydispersity is relatively high (~25%). The d_{TEM} values recorded were 9.0 ± 2.3 nm; 8.1 ± 1.6 nm; 9.2 ± 2.4 nm; 9.3 ± 2.5 nm; 7.9 ± 2.0 nm; and 7.5 ± 1.3 nm for the samples prepared with 1 mmol fine salt, 1 mmol coarse salt, 2 mmol fine salt, 2 mmol coarse salt, 3 mmol fine salt, and 3 mmol coarse salt in the synthesis respectively. All samples were prepared with 1 g of iron acetylacetonate and 20 mL of Benzyl Alcohol and refluxed for 7 hr. (Top right is an overlay of all samples, following this the histograms have been presented by NaCl concentration, and an overlay of the samples prepared using 3 concentrations of NaCl respectively, in both its coarse form and finely ground.

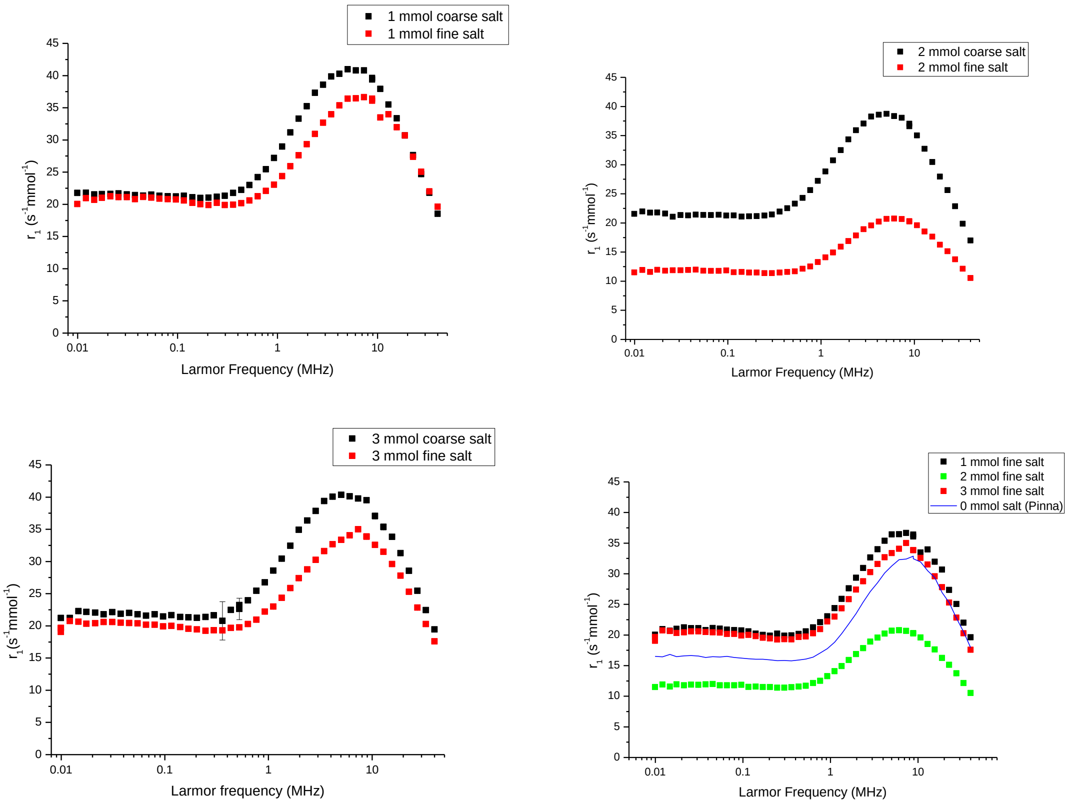

Figure 5. 30: NMRD profiles of NPs, in heptane, prepared using coarse and fine NaCl crystals over a range of NaCl concentrations.1mmol of NaCl (top left), 2 mmol NaCl (top right), 3 mmol NaCl (bottom right) and an overlay of the NP magnetic resonance responses for 0 mmol, 1 mmol, 2 mmol, and 3 mmol of fine NaCl (bottom right). It is clear that the change in NaCl surface area has a distinct impression on the magnetic response of the NPS produced (all samples were stabilized with oleic acid in heptane). The d_{TEM} *values recorded were 9.0 ± 2.3 nm; 8.1 ± 1.6 nm; 9.2 ± 2.4 nm; 9.3 ± 2.5 nm; 7.9 ± 2.0 nm; and 7.5 ± 1.3 nm for the samples prepared with 1 mmol fine salt, 1 mmol coarse salt, 2 mmol fine salt, 2 mmol coarse salt, 3 mmol fine salt, and 3 mmol coarse salt in the synthesis respectively.*

The NPs prepared with NaCl in the reaction mixture were then analysed by NMRD to investigate the effect of additional exposed surface area of NaCl in the reaction mixture. r_1 profiles were acquired over a range of Larmor frequency from 100kHz to 40 MHz, and are shown in Figure 5. 30. It can be seen clearly Figure 5. 30 that the increased surface area of NaCl available during the reaction results in a significant suppression in the r_1 signal particularly in the range 500 kHz – 20 MHz. There is also an apparent shift of r_{1max} to higher frequency, this is consistent with smaller NPs, although this shift is small and could possibly be attributed to the slight change in d_{TEM} observed between the samples prepared with coarse as opposed to finely ground NaCl. Suppression of r_1 was not expected to be as significant considering the quasi-spherical nature of the NPs produced. It is expected that NaCl with an even smaller crystal size (larger available surface area) would have further impact on both NP morphology and magnetic resonance properties. It is not clear whether there is any significant salt ionization in the reaction mixture, as the NaCl crystals do not dissolve during the reaction, however there is clearly a surface related affect, this indicates that some ionization is likely occurring, however the degree of ionization is likely to be different for each individual crystal. It should be noted that the NMR profiles were not reproducible with consecutive samples prepared under the same conditions, it is believed that this is due to the variation in NaCl crystal sizes and surface area between preparations.

As the available surface area of the Na^+ containing additive clearly affects the morphology and magnetic response of the NPs produced, a Na^+ salt with solubility in the reaction solvent would be preferable. A solubility test was performed on a number of sodium salts, to investigate if a more suitable candidate could be found. None of the materials tested had significant solubility in benzyl alcohol, with the exception of sodium oleate. A further approach was undertaken by preparation of sodium acetylacetonate. By incorporating Na(acac) as the source of sodium in the surfactant free thermal decomposition method, there would be no additional surfactants produced during the reaction, as acetylacetonate is already present from the iron precursor, thus it was determined to be the most likely candidate for a successful preparation of cubic nanoparticles by a surfactant free, thermal decomposition method.

5.6.2. Synthesis of Sodium Acetylacetonate

4 g (0.1 mol) of NaOH was dissolved in 5 mL of deionised water and added to 20 mL of methanol in a beaker. The NaOH solution was then added slowly to a conical flask containing 10 mL (0.098 moles) of acetylacetone. The mixture was shaken gently, then stoppered and cooled on ice for a minimum of 2 hours. The resulting white precipitate was filtered under vacuum and washed with a small volume of ice-cold methanol. The white filtrate was then dried in a vacuum oven at 80 °C for 3 hours. The powder was then transferred to a suitable glass container and stored at ambient temperature.

5.6.3. Thermal decomposition of Iron Acetylacetonate in the presence of Sodium Acetylacetonate

The thermal decomposition of iron acetylacetonate was performed as outlined in Chapter 3 with the addition of 0.25 g (2 mmol) of sodium acetylacetonate. The resultant black liquor was cleaned 3 times with acetone and a portion of the NPs produced were stabilized with oleic acid in heptane for TEM analysis, shown in Figure 5.31, below.

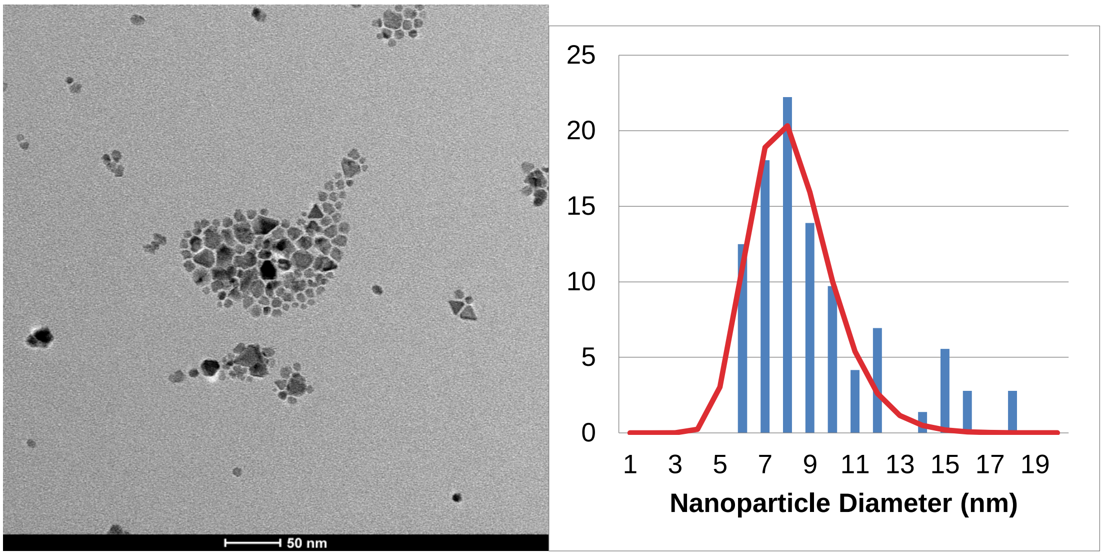

Figure 5. 31: A selection of TEM images and TEM data analysis of NPs prepared by the thermal decomposition of iron acetylacetonate in the presence of sodium acetylacetonate. It can be seen that some facet formation is observed however the particles produced are amorphous and polydisperse. D_{TEM} = 8.25 nm ± 1.83 nm.

As with the sodium chloride assisted thermal decomposition preparations an increased presence of facets was observed, however there does not appear to be sufficient control over the NP synthesis. This may be due to the absence of a surfactant, or due to the decreased reaction temperature compared to the majority of surfactant assisted thermal decomposition syntheses. There is some potential for the further development of a surfactant free thermal decomposition preparation of cubic iron oxide nanoparticles; however, this was not performed due to the lack of availability of a high purity iron acetylacetonate source after June 2016.

5.7. Chapter Conclusions

Ultimately our aim of generating a library of particles and synthesis conditions for well-defined NP sizes and morphology was not met; however, significant progress was made in identifying the difficulties associated with the preparation of cubic nanomaterials with superparamagnetic properties.

The proposed surfactant-free method for the generation of cubic nanoparticles would provide significant advantages towards the assembly process. However, issues with solubility of the Na salts in the reaction mixture, or the formation of stabilized materials such as those prepared with sodium citrate and sodium oleate, make this approach less attractive. Issues also arise with size control. A NP with reasonably reproducible size of approx. 8.5 nm can be achieved easily using this method. A multi-step, core shell approach, as outlined for spherical NPs in Chapter 3, may possibly be used to create a larger sized particle. However, this approach results in secondary nucleation and no significant increase in size.

Surfactant-assisted thermal decomposition on the other hand provides materials with high crystallinity and desired magnetic resonance properties. However, it was found that these approaches are hard to reproduce and there were difficulties with size control. In the case of iron (III) acetylacetonate, too many variables appear to affect the synthesis, and whether or not the synthesis will even produce particles, as discussed in Section 5.2. This coupled with the recent loss of a reliable source of high quality precursor; makes this method of nanoparticle synthesis less attractive.

Surfactant assisted thermal decomposition of iron oleate, while not a perfect method for the reproducible preparation of nanocubes is, therefore, the optimum method for the production of highly cubic NPs for assembly by PMA for biomedical applications, at this time. While iron oleate itself, seems to resist purification and is not a reliable precursor, it is possible to scale up the production of NPs significantly enough for assembly and analysis purposes, and there is no indication that the procedure cannot be further scaled.

The final Chapter in this thesis describes the assessment of iron oxide nanocubes prepared by the thermal decomposition of iron oleate, as nanomaterials for colloidal assembly using pluronic F127. The difficulties associated with the use of pre-stabilized material and the potential to assemble cubes in a controlled manner will be described.

Chapter 6: Towards the Application of Polymer Mediated Assembly to Cubic Nanoparticles

6.1. Introduction

The effect of the PMA process on the magnetic resonance properties of spherical nanoparticles was highlighted in Chapter 4. As cubic iron oxide nanoparticles are expected to have better magnetic resonance properties to their spherical counterparts, the application of the PMA method outlined in Chapter 3 to the cubic nanomaterials developed in Chapter 5 is the obvious next step. Some challenges are expected in the application of this method primarily due to the synthesis protocol used to prepare the nanocubes. Surfactant assisted thermal decomposition of iron oleate under optimized conditions, results in highly monodisperse, cubic NPs with an uncontrolled surface coating of oleic acid which allows them to be colloidally stable in a range of organic solvents.

The amount of oleic acid on the surface of the NPs relative to the amount of polymer added during the assembly process was shown in Chapter 3 to influence the controllability and reproducibility of the assembly process, therefore in the generation of highly controlled assemblies of cubic NPs a protocol must first be designed, to determine the concentration of oleic acid in the NP suspensions. This was attempted by a number of approaches, thermogravimetric analysis (TGA), UV-Vis Spectroscopy, and a HPLC assisted UV-Vis method. Following estimation of oleic acid on the surface of the NPs, assembly was attempted, and analysis of the resulting clusters is reported.

6.2. Estimation of the Surfactant Concentration in Cubic NPs Prepared by Thermal Decomposition of Iron Oleate

The small sample size and the low concentration of oleic acid required for the PMA process necessitate the use of techniques with high sensitivity and specificity. Thermogravimetric analysis (TGA) was the preferred choice given the sensitivity of the technique (only 10 mg of sample is required for an analysis) and the specificity, as the surfactant's boiling temperature is known it is possible to quantify the mass of surfactant relative to the mass of NPs and hence the concentration in a suspension, or the relative surface equivalent volume. Additionally, an alternative technique was attempted, UV-Vis Spectrometry as this technique is much faster and lower cost than the TGA analysis.

6.2.1. Thermogravimetric Analysis

Cubic NP samples in heptane, prepared by the thermal decomposition of iron oleate in the presence of sodium oleate and oleic acid as outlined in Chapter 5, were dried in a vacuum oven at 80 ^{o}C overnight. 10 mg of each sample was required for analysis, and this was placed into a platinum weighing boat. This weighing boat was then heated by the TGA instrument and the change in mass was determined using an empty reference cell under the same conditions. The sample was heated at a rate of 5 ^{o}C per min from 25 ^{o}C to 700 ^{o}C and the change in mass was recorded.

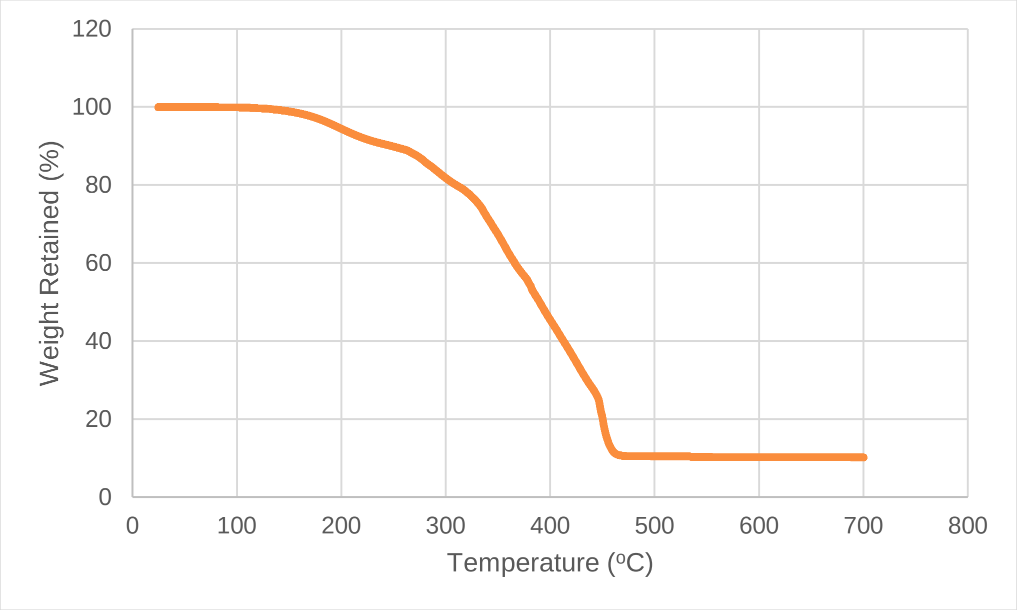

Figure 6. 1: Thermogravimetric analysis of cubic NPs prepared by thermal decomposition of iron oleate.

It can be seen from this analysis that a decrease of mass is observed at 120 °C, which can be attributed to volatiles such as residual solvent, a more major decrease is observed at 260 °C which can be associated with the evaporation of physisorbed oleic acid, total degradation of oleic acid begins at ~ 320 °C. Any further degradation above a temperature of 450 °C is not considered to be due to oleic acid as the boiling point of oleic acid is 360 °C. The relative mass of oleic acid to iron oxide was then calculated, and with a known NP size and concentration the relative surface coverage of oleic acid on the surface of the NPs can also be determined. One major disadvantage to this method of analysis is that trace amounts of residual squalene cannot be observed or quantified as they will be removed at a similar temperature to oleic acid (BP of squalene = 320 °C)

6.2.2. UV-Vis Spectrometry

While TGA is a useful technique for determining oleic acid in an NP sample, it is a very slow determination and thus alternative techniques were explored to improve the efficiency of OA determination, and to speed up the overall assembly process. UV-vis Spectroscopy was chosen as a potential technique as it is a rapid test, highly controlled and highly reproducible. Oleic acid has a small yet distinct UV-Vis peak at 269 nm as shown in Figure 6. 2, below, thus this technique was deemed suitable. As iron oxide is a black-brown colour even at low concentrations, it was decided that the NPs should be dissolved by acid digestion prior to analysis, allowing for a higher degree of sensitivity. 1 M hydrochloric acid was chosen to dissolve the NPs as iron oxide will degrade completely in HCl while the oleic acid will be unaffected. 1 mL of NPs in squalene was washed 3 x with 10 mL aliquots of acetone and centrifugation at 16,100 rcf, before redispersion in 200 µL of THF for ease of transfer. The entire sample was transferred to a 50 mL volumetric flask and the THF was allowed to evaporate. 1.5 mL of 1M HCl was then added to the flask and the NPs allowed to digest at room temperature for 30 mins, the flask was then made up to the mark with methanol. A series of oleic acid standards were prepared in the range 1-10 ppm, 1.5 mL of HCl and a 30 min digestion time was also applied to the standard solutions. The standards and samples were then analysed over the range 200-800 nm using a Varian Cary 50 UV-vis. It can be seen from Figure 6. 2, below that in the case of the standards, an increase in signal is observed in the region of 270 nm as expected. In the case of the NP sample it can be seen that an additional peak is observed above 400 nm which can be attributed to the yellow-orange iron chlorides produced by the digestion process. Unfortunately, it can also be seen that this signal dominates the spectrum below 400 nm making accurate determination of oleic acid, almost impossible.

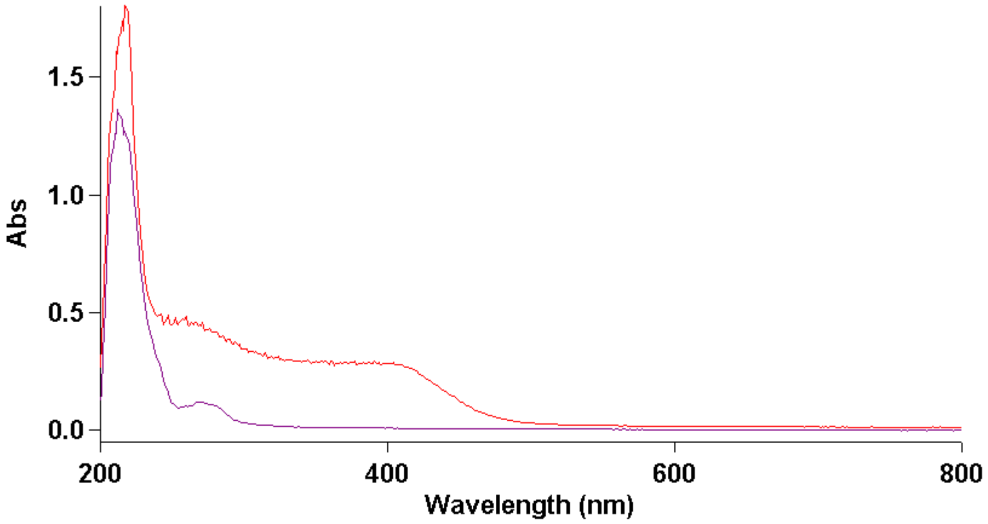

Figure 6. 2: UV-Vis spectrum of oleic acid in methanol (black), a small but distinct peak is observed at 269 nm, and a sample of cubic NPs prepared by thermal decomposition of iron oleate, acid digested and prepared in methanol (red)

As oleic acid only contains one double bond, the UV-Vis absorbance of OA is low, making this technique less sensitive to small changes in the concentration of OA in the NP suspensions. This low sensitivity could be addressed by derivatization of the OA. A number of derivatization methods are available to improve the UV absorbance of organic compounds, however the issue of the iron signal dominating the UV-vis spectrum would also need to be addressed. One possible approach would be to combine the derivatization experiment with a HPLC method (using a UV-vis detector), thus separating the OA signal from all other potential interferences. Alternatively, a technique such HPLC-MS could be used to separate the oleic acid from potential interferences, and may provide useful information without the need for derivatization. At this time method development is ongoing.

The need for multiple stage sample preparation prior to any meaningful quantitation of OA concentration in a sample makes this method less appealing. There is also the need for a higher volume of material to overcome any limits of detection. Thus TGA, while being a slow measurement, may be the most useful for any further analysis of NP suspensions.

6.3. Polymer Mediated Assembly of Cubic NPs

Following the determination of oleic acid concentration on the surface of the NPs, the concentration of the NP stock solution and the NP edge length was determined by ICP-AES and TEM respectively. The concentration of oleic acid was then adjusted so that each sample had a concentration of oleic acid equivalent to 5 times the volume required to completely cover the NP surface, if the sample is monodispersed and that all NPs are perfect cubes. A series of primary NP suspensions was then selected for assembly, prepared by surfactant assisted thermal decomposition of iron oleate using the method outlined in Chapter 5. These samples were separated into 5 categories based on their NP edge length as determined by TEM. The aim of this study was to investigate whether NPs of similar size produced NPCs of similar size and PDI. All NP samples were suspended in heptane, and the DLS, TEM and NMR analysis of the materials was performed in DCU prior to the clustering experiments.

Table 6. 1: Samples selected for assembly with core sizes given in brackets, the samples were divided into 5 groups based on the NP edge length as determined by TEM. Some additional samples were prepared by mixing of two NP samples with similar NP edge lengths (less than 0.5 nm difference between samples). Note the NP source at the time of these experiments was a collaborator in Barcelona, the materials were of a similar nature to those prepared in Chapter 5.

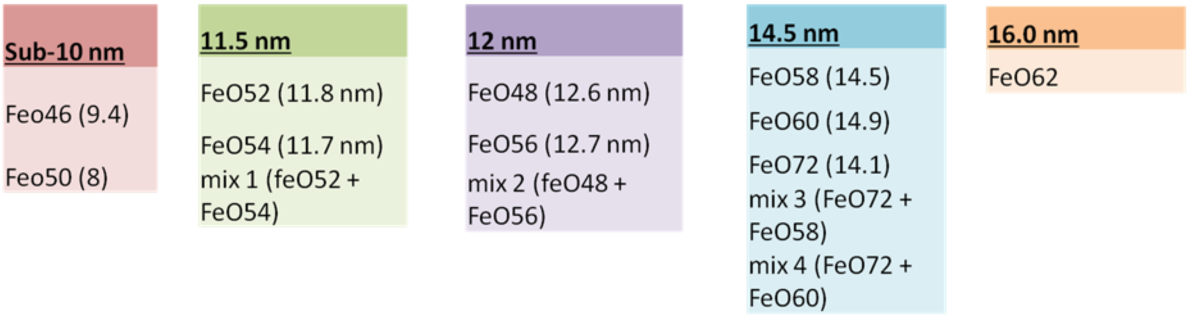

Sub-10 nm	**11.5 nm**	**12 nm**	**14.5 nm**	**16.0 nm**
Feo46 (9.4)	FeO52 (11.8 nm)	FeO48 (12.6 nm)	FeO58 (14.5)	FeO62
Feo50 (8)	FeO54 (11.7 nm)	FeO56 (12.7 nm)	FeO60 (14.9)	
	mix 1 (feO52 + FeO54)	mix 2 (feO48 + FeO56)	FeO72 (14.1)	
			mix 3 (FeO72 + FeO58)	
			mix 4 (FeO72 + FeO60)	

The oleic acid stabilized suspensions were prepared at a concentration of 56 mM in THF and, a series of clustering experiments was performed as follows. In a typical experiment 1 mL of NP suspension in THF was added to 2 mL of pluronic F127 (64 µM), in a 7 mL glass vial, the sample was then allowed to evaporate over 48 h on a rotary shaker, until all traces of THF had been removed. This experiment was repeated using 2, 3, 4, and 5 mL of NP stock suspension for a total of 5 assembly experiments per NP sample.

Table 6. 2: Results of the assembly experiments, the number provided in the table is d_{hyd} as determined by DLS measurement. In each case 3 measurements were taken to ensure that the samples were not precipitating over the course of the measurement. The symbol – has been used to denote samples that fell outside of tolerable limits, either by having a PDI greater than 0.15, or by having a dispersible yield of less than 1%

Sub-10 nm	**1**	**2**	**3**	**4**	**5**
Feo46 (9.4)	120.4	201.2	216.3	-	-
Feo50 (8)	148.4	113.7	195.6	232.9	255.6

11.5 nm	**1**	**2**	**3**	**4**	**5**
FeO52 (11.8 nm)	178	155.1	200.5	-	-
FeO54 (11.7 nm)	190.7	142.2	-	-	-
mix 1 (feO52 + FeO54)	162.8	-	-	-	-

12 nm	**1**	**2**	**3**	**4**	**5**
FeO48 (12.6 nm)	141.8	138.8	212.5	-	-
FeO56 (12.7 nm)	190.3	189.5	253.6	-	-
mix 2 (feO48 + FeO56)	179.9	154.8	258.3	-	-

14.5 nm	**1**	**2**	**3**	**4**	**5**
FeO58 (14.5)	195.1	161.9	-	-	-
FeO60 (14.9)	181.5	154.1	-	-	-
FeO72 (14.1)	144	-	-	-	-
mix 3 (FeO72 + FeO58)	182	136.9	198.8	-	-
mix 4 (FeO72 + FeO60)	177.1	143	-	-	-

16.0 nm	**1**	**2**	**3**	**4**	**5**
FeO62	223.1	223	108.9	-	-

It can be seen from the above data that there is no reproducibility in size between NPCs prepared under the same conditions but with primary NPs from a different synthesis. It can also be seen that there is no indication of controllability of the assembly, with NPC sizes having no correlation to the preparation conditions or the NP size used. This lack of reproducibility and control may be due to a number of reasons, the interparticle interactions may be altered due to the difference in NP shape, the TGA analysis may not be selective enough for an accurate OA determination, or most likely there may be residual squalene interacting with the NP surface effecting the assembly process, even in low volumes this could cause major interferences due to the highly sensitive relationship between oleic acid and polymer in the assembly process. Squalene is difficult to remove with solvent washing, even from glassware, and would go undetected by TGA analysis as it has a boiling point of 300 °C, so would overlap with the OA decomposition temperature. Also, as shown in Chapter 3, oleic acid concentration must be highly controlled, as any interferences remove the controllability and reproducibility of the assembly process. Despite this lack of reproducibility and controllability, a wide range of NPC samples were sucessfully prepared and as further analysis was performed to determine what effect, if any, assembly had on the magnetic resonance properties of these NPs.

TEM analysis was performed to determine the nature of the NPCs, as outlined in Chapter 4, it is believed that in controlled assembly PMA-NPCs have a densely packed outer shell with a hollow/less dense centre. It can be seen from the images acquired, Figure 6. 3, that the PMA-NPCs produced using cubic NPs were much less ordered than those reported in Chapter 3. The NPCs were not densely packed, as shown in Figure 6. 3, with many NPCs containing quite a small number of NPs.

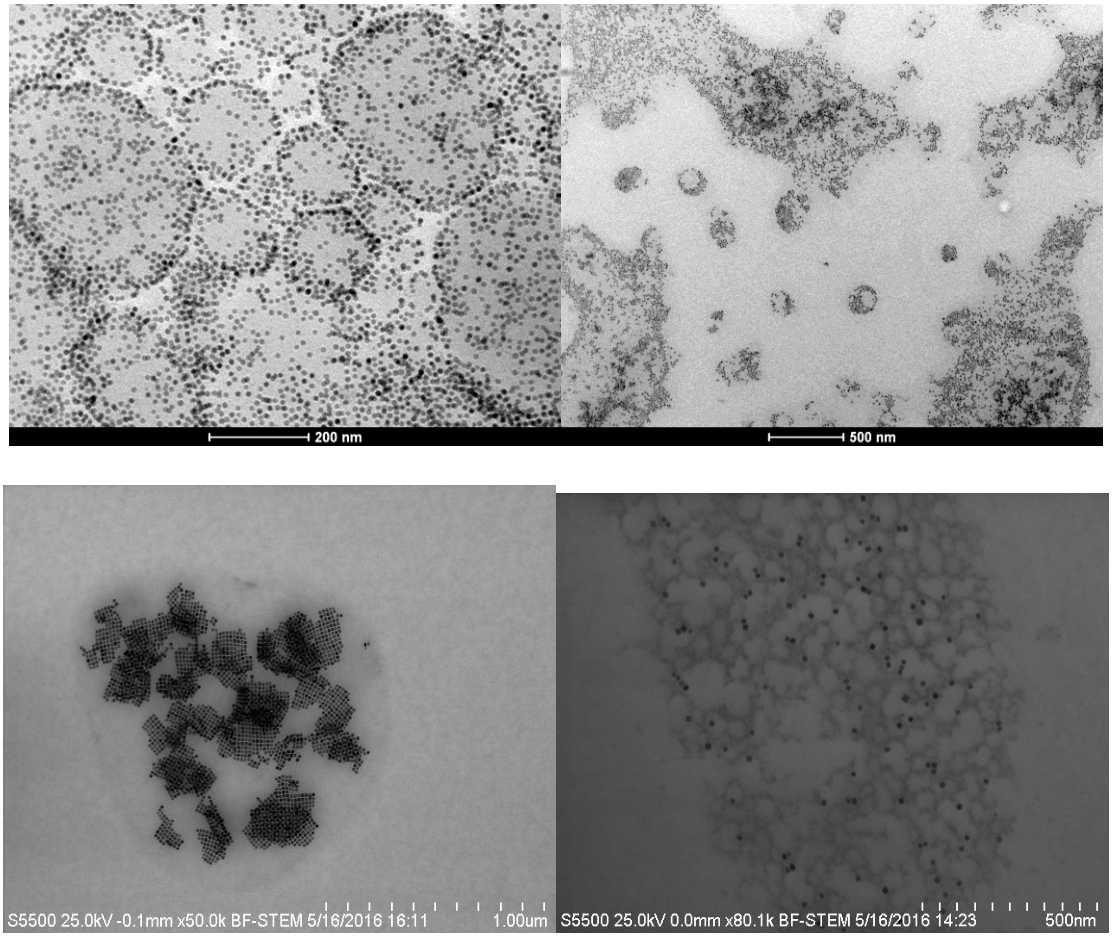

Figure 6. 3: TEM analysis of PMA-NPCs prepared with cubic NPs (prepared by surfactant assisted thermal decomposition of iron oleate.

Interestingly, despite the low concentration of NPs per NPC, the images obtained appear to correlate well with our previous findings on PMA-NPC architecture and ordering. In particular the image top left of Figure 6. 3, on first glance it appears as though the NPCs are flat, and that there is a multimodal distribution. The image top right of Figure 6. 3 also shows evidence of sample collapse with a large section of overlapping amorphous collections of NPs. This is probably the result of drying effects on the introduction of the samples to the vacuum of the TEM analysis chamber. As the number of NPs is low NPC collapse is more likely, due to the soft nature of the polymers used for assembly. The NPCs that are visible, appear to have a higher concentration of NPs at the perimeter of the NPC indicating that they may have been located in the NPC outer shell, with a hollow centre. The bottom left image also shows evidence of cluster collapse, as the NPs are contained in single sheets rather than overlapping.

While the PMA process did not provide us with the materials that we desired for further analysis, a large volume of material, which was colloidally stable and monodisperse in suspension as indicated by DLS, was available. Two sets of PMA-NPCs were selected to investigate the effect of clustering on the magnetic resonance properties of the NPs. For further reference the sample names were changed from those used to identify the specific NP synthesis, to the formula NPC, NPC diameter, NP edge length (e.g. NPC_110_8). The two sets represent:

- NPCs of the same size prepared with different NP sizes, NPC_145_8; NPC_145_11.7 and NPC_145_14.1; and
- NPCs of different sizes prepared with NPs of the same size, NPC_110_8; NPC_145_8; and NPC_200_9.4.

NMRD analysis of the samples was performed over a ^{1}H Larmor frequency range of 100 kHz – 40 MHz, all samples were in aqueous suspension and were monodisperse by DLS (PDI < 0.15), with a concentration of approximately 2 mM. It should be noted that while all NPC samples analysed fell under acceptable criteria by DLS, TEM clearly shows that the number of NPs per NPC is not consistent. Hence, caution should be used in comparing NMRD profiles. It should also be noted that the profiles were recorded on a similar instrument to the one used in all previous MRD analyses, but in a collaborator laboratory in Germany, as the Relaxometer in our Group was unavailable. The instrument used was of the same make and model, and operated under the same conditions.

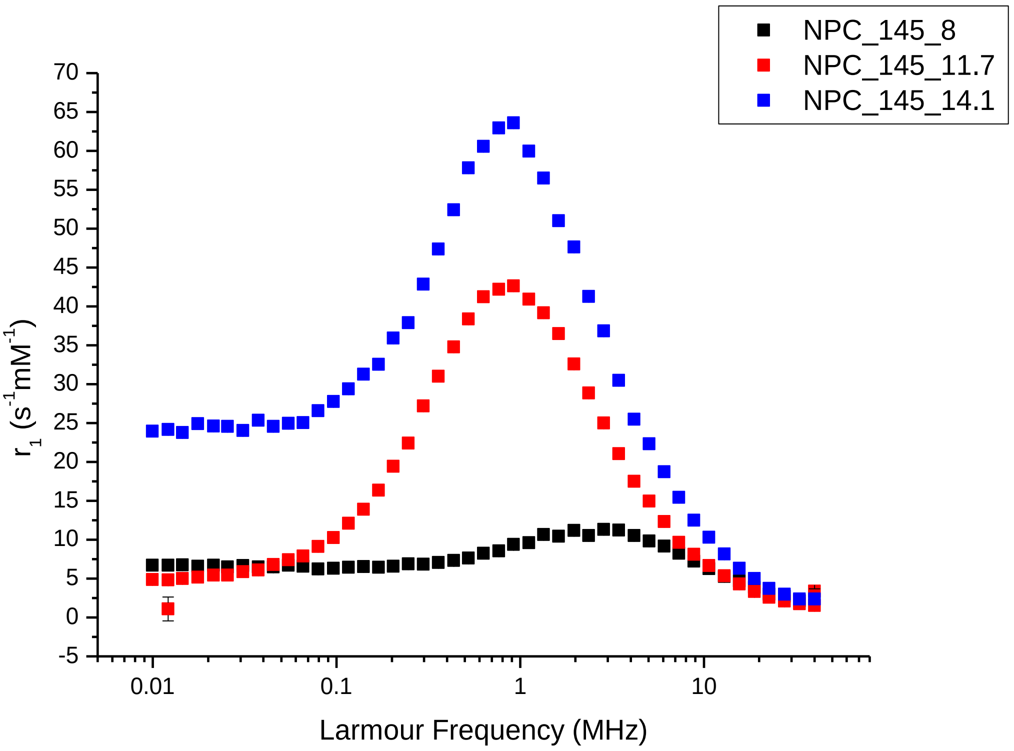

Figure 6. 4: NMRD profiles taken from three PMA-NPC samples with a d_{hyd} of 145 nm. The core size (edge length by TEM) was varied from 8 nm, to 11.7 nm, to 14.1 nm,

It can be seen in Figure 6. 4, that the profiles obtained for each of the 145 nm PMA-NPCs shows evidence of successful assembly. The "dip" characteristic of superparamagnetic NPs has disappeared and the r_{1max} value has shifted to lower field for the red and blue profiles in particular. The r_{1max} peak is also quite broad in each data set, which is possibly indicative of an inhomogeneous distribution of the magnetic material between the NPCs in suspension. It is very interesting that the r_{1max} shifts to lower field with increasing primary NP size, indicating that the primary NP not the

NPC size dictates the τ_D^{-1} value. All samples were found to be stable to the magnetic field (repeat measurement of T_1 gave a single value).

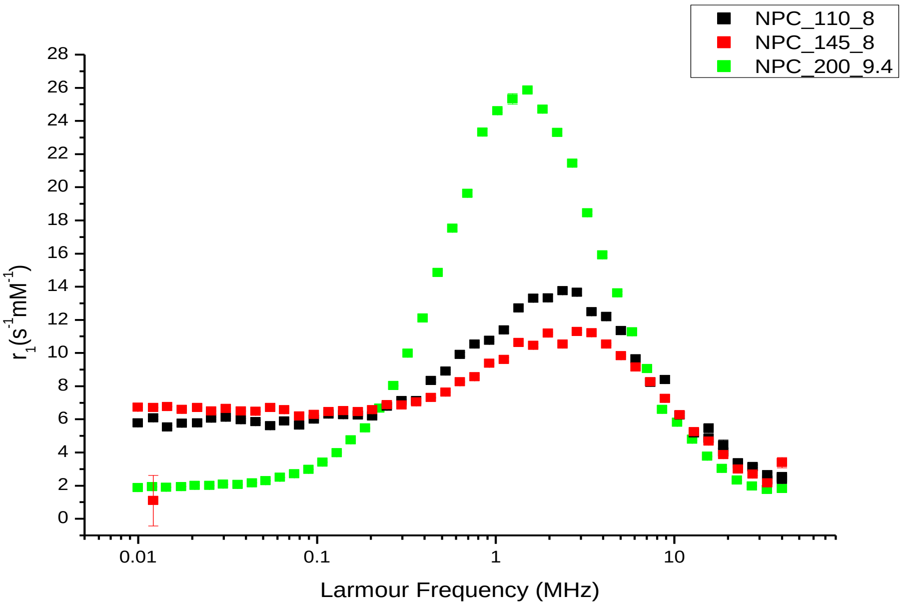

Figure 6. 5: NMRD profile extracted from PMA-NPCs with sizes of 110, 145 and 200 nm respectively. In this case the NP size (edge length by TEM) was maintained at 8 nm (black and red profiles) and 9.4 nm (green).

In the above data, the magnetic resonance response of NPCs of different sizes prepared with cubic NPs with sub 10 nm edge lengths (d_{TEM}) have been reported. As with Figure 6. 4, it can be seen in Figure 6. 5 that the “dip” has been lost, showing that assembly has occurred of these NPs. Interestingly, the profiles shown here in black and red, which were obtained from NPC_110_8 and NPC_145_8 respectively (same primary NP source) are very similar across the whole range of frequencies. The r_{1max} peak appears to be shifted to a slightly lower field for the larger NPCs as might be expected, however this shift is minimal. The peak for NPC_145_8 is also broader than that recorded for the smaller NPC, again possibly indicating a wider distribution of NPs within NPCs. The r_1 signal at low field is much lower for each sample than any obtained for PMA-NPCs of spherical NPs, however this may also be due to the reduced magnetic volume fraction within the NPC.

Table 6. 3: Magnetic resonance relaxivity data obtained at 16.3 MHz for PMA-NPCs prepared with cubic NPs (surfactant assisted thermal decomposition of iron oleate)

Sample Name	r_1	r_2	r_2:r_1 ratio	Sample Name	r_1	r_2	r_2:r_1 ratio
NPC 145, 8	4.4	280.3	63.9	**NPC 110, 8**	5.1	640.4	126.5
NPC 145, 11.7	3.8	724.0	189.3	**NPC 145, 8**	4.4	280.3	63.9
NPC 145, 14.1	6.0	1281.6	215.2	**NPC 200, 9.4**	3.5	1272.7	364.7

The r_2 relaxivity values were also measured for each of the samples at 16.3 MHz. As previously mentioned the samples prepared with 8 nm NPs are of the highest interest as these two samples were prepared with the same primary NPs. It can clearly be seen from the r_2 values obtained for NPC_110_8 and NPC_145_8, that the NPCs of different sizes have different magnetic resonance properties, this further indicates that the assembly was at least partially successful. It is found that clusters of larger NPs have much higher r_2 values indicating either a greater M_s or lower volume fractions. There are some anomalies e.g. for the NPCs of 8 nm NPCs, increasing d_{hyd} reduces r_2. That is an interesting result, but would require a more stable preparation for repeat measurements, as, due to the inhomogeneous nature of the NPCs in this Chapter (as shown in Figure 6. 3) over interpretation of these results should be avoided.

As discussed in Chapter 5, cubic NPs with a similar d_{hyd} to the spherical NPs prepared by surfactant-free thermal decomposition of iron acetylacetonate (Pinna Method) were successfully prepared and had interesting magnetic resonance properties in that, the profiles extracted could be directly overlaid when scaled by the total available surface area of the NPs. A PMA experiment was attempted on these particles to directly compare the effect of clustering on the magnetic resonance properties on these two NP types. 2 mL of pluronic f127 (64 µM) and 1 mL of NP suspension in THF were added to a 7 mL glass vial and allowed to tumble uncovered on a rotary shaker for 48 h in a fumehood. The resultant NPCs were diluted 1:10 with deionized water and centrifuged at 800 rcf for 5 min prior to DLS measurements. Interestingly the PMA-NPCs produced had vastly different sizes, the spherical NPs produced clusters of ~40 nm while the NPCs prepared from cubic NPs were ~200 nm in diameter.

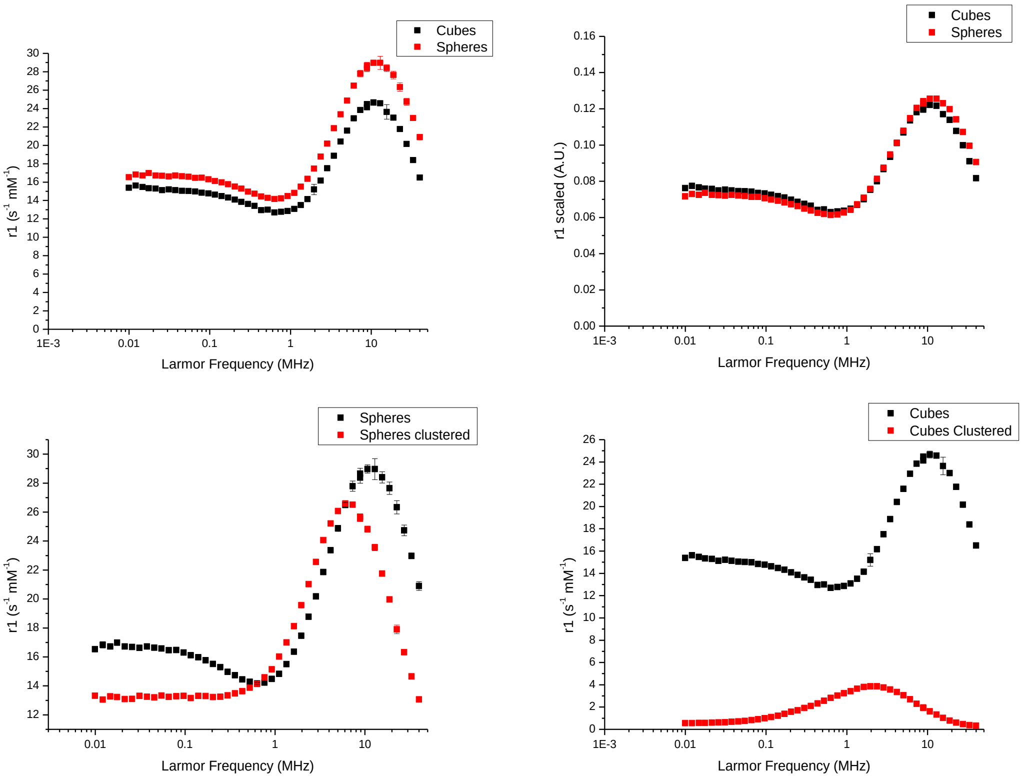

Figure 6. 6: NMRD profiles comparing the behaviour of spherical and cubic materials of similar d_{hyd} and how that behaviour is affected by clustering. Top shows the NMRD profile of the primary NPs in THF (left), (spherical NPs were prepared by surfactant free thermal decomposition, while the cubic NPs were prepared by surfactant assisted thermal decomposition of iron oleate) and the interesting observation that when scaled by NP surface area, the profiles overlap (right). The bottom figures show the effect of clustering on the magnetic resonance properties of NPs in H_2O, left – spherical NPs; right – cubic NPs. It should be noted that the two graphs at the top are taken from Figure 5.26 and it was these primary NPs that were used in the PMA process.

NMRD analysis was performed over a range of frequencies (100 kHz – 40 MHz), both samples were found to be stable to the field, by both DLS and NMR analysis. It can be seen from Figure 6. 6, that the PMA experiment has a significant impact on the magnetic resonance properties of cubic NPs. The r_1 signal suppression is much more significant than that observed for spherical NPs. There is a large shift of r_1 max to lower field, this is consistent with the large increase in d_{hyd}. The r_1 and r_2 relaxivities were also determined at clinical field (~1 T) and those results can be found in Table 6.4, below.

Table 6. 4: r_1 and r_2 relaxivities as determined by NMRD analysis at clinical field (1 T)

Sample	**d_{hyd} (nm)**	**r_1 (s^{-1} mM^{-1})**	**r_2 ($s^{-1}mM^{-1}$)**	**r_2:r_1 ratio**
Spheres (THF)	11.91	4.02	41.53	10.33
Cubes (THF)	13.04	20.58	124.92	6.07
Spheres Clustered (H_2O)	39.95	2.77	81.60	29.46
Cubes Clustered (H_2O)	194	0.15	39.94	266.28

It can be seen from the above data, Table 6. 4, that while the r_2 values for PMA-NPCs of spheres doubles on clustering, the opposite effect is seen for the NPCs prepared using cubic NPs. However, as the r_1 relaxivity decreases so significantly the r2: r1 ratio is much higher for PMA-NPCs of cubes, than PMA-NPCs of spheres. Unfortunately, it was not possible to control d_{hyd} sufficiently for detailed comparisons to be made.

A further clustering experiment was performed, in this case the NPs used were much larger than the standard NPs used for PMA experiments, edge length = 23 nm, prepared by our collaborators in Barcelona. These NPs were close to being ferromagnetic and were less stable to an external magnetic field, but were colloidally stable over a week in the absence of an external magnetic field. 2 mL of pluronic F127 (64 µM) and 1 mL of NP suspension in THF were added to a 7 mL glass vial and tumbled uncovered on a rotary shaker for 48 h in a fumehood, the resultant NPCs were diluted 1:10 with deionized water and centrifuged at 800 rcf for 5 min prior to DLS analysis. NMRD analysis was performed on the resultant NPCs, however this sample was not stable to the magnetic field over the course of the NMRD experiment, so no useable data could be extracted.

However, STEM analysis showed some very interesting results, which have been presented below, Figure 6. 7 - Figure 6. 9,

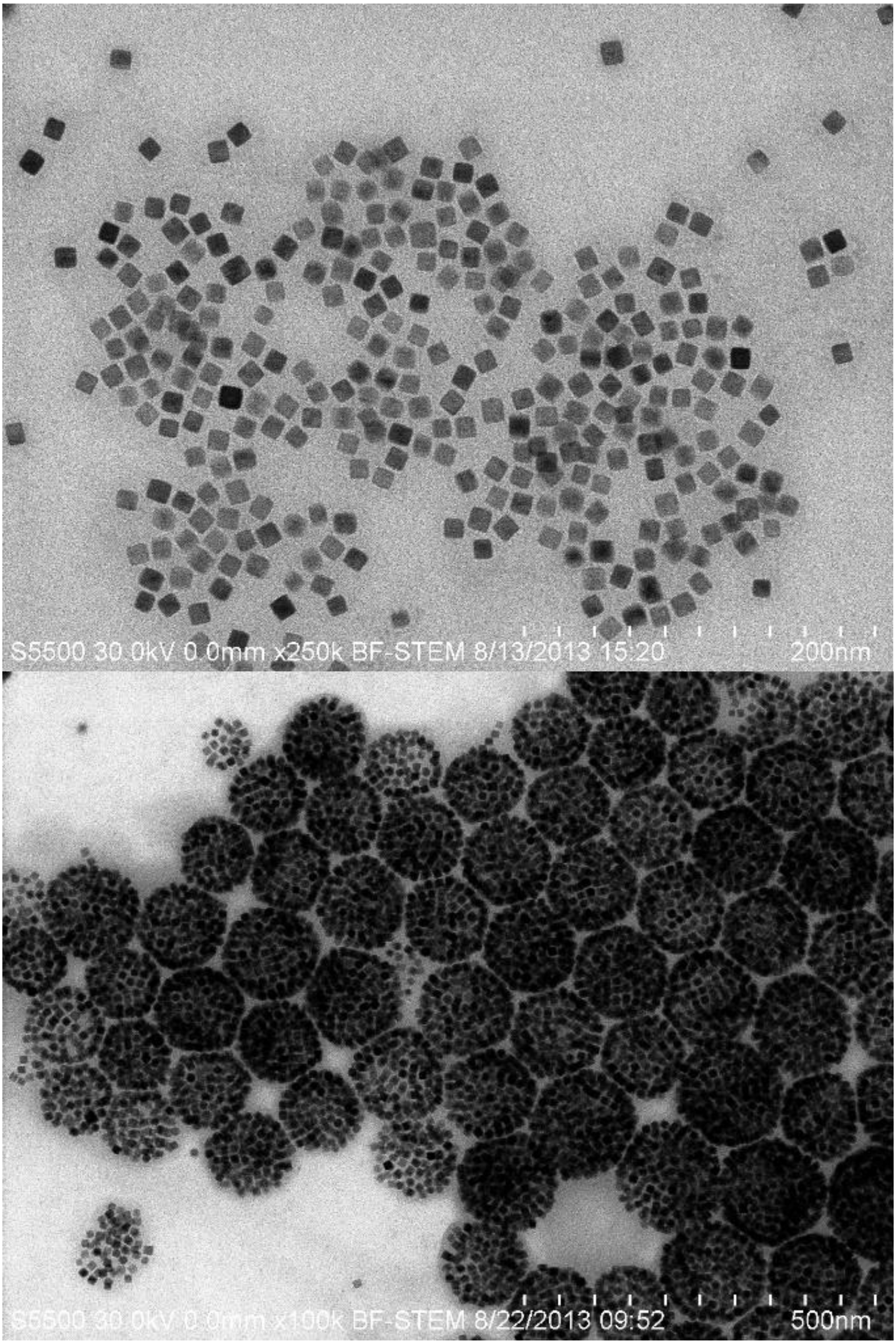

Figure 6. 7: STEM images of cubic NPs prepared by thermal decomposition of iron oleate prior to (top) and following (bottom) a successful clustering experiment.

It can be seen in Figure 6. 7 that the PMA experiment on ferromagnetic cubes successfully produced highly monodisperse spherical NPCs containing cubic NPs. Firstly, there are many such structures that have a uniform distribution of NPs, and the do not appear to be densely packed within the NPC similar to those described by Hickey *et. al,* Figure 3. 4. When densely packed on the TEM grid these spherical NPCs hexagonally close pack, and appear to deform slightly, into hexagonal structures. Even more interestingly, on close inspection it can been seen that the NPs on the edge of adjacent NPCs are interacting magnetically with each other, aligning, edge to edge, while the NPs in the centre of the NPC are randomly orientated. It can also be seen that the NPCs on the edge of the densely packed region are spherical in nature on the outside of the structure, while being aligned, i.e. magnetised on the NPC side facing into the pack. This strongly indicates that the NPCs are soft structures, the hexagonal aspect is imposed on the grid by close contact and that these NPCs are hollow specifically the fact that they dry with clearly no stacking of NPs towards the cluster centre, and the d_{TEM} and d_{hyd} correlate well with each other, confirming that these NPCs are hollow in suspension. A lower magnification image, Figure 6. 8, below shows clearly the monodispersity of the cluster suspension,

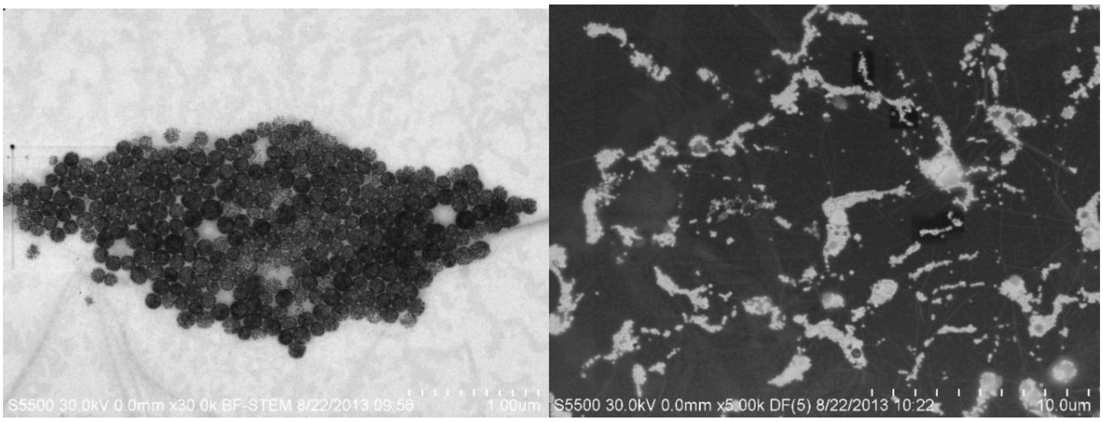

Figure 6. 8: Lower magnification STEM of a successful PMA-NPC experiment of nanocubes. It can be seen that the NPCs are monodisperse and spherical in nature over the whole sample, left shows a selection of NPCs at a magnification of 30kx while the image on the right is a dark field STEM image taken at a magnification of 5000x which shows evidence of similar behaviour over the entire grid.

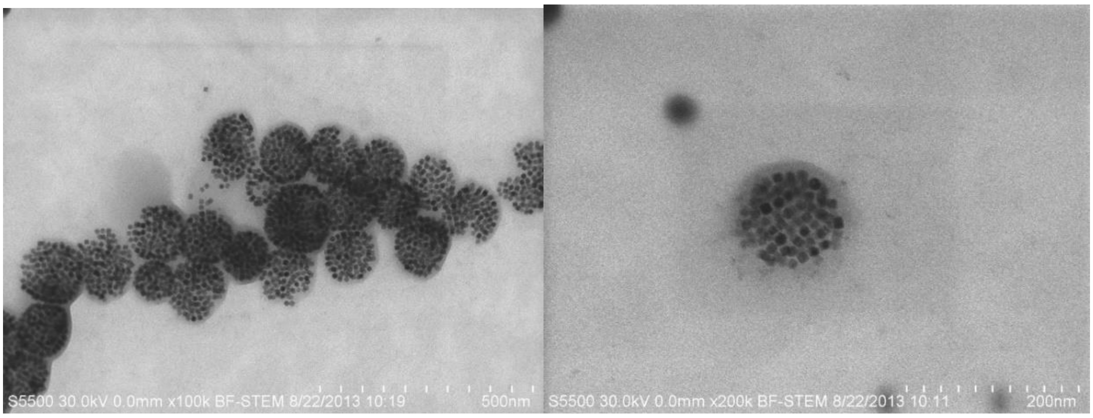

Figure 6. 9: Tilt-stage STEM analysis of PMA-NPCs prepared with cubic NPs, by tilting the NPCs in the FOV of the microscope the spherical nature of the NPCs becomes more apparent. The image of a single NPC, right, has a clearly visible spherical polymer layer surrounding the magnetic material.

Figure 6. 9, above shows (left) a region of hexagonally close packed NPCs on the TEM grid that has been tilted so they are being viewed at an angle rather than from directly above. This image clearly shows the spherical nature of the NPCs despite the deformation of the NP content into hexagonal shapes apparent when viewed from above. The image on the right, shows a single NPC with a clearly defined polymer sphere surrounding cubic NPs that are not ordered at the edges. This again confirms that the surface ordering observed in the densely packed region is primarily as a result of intercluster magnetic interactions.

These samples are incredibly monodisperse, ordered and contain low numbers of NPs (58±10 NPs per NPC). Hence, they are very interesting for applications (hyperthermia in particular). However, it proved not to be possible to reproduce this clustering.

6.4. Conclusions and Further Work

Significant progress has been made in the preparation of nanoparticle assemblies of cubic nanoparticles by the PMA method. Difficulties arise in the control of the assembly size and polydispersity, due to the variable concentration of oleic acid on the surface of the nanoparticles following synthesis and the difficulties associated with the removal of the solvent, squalene from the surface of the NPs. Using techniques, such as TGA, surface concentration of oleic acid can be roughly estimated and adjusted accordingly to the correct concentration for reproducible assembly conditions. However, even with the careful adjustment of OA concentration, assembly of cubic NPs remains challenging. It is likely that residual squalene remains on the NPs as it is notoriously difficult to remove, even from glassware. It seems that any residual squalene poses a much more difficult situation than that described in Chapter 3, as with consecutive washing of the NPs oleic acid is stripped from the NPs, causing irreversible agglomeration, but apparently squalene remains. It is possible that alternative high boiling solvents could be used in the synthesis of highly monodisperse cubic nanoparticles which have less affinity for the NPs, allowing for a much cleaner oleic acid stabilized cubic NP to be assembled. Alternatively, if production of cubes from a surfactant-free approach is successful in the future, these would be an ideal candidate for PMA trials.

Additionally, assembly of cubic NPs has shown further evidence that PMA-NPCs are soft materials, with low magnetic volume fraction. The NPs appear to orient themselves in a single layer at the surface of the NPC rather than aggregating into a dense core. Assembly of ferromagnetic materials also demonstrated some very interesting packing properties, with interparticle interactions being evident between adjacent NPCs. The clusters were also shown to deform when tightly packed, further highlighting their soft nature. A significant research goal for the Group remains production of highly monodisperse, internally-ordered low particle number NPCs. Cubes have advantages in this regard but further work on sample processing would be necessary.

Thesis Conclusions

In this body of work a successful method for the preparation of size controlled nanoparticle assemblies from spherical nanoparticles prepared by surfactant free thermal decomposition of iron acetylacetonate was presented. Through careful control of surfactant concentration, the ratio of iron to polymer, polymer properties and polymer concentration it was shown that a particular size of NPC could be targeted and selectively produced reproducibly. The capacity for scale up of the PMA method was also shown, with no significant effect on the size and polydispersity of the NPCs produced at 100x scale. The materials used in the preparation of these NPCs are widely commercially available at lost cost and high purity. They are non-toxic, and the polymers used have previously been FDA approved for selected bio-applications, also highlighting the potential for scale up to the industrially relevant scale.

Fundamental analysis of the PMA-NPCs has shown the clusters formed are hollow in nature, this was determined by in-depth investigation of the magnetic resonance properties and confirmed by electron microscopy analysis. Kymography was used in a novel way to assess the movement of PMA-NPC suspensions in the presence of an external magnetic field and proved that the NPCs could be actively directed using a magnet. Fluorescence labelling experiments showed the potential functionalization of PMA-NPCs with small molecules for use as drug delivery vehicles, or functionalization with biological moieties such as antibodies for active targeting processes. Toxicology results also indicated that unfunctionalized PMA-NPCs were non-toxic at all tested concentrations, a vital result for materials intended for biomedical applications.

While spherical NPs generate very interesting results on assembly, the magnetic resonance properties of cubic NPs make them highly desirable for biomedical applications. A process was optimized for the production of highly regular cubic NPs, with well-defined edges, vertices and uniform aspect ratio throughout the sample, using a surfactant assisted thermal decomposition method. While size control was ultimately not achieved, scaled up experiments allowed for the production of large batches of cubic NPs for further development projects, with no observable impact on the quality of the materials produced. An additional approach towards the production of cubic NPs by a surfactant free thermal decomposition approach was described, however this work is in the preliminary stages and highly cubic materials have not yet been observed. Despite the somewhat disordered nature of the NPs prepared by this approach, promising nuclear magnetic relaxation dispersion results indicate that further development would be a beneficial target of the Group in future work.

Finally, some progress has been made in the application of the PMA process to cubic NPs prepared by a surfactant assisted thermal decomposition approach. The initial results appear to verify our conclusions from the work with spherical NPs that the NPCs are hollow, this is determined largely by the interpretation of TEM analysis. NMRD analysis of PMA-NPCs of spheres and cubes with similar total volume indicates that the effect of assembly on the magnetic resonance properties of the suspensions is much more pronounced for cubic NPs than for spherical NPs. A successful assembly experiment with large cubic NPs (edge length = 23 nm) indicates strongly that magnetic intercluster interactions are occurring, as encapsulated NPs in neighbouring NPCs align with each other, while no NP ordering is observed in NPCs without close proximity to other NPCs. The assembly process is much less controlled in the application of the PMA method to cubic NPs, potentially due to the presence of residual surfactant and squalene on the NP surface. Method development is ongoing to accurately determine the concentration of surfactants and to probe the potential contamination of these materials as the development of a reproducible assembly method for cubic NPs would be a significant step forward in the generation of magnetic nanoparticle assemblies for biomedical imaging, and drug delivery processes.

Future Work

Moving forward it is clear that much groundwork has been done in the development and optimization of both synthesis and assembly methods. In this regard, for the assemblies of spherical NPs a highly reproducible method for the preparation of samples has been reported so future work using these materials could focus on the applicability of these materials as theranostic agents. An obvious route would be in the investigation of these materials as hyperthermic agents, either alone or as an NPC-drug conjugate. Also, along these lines, experiments functionalizing the NPCs with drug/sugar/protein/antibody moieties would be of interest to the Group in the area of targeted drug delivery and the potential for active site targeting with the NPCs.

Another obvious development would be the application of these materials to *in vivo* MRI. While NMRD is a good approximation of the magnetic resonance response of a material, it is a much-simplified model compared to MRI in a patient. The effects of the immune system, NPC solubility *in vivo* and other effects such as toxicity cannot be accurately gauged from an *in vitro* model.

With respect to the cubic NPs, it is clear that further work is required to reproducibly prepare cubic NPs of known size. The precursor cleaning experiment outlined in Section 5.3.3, clearly demonstrated the need for a highly pure organometallic precursor for controlled synthesis of highly cubic NPS, however the extensive washing procedure is both time consuming and produces vast quantities of aqueous waste. One potential project going forward could be the development of an automated cleaning system. This would not only reduce the time spent by the researcher preparing raw materials, but also reduce the random error caused by human action.

Additionally, more work is needed in the determination of the oleic acid content on the surface of as prepared cubic NPs, it is clear from our findings in Chapter 3 that the interaction between OA and the Polymer used in assembly must be highly controlled for assembly to be controlled. With better estimation of the surface layer of OA, better cleaning methods can be implemented to prepare the cubic NPs suitable for controlled and reproducible assembly of cubic NPs.

Alternatively, the preparation of cubic NPs using a surfactant free approach is another obvious target. This would allow for the preparation of NPs with no surface layer of surfactant to quantify, meaning that surface chemistry could be accurately determined and carefully controlled. This would allow assembly experiments to be performed under identical conditions to the spherical NPs. While it is clear that the presence of Na^+ in a synthesis is influential in the formation of facets during NP growth, NaCl is unsuitable as it is insoluble in the reaction mixture, similarly Na salts with long aliphatic chains such as sodium oleate should be avoided as the long hydrocarbon chain could be influential as a surfactant in its own right. Short chain Na salts such as sodium citrate, sodium phosphate and sodium carbonate, are possible starting points for further investigation, as the anionic portion of each of these molecule is known to have a lower affinity for iron oxide than the oleic acid that would be used in the stabilization process prior to assembly, thus subsequent phase transfer would be simplified, if even necessary.

Bibliography

(1) Guardia, P.; Di Corato, R.; Lartigue, L.; Wilhelm, C.; Espinosa, A.; Garcia-Hernandez, M.; Gazeau, F.; Manna, L.; Pellegrino, T. *ACS Nano* **2012**, *6* (4), 3080–3091.

(2) Guardia, P.; Pérez, N.; Labarta, A.; Batlle, X. *Langmuir* **2010**, *26* (8), 5843–5847.

(3) Bae, K. H.; Park, M.; Do, M. J.; Lee, N.; Ryu, J. H.; Kim, G. W.; Kim, C.; Park, T. G.; Hyeon, T. *ACS Nano* **2012**, *6* (6), 5266–5273.

(4) Guardia, P.; Labarta, A.; Batlle, X. *J. Phys. Chem. C* **2011**, *115* (2), 390–396.

(5) Lee, N.; Choi, Y.; Lee, Y.; Park, M.; Moon, W. K.; Choi, S. H.; Hyeon, T. *Nano Lett.* **2012**, *12* (6), 3127–3131.

(6) Lee, J. H.; Kim, J. W.; Cheon, J. *Molecules and Cells*. 2013, pp 274–284.

(7) Robinson, I.; Thanh, N. *New Chemical Methods for Synthesis of Magnetic Nanoparticles for Biomedical Applications*; 2010; Vol. 1275.

(8) Papaefthymiou, G. C. *Nano Today* **2009**, *4* (5), 438–447.

(9) Arruebo, M.; Fernández-Pacheco, R.; Ibarra, M. R.; Santamaría, J. *Nano Today* **2007**, *2* (3), 22–32.

(10) Bisht, V.; Rajeev, K. P. *arXiv Prepr. arXiv1008.5245* **2010**.

(11) Brown, M. A.; Semelka, R. C. *MRI Basic Priciple and Applications*; 2003.

(12) Sun, C.; Lee, J. S. H.; Zhang, M. *Advanced Drug Delivery Reviews*. 2008, pp 1252–1265.

(13) Huang, Y.; Hu, L.; Zhang, T.; Zhong, H.; Zhou, J.; Liu, Z.; Wang, H.; Guo, Z.; Chen, Q. *Sci. Rep.* **2013**, *3*, 2647.

(14) Smolensky, E. D.; Park, H. E.; Zhou, Y.; Rolla, G. a.; Marjańska, M.; Botta, M.; Pierre, V. C. *J. Mater. Chem. B* **2013**, *1* (22), 2818–2828.

(15) Bonnemain, B. *J. Drug Target.* **1998**, *6* (3), 167–174.

(16) Toth, E.; Helm, L.; Merbach, A. *The Chemistry of Contrast Agents in Medical*

Magnetic Resonance Imaging; 2002; Vol. 221.

(17) James, T. L. *Control* **1998**, *27*, 1–31.

(18) Reich, H. J. No Title https://www.chem.wisc.edu/areas/reich/nmr/08-tech-01-relax.htm.

(19) Ridgway, J. P. *J. Cardiovasc. Magn. Reson.* **2010**, *12* (1), 71.

(20) de Dios, A. C. No Title https://bouman.chem.georgetown.edu/nmr/dipolar/dipolar.htm .

(21) Roch, A.; Gossuin, Y.; Muller, R. N.; Gillis, P. *J. Magn. Magn. Mater.* **2005**, *293* (1), 532–539.

(22) Laurent, S.; Forge, D.; Port, M.; Roch, A.; Robic, C.; Vander Elst, L.; Muller, R. N. *Chem. Rev.* **2008**, *108* (6), 2064–2110.

(23) Stolarczyk, J. K.; Meledandri, C. J.; Clarke, S. P.; Brougham, D. F. *Chem. Commun.* **2016**, *52* (91), 13337–13340.

(24) Stolarczyk, J. K.; Deak, A.; Brougham, D. F. *Adv. Mater.* **2016**, *28* (27), 5400–5424.

(25) Al-Tamimi, M.; Sulong, G. *Tumor Brain Detection Through MR Images: A Review of Literature*; 2015.

(26) Slice-selective excitation - Questions and Answers in MRI http://mri-q.com/slice-selective-excitation.html (accessed May 2, 2017).

(27) Weishaupt, D.; Köchli, V. D.; Marincek, B. *How does MRI work?: an introduction to the physics and function of magnetic resonance imaging*; Springer Science & Business Media, 2008.

(28) Adolphi, N. L. *J. Forensic Radiol. Imaging* **2016**, *4*, 27–34.

(29) Chatterjee, D. K.; Diagaradjane, P.; Krishnan, S. *Ther. Deliv.* **2011**, *2* (8), 1001–1014.

(30) Hergt, R.; Andra, W.; d'Ambly, C. G.; Hilger, I.; Kaiser, W. A.; Richter, U.; Schmidt, H. G. *IEEE Transactions on Magnetics*. 1998, pp 3745–3754.

(31) Gilchrist, R. K.; Medal, R.; Shorey, W. D.; Hanselman, R. C.; Parrott, J. C.; Taylor, C. B. *Ann. Surg.* **1957**, *146* (4), 596–606.

(32) Chou, C. K. *Int. J. Hyperth. Off. J. Eur. Soc. Hyperthermic Oncol. North Am. Hyperth. Gr.* **1990**, *6* (2), 367–370.

(33) Jordan, A.; Scholz, R.; Wust, P.; Fähling, H.; Felix, R. *J. Magn. Magn. Mater.* **1999**, *201* (1), 413–419.

(34) Akbarzadeh, A.; Samiei, M.; Davaran, S. *Nanoscale Res. Lett.* **2012**, *7* (1), 144.

(35) Xu, Z.; Shen, C.; Tian, Y.; Shi, X.; Gao, H.-J. *Nanoscale* **2010**, *2* (6), 1027–1032.

(36) Massart, R. *IEEE Trans. Magn.* **1981**, *17* (2), 1247–1248.

(37) Massart, R.; Dubois, E.; Cabuil, V.; Hasmonay, E. *J. Magn. Magn. Mater.* **1995**, *149* (1–2), 1–5.

(38) Shen, L.; Laibinis, P. E.; Hatton, T. A. *Langmuir* **1999**, *15* (2), 447–453.

(39) Wu, W.; He, Q.; Jiang, C. *Nanoscale Res. Lett.* **2008**, *3* (11), 397–415.

(40) Yu, W. W.; Falkner, J. C.; Yavuz, C. T.; Colvin, V. L. *Chem Commun* **2004**, No. 20, 2306–2307.

(41) Sun, S.; Zeng, H. *J. Am. Chem. Soc.* **2002**, *124* (28), 8204–8205.

(42) taeghwan Hyeon, Su Seong Lee, Jongnam Park, Y. C. and H. B. N. *J. Ameriacan Chem. Soc.* **2001**, *123* (8), 12789–12801.

(43) Pinna, N.; Grancharov, S.; Beato, P.; Bonville, P.; Antonietti, M.; Niederberger, M. *Chem. Mater.* **2005**, *17* (11), 3044–3049.

(44) Pinna, N.; Niederberger, M. *Angewandte Chemie - International Edition*. 2008, pp 5292–5304.

(45) Kodama, R. H. *J. Magn. Magn. Mater.* **1999**, *200* (1–3), 359–372.

(46) Hervault, A.; Dunn, A. E.; Lim, M.; Boyer, C.; Mott, D.; Maenosono, S.; Thanh, N. T. K. *Nanoscale* **2016**, *8* (24), 12152–12161.

(47) Xiong, F.; Tian, J.; Hu, K.; Zheng, X.; Sun, J.; Yan, C.; Yao, J.; Song, L.; Zhang,

Y.; Gu, N. *Nanoscale* **2016**, *8* (39), 17085–17089.

(48) Lu, Z.; Yin, Y. *Chem. Soc. Rev.* **2012**, *41* (21), 6874.

(49) Yan, Q.; Purkayastha, A.; Gandhi, D.; Li, H.; Kim, T.; Ramanath, G. *Adv. Mater.* **2007**, *19* (20), 3286–3290.

(50) Shenhar, R.; Norsten, T. B.; Rotello, V. M. *Adv. Mater.* **2005**, *17* (6), 657–669.

(51) Meledandri, C. J.; Brougham, D. F. *Anal. Methods* **2012**, *4* (2), 331–341.

(52) Langsam, Y. (Brooklyn C. No Title http://eilat.sci.brooklyn.cuny.edu/cis1_5/OldHWs/HW2d_C_files/image001.gif.

(53) Wittenberg, T.; Tigges, M.; Mergell, P.; Eysholdt, U. *J. Voice* **2000**, *14* (3), 422–442.

(54) Brocklehurst, J. C.; Carty, M. H.; Skorecki, J. *Curr. Med. Res. Opin.* **1978**, *5* (8), 663–668.

(55) Pereira, A. J.; Maiato, H. *Methods* **2010**, *51* (2), 214–219.

(56) Iomini, C.; Babaev-Khaimov, V.; Sassaroli, M.; Piperno, G. *J. Cell Biol.* **2001**, *153* (1), 13 LP-24.

(57) Levitzky, M. G. *Pulmonary physiology*, 8th ed.; McGraw-Hill Medical Publishing, 2013.

(58) Luo, B.; Song, X. J.; Zhang, F.; Xia, A.; Yang, W. L.; Hu, J. H.; Wang, C. C. *Langmuir* **2010**, *26* (3), 1674–1679.

(59) Xia, H. B.; Foo, P.; Yi, J. B. *Chem. Mater.* **2009**, *21* (12), 2442–2451.

(60) Ge, J.; Hu, Y.; Biasini, M.; Beyermann, W. P.; Yin, Y. *Angew. Chemie - Int. Ed.* **2007**, *46* (23), 4342–4345.

(61) Ditsch, A.; Laibinis, P. E.; Wang, D. I. C.; Hatton, T. A. *Langmuir* **2005**, *21* (13), 6006–6018.

(62) Corr, S. A.; Byrne, S. J.; Tekoriute, R.; Meledandri, C. J.; Brougham, D. F.; Lynch, M.; Kerskens, C.; O'Dwyer, L.; Gun'ko, Y. K. *J. Am. Chem. Soc.* **2008**, *130* (13), 4214–4215.

(63) Sondjaja, R.; Alan Hatton, T.; Tam, M. K. C. *J. Magn. Magn. Mater.* **2009**, *321* (16), 2393–2397.

(64) Dan, N.; Zubris, M.; Tannenbaum, R. *Macromolecules* **2005**, *38* (22), 9243–9250.

(65) Tannenbaum, R.; Zubris, M.; Goldberg, E. P.; Reich, S.; Dan, N. *Macromolecules* **2005**, *38* (10), 4254–4259.

(66) Lattuada, M.; Hatton, T. A. *Langmuir* **2007**, *23* (4), 2158–2168.

(67) Liu, Q.; Shen, S.; Zhou, Z.; Tian, L. *Mater. Lett.* **2009**, *63* (30), 2625–2627.

(68) Frka-Petesic, B.; Fresnais, J.; Berret, J. F.; Dupuis, V.; Perzynski, R.; Sandre, O. *J. Magn. Magn. Mater.* **2009**, *321* (7), 667–670.

(69) Berret, J.-F.; Schonbeck, N.; Gazeau, F.; El Kharrat, D.; Sandre, O.; Vacher, A.; Airiau, M. *J. Am. Chem. Soc.* **2006**, *128* (10), 1755–1761.

(70) Fresnais, J.; Lavelle, C.; Berret, J. F. *J. Phys. Chem. C* **2009**, *113* (37), 16371–16379.

(71) Chiang, W. H.; Ho, V. T.; Chen, H. H.; Huang, W. C.; Huang, Y. F.; Lin, S. C.; Chern, C. S.; Chiu, H. C. *Langmuir* **2013**, *29* (21), 6434–6443.

(72) Yang, X.; Grailer, J. J.; Rowland, I. J.; Javadi, A.; Hurley, S. A.; Matson, V. Z.; Steeber, D. A.; Gong, S. *ACS Nano* **2010**, *4* (11), 6805–6817.

(73) Isojima, T.; Lattuada, M.; Vander Sande, J. B.; Hatton, T. A. *ACS Nano* **2008**, *2* (9), 1799–1806.

(74) Lattuada, M.; Hatton, T. A. *J. Am. Chem. Soc.* **2007**, *129* (42), 12878–12889.

(75) Perro, A.; Meunier, F.; Schmitt, V.; Ravaine, S. *Colloids Surfaces A Physicochem. Eng. Asp.* **2009**, *332* (1), 57–62.

(76) Stolarczyk, J. K.; Ghosh, S.; Brougham, D. F. *Angew. Chemie Int. Ed.* **2009**, *48* (1), 175–178.

(77) Pöselt, E.; Fischer, S.; Foerster, S.; Weller, H. *Langmuir* **2009**, *25* (24), 13906–13913.

(78) Pöselt, E.; Kloust, H.; Tromsdorf, U.; Janschel, M.; Hahn, C.; Maßlo, C.; Weller, H. *ACS Nano* **2012**, *6* (2), 1619–1624.

(79) Hickey, R. J.; Haynes, A. S.; Kikkawa, J. M.; Park, S. J. *J. Am. Chem. Soc.* **2011**, *133* (5), 1517–1525.

(80) Hu, J.; Qian, Y.; Wang, X.; Liu, T.; Liu, S. *Langmuir* **2012**, *28* (4), 2073–2082.

(81) Zhuang, J.; Wu, H.; Yang, Y.; Cao, Y. C. *J. Am. Chem. Soc.* **2007**, *129* (46), 14166–14167.

(82) Zhuang, J.; Wu, H.; Yang, Y.; Cao, Y. C. *Angew. Chemie Int. Ed.* **2008**, *47* (12), 2208–2212.

(83) Escobar-Chavez, J. J.; Lopez-Cervantes, M.; Naik, A.; Kalia, Y. N.; Quintanar-Guerrero, D.; Ganem-Quintanar, A. *J. Pharm. Pharm. Sci.* **2006**, *9* (3), 339–358.

(84) Hartikka, J.; Sukhu, L.; Buchner, C.; Hazard, D.; Bozoukova, V.; Margalith, M.; Nishioka, W. K.; Wheeler, C. J.; Manthorp, M.; Sawdey, M. *Mol Ther* **2001**, *4* (5), 407–415.

(85) McNeill, V. F.; Wolfe, G. M.; Thornton, J. A. *J. Phys. Chem. A* **2007**, *111* (6), 1073–1083.

(86) Sezgin, Z.; Yüksel, N.; Baykara, T. *Eur. J. Pharm. Biopharm.* **2006**, *64* (3), 261–268.

(87) Reimer, P.; Parizel, P. M.; Meaney, J. F. M.; Stichnoth, F. A. *Clinical MR imaging*; Springer, 2010.

(88) Walpole, S. C.; Prieto-Merino, D.; Edwards, P.; Cleland, J.; Stevens, G.; Roberts, I. *BMC Public Health* **2012**, *12* (1), 439.

(89) Xie, J.; Lee, S.; Chen, X. *Adv. Drug Deliv. Rev.* **2010**, *62* (11), 1064–1079.

(90) Michalet, X.; Pinaud, F. F.; Bentolila, L. A.; Tsay, J. M.; Doose, S.; Li, J. J.; Sundaresan, G.; Wu, A. M.; Gambhir, S. S.; Weiss, S. *Science (80-.).* **2005**, *307* (5709), 538–544.

(91) Shen, J.; Zhu, Y.; Yang, X.; Li, C. *Chem. Commun.* **2012**, *48* (31), 3686–3699.

(92) Hu, M.; Chen, J.; Li, Z.-Y.; Au, L.; Hartland, G. V; Li, X.; Marquez, M.; Xia, Y.

Chem. Soc. Rev. **2006**, *35* (11), 1084–1094.

(93) Liu, Z.; Li, X.; Tabakman, S. M.; Jiang, K.; Fan, S.; Dai, H. *J. Am. Chem. Soc.* **2008**, *130* (41), 13540–13541.

(94) De La Zerda, A.; Zavaleta, C.; Keren, S.; Vaithilingam, S.; Bodapati, S.; Liu, Z.; Levi, J.; Smith, B. R.; Ma, T.-J.; Oralkan, O. *Nat. Nanotechnol.* **2008**, *3* (9), 557–562.

(95) Na, H. Bin; Song, I. C.; Hyeon, T. *Adv. Mater.* **2009**, *21* (21), 2133–2148.

(96) Lee, N.; Hyeon, T. *Chem. Soc. Rev.* **2012**, *41* (7), 2575–2589.

(97) Lee, N.; Hyeon, T. *Chem. Soc. Rev.* **2012**, *41* (7), 2575–2589.

(98) Ai, H.; Flask, C.; Weinberg, B.; Shuai, X.-T.; Pagel, M. D.; Farrell, D.; Duerk, J.; Gao, J. *Adv. Mater.* **2005**, *17* (16), 1949–1952.

(99) Gonzales-Weimuller, M.; Zeisberger, M.; Krishnan, K. M. *J. Magn. Magn. Mater.* **2009**, *321* (13), 1947–1950.

(100) Gonzales-Weimuller, M.; Zeisberger, M.; Krishnan, K. M. *J. Magn. Magn. Mater.* **2009**, *321* (13), 1947–1950.

(101) Davis, M. E.; Chen, Z. (Georgia); Shin, D. M. *Nat Rev Drug Discov* **2008**, *7* (9), 771–782.

(102) Byrne, J. D.; Betancourt, T.; Brannon-Peppas, L. *Adv. Drug Deliv. Rev.* **2008**, *60* (15), 1615–1626.

(103) Borase, T.; Ninjbadgar, T.; Kapetanakis, A.; Roche, S.; O'Connor, R.; Kerskens, C.; Heise, A.; Brougham, D. F. *Angew. Chem. Int. Ed. Engl.* **2013**, *52* (11), 3164–3167.

(104) Neuberger, T.; Schopf, B.; Hofmann, H.; Hofmann, M.; Vonrechenberg, B. *J. Magn. Magn. Mater.* **2005**, *293* (1), 483–496.

(105) Singh, R.; Lillard, J. W. *Exp. Mol. Pathol.* **2009**, *86* (3), 215–223.

(106) Malam, Y.; Loizidou, M.; Seifalian, A. M. *Trends Pharmacol. Sci.* **2009**, *30* (11), 592–599.

(107) Roch, A.; Muller, R. N.; Gillis, P. *J. Chem. Phys.* **1999**, *110* (11), 5403–5411.

(108) Ninjbadgar, T.; Brougham, D. F. *Adv. Funct. Mater.* **2011**, *21* (24), 4769–4775.

(109) Meledandri, C. J.; Ninjbadgar, T.; Brougham, D. F. *J. Mater. Chem.* **2011**, *21* (1), 214–222.

(110) Vuong, Q. L.; Berret, J. F.; Fresnais, J.; Gossuin, Y.; Sandre, O. *Adv. Healthc. Mater.* **2012**, *1* (4), 502–512.

(111) Xiao, L.; Li, J.; Brougham, D. F.; Fox, E. K.; Feliu, N.; Bushmelev, A.; Schmidt, A.; Mertens, N.; Kiessling, F.; Valldor, M.; Fadeel, B.; Mathur, S. *ACS Nano* **2011**, *5* (8), 6315–6324.

(112) Xiao, L.; Li, J.; Brougham, D. F.; Fox, E. K.; Feliu, N.; Bushmelev, A.; Schmidt, A.; Mertens, N.; Kiessling, F.; Valldor, M.; Fadeel, B.; Mathur, S. *ACS Nano* **2011**, *5* (8), 6315–6324.

(113) Leong, S. S.; Ahmad, Z.; Lim, J. *Soft Matter* **2015**, *11* (35), 6968–6980.

(114) Image https://www.thermofisher.com/ie/en/home/life-science/protein-biology/protein-biology-learning-center/protein-biology-resource-library/pierce-protein-methods/amine-reactive-crosslinker-chemistry.html.

(115) Suthiwangcharoen, N.; Nagarajan, R. *RSC Adv.* **2014**, *4* (20), 10076–10089.

(116) Zhen, G.; Muir, B. W.; Moffat, B. a.; Harbour, P.; Murray, K. S.; Moubaraki, B.; Suzuki, K.; Madsen, I.; Agron-Olshina, N.; Waddington, L.; Mulvaney, P.; Hartley, P. G. *J. Phys. Chem. C* **2010**, *115* (2), 327–334.

(117) Kloust, H.; Zierold, R.; Merkl, J.-P.; Schmidtke, C.; Feld, A.; Pöselt, E.; Kornowski, A.; Nielsch, K.; Weller, H. *Chem. Mater.* **2015**, *27* (14), 4914–4917.

(118) Fortner, W. L. and S. S. L. and J. W. and C. H. H. and J. D. *Nanotechnology* **2016**, *27* (32), 324002.

(119) Bao, L.; Low, W.-L.; Jiang, J.; Ying, J. Y. *J. Mater. Chem.* **2012**, *22* (15), 7117–7120.

(120) Zhao, Z.; Zhou, Z.; Bao, J.; Wang, Z.; Hu, J.; Chi, X.; Ni, K.; Wang, R.; Chen, X.; Chen, Z.; Gao, J. *Nat. Commun.* **2013**, *4*, 2266.

(121) Khurshid, H.; Li, W.; Chandra, S.; Phan, M.-H.; Hadjipanayis, G. C.; Mukherjee, P.; Srikanth, H. *Nanoscale* **2013**, *5* (17), 7942–7952.

(122) Salazar-Alvarez, G.; Qin, J.; Šepelák, V.; Bergmann, I.; Vasilakaki, M.; Trohidou, K. N.; Ardisson, J. D.; Macedo, W. A. A.; Mikhaylova, M.; Muhammed, M.; Baró, M. D.; Nogués, J. *J. Am. Chem. Soc.* **2008**, *130* (40), 13234–13239.

(123) Martin-Hernandez, F.; García-Hernández, M. M. *Geophys. J. Int.* **2010**, *181* (2), 756–761.

(124) Kim, D.; Lee, N.; Park, M.; Kim, B. H.; An, K.; Hyeon, T. *J. Am. Chem. Soc.* **2009**, *131* (2), 454–455.

(125) Guardia, P.; Riedinger, A.; Nitti, S.; Pugliese, G.; Marras, S.; Genovese, A.; Materia, M. E.; Lefevre, C.; Manna, L.; Pellegrino, T. *J. Mater. Chem. B* **2014**, *2* (28), 4426–4434.

(126) Pichon, B. P.; Gerber, O.; Lefevre, C.; Florea, I.; Fleutot, S.; Baaziz, W.; Pauly, M.; Ohlmann, M.; Ulhaq, C.; Ersen, O.; Pierron-Bohnes, V.; Panissod, P.; Drillon, M.; Begin-Colin, S. *Chem. Mater.* **2011**, *23* (11), 2886–2900.

(127) Shavel, A.; Liz-Marzán, L. M. *Phys. Chem. Chem. Phys.* **2009**, *11* (19), 3762–3763.

(128) Kovalenko, M. V; Bodnarchuk, M. I.; Lechner, R. T.; Hesser, G.; Schäffler, F.; Heiss, W. *J. Am. Chem. Soc.* **2007**, *129* (20), 6352–6353.

(129) Bronstein, L. M.; Huang, X.; Retrum, J.; Schmucker, A.; Pink, M.; Stein, B. D.; Dragnea, B. *Chem. Mater.* **2007**, *19* (15), 3624–3632.

(130) Bronstein, L. M.; Atkinson, J. E.; Malyutin, A. G.; Kidwai, F.; Stein, B. D.; Morgan, D. G.; Perry, J. M.; Karty, J. A. *Langmuir* **2011**, *27* (6), 3044–3050.

Publications

Poster Presentations

The Effect of Assembly Conditions and Nanoparticle Conditions on Size, Morphology and Polydispersity of Magnetic Nanoparticle Clusters; Sarah M. Martyn and Dr. Dermot F. Brougham; First Joint SMG/MSI Symposium, Glasgow, 27-28 November, 2014

The Effect of Assembly Conditions and Nanoparticle Conditions on the Physical and Magnetic Properties of Magnetic Nanoparticle Clusters; Sarah M. Martyn and Dr. Dermot F. Brougham;Nanotech France, Paris, 15-17 June, 2015

Oral Presentations

Magnetic Nanoparticles and Their Assemblies – Applications in Biomedicine, Sarah Martyn and Dr. Dermot F. Brougham, Inaugural Chemistry Day, Dublin City University, June 18th, 2015

Polymer Mediated Assembly of Iron Oxide Nanoparticles– Applications in Biomedicine, Sarah Martyn and Dr. Dermot F. Brougham, EMRS, Warsaw, 15-18 September, 2015

Polymer Mediated Assembly of Iron Oxide Nanoparticles– Applications in Biomedicine, Sarah Martyn and Dr. Dermot F.Brougham, MSI Symposium, 9th June, 2016

Peer-reviewed Publications

Cyclen lanthanide-based micellar structures for application as luminescent [Eu(III)] and magnetic [Gd(III)] resonance imaging (MRI) contrast agents. Esther M. Surender, Steve Comby, Sarah Martyn, Brenton Cavanagh, T. Clive Lee, Dermot F. Brougham and Thorfinnur Gunnlaugsson, ***Chem. Commun.***, 2016,**52**, 10858-10861